Even things that are true

can be proved

(Oscar Wilde)

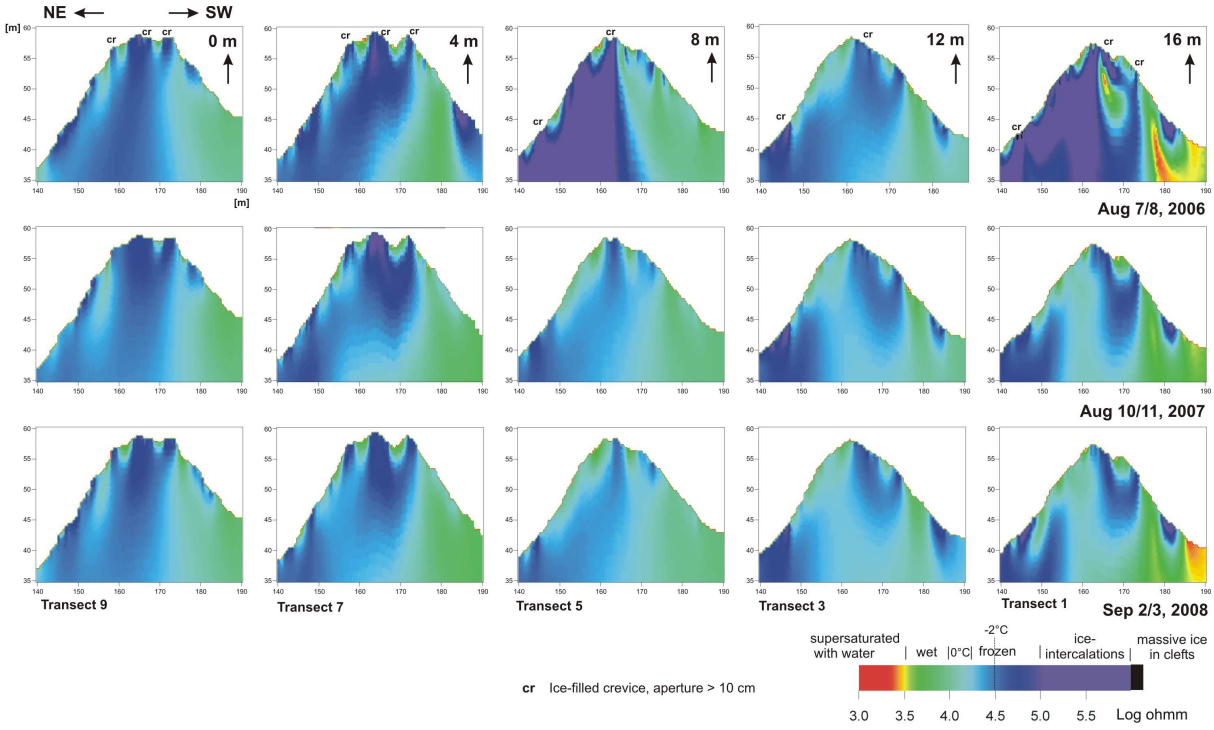

Gewidmet meinen Eltern, Harald, Stephan und Ronja für ihre stetige Unterstützung.

Geographisches Institut der Universität Bonn

Detection and quantification of permafrost change in alpine rock walls

and implications for rock instability

Dissertation

zur Erlangung des Doktorgrades (Dr. rer. nat.)

der

Mathematisch-Naturwissenschaftlichen Fakultät

der

Rheinischen Friedrich-Wilhelms-Universität Bonn

vorgelegt von

Michael Krautblatter

aus

Erlangen

Bonn, den 9.3.2009

Angefertigt mit Genehmigung der Mathematisch-Naturwissenschaftlichen Fakultät

der Rheinischen Friedrich-Wilhelms-Universität Bonn

Gutachter: 1. Prof. Dr. R. Dikau

2. Prof. Dr. W. Haeberli

3. Prof. Dr. A. Kemna

4. Prof. Dr. M. Moser

Datum der Promotion: 1. Juli 2009

Comment:

This Ph.D.-thesis was written in accordance with the rules for "Kumulative Dissertationen" issued on the 12th of December, 2008. Text of articles is printed in the original version in American English. The letter of acceptance for "Krautblatter et al., accepted" arrived too late to include the revision and, thus, the submitted version is presented. The following articles have been incorporated in the thesis:

- Krautblatter, M. and Zisser, N. (submitted): Laboratory evidence for linear temperature-resistivity pathways of thawed, supercooled and frozen permafrost rocks. Geophysical Research Letters.
- Krautblatter and Hauck (2007). Electrical resistivity tomography monitoring of permafrost in solid rock walls. Journal of Geophysical Research, Earth-Surface. Vol. 112(F2), doi: 10.1029/2006JF000546.
- Krautblatter (2009). Patterns of multiannual aggradation of permafrost in rock walls with and without hydraulic interconnectivity (Steintälli, Valley of Zermatt, Swiss Alps). Lecture Notes in Earth Sciences. Vol 115: 199-219.
- Krautblatter, M., Verleysdonk, V., Flores-Orozco, A. and Kemna, A. (accepted): Quantitative temperature-calibrated imaging of seasonal changes in permafrost rock walls by high-resolution ERT and implications for rock slope stability (Zugspitze, German/Austrian Alps). Journal of Geophysical Research, Earth-Surface.
- Krautblatter (2008). Rock Permafrost Geophysics and its Explanatory Power for Permafrost-Induced Rockfalls and Rock Creep: a Perspective. Paper presented at the 9th Int. Conf. on Permafrost, Fairbanks, Alaska, US: 999-1004.

Contents:

1 Abstract

The perennial presence of ice in permafrost rock walls alters thermal, hydraulic and mechanic properties of the rock mass. Temperature-related changes in both, rock mechanical properties (compressive and tensile strength of water-saturated rock) and ice mechanical properties (creep, fracture and cohesive properties) account for the internal mechanical destabilisation of permafrost rocks. Two hypothetical ice-/rock mechanical models were developed based on the principle of superposition. Failure along existing sliding planes is explained by the impact of temperature on shear stress uptake by creep deformation of ice, the propensity of failure along rock-ice fractures and reduced total friction along rough rock-rock contacts. This model may account for the rapid response of rockslides to warming (reaction time). In the long term, brittle fracture propagation is initialised. Warming reduces the shear stress uptake by total friction and decreases the critical fracture toughness along rock bridges. The latter model accounts for slow subcritical destabilisation of whole rock slopes over decades to millennia, subsequent to the warming impulse (relaxation time).

To gain further understanding of thermal, hydraulic and mechanic properties of permafrost rocks, multi-dimensional and multi-temporal insights into the system are required. This Ph.D. adopted, modified and calibrated existing ERT (electrical resistivity tomography) techniques for the use in permafrost rocks. Laboratory analysis of electrical properties of eight rock samples from permafrost summits brought upon evidence that the general exponential temperature-resistivity relation, proposed by McGinnis (1973), is not applicable for frozen rocks, due to the effects of freezing in confined space. We found, that separate linear temperature-resistivity (T-ρ) approximation of unfrozen, supercooled and frozen behaviour offers a better explanation of the involved physics. Frozen T-ρ gradients approach 29.8 ±10.6 %/°C while unfrozen gradients were confirmed at 2.9 ±0.3 %/°C. Both increase with porosity. Path-dependent supercooling T-ρ behavior (3.3 ±2.3 %/°C) until the spontaneous freezing temperature -1.2 (±0.2) °C resembles unfrozen behavior. Spontaneous freezing subsequent to supercooling coincides with sudden self-induced temperature increases of 0.8 (±0.1) °C and resistivity increases of 2.9 (±1.4) kΩm. As temperature-resistivity gradients of frozen rocks are steep, temperature-referenced ERT with accuracies in the range of 1 °C is technically feasible in frozen rock. Technical design for field measurements in permafrost-affected bedrock was developed from 2005 to 2008 in consecutive measurements at a rock crest in the Swiss Alps (Steintaelli, 3150 m a.s.l., Matter Valley) and in a gallery along a north face in the German/Austrian Alps (Zugspitze, 2800 m a.s.l.). 2D measurements in the Steintaelli along S-, NE-, NW- and W-facing rock walls showed that ERT provides information on temporal and spatial patterns of thawing, refreezing, cleftwater flow and permafrost distribution in a decameter scale. Monthly, annual and multiannual data were compared using a time-lapse inversion technique and showed consistent results. Seasonal thaw at the Zugspitze was observed in February and monthly from May to October 2007 with high-resolution ERT (140 electrodes). An error model based on the measured offset of normal-reciprocal measurements was operated to empirically fit inherent error. A smoothness-constrained, error-controlled inversion routine (CRTomo) was applied to gain quantitatively reliable ERT data. Application of temperature-referenced laboratory data is consistent with temperature data observed in the adjacent borehole and with temperature logger data. Calculated temperature changes are in accordance with slow thermal conduction away from the rock surface and subsequent refreezing from the rock face in September/October. Smoothness-constrained, error-controlled inversion was transferred to pseudo-3D measurements collated from five 2D-transects with an offset of 4 m across a NE-SW facing ridge in the Steintaelli. In spite of the enormous topography, ERT transects were capable of resolving permafrost and thaw dynam-

ics at the NE facing slope and along ice-filled crevices as well as disclosing unfrozen rock on the SW-facing rock slope. Consecutive measurements of 2006, 2007 and 2008 provide coherent results in line with temperature logger data.

ERT measurements confirm that aspect is the most important control of permafrost distribution in rock walls, for a given altitude. At 3150 m a.sl., rock permafrost was found in NE-, NW- and E-facing rock walls in the Steintaelli but not in S-facing transects. Multiannual 3D data show that all NE-facing rock slopes still comprise decameter large permafrost bodies, but the $10^{4.5}$ Ωm (31.6 kΩm) line which represents a definite transition to the –2 °C range is not reached in any of the transects apart from the surrounding of ice-filled clefts or at the surface. Semiconductive effects of centimetre to decimetre wide frozen fractures significantly cool ambient bedrock and have a dominant influence on the spatial distribution of permafrost under the crestline. Multiannual 2D data reveal that cleftwater inundation in two fracture systems can effectively prevent a decametre large rockwall from cooling below –1 °C (20 kΩm) during two years with permafrost aggradation (August 2005 to August 2007) in sheltered positions. An adjacent rockwall with similar surface characteristics but no hydraulic interconnectivity cooled significantly below –3 °C (> 60 kΩm) in the same time. Steep, highly dissected rock masses can create local permafrost occurrences of meter size even on SW-facing rock slopes.

Seasonal thaw of rock permafrost occurs much faster than expected. Monthly measurements at the Zugspitze showed that maximum thaw depth in 2007 was already reached in July/August. In May, rapid warming of permafrost rocks with a resistivity increase equivalent to 1.5 °C warming and more was observed along a fracture zone with active cleftwater flows up to 30 m away from the rock face.

Eighteen extensometer transects along the 3D-ERT array in the Steintaelli indicate that rock deformation on the permafrost-affected crest line and in the NE-facing slope is 3-4 times higher than in the non-perennially-frozen SW-facing slope. The velocity of rock displacements in late summer is 20 times higher than in all-season measurements. Velocities along a directly ERT-approved permafrost rock slope respond exponentially to mean air temperature during observation period with an R^2 of 0.86. These findings support the hypothesised rapid sliding response to temperature change due to enhanced ice-creep and failure of ice in fractures.

2 Zusammenfassung

Das ganzjährige Auftreten von Eis in Permafrost-Felswänden verändert die thermalen, hydraulischen und mechanischen Eigenschaften des Gesteinsverbandes. Temperaturabhängige Veränderungen der felsmechanischen Eigenschaften (Druck- und Zugfestigkeit wassergesättigter Gesteine) und eismechanische Eigenschaften (Kriechen, Bruch und kohäsive Eigenschaften) steuern die interne mechanische Destabilisierung von Permafrostfelsen. Zwei hypothetische eis-/felsmechanische Modelle wurden mithilfe des Prinzips der Superposition entwickelt. Erwärmung kann zu eismechanischem Versagen entlang bereits bestehender Gleitflächen führen, durch verminderte Scherspannungsaufnahme von kriechender Eisdeformation, durch schnelleres Versagen von Eis in Klüften und durch reduzierte totale Reibung entlang von rauen Felskontakten. Dieses Model erklärt die schnelle Reaktion von Felsgleitungen auf Erwärmung (Reaktionszeit). Längerfristig werden neue Gleitflächen durch sprödes Versagen intakter Felsbrücken angelegt. Eine Temperaturzunahme reduziert die Scherspannungsaufnahme durch totale Reibung und vermindert die kritische Bruchfestigkeit entlang intakter Felsbrücken. Dieses Model beschreibt die langsame subkritische Destabilisierung von ganzen Felswänden über Jahrzehnte bis Jahrtausende nach einem Erwärmungsimpuls (Relaxationszeit).

Um ein besseres Verständnis der thermalen, hydraulischen und mechanischen Eigenschaften von Permafrostfelsen zu erlangen, bedarf es multidimensionaler und multitemporaler Einblicke in das System. In dieser Dissertation wurden bestehende Techniken der elektrischen Resistivitäts–Tomographie für Permafrostfelsen adaptiert, modifiziert und kalibriert. Eine Laboranalyse der elektrischen Eigenschaften von acht Felsproben von Permafrost-Felsgipfeln belegt, dass das generelle von McGinnis (1973) eingeführte exponentielle Temperatur-Resistivitäts-Verhalten nicht für gefrorene Festgesteine anwendbar ist, aufgrund des Gefriervorganges im beengten Porenraum. Eine separate lineare Approximation der Temperatur-Resistivitäts (T-ρ) Pfade beschreibt die physikalischen Veränderungen von ungefrorenen, gefrorenen und unterkühlten Felsproben wesentlich exakter. Gefrorene T-ρ Gradienten liegen bei 29,8 ±10,6 %/°C während ungefrorene bei 2,9 ±0,3 %/°C bestätigt werden konnten. Beide nehmen mit Porosität zu. Pfadabhängiges Verhalten unterkühlter Felsproben (3,3 ±2,3 %/°C) bis zum spontanen Gefrierpunkt von –1,2 (±0.2) °C ähnelt dem ungefrorenen Verhalten. Bei spontanen Gefrierprozessen nach Unterkühlung treten Temperatursprünge von 0,8 (±0,1) °C und Resistivitätssprünge von 2,9 (±1,4) kΩm auf. Aufgrund der steilen T-ρ Gradienten in gefrorenen Felsen könnte die Anwendung der elektrischen Resistivitäts-Tomographie (ERT) Temperaturunterschiede bis zu einer Genauigkeit von ca. 1 °C auflösen. Im Jahr 2005 wurden bei Feldmessungen in den Schweizer Alpen (Steintälli, 3150 m NN., Mattertal) ERT erstmals erfolgreich in Permafrostfelsen angewendet. Bei zahlreichen Folgemessungen in den Jahren 2005 bis 2008 im Steintälli und in einem Stollen an der Zugspitz-Nordwand (Deutsch/Österreichischen Alpen, 2800 m NN.) wurde die technische Umsetzung von ERT-Messungen in Permafrostfelsen ausgeweitet und optimiert. 2D-Messungen im Steintälli an S-, NE-, NW- und W-exponierten Felsen zeigen, dass ERT zeitliche und räumliche Muster des Auftauens, Wiedergefrierens, der Kluftwasserströme und der Permafrostverbreitung in einer Dekameter großen Felswand auflösen kann. Monatliche, jährliche und mehrjährige Datensätze wurden im Time-Lapse Verfahren miteinander verglichen und zeigten konsistente Resultate. Saisonales Auftauverhalten an der Zugspitze wurde im Februar und monatlich von Mai bis Oktober 2007 mit hochauflösender ERT (140 Elektroden) gemessen. Aufgrund von normal-reziproken Fehlermessungen und einem darauf basierenden Fehlermodel wurde der inhärente Fehler in den Messungen empirisch bestimmt. Um quantitativ verlässliche Daten zu erhalten, wurden die Datensätze in einem individuell auf die Fehlermodelle hin optimierten Inversions-Algorithmus (CRTomo, smoothness-

constrained) prozessiert. Anhand von temperaturreferenzierten Labordaten für Wettersteinkalk konnten den Zugspitztomographien Temperaturbereiche zugeordnet werden. ER Tomographien liefern ähnliche Temperaturwerte wie das nahe gelegene Permafrostbohrloch und die entlang der Messtransekte angebrachten Temperaturlogger. Die aus der ERT errechneten monatlichen Temperaturveränderungen decken sich mit der zu erwartenden langsamen Wärmekonduktion von der Felsoberfläche weg und dem nachfolgenden von der Felsoberfläche ausgehenden Wiedergefrieren im September/Oktober. Die fehlerreferenzierte Inversionsmethode wurde auf eine Pseudo-3D Messungen übertragen, die aus fünf parallelen 2D-Transekten mit einem Abstand von 4 m zusammengesetzt ist. Die verwendeten 2D-Transekte bilden vertikale Schnitte durch den NE- und SW-exponierten Steintälligrat ab. Trotz der enormen Topographie konnten die ERT-Transekte Permafrost und dessen Auftaudynamik am NE-exponierten Hang und entlang eisgefüllter Klüfte abbilden und ungefrorenen Fels auf der SW-Flanke ausweisen. Folgemessungen in den Jahren 2006, 2007 und 2008 zeigen kohärente Ergebnisse in genereller Übereinstimmung mit Temperaturloggerdaten.

ERT-Messungen bestätigen, dass die Exposition bei gleicher Meereshöhe der wichtigste Faktor für Permafrostentwicklung in Felswänden ist. In 3150 m NN. wurde Permafrost in E-, NW- und NE-exponierten Felsen gefunden, aber nicht in S-Exposition. Mehrjährige 3D-Daten zeigen, dass alle NE-exponierten Felswände Dekameter große Permafrostkörper enthalten. Die $10^{4.5}$ Ωm Linie, die den definitiven Übergang zu Temperaturen unter –2 °C repräsentiert, wurde nirgends in den Transekten erreicht, außer in der Umgebung eisgefüllter Klüfte und nahe der Oberfläche. Semikonduktive Effekte in den Zentimeter bis Dezimeter breiten eisgefüllten Klüften kühlen ihre Umgebung signifikant ab und haben einen dominanten Einfluss auf die räumliche Verteilung von Permafrost unter dem Grat. Mehrjährige 2D-Daten belegen, dass die Wasserintrusion in zwei Kluftsystemen das Abkühlen einer 40 m langen Felswand unter –1 °C (20 kΩm), in zwei Jahren (August 2005 - August 2007) mit ansonsten deutlicher Permafrostaggradation in abgeschirmten Bereichen, verhindern kann. Eine nahe gelegene Felswand mit ähnlichen Oberflächen-Charakteristika, aber ohne hydraulische Interkonnektivität, kühlte sich im gleichen Zeitraum deutlich unter –3 °C (>60 kΩm) ab. Steile, stark zerlegte Felspartien können auch auf den SW-exponierten Felswänden lokale Meter große Permafrostkörper schaffen.

Das saisonale Auftauen von Permafrost geschieht schneller als erwartet. Monatliche Messungen an der Zugspitze zeigen, dass die maximale Auftautiefe 2007 bereits im Juli/August erreicht wurde. Im Mai wurde das rasche Auftauen entlang einer 30 m weit in den Fels hineinragenden Kluftzone mit zeitgleich beobachtetem Kluftwasseraustritt gemessen, mit einem Resistivitätsanstieg äquivalent zu 1,5 °C (und mehr) Erwärmung in den umliegenden Permafrostfelsen.

Achtzehn Extensometer-Transekte entlang des 3D-ERT Aufbaus im Steintälli zeigen, dass Felsdeformationen in den vom Permafrost betroffenen Bereichen drei- bis vierfach schneller erfolgen als im permafrostfreien SW-Hang. Die Geschwindigkeit der Felsdeformation nimmt im Spätsommer auf das 20-fache gegenüber Ganzjahresmessungen zu. Geschwindigkeiten entlang einer NE-Wand, in der die Permafrostverbreitung unmittelbar durch ein ERT-Transekt abgesichert ist, zeigen einen exponentiellen Zusammenhang zwischen durchschnittlicher Lufttemperatur und der Bewegungsgeschwindigkeit (R^2 = 0,86). Diese Beobachtungen stützen das Model der schnellen eismechanischen Reaktion auf Erwärmung aufgrund verstärkter Kriechdeformation von Eis und dem mechanischen Versagen entlang des Fels-Eis-Kontaktes.

3 Introduction

An increasing number of hazardous rockfalls and rockslides of all magnitudes is reported from permafrost-affected rock walls. Ice-rock avalanches of bergsturz-size (>1 mio. m³) were documented e.g. at Mt. Steller, Alaska ($5(\pm1)*10^7$ m³) in 2005, at Dzhimarai-Khokh, Russian Caucasus ($4*10^6$ m³) in 2002 as well as at the Brenva ($2*10^6$ m³) and the Punta Thurwieser ($2*10^6$ m³) in the Italian Alps in 1997 and 2004 (Bottino et al., 2002; Crosta et al., 2007; Haeberli et al., 2004; Huggel et al., 2008). Accordingly, enhanced activity of cliff falls (10^4-10^6 m³), block falls (10^2-10^4 m³), boulder falls (10^1-10^2 m³) and debris falls (<10 m³) was observed from permafrost-affected rock faces (Fischer et al., 2007; Rabatel et al., 2008; Ravanel et al., 2008; Sass et al., 2007). The time-gap between climate warming and rockfall response is expected to increase with rockfall magnitude from years to millennia for hundreds of meters thick rockslides (Wegmann, 1998). In that sense the detachment of a $3.5(\pm0.5)*10^8$ m³ rockslide in 3700 B.P. from the permafrost-affected Zugspitze North Face (today 2962 m a.s.l.) was interpreted as a delayed response to the Holocene Climatic Optimum (Gude and Barsch, 2005; Jerz and Poschinger, 1995). Following this line of argument, permafrost degradation was considered as one of the "striking environmental changes in the middle Holocene" (Prager et al., 2008) that caused a peak in large rock slope failure activity in the Italian Dolomites, the Bavarian Alps, the Tyrolean Alps and Swiss Central Alps (Jerz, 1999; Soldati et al., 2004; Tinner et al., 2005).

Heat transfer from the exposed snow-free rock faces to the cool atmosphere in winter is the main constituent factor for rock permafrost, while insulation, warm summer temperatures and hydrological heat transfer inhibit its development (Wegmann, 1998). As most permafrost rock walls in lower altitudes face northerly directions (Gruber et al., 2004b), changes in air temperatures will play a vital role in permafrost degradation. The mean temperature anomaly of Switzerland towards the end of the 20th century (0.5-1.25 °C) exceeded the global anomaly (0-0.5 °C) by far (Jungo and Beniston, 2001). This is due to an unprecedented shift in minimum and maximum temperature trends in Switzerland. The trend is especially pronounced for winter minimum temperatures, which are a key factor for rock permafrost development. According to Beniston (2004: 162) "minimum temperatures have exhibited the strongest warming in the second half of the 20th century, and there is a distinct amplification of this warming at high elevations." Warming of winter temperatures at high elevations systematically corresponds to an increased NAO (North Atlantic Oscillation) Index (Hurrel and van Loon, 1997) and is, therefore, believed to proceed with global warming. Present climate change scenarios for Switzerland herald a rise in temperature of 3 °C by 2050, with possibly increased precipitation in winter and substantial decrease in summer (Beniston, 2004: 202). This points towards an increase in factors (minimum temperatures, maximum temperatures, summer radiation) to which rock permafrost degradation is very susceptible. More generally, Nogués-Bravo et al. (2007) compared the predictions of five different Atmosphere-Ocean Circulation Models and four different IPCC scenarios for 13 different mountain chains in the world. They anticipate a 3-4 °C warming for 2055 for mid-latitude alpine environments and a 4-7 °C warming for high-latitude mountain environments for constant CO_2 emissions scenarios and, respectively, a 2-3 °C and 3-5 °C warming for reduced CO_2 emissions.

While extreme responses to the warm last two decades were reported for all permafrost environments (Isaksen et al., 2007; Jorgenson et al., 2006; Lawrence and Slater, 2005), permafrost decay in high-alpine environments is more difficult to predict for a number of reasons. These include the high importance of local topography, aspect, shading, microclimate, local wind patterns, glacier-permafrost interconnectivity and human interaction. In addi-

tion, there is certain evidence that alpine permafrost systems react more sensitive than Nordic permafrost systems (Haeberli and Beniston, 1998; Kukkonen and Safanda, 2001). As Harris et al. (2003b) point out, observed permafrost temperature changes are more variable in the Alps than in the Nordic permafrost boreholes due to the effects of topography, aspect and local heat transfer. In addition, Alpine permafrost is warmer and closer to thawing. The temperature of alpine permafrost in the upper tens of meters has increased by about 0.5-0.8 °C in the last century (Harris et al., 2003b). This corresponds to an increase of the altitude of the lower permafrost line of 100 m (Frauenfelder, 2005; Haeberli and Beniston, 1998). Salzmann et al. (2007) calculated 36 high-mountain topographic scenarios on the basis of Regional Climate Model scenarios and found that aspect will play a greater role for susceptibility to permafrost degradation than altitude and slope. North-faces will be most affected by climate change. An extensive review of permafrost borehole temperatures by Harris et al. (2009) yielded that shorter-term extreme climatic events are equally important as they are immediately reflected by changes in active layer thickness. The recovery time of active layer thickness subsequent to the summer 2003 is in the range of several years at the surface (Hilbich et al., 2008) and there is a lack of understanding of longer term transient effects initiated by such events (Noetzli, 2008). In some respect, the immediate response of permafrost rockfalls to the 2003 heat wave (Gruber et al., 2004a), can be interpreted as a "shape of things to come" (Beniston, 2004: 186), reflecting the "extremes of temperatures that summers are projected in the later decades of the 21st century."

Among mountain permafrost systems, rock walls could play a vital role in future research due to their enormous hazard potential constituted by the great potential energy that is released in case of instabilities. Present knowledge of several system components of permafrost rock walls is poor such as the impact of partial snow cover (Gruber and Haeberli, 2007), importance of rock wall hydrology (Fischer et al., 2007), the system response of coupled glacier-permafrost systems (Moorman, 2005; Wegmann et al., 1998) and the importance of heat transfer along fractures (Hasler et al., 2008). Such knowledge is needed for the reassessment and reconstruction of infrastructure in and below rock permafrost environments (tourist infrastructure, dams, roads, railways etc.) as many construction sites were built at a time when permafrost-related stability problems were not taken into consideration (Haeberli, pers. comm.).

The aim of this work is to contribute to the thermal, hydraulic, mechanic and geomorphic system understanding of permafrost rocks at the scale of rock instability. The meaning of scale here includes both, the temporal and the spatial scale of rock instability. Anisotropy is the basic problem of all research that focuses on fractured rock. If anisotropy is defined as subscale heterogeneity (Vogel et al., 2006) it is a matter of scale to resolve this heterogeneity in the first place and to find accurate proxies for its description in the larger scale. Most of this work is dedicated to create quantitative reliable, temperature-calibrated and multidimensional ERT with implications for thermal, hydraulic and mechanic applications in fractured permafrost rock. The theoretical requirement is the development of a coupled rock-/ice-mechanical and geomorphological model that accounts for reaction time and relaxation time of permafrost rocks subsequent to warming in terms of brittle fracture propagation and failure on existing sliding planes.

"Periglacial geomorphology must always change in response to the larger scientific context of which it is part", (French and Thorn, 2006) and perhaps this poses both, a conceptual and a technical challenge.

4 Hypotheses

4.1 Theory

1. A better understanding of the instability of permafrost-affected bedrock subsequent to warming could derive from a combination of the relaxation time concept (Brunsden and Thornes, 1979) and its rock mechanical analogue, the subcritical and time-dependent brittle fracture propagation (Kemeny, 2003).
2. Thermal and the geomorphologic understanding of “transience”, while different, provide an approach to understand path-dependent behaviour where the thermal balance was upset by large rock slides or climate change.

4.2 Methodology

3. Resistivity is an accurate proxy of rock temperature.
4. ERT can monitor changes in active layer thickness as well as multiannual permafrost aggradation and degradation accurately in a two-dimensional and three-dimensional space.
5. Quantitative interpretation of temperature and ice-content is possible.

4.3 System understanding

6. Ice- and water-filled discontinuities have a dominant influence on permafrost development in fractured rocks. Hydraulic interconnectivity of dissected rock may prevent effective cooling of decametre large rock walls. Ice in rock factures can dominate permafrost development in dissected rock.
7. Local topography can create limited permafrost bodies in all aspects.
8. ER tomographies operate at the scale of permafrost rock instability and help to gain insight into the principles of rock destabilisation.

5 Rock permafrost: a systems approach

Permafrost is a thermally defined phenomenon as ground that remains below 0 °C for at least two years irrespective of the presence of water in the system (NRC-Permafrost-Subcommitee, 1988). Rock permafrost is generally not synonymous with perennially frozen rock as rock often only freezes significantly below the datum freezing point T_0 (0 °C). Stable alterations of the equilibrium freezing point T_e occur mostly due to the effects of solutes, pressure, pore diameter and pore material (for equations see 6.1.2.1). Below T_e unfrozen supercooled water can still exist in rock pores until the spontaneous freezing point T_s. Strictly defined, the range between T_0 and T_e is attributed to as superheated and the range between T_e and T_s is attributed to as supercooled (Lock, 2005). Colloquially, any unfrozen state below 0 °C is referred to as supercooled. While in water-saturated rocks T_e often approaches values between 0 °C and 1 °C, T_e decreases with low saturations and can approach values of minus several degrees if the water content is reduced to a level close to the adsorbed water content (Mellor, 1973). However, this is rarely the case in alpine rock permafrost settings.

The definition of permafrost includes all rock systems where ice can persist for at least two years in open and confined space. The systemic difference between non-permafrost rocks and permafrost rocks is, thus, the perennial presence of ice (see also French and Thorn, 2006) that has a number of serious implications on the system:

(i) Ice significantly alters *thermal properties* of permafrost rocks at the surface and at depth. On the rock surface, ice occurs as snow, onfrozen ice and glacier ice and significantly alters heat exchange due to long- and short-wave radiation and due to sensible and latent heat fluxes. Inside the rock mass, the good thermal conduction of ice (k = 2.2 W/(m*K)) in pores and rock discontinuities increases heat flux especially across otherwise air-filled discontinuities. The enormous latent melting energy of 334 MJ/m³ buffers frozen rock systems at the surface and at depth and can result in persistent high thermal gradients between frozen rock and the atmosphere with effective heat conduction.

(ii) *Hydraulic properties* of permafrost rocks are affected by the sealing of rock discontinuities and decreased permeability of the intact rock mass. Perched water-tables result in enormous hydrostatic pressures that significantly alter rock stability. Ice effectively stores water in permafrost rocks and dispenses water in summer and autumn with implications for weathering, ice segregation and rock stability.

(iii) *Mechanical properties* undergo significant alterations around the freezing point. Compressive and tensile rock mass strength in frozen rocks strongly decreases with increasing temperature close to thawing point. Ice mechanical properties of deformation and cracking become increasingly important. The presence of ice creates cohesive connections in rock discontinuities which are otherwise often absent (Cruden, 2003). Ice segregation may play an important role due to the dilatation and dislocation of shear surfaces.

(iv) The *geomorphic systems* of permafrost rocks is significantly different from other rock environments. While temperate rocks are affected by changing climate mostly at the surface due to alterations in weathering, mechanical and hydraulical properties of permafrost rocks in all depths undergo permanent changes due to thermal signals of climatic fluctuations. The described sensitivity

in combination with long relaxation times in respect to the slow speed of thermal conduction turns permafrost rocks into a highly path-dependent system. The interplay of slow and reversible heat conduction processes and the rapid, irreversible heat transfers evoked by cleft water in an anisotropic medium causes complex behaviour that is not exactly predictable in deterministic terms.

5.1 Thermal properties

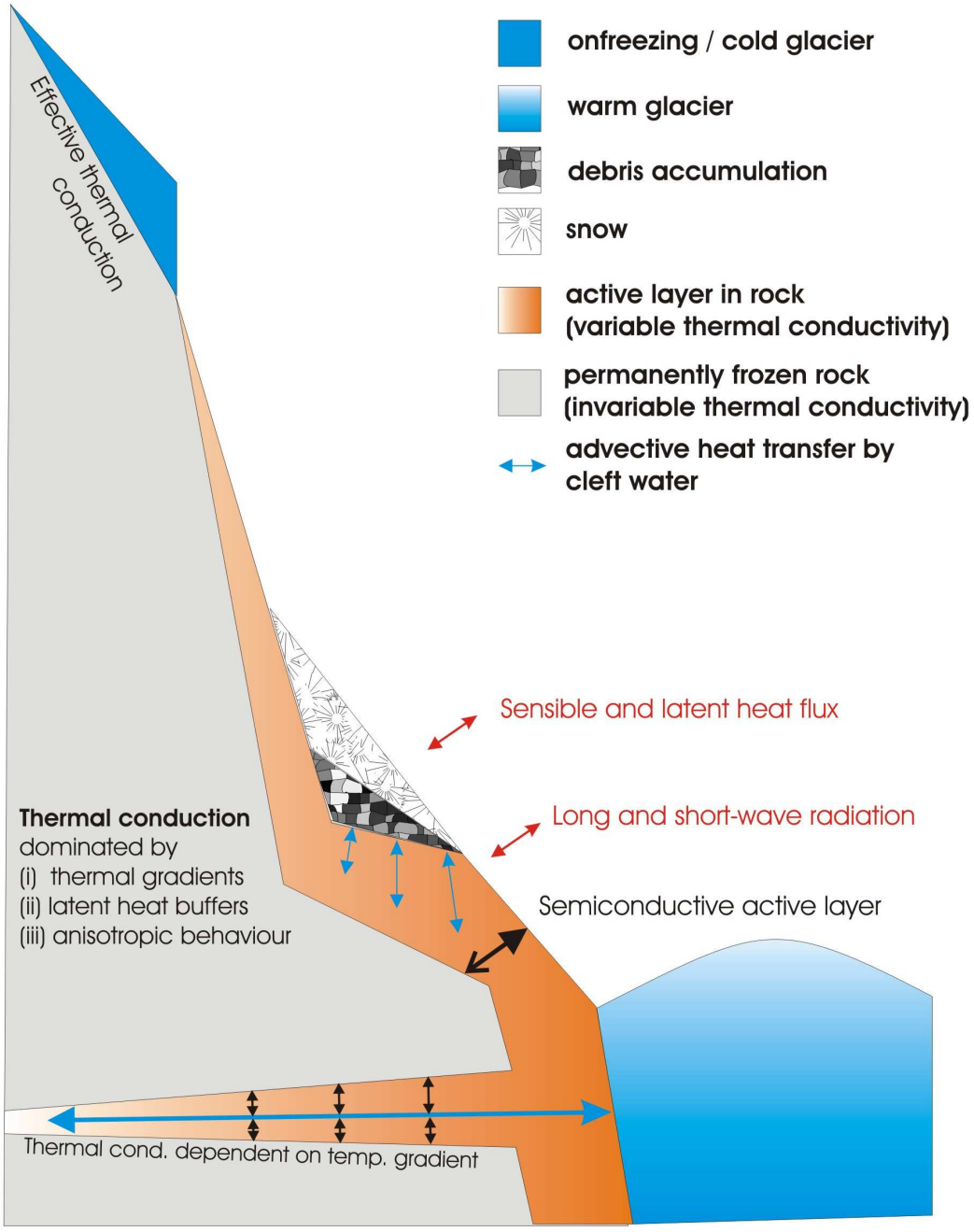

Fig. 1: A conceptual model for the thermal development of rock permafrost including two-dimensional sources of heterogeneity.

Geophysical methods described in Section 6 detect and monitor active layer dynamics and permafrost distribution on a meter to decametre scale and cover significant heterogeneity due to local snow cover, onfreezing and hydraulic interconnectivity. Fig. 1 shows a conceptual approach to major sources of heterogeneity on this scale based on the following assumptions: (i) Active layer thickness at the surface decreases with altitude (Gruber et al., 2004a). (ii) Onfrozen glacierets and cold glaciers are situated directly on perennially frozen rocks (Huggel, in press). (iii) Debris accumulations in rock faces have maximum angles of 45° (max. angle of repose) and are therefore snow-covered in winter. They usually do not consist of large blocks as preferably small particles accumulate on small and inclined ledges (Dorren, 2003). (iv) Warm glaciers conduct massive advective heat transfer with adjacent rocks (Moorman, 2005; Wegmann et al., 1998). (v) The active layer is "semiconductive" as thermal conduction in the frozen intact rock mass and across ice-filled rock discontinuities performs better than in unfrozen rock and across air-filled rock discontinuities.

5.1.1 Basic system

Besides the rock matrix, bedrock permafrost systems involve ice, air and often a residuum of unfrozen water in pores and rock discontinuities. Thus, the rock permafrost system basically consists of rock, ice, air and water. The thermal energy ($U_{thermal}$) of this system is added up by both,

$$U_{thermal} = U_s + U_l$$

Equ. 5.1

sensible energy (U_s), that is related to the molecular kinetic energy (translation, rotation, vibration and spin) and latent energy (U_l) that is associated with phase transition. Any heat (Q) put into or taken out of the system will result in a change of the thermal energy $\Delta U_{thermal}$ equal to Q.

5.1.2 External heat fluxes

Four types of *external* heat fluxes alter the thermal energy (Section 5.1.3) of permafrost rock systems: long- and short-wave radiation, sensible and latent heat fluxes at the surface, geothermal heat fluxes and transient thermal fluxes that derive from past climatic changes. Heat transfer in fractures is discussed in Section 5.1.3.5.

5.1.2.1 Long-wave and short-wave radiation

The heat Q_r [W] put into or taken out of the system by the net radiation flux R_n [W/m²] is given by

$$Q_r = AR_n$$

Equ. 5.2

where A [m²] is the surface area that receives and emits radiation. The net radiation is

$$R = S_{in}(1-\alpha) + L_{in} - L_{out}$$

Equ. 5.3

where S_{in} is the incoming short-wave radiation (<4 µm), α is the albedo, L_{in} is the incoming long-wave radiation (>4 µm) and L_{out} is the outgoing long-wave radiation. The total incoming short-wave radiation S_{in} is

$$S_{in} = S_{dir} + S_{dif} + S_{ref}$$

Equ. 5.4

where S_{dir} is direct irradiance, S_{dif} is diffuse irradiance and S_{ref} is reflected irradiance. The direct potential solar irradiance S_0 that could be received at a sloping site in the absence of atmosphere is

$$S_0 = \frac{24I}{r^2\pi}\cos\phi\cos\delta(\sin\eta - \eta\cos\eta)$$

Equ. 5.5

where I is the solar constant, r is the ratio of the actual Earth-Sun distance to its mean, δ is the solar declination, and ϕ and η are functions of terrestrial latitude, slope angle and aspect (for details see Moore et al., 1993). The mean annual potential solar radiation in Switzerland received in steep rock walls (60-105°) usually ranges between 50 W/m² (N/NW) and 270 W/m² (S/SE) (Peter, 2003). The diffuse irradiance is a result of the scattering processes determined by thickness and composition of the atmosphere and also depends on the albedo of the surrounding surfaces. The proportion of diffuse irradiance reaches 100 %, if the sky is totally covered by clouds (Hoelze, 1994). The albedo quantifies the proportion of incoming short-wave radiation that is reflected and depends mainly on material and surface roughness. Snow in less inclined positions and ice-coating can heavily affect surface albedo in rock faces. Hoelzle at al. (2001) showed that up to 80 % of the incoming irradiation were reflected on the Murtèl rock glacier when it was thickly covered with snow in spring. Even if snow does usually not accumulate on rock slopes steeper than 60°, all larger rock-walls include ledges and less inclined sections with significant snow-accumulation. Variations in the short-wave radiation balances are a major source of inter-annual variations in thaw depth.

Incoming and outgoing long-wave radiation can be approached by the Stefan-Boltzmann Law that defines the emission of long-wave radiation of a black body. Applying it to a grey body, that does not emit or absorb the radiative flux totally, the emission of long-wave radiation L_{out} can be calculated as

$$L_{out} = \varepsilon_s \sigma T^4$$

Equ. 5.6

where ε_s is the surface emissivity, σ is the Stefan-Boltzmann constant ($5.67*10^{-8}$ J/(s*m²*K⁴)) and T is the temperature [K]. In practice, the emissivity is dependent on the wave-length, surface roughness and material. It typically approaches values from 0.45 (granite) to 0.95 (limestone) for rocks and even higher values for ice (0.97-0.98). The emissivity of snow ranges typically from 0.8-0.9. As snow is a good insulator, snow surface tempera-

tures can decline rapidly and decrease heat long-wave emission effectively. Hoelzle (1994) could show that the long-wave emission in permafrost environments shows strong spatial and seasonal variations due to the influence of snow cover.

The incoming long-wave radiation L_{in} can be approached by

$$L_{in} = \varepsilon_a \sigma T_a^4 \upsilon + (1-\upsilon) L_{out}$$

Equ. 5.7

where ε_a is the atmospheric emissivity, which is a function of air temperature, vapour pressure and cloudiness, T_a is the mean air temperature and υ is the fraction of sky that can be seen from a sloping surface (skyview factor).

Hoelzle et al. (2001) could show that in the case of the Murtel rock glacier L_{out} ranges mostly between 250 and 350 W/m² and persistently exceeds L_{in} by tens of W/m². This is balanced by an excess of incoming short-wave radiation of up to 100 W/m² when snow is absent (Stocker-Mittaz et al., 2002).

This has number of implications for the radiation heat flux on rock slopes: (i) Generally spoken, variations in short-wave irradiance due to aspect, slope angle and shading are the most important factors that account for the heterogeneity of mountain rock permafrost. (ii) Variations in *potential* short-wave incoming radiation and the albedo due to snow- and ice-cover have a major impact on the seasonal dynamics of rock permafrost. (iii) Inter-annual variations in the *real* incoming short-wave radiation, due to mean atmospheric conditions and reduced albedo (such as during the hot summer 2003), are a major source of annual fluctuations in thaw depth. (iv) Incoming long-wave radiation is heavily dependent on the skyview factor, while outgoing long-wave radiation is less affected. Thus, the excess of long-wave emission may become more important in steep and shielded positions in dissected rock masses. (v) Surface emissivity of different rock materials varies by a factor of two (granite-limestone) and could have a certain impact on long-wave radiation balances. (vi) Not only short-wave irradiation but also long-wave emission shows strong seasonal fluctuations (Hoelze, 1994; Hoelzle et al., 2001; Stocker-Mittaz et al., 2002). Both, thin snow cover (Keller and Gubler, 1993) and ice-coating with an emissivity close to a black body could effectively increase outgoing long-wave radiation. (vii) In shielded positions and in dissected rock masses, the area that emits long-wave radiation can be much larger than the area that receives incoming short-wave and long-wave radiation.

5.1.2.2 Sensible and latent surface heat fluxes

External sensible and latent heat fluxes occur on the rock surface and inside the rock mass along discontinuities. The latter will be specified in Section 5.1.3.5. The sensible heat flux Q_s on a surface can be approximated by

$$Q_s = -\overline{\rho_a} c_{pa} K_m \left(\frac{dT}{dz} + T_d\right)$$

Equ. 5.8

where ρ_a is the density of the air, c_{pa} is the heat capacity of air, dT/dz is the temperature gradient, T_d is the dry adiabatic lapse rate (9.8 °C/km) and K_m is the turbulent transport coefficient. The latter is influenced by wind speed, surface roughness and the difference between surface and air temperature.

The latent heat flux can be approached by

$$Q_l = -\overline{\rho}_a L K_m \left(\frac{d\overline{q}}{dz}\right)$$

Equ. 5.9

where L is the heat of vaporization (2.5 KJ/g at 0 °C) and dq/dz is the gradient of the specific humidity [g/g]. The overall magnitude of latent and sensible heat fluxes on the surface is an order of magnitude smaller than radiation heat fluxes (Hoelzle et al., 2001). Turbulent latent and sensitive heat fluxes range between –20 W/m² and + 20 W/m² for the Murtèl rock glacier (Mittaz et al., 2000). The turbulent heat flux is strongly reduced in winter as snow cover reduces aerodynamic roughness length, emissivity and insulation. The latent heat flux is strongly reduced on inclined surfaces such as rock slopes and is probably not very important for rock slopes. Sensible heat fluxes may become more important for high wind speed or for high surface roughness on dissected rock walls. Hanson and Hoelze (2004) could show that heat exchange along rock boulders derives from a complex pattern of advective air currents and vertical displacement due to density differences and air pumping rather than a “continuous exchange with the atmosphere”. Vertical heat exchanges become important especially at low temperatures and effective turbulent fluxes only occur when the snow above the blocky matrix was thinner than 0.6 m.

(i) Turbulent heat fluxes are an order of magnitude smaller than radiation heat fluxes. (ii) The importance of latent fluxes at the rock surface is perhaps important for phenomena such as icing and onfreezing of snow but it is reduced for the evaporation at the rock surface as this affects only a small amount of water in the upper centimetres of the rock surface. (iii) Turbulent heat fluxes show complex behaviour which is evident for the turbulent transport coefficient, that is strongly susceptible to factors such as (turbulent) wind speed and surface roughness (with/without snow). Both factors are highly variable in time and space. (iv) Empiric-statistical models of emerging patterns such as chimneys in dissected block masses could help to approximate the importance of turbulent heat flux processes.

5.1.2.3 Geothermal and transient thermal fluxes

The geothermal heat flux from depth is usually around 0.05 W/m² and, thus, several orders of magnitude lower than the external heat fluxes described above. Borehole profiles in permafrost bedrock indicate that past climatic signals still persist in several decametres depth and more (Kukkonen and Safanda, 2001; Lachenbruch and Marshall, 1986; Wegmann, 1998). Kohl (1999) could show that even signals in several hundred meters depth can be modified by topography. Several studies provided evidence that it is necessary to consider transient effects on a Holocene time scale (Little Ice Age, Climatic Optima) as well as on a Quaternary time scale (Last Glacial Maximum) for adequate modelling of present thermal fluxes (Kohl and Gruber, 2003; Noetzli, 2008; Wegmann et al., 1998).

5.1.3 Internal heat uptake and transmission

Strongly modified from Section 2 "System considerations" from Krautblatter (2009). Patterns of multiannual aggradation of permafrost in rock walls with and without hydraulic interconnectivity (Steintaelli, Valley of Zermatt, Swiss Alps). Lecture Notes in Earth Sciences. Vol 105.

5.1.3.1 Basic sensitive system

Let us first consider a closed system that exclusively consists of rock without pores and discontinuities, has theoretically no spatial extension and no heat exchanges with the lithosphere below or the atmosphere above. Any heat (Q) put into or taken out of the system (ΔU_s=Q) will result in a change of temperature (ΔT),

$$\Delta T = \Delta U_s / (c * m)$$

Equ. 5.10

where *m* is the rock mass and *c* is the specific heat capacity. Vosteen and Schellschmidt (2003) sampled 26 Eastern Alpine rocks and showed that *c* (close to 0 °C) of magmatic and metamorphic rocks approaches values of 0.75-0.8 kJ/(kg*K) while sedimentary rocks vary more and *c* approaches values of 0.8 to 0.9 kJ/(kg*K).

5.1.3.2 Spatial dimension

As soon as the closed rock system has a certain spatial extent (and is observed for a restricted time) the entropy concept becomes important. According to the second law of thermodynamics, heat energy added to one part of the system will not be fully dispersed in the system but part of it will rather serve to increase the entropy of a system. This has two fundamental consequences. Heat will always be transferred from the warmer to the colder part and the speed of this transfer will decrease with lower temperature differences corresponding to an increase in entropy. A quantity of heat ΔQ

$$(\Delta Q / A) = (k / l) * \Delta T * t$$

Equ. 5.11

is transmitted during time *t* perpendicular to rock surface *A* through a rock wall thickness *l* for a given temperature gradient ΔT. The thermal conductivity *k* approaches values from 1-3.5 W/(m*K) for most rock types. Vosteen and Schellschmidt (2003) showed that *k* close to 0 °C of igneous and metamorphic rocks mostly approaches values of 1.5-3.5 W/(m*K) while *k* in sedimentary rocks approach on average values from 2 to 4 W/(m*K).

5.1.3.3 Latent phase transitions

While the presence of non-circulating air with its low heat capacity in pores is not very important in the system, water has a significant influence, as the phase transition from ice to water requires latent energy (U_l),

$$\Delta U_l = V_r * p_w * 334(MJ / m^3)$$

Equ. 5.12

where V_r is the volume of rock (in m³) and p_w is the porosity. E.g. to increase the temperature of a m³ of granite or limestone (2700 kg) with water-filled porosity of 5 % (50 kg) from –0.5 to 0.5 °C, approximately 2.2 MJ of sensible energy and 16.7 MJ of latent energy are required. Thus, frozen and thawed rocks are separated by a phase transition with enormous energy consumption as soon as water is present in the system (Wegmann, 1998).

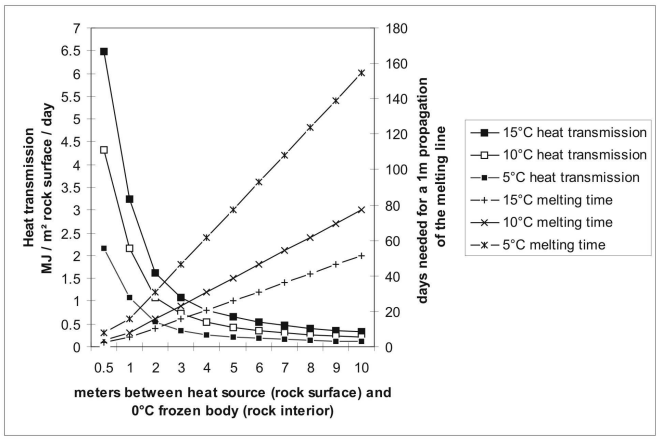

Fig. 2: Theoretical heat transmission and melting time at different depths.

The left axis describes how much heat (MJ/day) is transmitted if a temperature difference of 5 °C, 10 °C or 15 °C persists continuously between rock surface and the rock interior at a certain depth. The right axis shows how many days this specific heat flow must theoretically continue to let the melting line propagate one meter further. A steady state system is assumed with unidirectional heat flow, a k-value of 2.5, and a latent energy consumption of 16.7 MJ for melting one m³ of rock with 5 % water-filled porosity,.

5.1.3.4 Discontinuous heat flow

Heat transmission with constant temperature gradients as presented in Fig. 2 is not realistic due to two reasons. Firstly, rock surface temperatures change steadily according to differences in radiation, air temperatures and other factors such as snow cover or ice-coating. Secondly, during heat transmission, the temperature gradient changes as the temperature in the rock interior alters. This has major implications: (i) Heat transmission to greater depths adjusts to the integral temperature gradients over a longer time. (ii) Heat transmission by short rock surface anomalies initiates warm/cool waves that propagate through the rock according to the laws of ther-

mal conduction. (iii) These waves are often absorbed at depths where latent phase transitions occur. (iv) Heat transfer is a multidirectional phenomenon whose most effective direction is adjusted to thermal gradients.

5.1.3.5 Heat transfer in clefts

Anisotropic behaviour of clefts becomes important in the case of rock discontinuity systems with significant cross-sectional and longitudinal extension to allow fluids and air to circulate or ice to seal clefts. Air filled-discontinuities are most common at the rock surface, while below the internal rock water level most discontinuities are filled with either ice or water. In permafrost rocks, the blocking of discontinuities against seepage by ice generally causes high water levels. Anisotropic behaviour of ice-filled clefts is a relatively straightforward concept explained by the thermal conduction of ice. Thoroughly frozen rock along ice-filled discontinuities can be explained by the good thermal conduction (k = 2.2 W/(m*K)) of ice without latent buffers in the readily frozen ice in clefts.

In the case of mass transfer in water-filled clefts between the rock permafrost system and its surroundings, the concept of entropy becomes increasingly important. This is best explained by the following example. The system setting is frozen rock at 0 °C, but still with ice-filled pores. Fluid water from the surrounding intrudes into permafrost rocks via cleft systems. If water temperature is above 0 °C, water will be cooled as the heat flow away from the cleft system is proportional to the temperature gradient (Equ. 5.11). At 0 °C, cleft water still contains 334 MJ/m³ of latent energy, but this latent energy is no longer available for melting apart from the cleft, as heat transmission away from the cleft is determined by sensible temperature differences. During the described cooling process, entropy, the unavailability of the system to do work, increases to a maximum. While the heat uptake of sensible heat alongside the cleft follows equation Equ. 5.11, the entropy (S) [J/K] change in the system is theoretically approached by

$$\frac{dS}{dt} = \sum_{k=1}^{K} \dot{M}_k \hat{S}_k + \sum_{j=1}^{J} \frac{\dot{Q}_j}{T_j} + \dot{S}_{\text{int}}$$

Equ. 5.13

,where $\sum_{k=1}^{K} \dot{M}_k \hat{S}_k$ is the net rate of entropy flow due to mass exchange with the surroundings, $\sum_{j=1}^{J} \frac{\dot{Q}_j}{T_j}$ is the net rate of entropy due to the heat exchange with the surroundings and $\dot{S}_{\text{int}}$ is the internal entropy generation. This means that in the case of cleft water close to 0 °C, the thermal effect is determined by hydraulic flow patterns in fractured rocks as heat transmission away from the clefts is not very effective.

5.1.3.6 Feedbacks

The ice-water transition in the rock permafrost systems causes some positive/negative feedbacks. E.g. a rock mass with ice-filled porosity has a slightly higher k-value than thawed rock with water-filled porosity. This results in a slightly more effective cooling during the freezing period in comparison to warming in the summer

period. The same is true for small clefts in which no turbulent mixing processes take place (Hasler et al., 2008). However, these feedbacks are possibly not relevant on a larger scale.

5.1.3.7 Response times

According to the mentioned thermodynamic rules, one can outline some general findings for rock permafrost response times: (i) The temporal dimension of response times is governed by the speed of heat propagation. (ii) Dynamics and direction of heat propagation are dominated by sensitive thermal gradients. (iii) Discontinuous heat flux at the rock surface causes steadily changing temperature gradients and results in daily warm/cold pulses in the upper meter, a propagation of several meters for pulses generated during several day-lasting unusual cold/warm periods and integral seasonal pulses that usually reach a penetration depth in the range of one decametre (Gruber et al., 2004b). (iv) Latent heat transfer from frozen to thawed rock requires high amounts of energy, often stops heat pulses and increases response times at greater depths enormously (Wegmann, 1998). (v) Permafrost rocks perform more heat transfer with the surroundings than non-permafrost rocks as latent phase transitions keep temperature gradients constant and as frozen rock has a higher thermal conductivity. (vi) Anisotropic behaviour of well-jointed rock masses significantly influences heat transfer and response times. (vii) In the case of hydraulic interconnectivity with water temperatures close to 0 °C, spatial patterns of melting are orientated directly along hydraulic pathways as heat propagation away from clefts is not effective.

5.1.4 Empiric data

This section aims to give a short review on what is known and implemented in existing thermal rock permafrost models to reveal how an where temperature-referenced geophysics can contribute to the thermal understanding of permafrost rocks.

5.1.4.1 Rock surface temperatures and extrapolation of thaw depth

Based on 15 Loggers placed in rock walls with different aspects in SE-Switzerland, SW-Switzerland and Central Switzerland, Peter (2003) and Gruber at al. (2004b) identified general statistical trends of rock surface measurements based on a one year data set from 2001 to 2002. Temperature sensors were placed in 10 cm rock depth in homogeneous, undissected rock walls steeper than 60° and more than 5 m above ground that allows the accumulation of snow. They showed that the mean annual rock temperature (MART) correlates best with altitude ($R = 0.81$) and less with aspect ($R = 0.43$), while net radiation is badly correlated ($R = 0.25$). In contrast, daily and monthly temperature amplitudes are well explained by aspect ($R > 0.8$), while altitude becomes most important for annual amplitudes ($R = 0.57$). Radiation and aspect are important to explain the difference between mean annual air temperature (MAAT) and MART ($R > 0.8$). Based on the empiric-statistical relations developed by Gruber and Hoelzle (2001), Peter (2003) developed an empirical relationship for the difference of T_{MAAT} and T_{MART}

$$T_{MAAT} - T_{MART} = 0.031 + 0.034 * S_0$$

Equ. 5.14

where S_0 is the direct potential radiation (see section 5.1.2.1). This relation can then be used to approach the maximum thaw depth z_a

$$z_a = \sqrt{\frac{k * P}{\rho c \pi}} \ln \frac{A_0}{T_{MART}}$$

Equ. 5.15

where k is the thermal conductivity, P is the period (1 year), ρ is the rock density, c is the specific heat capacity of the rock and A_0 is the annual temperature amplitude approached by a sine function (Peter, 2003). Thaw determined with this method ranges from 9 m in the Monte Rosa East Face at 4545 m a.s.l. to 11.5 m at the Klein Matterhorn South Face at 3850 m a.sl.. Values similar to north facing conditions at the study site Steintaelli (Valais, Switzerland, Section 6) at 3150 m a.s.l. were obtained at the Eiger NW Face (2860 m a.s.l.; 11.4 m thaw depth) and at the Corvatsch North Face (3290 m; 9.3 m thaw depth).

5.1.4.2 Borehole temperatures close to the study sites

A vast amount of permafrost borehole information has been gathered in the last 20 years and outcomes have been reviewed in several papers (Harris et al., 2009; Harris et al., 2003b). I will concentrate on two boreholes close to the study sites Zugspitze (Germany) and Steintaelli (Switzerland) described in Section 6. In August 2007, a 44 m long borehole was drilled from the south face to the north face under the Zugspitze summit on behalf of the Bavarian Environment Agency at approximately 2930 m a.s.l.. 25 temperature loggers in the borehole provide point and gradient information. Measurements from 2007 to 2008 indicate that minimum temperatures are close to –4 °C and occur at 10-15 m distance from the north face. Active layer depth in 2008 was 1.5 m on the north-face and 7 m on the south-face while seasonal variations in temperature greater than ±0.5 °C are restricted to the upper 12-13 m from the north face and approximately 10 m from the south face. Permafrost core temperature values range between –3 °C and –4 °C.

The closest deep permafrost borehole to the study site Steintaelli with bedrock conditions is the Stockhorn Plateau at a distance of approximately 25 km and at an altitude of 3410 m a.s.l. However, the topography of the gentle Stockhorn Plateau is different from the relatively steep Steintaelli crest line. The 100 m deep borehole is placed on the plateau at a distance of ca. 20 m from the northern slope. The lowest mean annual temperatures close to –2.5 °C (October 2001 to October 2002) occur at approximately 20-40 m depth and at greater depths temperatures increase up to –1.3 °C in 100 m depth (Gruber et al., 2004b). Extrapolated temperature gradients indicate a permafrost thickness of 170-180 m. Maximum thaw depth with long zero-curtain effects was observed at 3.3 m depth. Another 17 m deep borehole is placed at the gentle southern slope. Temperatures below –1 °C only occur in 7-17 m depth, temperatures above range between –0.5 and –1 °C. There are some indications that surface borehole temperatures are disturbed by installations (Gruber et al., 2004b).

5.1.4.3 Thermal modelling

The application of physically-based models in rock permafrost is facilitated by the fact that rock permafrost often lacks the isolating cover of debris and snow. Wegmann et al. (1998) introduced one- and two-dimensional models that parameterise sensible and latent fluxes on exposed bedrock surfaces in response to glacier retreat at a decadal scale. Kukkonen and Safanda (2001) modeled Holocene fluctuations in bedrock permafrost thickness using a one- and two-dimensional physically-based model. In both models, the amount of latent heat that is necessary for a water/ice phase transition is a key factor influencing thermal inertia and makes them highly sensitive to rock porosity values. Gruber et al. (2004b; 2003) developed a physically-based model that is especially adopted to high-mountain topography (TEBAL, Topography and Energy Balance Model) based on the existing PERMABAL model (Stocker-Mittaz et al., 2002). The adoption included the implementation of a latent heat module (Crank-Nikolson Scheme according to Wegmann et al. (1998)), terrain shading and solar geometry as well as radiation neighbourhood effects (Gruber, 2005). This model has been validated with near-surface rock temperature measurements (Gruber et al., 2004b; Gruber et al., 2003) using meteorological and terrain parameters as input data. However, for many applied and scientific applications such as the investigation of slope instability, the identification of more local distribution patterns on slopes is demanded (Harris et al., 2001). Therefore, refining models to create higher resolutions is essential for a better process understanding within complex three-dimensional mountain topography (Harris et al., 2009).

5.1.4.3.1 Rock surface temperatures modelled by TEBAL

TEBAL (Gruber, 2005; Noetzli et al., 2007) basically calculates the radiation balance at the rock surface, based on short-wave and long-wave incoming and outgoing radiation, as well as sensitive heat transfer. Latent heat transfer is extremely reduced for steep rock surfaces.

Data input includes data on topography, climatic conditions, surface properties and subsurface characteristics. Topography is implemented via DEMs. Climate data includes air temperature, air pressure, air humidity, wind speed and direction, precipitation and global radiation balances. Surface properties of rock are implemented via albedo, emissivity and surface roughness. Subsurface thermal properties are approached via thermal conductivity, heat capacity and pore volume.

The generated model output is basically a 3D-grid of average surface temperatures. Heat conduction to the subsurface can thus be considered as the residual of surface energy balances. Recently, much attention is spent on transient thermal signals (Noetzli, 2008).

5.1.4.3.2 Rock internal energy fluxes

Energy fluxes inside the rock were originally modelled with FRACTURE, „Flow, Rock and Coupled Temperature Effects" (Kohl, 1999) and are presently implemented in a new COMSOL environment. 3D-heat propagation inside the rock mass is modelled applying the laws of 3D heat conduction and latent phase changes are imple-

mented (Wegmann, 1998). Data input are the thermal TEBAL-residual and rock mass properties. Usually a thermal conductivity of 2.5 [W / (K*m)] is assumed, heat capacity is $2*10^6$ J / (m^3*K) and porosity is set to 3 %. The model output is a 3D-time series of thermal conduction, temperature and temperature change.

5.1.4.3.3 Application to the study sites Steintaelli and Zugspitze

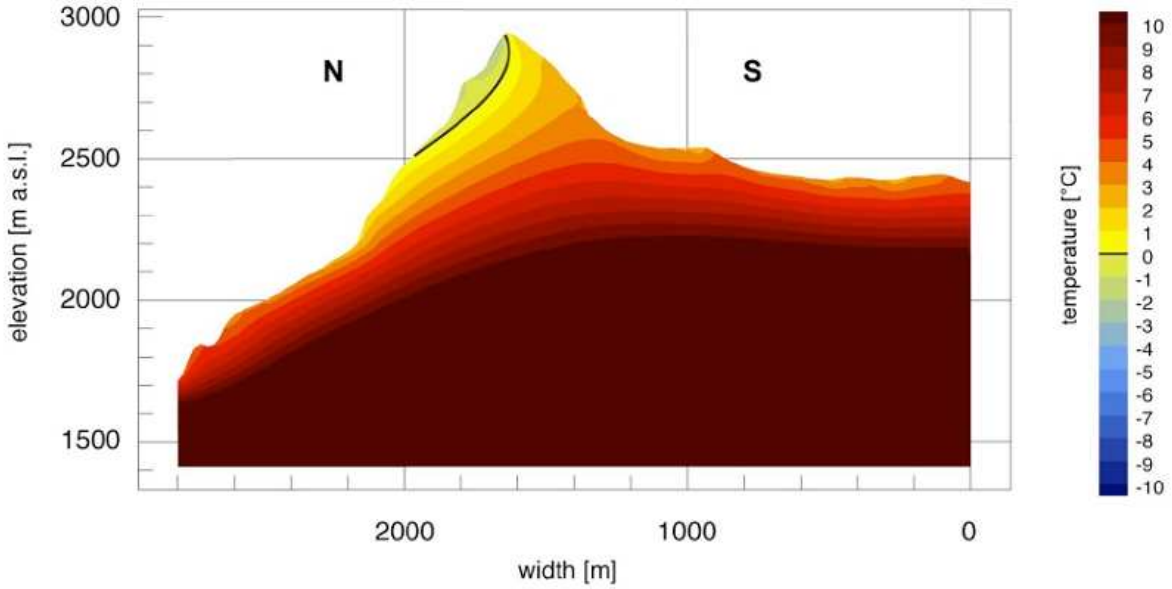

Fig. 3: North-South-Transect cutting through the Zugspitze summit at Gauss-Krueger coordinates 4423552.

With friendly permission from J. Noetzli.

For conditions present in the Steintaelli (Sections 6.2, 6.3 and 6.4), i.e. a 70° steep and NE-facing rock slope at 3150 m a.s.l., model results by Gruber et al. (2004a) suggest that for the last 21 years mean annual ground surface temperatures ranged between 0 °C and –2 °C. Due to the warming tendency in the 20th century, a 1 °C warming of mean annual ground surface temperature or a 150 m uplift of the 0 °C line is expected to better approach the present situation (Gruber et al., 2004a; Haeberli and Beniston, 1998). This corresponds to a transient range of rock permafrost, where only some years have mean annual ground surface temperatures below 0 °C.

Fig. 3 shows the initial approach to model permafrost distribution in the Zugspitze summit. Modelling was based on empirical relationships obtained in Switzerland and a comparison with borehole data (above) shows that permafrost in the Northern Alps may occur at lower elevations and is colder than in resembling topographic conditions in the Central Swiss Alps.

5.1.4.3.4 Model "shortcomings"

A number of surface properties and subsurface properties that may significantly influence permafrost development have not been implemented in modelling, so far. Among the surface properties snow and differential heat

conduction of heavily dissected rock masses may play an important role (Gruber and Haeberli, 2007; Hanson and Hoelzle, 2004). Another factor that is not yet implemented is the effect of subscale topography such as overhang positions or local shielding effects that may also strongly disturb long wave net balances (Section 5.1.2.1). Inside the rock, anisotropy and heterogeneity may still be the most challenging factors. All types of energy transport along rock fractures can cause significant thermal disturbances in the rock. Air-filled fractures may be important where air can circulate through the system. Percolation through water-filled clefts and enhanced thermal conduction along ice-filled clefts is probably even more important. While the impact of fractures has been observed at different field sites, more or less no data is available to evaluate their importance in terms of permafrost evolution (Hasler et al., 2008). As the time gap between rockfall occurrence and maximum thaw depth shows, seasonal heat propagation appears to be poorly understood. Finally, it should be considered that petrophysical factors such as (long-wave) emissivity, albedo, thermal conductivity and the degree of interconnected factures widely varies in different lithologies and geomorphologic settings. This has not been taken into account yet.

5.2 Hydraulic properties

A number of hydraulic properties undergo significant changes in permafrost-affected bedrock. These include (i) permeability, which causes perched cleft-water levels during the thaw season in combination with high hydrostatic pressures and (ii) water storage in the system due to the presence of ice in pores and rock discontinuities.

5.2.1 Laminar and turbulent fluid flow in fractured rock

Based on Darcy's law, laminar fluid flow though a planar equal-spaced rock fracture can be approached by the "parallel plate model" as

$$\frac{Q}{\Delta h} = \frac{C(2b)^3}{f}$$

Equ. 5.16

where $Q/\Delta h$ is the flux per unit drop in head, C is a constant that depends on the geometry of the flow field and $2b$ is the aperture of the fracture for $f > 1$. According to empirical studies by G. M. Lomize in the 1950s, f accounts for the deviation of flow conditions of rough surfaces from ideal laminar flow between glass plates and can be calculated as

$$f = 1.0 + 6.0\left(\frac{\varepsilon}{2b}\right)^{1.5}$$

Equ. 5.17

where ε is the absolute height of asperities (Witherspoon, 2000).

Between relatively smooth surfaces ($\varepsilon/2b < 0.1$) the transition from laminar to turbulent flow occurs at a Reynolds number of about 2400. Between rough surfaces it occurs at a significantly lower Reynolds number

(Witherspoon, 2000). While some empiric data sets show a relatively good fit with this simple model, fluid flow in fractured rocks often shows highly nonlinear, chaotic behaviour and many aspects are still poorly understood (Berkowitz, 2002; Kolditz, 2001).

5.2.2 Influence of permafrost on permeability in fractured rock

The impact of permafrost on hydraulic rock permeability has not received much attention yet. Kleinberg and Griffin (2005) could show with nuclear magnetic resonance that the hydraulic permeability of porous media strongly depends on the unfrozen water content. This may be interesting where a significant proportion of flow occurs in the rock matrix, which is rarely the case in low-permeable rocks. Eight permafrost specimen sampled from different alpine rock summits yielded permeabilities of 0.06 – 30 μD (see section 6.1), which restricts effective fluid flow to fractures in the rock mass.

According to my knowledge, only one accessible study exists on the permeability of frozen fractured rock. Pogrebiskiy and Chernyshev (1977) conducted experimental pumping and pressurization in frozen and unfrozen fissured (up to 10 cm) granites in Kolyma (Russia). They found that permeability of frozen fissured rock is one to three orders of magnitude higher than the permeability of identical thawed rock. The ratio increased for highly weathered rocks close to the surface with more segregation ice. Perhaps most important, the anisotropy of the permeability in the rock mass strongly increases when freezing to factors of 20 and more.

The combination of perched water levels and deep-reaching unfrozen cleft systems regularly causes significant problems for tunnelling structures in permafrost rocks as have been reported by inundating water e.g. at the Aiguille du Midi (France) and at the Jungfrau (CH) in 2003 as well as for the Kunlun Mountain tunnel of the QingHai-Tibetian railway track (Hasler et al., 2008; Tang and Wang, 2006; Wegmann, 1998). Moreover, hydrostatic pressures due to the sealing of rock surfaces by ice can play a vital part in the destabilisation of rock slopes as has been outlined already by Terzaghi (1962) and was confirmed by coupled hydro-mechanical modelling of the $3*10^5$ m³ Tschierva rock avalanche in 1988 by Fischer and Huggel (2008).

A number of studies have observed water storage in relation to geomorphology and active layer depths in arctic permafrost systems (Quinton and Carey, 2008; Quinton et al., 2005; Zarnetske et al., 2007). Coupled hydro-mechanical modelling for repository changes in fractured bedrock in response to increased pressure head during the Last Glacial Maximum was conducted by Chan et al. (2005). Even if several studies emphasized the importance of pressurised water in rock instability (outflow was observed e.g. at the scarps of Kolka-Karmadon and Mt. Steller subsequent to failure) (Gruber and Haeberli, 2007; Haeberli, 2005; Haeberli et al., 2004; Haeberli et al., 1997; Huggel et al., 2008) no detailed study exits on repository effects and hydrostatic pressure effects in alpine permafrost rock walls.

5.3 Mechanic properties

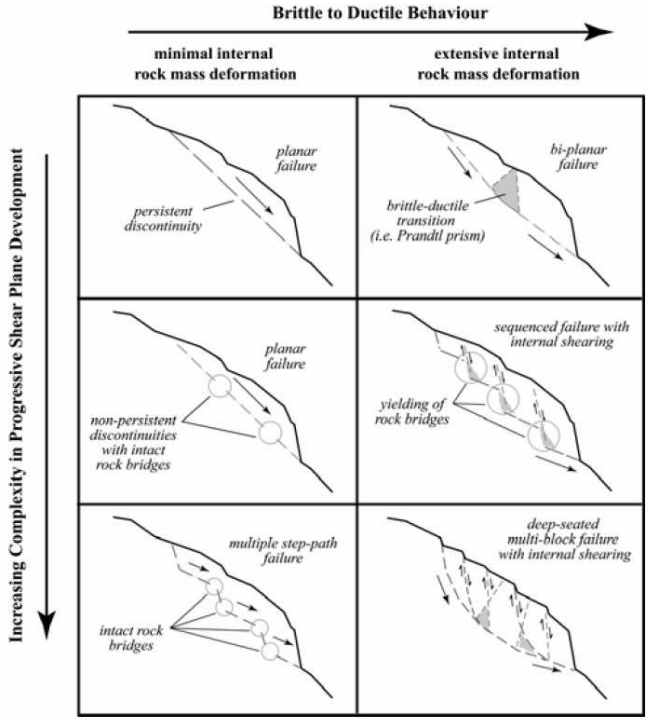

Fig. 4: Mechanisms of rock slope failure controlled by progressive shear plane development or by internal rock mass deformation and shear (Eberhardt et al. 2004).

As Eberhardt et al. (2004) point out, the existence of a fully interconnected discontinuity system bounding the moving mass is a mechanic key requirement for rock slope failure. Especially in sedimentary rocks, extensive basal sliding planes can be orientated along existing bedding planes (Abele, 1972; Erismann and Abele, 2001; Petley and Petley, 2005). However, lateral release scraps include breaking of intact rock bridges. Fully persistent discontinuities rarely exist in igneous rocks and metamorphic rocks and are also absent in many compact sedimentary rocks. Warming and thawing of fractured permafrost rocks changes (i) brittle fracture propagation in rock, (ii) friction along existing rough sliding surfaces, (iii) continuum creep deformation of ice in joints and (iv) induces “failure” of ice-filled fractures. Factors of complexity such as dislocation and disconnection of rough shear surfaces due to segregation ice will be addressed in Section 5.3.4.

5.3.1 Basic rock mechanical considerations

The following section will use the Mohr-Coulomb failure criterion which represents a simplification of actual rock stability behaviour in respect to the following aspects: Failure is only controlled by minimum and maximum principal stresses, a quasi-linear elastic relationship between stress and strain is postulated, unconfined compression is considered and the ratio of compressive and tensile strength is underestimated (Jaeger et al., 2007).

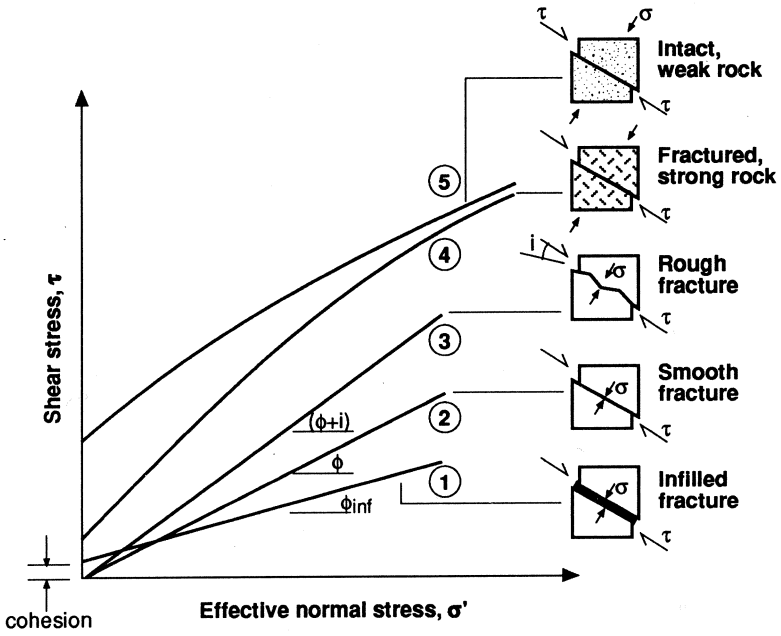

Fig. 5: Failure curves for different rock discontinuity settings (Wyllie and Norrish, 1996).

Applying the Mohr-Coulomb criterion, the absolute value of shear stress |τ|, at which failure occurs, is

$$|\tau| = c + \sigma' \tan \varphi$$

Equ. 5.18

where c is cohesion, σ' is the effective normal stress and φ is the angle of internal friction. While rock-mechanical models often describe movement without cohesion along the shear surface (Cruden, 2003), significant cohesion can occur if discontinuities are filled with cohesive materials such as fine-grained fillings or ice (Fig. 5). Moreover, ice can also decrease the effective normal stress applied to rock surfaces or alter the angle of internal friction.

5.3.1.1 Compressive and tensile strength of frozen and unfrozen rock

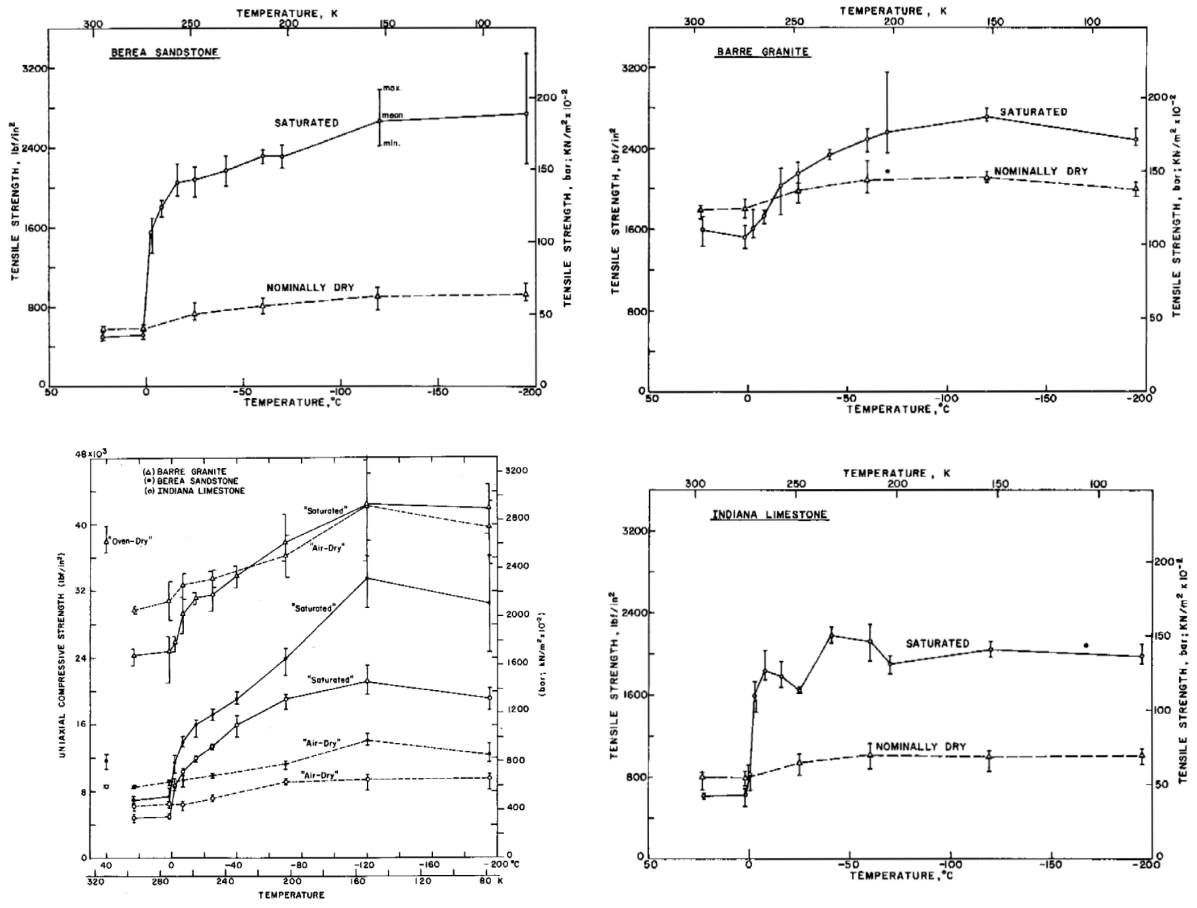

Fig. 6: Uniaxial compressive and tensile strength of unfrozen and frozen Barre granite, Berea sandstone and Indiana limestone (Mellor, 1973).

The scale on the right side is in bar (1 bar equals 10^5 N/m² or 10^5 Pa).

Experiments conducted by Mellor (1973) show an “abrupt increase” of compressive and tensile strength of all saturated rocks when pore water froze. In Fig. 6, tensile strength increases up to 300 % between 0 °C and –5 °C and compressive strength can increase 250 %, respectively. Mellor (1973) postulates that the strength of frozen rock increases with water saturation while the strength of unfrozen rock decreases with water saturation. This has serious implications for the stability of thawing rocks that are often incorporated in a permafrost rock environment supersaturated with water (Section 5.2). Possibly, no other environmental factor is capable of reducing matrix rock mass strength of a whole rock wall as fast as thawing.

5.3.1.2 Total friction along a rough surface

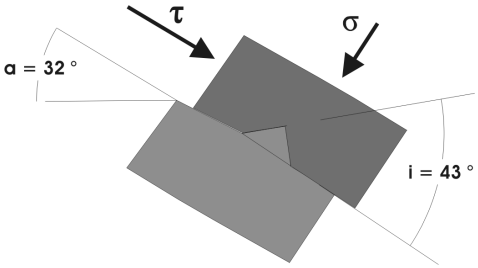

Fig. 7: Patton's dilatation concept to quantify the influence of surface roughness.

In natural rock fractures with rock-rock contact, the friction angle of discontinuities is determined by the rock material and the rock surface roughness (Patton, 1966). According to his dilatation concept, the impact of asperities on total friction can be approached by a series of sawteeth with an inclination (*i*) of the asperities relative to the fracture surface (Fig. 7). The failure criterion can then be calculated as

$$|\tau| = \sigma' \tan(\varphi + i)$$

Equ. 5.19

where $(\varphi + i)$ is referred to as the angle of total friction. To estimate *i* on natural rock surfaces, Barton and Choubey (1977) introduced an empirical measure of rock surface roughness, the joint roughness coefficient (*JCR*). The failure criterion can thus be approached by

$$|\tau| = \sigma' \tan(\varphi + JRC * \log 10(\frac{\sigma_c}{\sigma'}))$$

Equ. 5.20

where σ_c is the compressive strength of the rock material at the fracture surface (Empirical values of the JRC and total friction are listed in Hoek, 2007; Hoek and Bray, 1981). Considering the significant changes of uniaxial compressive strength at the melting point, the shear stress needed for failure along a rough joint decreases significantly between –5 °C and 0 °C. According to Equ. 5.20, potential high magnitude rockslides, where the compressive strength is close to normal stress, will react more sensitive to such temperature changes.

5.3.1.3 Brittle fracture propagation

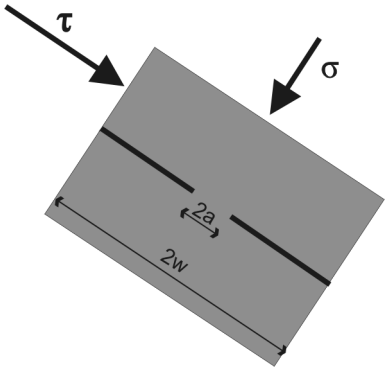

Fig. 8: Fracture mechanics model of 2a large single rock bridge under far field normal and shear stress.

While Section 5.3.1.2 introduced a mechanism that can reactivate shear processes on existing disconnected sliding planes during thaw, the creation of new shear planes always includes brittle fracture propagation. Kemeny (2003) introduced a time-dependent model for the cracking of rock bridges along discontinuities. The failure criterion can be approximated by

$$|\tau| = \frac{K_c\sqrt{\pi a}}{2w} + \sigma' \tan(\varphi + i)$$

Equ. 5.21

where K_c $[MPa\sqrt{m}]$ is the (Mode II-) critical fracture toughness and *a* and *w* relate to the geometry of the rock bridge (Fig. 8). Thus, any reduction in internal friction $\sigma' \tan(\varphi + i)$, as shown for melting in section 5.3.1.2, will increase the stress applied to the rock bridge and promote crack nucleation. Following the assumption of Kemeny (2003) and Chang et al. (2002), Mode I and Mode II behaviour show resembling behaviour. Chang et al. (2002) showed that (Mode I-) critical fracture toughness K_c

$$K_c = 4.28 * 10^{-3} \sigma_c + 1.05$$

Equ. 5.22

is a function of uniaxial compressive strength σ_c. Even small reductions in K_c can initiate cracking of rock bridges. As microcrack growth starts already at subcritical conditions, it is not necessary to overcome a final stress threshold for crack nucleation (Atkinson, 1984), and fatigue of rock bridges is a function of time (Kemeny, 2003). Thus, it can be stated, that warming of rock between –5 °C and 0 °C causes (i) a reduction of total friction along rough rock fractures and (ii) also a reduction of critical fracture toughness of rock bridges. Both factors promote the progressive creation of new shear planes.

5.3.2 Basic ice mechanical considerations

Many studies have shown that most discontinuity systems in Alpine permafrost rocks are ice-filled (Gruber and Haeberli, 2007; Haeberli, 1992; Körner and Ulrich, 1965; Ulrich and King, 1993). Ice may totally alter mechanical properties along fractures in a yet poorly understood way. While good progress has been made for mechanical properties of unconsolidated ice-affected materials (Arenson, 2003; Arenson et al., 2002; Arenson et al., 2004; Arenson and Springman, 2005a; Arenson and Springman, 2005b; Harris et al., 2003a; Springman and Arenson, 2008; Springman et al., 2003) few publications cover the mechanical effects of ice in rock discontinuities (Davies et al., 2001; Davies et al., 2003; Davies et al., 2000; Guenzel, 2008).

Ice does not deform in a purely elastic, viscous or plastic way and, thus, does not readily lend itself to classical engineering analysis (Sanderson, 1988). When stress is applied to ice it responds instantaneously by elastic deformation and creep. For stresses of 1-5 MPa creep deformation exceeds elastic deformation after seconds to minutes. Ice properties can be separated in two parts: continuum behaviour due to elastic and ductile creep deformation without fracture and fracture behaviour due to brittle and brittle-ductile behaviour. Theoretically, it is inappropriate to use the terms “strength” and “failure” for ice. However, several studies have used them for a straightforward characterisation of ice-mechanical properties.

Section 5.3.2.1 introduces physical equations for continuum behaviour of ice. Two factors impede their direct application: (i) non-uniform distribution of stress can cause significant fracturing in ice especially under tensile conditions (section 5.3.2.2) and (ii) deformation must not necessarily occur inside the ice body but can also occur along the rock-ice contact (section 5.3.2.3).

5.3.2.1 Continuum behaviour

Text and equations were partly copied and modified from Krautblatter (2008). Rock Permafrost Geophysics and its Explanatory Power for Permafrost-Induced Rockfalls and Rock Creep: a Perspective. Paper presented at the 9th Int. Conf. on Permafrost, Fairbanks, Alaska, US: 999-1004. (Section 7.3.4.1).

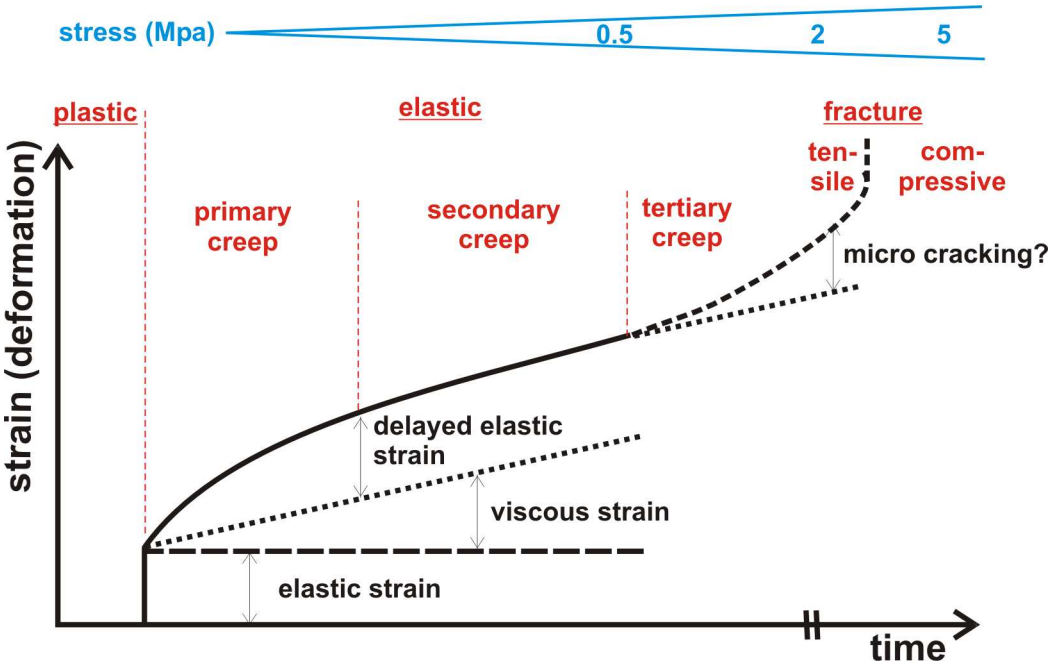

Fig. 9: Schematic illustration of time- and stress-dependent evolution of ice-mechanical properties.

Modified from Sanderson (1988).

It is assumed that ice-filled discontinuities react according to stress-strain behaviour of weight-loaded poly-crystalline ice. The deformation of ice at constant stress is characterized by four phases: Elastic deformation (1) that is followed by permanent deformation, firstly at a decreasing rate (2, primary creep), then at a constant rate (3, secondary creep) and finally at an increasing rate (4, tertiary creep) (Budd and Jacka, 1989) (see Fig. 9). Mostly secondary creep and tertiary creep occur at speeds relevant for mass movements. The flow relation for secondary creep relates the shear strain rate ε_{xy} to the shear stress τ_{xy},

$$\varepsilon_{xy} = A\tau_{xy}^{n}$$

Equ. 5.23

where A depends mainly on ice temperature, anisotropic crystal orientation, impurity content and water content. n increases at shear stresses greater than 500 kPa (Barnes et al., 1971). Crystal orientation, impurity content and shear stresses remain more or less constant over short timescales. In contrary, ice temperature and water content in mass movement systems are subject to major annual and interannual changes. Thus, for temperatures above -10 °C, A can be approached by

$$A = A_0 \exp(-\frac{Q}{RT}) \approx A_0 \exp(-\frac{16700}{T})$$

Equ. 5.24

where A_0 is independent of temperature, R is the universal gas constant and Q is the activation energy (Weertman, 1973) and A_{0t} for tertiary creep

$$A_{0t} = (3.2 + 5.8W) * 10^{-15} (kPa)^{-3} s^{-1}$$

Equ. 5.25

can be related to the water content W [%]. Paterson (2001) states that 2 °C is the lowest temperature at which the effect of water in the ice is relevant for the stress-strain behaviour. Equ. 5.24 and Equ. 5.25 show, that both, ice temperature and water content play a dominant role for the mechanical behaviour of ice-filled clefts at temperatures close to 0 °C. Assuming moderate water content of 0.6 %, the creep rate at 0° C is three times the rate at 2 °C (Paterson, 2001), which has serious effects on displacement rates and factors of safety considerations of mass movements.

5.3.2.2 Fracture behaviour

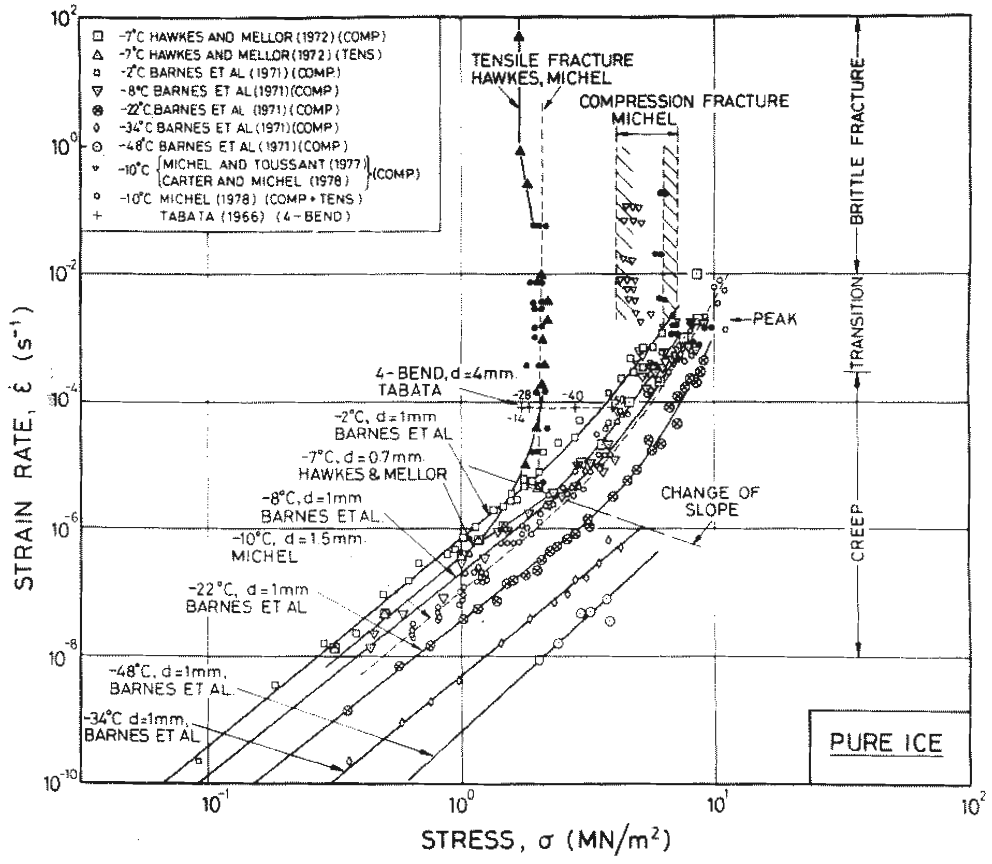

Fig. 10: Uniaxial loading in pure polycrystalline ice (Hallam 1986 in Sanderson 1988).

The transition between continuum behaviour and fracture behaviour is dependent on normal stress (Fig. 10). Thresholds for the initiation of fracture can be defined for both, stress and for the strain rate $\dot{\varepsilon}$

$$\dot{\varepsilon} = \frac{v}{l_o}$$

Equ. 5.26

where l_0 is the original length of the sample and v is the speed of deformation. Fracture occurs at uniaxial compression above 5 MPa, at uniaxial tension of 1-2 MPa and at strain rates exceeding 10^{-3} s^{-1}. As 1 MPa equals the normal stress of 40 m rock overburden, one could expect that fracturing phenomena may only influence thick rockslides. However, stress is very unequally distributed in instable rocks (Eberhardt et al., 2004) and thus tensile and compressive stresses in the range of 1 MPa (equals gravitational force of 10 kg on a cm²) can exist locally even in rockslides of a few meters thickness. On the other hand, Renshaw and Schulson (2001) showed that both, rock and ice materials tend to react rather ductile than brittle under high confinement. However, this becomes mainly important for more than hundred meter thick rockslides. To reconcile this apparently contradictory viewpoints, it can be stated that brittle fracture behaviour of ice in discontinuities is important for 10 m to more than 100 m thick rockslides, i.e. most larger rock failures.

5.3.2.3 Failure in ice-filled rock fractures: empiric data

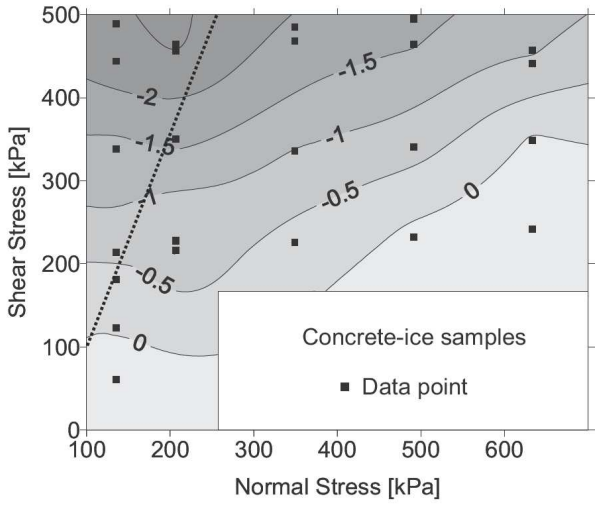

Fig. 11: Temperature at failure during constant stress test with concrete-ice samples (Guenzel, 2008).

A small number of shearing experiments were conducted using high-strength concrete with sawteeth surface as an analogue to natural fractures. Davies et al. (2001; 2000) could show in *constant strain* shearing experiments with concrete-ice samples that maximum sustained shear stress at "fracture" strongly declines with increasing temperature between –5 °C and 0 °C. They postulated that ice-filled rock fractures at –0.5 °C may even be more

unstable than totally thawed fractures. The implications for rock slopes were underlined by centrifuge testing (Davies et al., 2001; Davies et al., 2003). Guenzel (2008) conducted shearing experiments at *constant stress* with concrete-ice samples (Fig. 11). As natural rock systems are controlled by more or less constant stress fields, constant-stress experiments provide a better analogue for real conditions. She found a strong relation between temperature and shear strength at "failure" at all applied normal stresses. Normal stresses applied to concrete-ice samples equal rock overburden in the range of 5-25 m and results can be expected to apply well for that range.

5.3.2.4 A preliminary model for the failure of ice in rock clefts

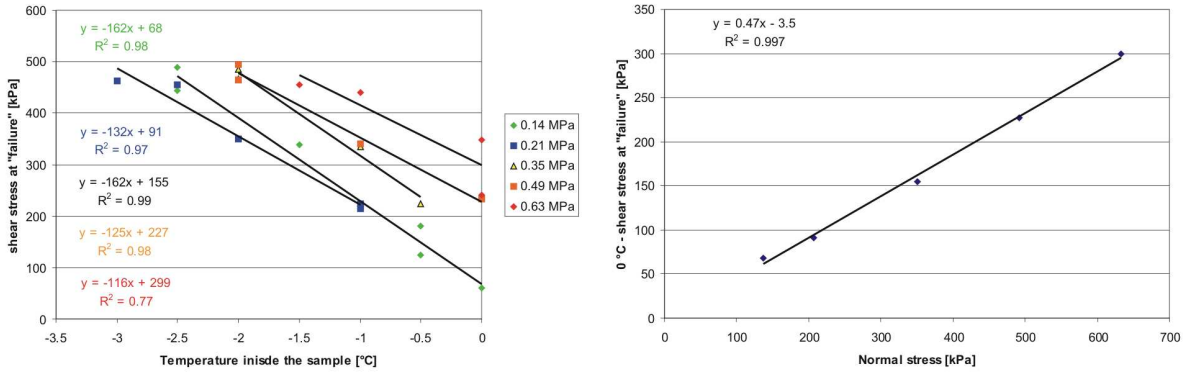

Fig. 12: Own reanalysis of data provided by Guenzel (2008) (see Fig. 11).

Data from Guenzel (2008) was extracted from Fig. 11 and plotted separately in respect to (i) the temperature impact on shear stress and (ii) the impact of normal stress on the shear stress at 0 °C. Both plots show that obtained values can be well explained by linear functions inside the limits of the experiment. The shear stress at failure for ice-filled clefts τ_{fi} [kPa] can, thus, be approximated by

$$\tau_{fi} = -145 * T_C + \tau_0$$

Equ. 5.27

where T_c [°C] is the temperature of the ice in the rock fracture and τ_0 is the (hypothetical) shear stress at failure at 0 °C. According to Fig. 11, τ_0 can be approached by

$$\tau_0 = 0.47 * \sigma' - 3.5$$

Equ. 5.28

where σ' is the effective normal stress. This simple model can explain the data provided by Guenzel (2008) with an average deviation of 10 % (Table 1). Unfortunately, there is yet no other constant stress dataset for concrete-ice contacts to validate this model. We expect this model to apply well for rock-ice contacts in the temperature range of -3 °C to 0 °C and for normal stresses equal to 5-25 m rock overburden.

Table 1: Measured shear stress based on raw data by Guenzel (2008) compared to model results.

Ice temperature [°C]	Normal stress [Mpa]	Measured shear stress at "failure" [MPa]	Modelled shear stress at "failure" [MPa] (Equ. 5.27, Equ. 5.28)	Deviation [%]
0.0	0.14	0.06	0.06	2
-0.5	0.14	0.12	0.13	7
-0.5	0.14	0.18	0.13	36
-1.0	0.14	0.22	0.21	5
-1.5	0.14	0.34	0.28	22
-2.5	0.14	0.44	0.42	5
-2.5	0.14	0.49	0.42	15
-1.0	0.21	0.22	0.24	10
-1.0	0.21	0.22	0.24	6
-2.0	0.21	0.35	0.38	9
-2.5	0.21	0.45	0.46	0
-3.0	0.21	0.46	0.53	12
-2.0	0.35	0.49	0.45	8
-2.0	0.35	0.47	0.45	3
-1.0	0.35	0.34	0.31	9
-0.5	0.35	0.22	0.23	4
0.0	0.49	0.23	0.23	3
-1.0	0.49	0.34	0.37	9
-2.0	0.49	0.46	0.52	10
-2.0	0.49	0.50	0.52	4
-1.5	0.63	0.46	0.51	11
-1.0	0.63	0.44	0.44	0
0.0	0.63	0.35	0.29	18
0.0	0.63	0.24	0.29	18
				10

5.3.3 A preliminary rock- and ice-mechanical model for rock instability in thawing permafrost rocks

Based on the Mohr-Coulomb assumption, we can now define the failure criterion of an ice-filled rock cleft, with cohesive rock bridges (Kemeny, 2003), contact of rough fracture surfaces (Barton and Choubey, 1977; Patton, 1966), ductile secondary creep of ice (Barnes et al., 1971; Paterson, 2001; Weertman, 1973) and with a representation of rock-ice "failure" mechanisms along the surface and inside the ice body (Own preliminary model based on data from Guenzel (2008)). The synoptic models are based on the principle of superposition (Kemeny, 2003), i.e. that shear stress "absorbed" by one component reduces the amount of shear stress applied to the other components.

5.3.3.1 Brittle fracture propagation of new sliding planes

Assuming that deformations that destruct rock bridges are (i) too slow to cause ice fracture (strain rate threshold see Sanderson, 1988) and (ii) are too slow to loose significant amounts of stress to creep deformation of ice (velocity dependent shear resistance Equ. 5.23), the failure criterion for the preparation of new sliding planes can be calculated as

$$|\tau| = \frac{(4.28 * 10^{-3}\sigma_c + 1.05)\sqrt{\pi a}}{2w}$$ fracture of rock bridges

$$+\sigma' \tan(\varphi + JRC * \log 10(\frac{\sigma_c}{\sigma'}))$$ total friction due to fracture roughness

Equ. 5.29

where the uniaxial compressive strength σ_c decreases up to three times between –5 °C and 0 °C.

5.3.3.2 Failure along existing sliding planes

After the destruction of cohesive rock bridges, the failure criterion of a thawing fracture is governed by

$$|\tau| = \frac{\varepsilon_w}{A_0 \exp(-\frac{16700}{T})}$$ reduction of effective shear stress due to secondary/tertiary creep of ice

$$+(-145 * T_C + 0.47 * \sigma' - 3.5)$$ failure criterion of ice in rock clefts

$$+\sigma' \tan(\varphi + JRC * \log 10(\frac{\sigma_c}{\sigma'}))$$ total friction due to fracture roughness

Equ. 5.30

where an increase in T [K] decreases the amount of shear stress that is "absorbed" by the creep of ice. The amount of stress absorbed by the total friction at rough fracture surfaces decreases with warming due to declining compressive rock strength. An increase of T_c [°C] facilitates the failure of ice in rock clefts.

Equ. 5.29 and Equ. 5.30 show that warming of permafrost rocks between –3 °C and 0 °C promotes both, the progressive development of new shear planes and failure along existing sliding planes.

5.3.4 Complexity factors: stress heterogeneity, hydrostatic pressure and dilatation by ice segregation

As thermal regimes and hydraulic regimes in permafrost appear to be complex, it is not surprising that the mechanic behaviour shows a high level of complexity. The most important factors are: (i) The key characteristic of rock instability, the lack of cohesion across discontinuities (Cruden, 2003), is not valid for permafrost rocks. For the case of foliated metamorphic rocks, tensile strength of ice (2 MPa) may well be higher than the typical tensile strength of rocks (1 MPA for foliated gneiss according to (Eberhardt et al., 2004)). There is no reliable method to estimate the spatial distribution and the overall impact of cohesion in permafrost-affected bedrock. (ii) Permafrost rocks and the active layer above are subject to intense weathering processes (Matsuoka, 2008; Murton et al., 2000). Bedrock facture due to ice-segregation may disconnect and dislocate existing shear surfaces as well as create new sliding planes (Murton et al., 2006). (iii) Rock is a highly anisotropic and heterogeneous me-

dium and is subject to highly variable stress fields. Modelling stress fields is not only a problem of model resolution but it must be recognised that modelling techniques have advanced beyond the capability to confidently constrain the necessary data (Eberhardt et al., 2004). (iv) Hydrostatic pressures affect rock strength from a pore scale (Atkinson, 1984) to the scale of a complete rock wall (Fischer et al., 2006). In view of the anisotropy of permeability in frozen fractured rock (Pogrebiskiy and Chernyshev, 1977) and pressure build-up during freeze-thaw processes, hydrostatic conditions in permafrost rocks may results in pressure patterns that are unparalleled in other rocks masses. (v) Effective normal stress is not only affected by hydrostatic pressure but also by cryostatic pressure caused e.g. by ice segregations and may reduce effective normal stress to a zero-level in some cases.

5.4 The geomorphic system

Gruber and Haeberli (2007) postulate that "the destabilisation of steep bedrock by permafrost degradation implies a portion of bedrock slopes in permafrost that is steeper than it would be when thawed." This has a number of geomorphologic implications: (i) The argument implicitly describes the existence of equilibrium and disequilibrium slopes. (ii) We need a concept that is capable of describing the sensitivity of slopes to climate change i.e. we need to define the portion of slopes that reacts. (iii) We need to define the time scale of adaptation. (iv) We need a concept to describe the transience from one configural state to another. (v) We need to question the predictability of adaptation in terms of complexity.

5.4.1 Equilibrium and non-equilibrium slopes

The use of the term equilibrium for slopes has been much influenced by the work of Ahnert (1970) and Hack (1960). The use of "dynamic equilibrium" is defined by Ahnert (1994) as an "equilibrium of process rates". In respect to the range of definitions provided by Chorley and Kennedy (1971) this would be referred to as a "steady state equilibrium". Applied to a permafrost rock face, this could be achieved by an equilibrium of the rate of back weathering and the rate of mass wasting from the cliff, which could result in a constant inclination of the rock slope. Penck (1924) anticipated the idea that straight rock slopes are threshold slopes, which are determined by rock stability and removal rates. Later, it has been developed into the concept of a threshold hillslope that maintains a critical slope while being denudated by highly non-linear mass movements and mass transport processes (Montgomery, 2001). Selby (1980) introduced a simple rock mass strength concept based on an estimate of uniaxial compressive strength and other factures such as joint spacing and rock wall hydrology. This value was successfully correlated to slope morphology in several case studies (Augustinus, 1992; Moon, 1984; Selby, 1989). Montgomery (2001) outlined that the development of threshold hillslopes depends on both, the relative uplift rate and the time since the uplift rate commenced. Korup (2008) investigated greywacke and schist slopes in several active mountain ranges in New Zealand and found "a conspicuous tendency in hillslope evolution to adjust to rock mass strength irrespective of the intensity of tectonic an climatic forcing." However, a large portion of high-alpine rock permafrost walls is significantly exposed above any local erosion base and thus highly weathering-limited. Hovius et al. (2004) describe the slope angle α for such a infinite (steady state equilibrium) slope by

$$\tan\alpha = (\frac{C}{\rho g y \cos 2\alpha}) + \tan\varphi$$

Equ. 5.31

where C is the cohesion of the rock mass, ρ is the density, φ is the internal friction, g is the gravitational acceleration and y is the depth of the sliding plane. They point out that the equilibrium ends if "there were a change in any of the parameters involved." As has been shown in section 5.3, cohesion and total friction change abruptly close to the melting point. Thus, thawing rock permafrost slopes are non-equilibrium slopes and significant change of their morphometric characteristics would be required to bring them back to an equilibrium state.

5.4.2 The sensitivity concept

A strict application of Equ. 5.31 would postulate that a readjustment (i.e. smoothing) of all rock slopes which are affected by melting close to 0 °C must be expected. According to Brunsden and Thornes (1979) the sensitivity of a landscape to change is expressed as the likelihood that a given change in the controls of a system will produce a sensible, recognisable and persistent response. This includes two aspects: the *propensity for change* and the *capacity* of the system *to absorb* the *change*. The propensity for change is given by driving forces and barriers to that change. The capacity of the system to absorb change is the ability of the system to absorb and store energy, water and materials. Once change has been initiated, the rate of change determines the relaxation time or the persistence of characteristics of the former state.

Exposed rock summits in high alpine conditions have persisted in these positions for millions of years during several climatic fluctuations. As enormous "driving forces" in terms of potential energy are available for instable rock slopes, two explanations must be considered: (i) significant barriers to change exist and/or (ii) the relaxation time spans a long time-frame. Apparently, significant barriers to change exist in a fractured rock wall of highly cohesive rock material where immediate adaptation can only occur along predefined planes of weakness. This shows that the understanding of relaxation time is a key concern in permafrost rocks.

5.4.2.1 Reaction time

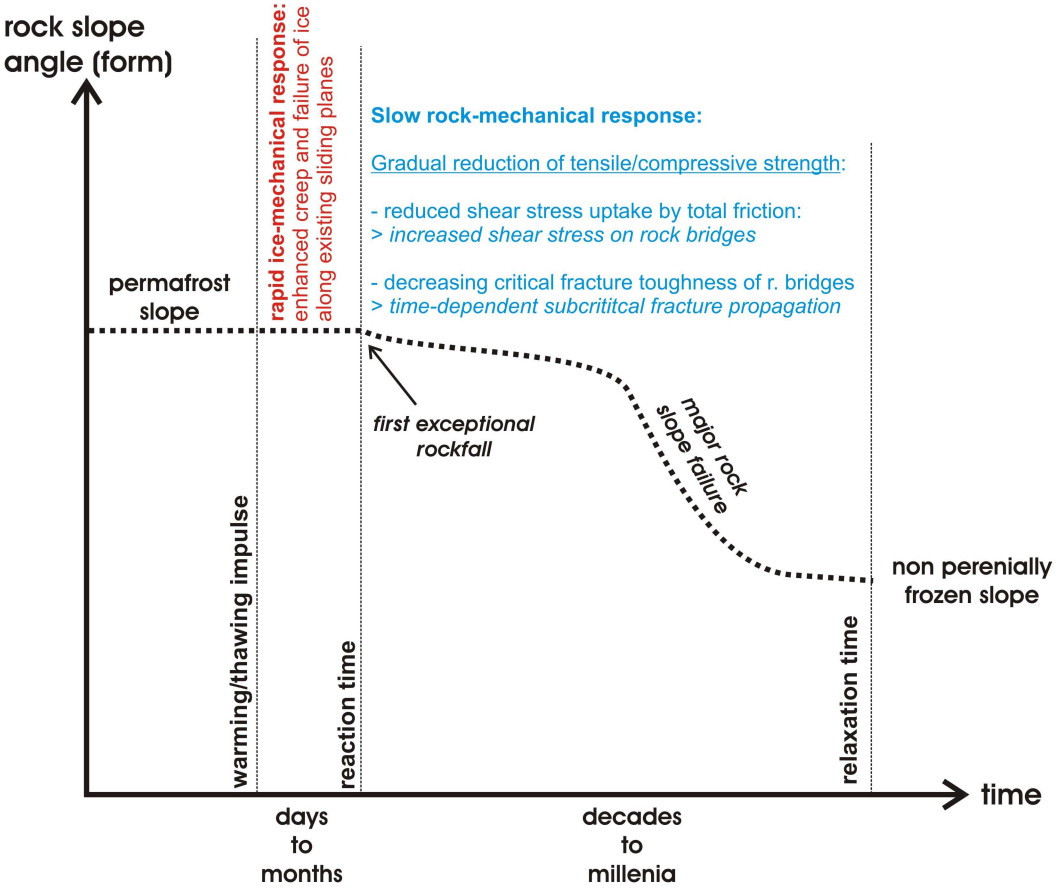

Fig. 13: Reaction time and relaxation time of thawing permafrost rock slopes.

Own concept based on (Brunsden and Thornes, 1979).

In the following section an attempt is made to combine rock-/ice-mechanical theory with the geomorphologic sensitivity concept. In Fig. 13, the reaction time (lag) is the time taken to react to an impulse of change (Brunsden, 2004). This is followed by the relaxation (recovery, form adjusting) time, which persists until the new equilibrium slope is approached.

The first “sensible” impulse of change of an equilibrium permafrost rock slope that develops towards a more gentle slope angle is given by the first rockfall that exceeds the limits of the mass wasting rates, which defined the steady state equilibrium of the prior slope. In practice, this could be a rockslide that exceeds the magnitude of prior events and whose instability refers to change induced by a temperature increase. The first rockslides will occur along existing planes of weakness. In section 5.3.3.2, the stability criterion of such slides was defined as

$$|\tau| = \frac{\varepsilon_w}{A_0 \exp(-\frac{16700}{T})}$$ reduction of effective shear stress due to secondary/tertiary creep of ice

$$+(-145 * T_C + 0.47 * \sigma' - 3.5)$$ failure criterion of ice in rock clefts

$$+\sigma' \tan(\varphi + JRC * \log 10(\frac{\sigma_c}{\sigma'}))$$ total friction due to fracture roughness

Equ. 5.30

which shows that they are principally influenced by temperature changes of ice in fractures. The reaction occurs instantaneously as soon as the thermal signal has reached the ice inside the rock fracture. The reaction time in a rock-/ice-mechanical sense is, thus, given by the speed of propagation of the thermal signal.

Fig. 14: Massive ice at the detachment zone of the 2003 rockfall in July below the Carrel (photo by L. Trucco in Gruber and Haeberli, 2007)

The response of rockslides to warm summers occurs immediately. The highest frequency of rockfalls in summer 2003, which was 5 °C above mean summer temperatures in Switzerland, was observed in July (e.g. Matterhorn) and August (e.g. Dent Blanche) 2003, which is earlier in the year than expected from thermal modelling (Gruber et al., 2004a). This observation has been confirmed by a number of field studies often with the observation of ice or running water on the detachments zone (Deline et al., 2008; Fischer et al., 2006; Gruber and Haeberli, 2007; Haeberli et al., 2004; Huggel et al., 2008; Rabatel et al., 2008; Ravanel et al., 2008). The reaction time to thermal impulses is in the range of weaks or less on permafrost rock faces with significant influence of ice-filled clefts near the rock surface.

5.4.2.2 Relaxation time

Total adjustment is achieved as soon as the new equilibrium slope is approached (Brunsden, 2004), i.e. as soon as the slope angle reflects the rock mass stability of unfrozen rock. In terms of rock-/ice-mechanics this long-term mechanical failure criterion can be approached by

$$|\tau| = \frac{(4.28 * 10^{-3}\sigma_c + 1.05)\sqrt{\pi a}}{2w} \quad \text{fracture of rock bridges}$$

$$+\sigma' \tan(\varphi + JRC * \log 10(\frac{\sigma_c}{\sigma'})) \quad \text{total friction due to fracture roughness}$$

Equ. 5.29

where temperature-induced change in the compressive strength σ_c will onset a long-lasting adaptation process that includes progressive extensile fracture along rock bridges and smoothing of rock surfaces. Kemeny (2003) integrated the time-dependent Charles-Power law into the rock bridge problem and yielded a time dependent cohesion *C*

$$C(t) = \frac{\sqrt{\pi}[a_0^{1+n/2} - (1+\frac{n}{2})At(\frac{2w(\pi - \sigma_n \tan\varphi}{K_c\sqrt{\pi}})^n]^{1/(2+n)}}{2w}$$

Equ. 5.32

where a_0 and *w* define dimensional properties of the rock bridge (Fig. 8), *A* and *n* are material properties and *t* is time in seconds. While $a_0^{1+n/2}$ describes the "barrier to change" by the original „effective" length of the rock bridge (Fig. 8), $(1+\frac{n}{2})At(\frac{2w(\pi - \sigma_n \tan\varphi}{K_c\sqrt{\pi}})^n$ describes impact of the reduction of the effective length of the rock bridge through time. It is obvious that the speed of rock bridge destruction (effective length reduction) increases with decreased critical fracture toughness K_c (that relates to uniaxial compressive strength). This means that in rock-/ice-mechanical terms, the reduction in uniaxial compressive strength onsets an effect that causes brittle fracture propagation over a longer time frame. The time frame depends on the degree of interlocking prior to the warming impulse, and to the degree to which the system is affected by a decrease in critical fracture toughness (i.e. uniaxial compressive strength). t_o, the onset of the rock bridge destruction, is given by the time when the thermal impulse reaches the affected rock fracture.

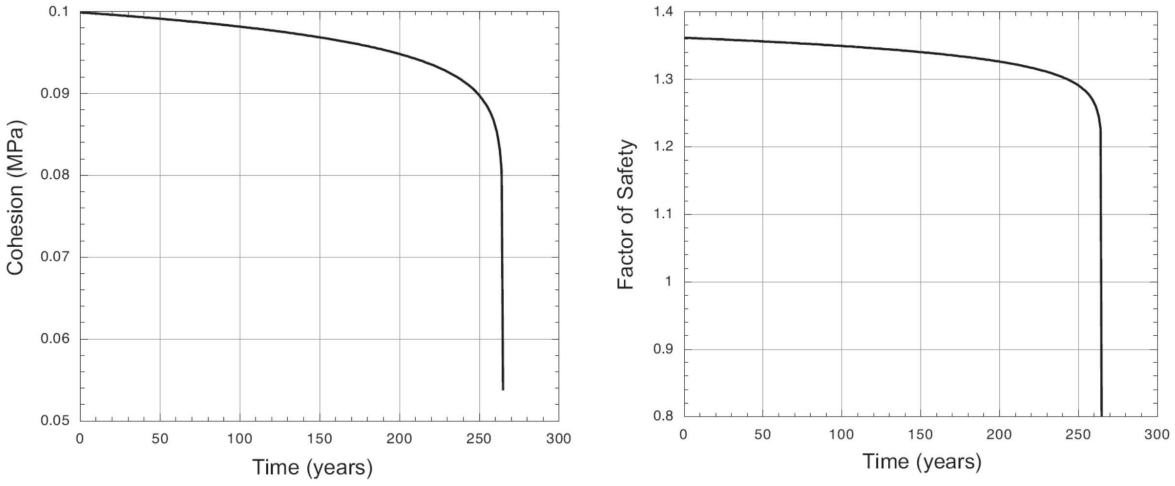

Fig. 15: Time-dependent development of cohesion along rock bridges and resulting factor of safety of a hypothetical rockslide (Kemeny, 2003).

Fig. 15 presents a rock-mechanical analogue to the geomorphologic understanding of relaxation time and is path-dependent to warming due to the parameters implemented in Equ. 5.29. Of course, this mechanical approach cannot explain all aspects of relaxation. For instance, initial rockslides cause positive feedbacks by enhanced warming due to increased exposure behind rockfall scarps. Fracturing of the surrounding area may occur coincidently to rockslide occurrence. Negative feedbacks can derive from reduced overload below rockfall scarps.

The geomorphologic expertise to the relaxation time is based on two assumptions: (i) Linear thermodynamic laws apply for the future occurrence of rockslides. Larger rockslides require an quasi-exponentially increasing relaxation time. (ii) The timing of rockslides after the Holocene Climatic Optimum is indicative of relaxation time if these were triggered by permafrost degradation.

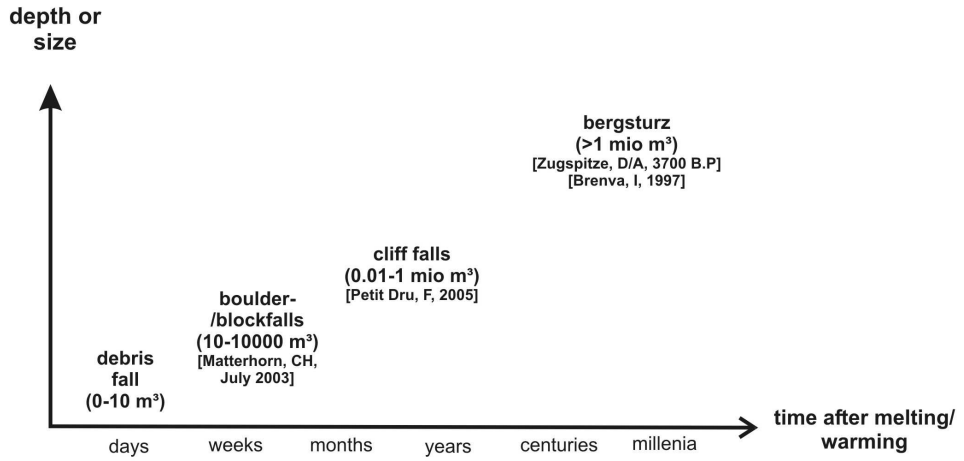

Fig. 16: Time after warming versus rockfall size.

Modified from Haeberli et. al. (1997). CH, Switzerland; F, France, D/A, Germany/Austria, I, Italy.

Plotting rockfall size versus time after impulse has become a generally accepted conceptual model in permafrost research (Haeberli and Beniston, 1998; Haeberli et al., 1997; Harris et al., 2009). The scientific foundation for this assumption is the quasi-exponential decrease of the speed of thermal propagation with depth (Wegmann, 1998; Wegmann et al., 1998) and the geomorphologic observation of deep-reaching and long-lasting changes (Deline, 2002).

The second line of evidence derives from the timing of large rockslides subsequent to the Holocene Climatic Optimum. Prager et al. (2008) plotted 60 dated rock slides in Tyrol, and surrounding areas in Germany, Switzerland and Italy and found two peaks of rock slope failure from 10500-9400 cal. B.P. and from 4200-3000 cal. B.P.. As the first peak occurred significantly after deglaciation, they postulated a relaxation time of a few 1000 years, due to brittle fracture propagation in rock masses (as described above). No obvious trigger is found for the second peak of rockfall activity. Prager et al. (2008) suggest “striking environmental changes in the middle Holocene”. A number of articles postulate that rockfalls within this time frame that originated from present-day permafrost rock walls could be a response to permafrost degradation subsequent to the Holocene Climatic Optimum (Gude and Barsch, 2005; Jerz and Poschinger, 1995; Jerz, 1999). In accordance, Soldati et al. (2004) found clusters of peak activity from 13000 to 9000 cal. B.P. and from 6500-2300 cal. B.P. in the Italian Dolomites and related them to deglaciation, increased precipitation and permafrost degradation. Tinner et al. (2005) follow that line of evidence and also suggest permafrost degradation as a possible trigger for the Kandertal rockslide. However, the trigger of past rockslides remains an “abductive” problem as long as no “smoking gun” provides undisputable evidence for one or another theory.

Perhaps more important is the fact that very few large rock slides (> 100 mio. m^3) occur before 10 ka B.P. (Prager et al., 2008), 6000 years after ice had retreated from the flanks of the valleys in the Central Eastern Alps (Ivy-Ochs et al., 2006). This provides good evidence for a relaxation time that is in the range of millenia for large rockslides. According to Hormes et al. (2001), Holocene Climatic Optimum conditions with glacier extensions smaller than today existed from 5290-3870 and from 3640-3360 cal. B.P.. One could expect that permafrost-triggered rockslides should culminate towards the end of that period or even few millennia later, if (!) the mechanism of brittle fracture propagation follows the same line as after deglaciation.

5.4.2.3 Disequilibrium and transience

Considering millennia as a typical relaxation time for large alpine slopes, the question of whether a new equilibrium can be reached becomes increasingly important. Renwick (1992) introduced a distinction between disequilibrium landforms that tend towards equilibrium but have not had sufficient time to reach such a condition and nonequilibrium systems that do not tend toward equilibrium even with relatively long periods of environmental stability. Considering the fact the climatic fluctuations are the main trigger, this is not a very useful concept as there will never be a “long enough period of environmental stability.” According to Brunsden (2004) any situation where the interval between form-changing events is smaller than the response time (reaction + relaxation time) can be referred to as transient. Even if the thermodynamic application of the term transience (Kohl, 1999; Noetzli, 2008) is quite different from the geomorphologic definition, it may point towards the same direction:

Large rock masses inherit (thermal) signals that date back several thousand years and still influence present systems.

5.4.3 The complexity concept and path-dependence

Many of the aspects discussed in Section 5 such as transient thermal impulses, anisotropic permeability as well as temperature and time-dependent stability show that the complexity in a rock wall system significantly increases when it is affected by permafrost. Considering the strong path-dependence of permafrost rock systems, which inherit signals that date back decades, centuries and thousands of years, the explanatory power of present-day thermal measurements at the rock surface becomes limited to a thin tens of meters thick crust that is exposed to the present-day regime. High magnitude rockslides may respond to thermal properties which are still reminiscent of the Holocene Climatic Optimum or the Last Glacial Maximum. It is questionable whether the right question I being asked, if the surface temperature fluctuations at the Zugspitze (Section 6.4) are meticulously observed irrespective of the fact that a 200 m thick rock slice was removed from the north face 3700 years ago and uncovered a previously decoupled permafrost system in the core of the summit. Presently, there is no explicit article on complexity in permafrost systems while such considerations have long been established in weathering science and other fields of geomorphology. Next to new research ideas and questions, a major concern of complexity research could be to what degree prediction is possible in permafrost systems by means of present understanding and chaotic behaviour (Dikau, 2006; Phillips, 2006).

6 2D and 3D-detection and quantification of permafrost changes in rock walls with ERT

6.1 Laboratory analysis

Source: Krautblatter, M. and Zisser, N. (submitted): Laboratory evidence for linear temperature-resistivity pathways of thawed, supercooled and frozen permafrost rocks. Geophysical Research Letters.

Temperature-resistivity (T-ρ) paths are a key proxy in permafrost research. Testing 8 sedimentary, metamorphic and igneous rocks from permafrost rock summits, we found evidence that exponential T-ρ paths developed in the 1970s do not describe the physics of hard rocks correctly, as freezing occurs in confined space. We hypothesize that bilinear functions of unfrozen and frozen T-ρ paths offer a better approximation with an R^2 of 0.88 to 1.00. Frozen T-ρ gradients approach 29.8 ±10.6 %/°C while unfrozen gradients were confirmed at 2.9 ±0.3 %/°C. Both increase with porosity. Path-dependent supercooling T-ρ behavior (3.3 ±2.3 %/°C) until the spontaneous freezing temperature -1.2 (±0.2) °C resembles unfrozen behavior. Spontaneous freezing subsequent to supercooling coincides with sudden self-induced temperature increases of 0.8 (±0.1) °C and resistivity increases of 2.9 (±1.4) kΩm. Separate linear approximation of unfrozen, supercooled and frozen T-ρ behavior could help to provide accurately temperature-referenced ERT of instable permafrost rocks.

6.1.1 Introduction

Rockfalls and rockslides of all magnitudes have been reported recently from permafrost-affected rock walls (Huggel, in press; Rabatel et al., 2008). Stability of permafrost rocks strongly declines between –5 °C and –0 °C due to a reduction of compressive and tensile strength of the intact rock matrix (Mellor, 1973) and due to a loss of ice-mechanical strength in ice-filled rock discontinuities and along rock-ice contacts (Guenzel, 2008). Supercooled water in this temperature range favors ice segregation (Murton et al., 2006) that may disconnect stability-relevant shear surfaces. Accurate monitoring of temperatures between –5 °C and 0 °C is a prerequisite for stability analysis of hazardous permafrost rocks. Seguin (1978) used laboratory studies to show that resistivity is an accurate proxy of rock temperature that may substitute temperature measurements where drilling is impossible. Field methods evolved significantly and represent a cost-effective approach to permafrost characterization (Kneisel et al., 2008). Sass (2004) proved that ERT is capable of measuring temporal variations of freeze and thaw limits even in solid rock faces. Krautblatter and Hauck (2007) applied ERT to investigate active-layer processes in permafrost-affected rock faces. Permafrost geophysics are currently evolving towards quantitative characterization of physical properties of permafrost (Hauck et al., 2008).

Accurate approximation of T-ρ paths is a prerequisite for temperature-referenced ERT of instable permafrost rocks. This article hypothesizes that the assumed exponential relation of temperature and resistivity below 0 °C (McGinnis et al., 1973) is not valid for most permafrost rocks as (i) the equilibrium freezing point is significantly

lower than 0 °C, (ii) path-dependent, metastable supercooling occurs to a significant degree and (iii) frozen low-permeability rocks with confined pore water indicate a linear T-ρ relation.

6.1.2 Theoretical system setting

6.1.2.1 Freezing point depression and supercooling

Equilibrium freezing temperature T_e regularly deviates from the datum freezing point T_0 = 0 °C due to pressure, solute concentrations and interface curvature. T_e due to solute concentration can be calculated as

$$T_0 - T_e = K_f * m_B$$

Equ. 6.1

where K_f is the cryoscopic constant of water [1.86 K*kg/mol] and m_B is the molality [mol/kg] of the solution. Pore water solutes in permafrost rocks mostly include low soluble oxides, carbonates and hydroxides which effect eutetic alterations significantly below 0.5 °C. T_e due to pressure p_m can be expressed by

$$p_m = 0.611657[kPa] * (1 - 626000 * (1 - (\frac{T_e}{T_t})^{-3}) + 197135 * (1 - (\frac{T_e}{T_t})^{21.2}))$$

Equ. 6.2

where T_t is 273.16 K (Wagner et al., 1994). Pore-size dependent melting point depression ΔT_m can be calculated as

$$\Delta T_m = C_{GT} / (R - t)$$

Equ. 6.3

where C_{GT} is the Gibbs-Thomson constant for water (51.9±4 K nm), R is the pore radius [nm] and t is 0.6 nm (Jähnert et al., 2008). Thus, T_e of –1 °C could derive from pressure equivalent to 400 m rock overburden, exceptional pore water molality of 0.54 mol/kg or most likely due to on average 50 nm large pores. Below T_e, metastable supercooled water can exist until the spontaneous freezing temperature T_s (Lock, 2005).

6.1.2.2 Electrical properties of rocks

Bulk conductivity of water-saturated rocks is a function of electrolytic conductivity, surface conductivity and electronic conductivity of the matrix. The effective medium theory (Bussian, 1983) describes infinitely resistive matrix grains with a specific surface conductance immersed in a conductive medium (Hayley et al., 2007). Thus, rock conductivity reflects the amount of interconnected pores and the tortuosity of the flow paths. Archie devel-

oped an empirical law relating resistivity ρ_e to fractional porosity Φ, pore space occupied by liquid water S, and resistivity of pore water ρ_w,

$$\rho_e = \sigma^{-1} = a\Phi^{-m} S^{-n} \rho_w$$

Equ. 6.4

where n and m are rock specific constants and a has no physical meaning (Bussian, 1983). Porosity remains constant over short time scales and Roberts (2002) showed that wetting of microporous rocks between 40 and 100 % has little effect on resistivity in comparison to significant temperature changes. Temperatures changes above T_e affect the mobility of ions and thus ρ_w. Unfrozen resistivity ρ behavior can be calculated as a quasi-linear decrease

$$\rho = \frac{\rho_0}{1 + \alpha(T - T_0)} \quad .$$

Equ. 6.5

where T is the actual temperature, ρ_0 is the resistivity value at a reference temperature T_0 and α approaches values of 0.025 K^{-1} (Keller and Frischknecht, 1966). Below the freezing point, resistivity depends mainly on unfrozen water content until most of the pore water is frozen (Mellor, 1973). Commonly, resistivity below the freezing point (T_f) is calculated as an exponential response to the temperature according to McGinnis et al. (1973):

$$\rho = \rho_0 e^{b(T_f - T)}$$

Equ. 6.6

where b determines the rate of resistivity increase and can be derived empirically (Hauck, 2001).

6.1.3 Methods

6.1.3.1 Petrophysical characterization

Plan-parallel cylindrical plugs with diameter and length of 30 mm were prepared. Three plugs orientated perpendicular to each other were sampled to observe heterogeneity and anisotropy. Plugs were dried and stored in a vacuum vessel to avoid adsorbance of air humidity. Porosity was measured using a gas compression/expansion method in a Micromeritics Multivolume Pycnomter 1305. As flow density of low-permeability rocks was too low for standard flow meters, a pressure transient method with argon gas in a 5 MPa gas-autoclave was applied (Zisser and Nover, in press). Permeability can be calculated analytically, correcting the “Klinkenberg-Effect”. Qualitative and quantitative mineralogical composition was determined by X-ray powder diffraction analysis using the “Rietveld-method”. We applied 20 g samples of granulometric homogenous and completely disoriented powder measured in a Siemens D5000 diffractometer.

6.1.3.2 Resistivity measurements

Resistivity behavior was measured using representative 5-30 kg cuboid samples taken from permafrost study sites. Samples were submerged in low conductive 0.032 (±0.002) S/m water in an undisturbed closed basin to approach their chemical equilibrium. Pore space was fully saturated under atmospheric pressure until at 20 °C resistivity did not decline further, as free saturation resembles the field situation more closely than saturation under vacuum conditions (Krus, 1995; Sass, 2005a). Samples were cooled with increments of 0.1-0.2 °C in a range of 20 to –4 °C. Ventilation was applied to avoid thermal layering. Samples were loosely coated with plastic film to protect them against drying. Calibrated 0.03 °C-accuracy thermometers measured rock temperature at the median depth of electric current flow according to Barker (1989) for the employed Wenner four-electrode configuration. This array provides a laboratory analogue to the geometry of most field measurements (Kneisel et al., 2008). Stainless steel electrodes of 5 mm diameter and 16 mm length were firmly placed in holes drilled to a depth of 2-3 millimeters with a constant separation ranging from 5-13 cm on different samples. Galvanic contact was improved by conductive grease along the rock-electrode contact. Resistance was measured repeatedly with reversed currents with an ABEM SAS 300B device at 0.2 mA and up to 160 V. Deviation of repeated identical measurements is practically below 0.05 %. Resistivity was calculated under the assumption of a half-space measurement geometry. This assumption is justified given the dimensions of the rock samples compared to the electrode array length (Barker, 1989).

6.1.4 Results

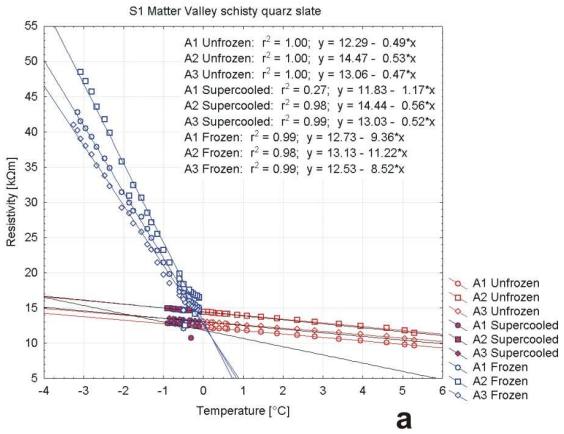
S1 Matter Valley schisty quarz slate
A1 Unfrozen: r² = 1.00; y = 12.29 - 0.49*x
A2 Unfrozen: r² = 1.00; y = 14.47 - 0.53*x
A3 Unfrozen: r² = 1.00; y = 13.06 - 0.47*x
A1 Supercooled: r² = 0.27; y = 11.83 - 1.17*x
A2 Supercooled: r² = 0.98; y = 14.44 - 0.56*x
A3 Supercooled: r² = 0.99; y = 13.03 - 0.52*x
A1 Frozen: r² = 0.99; y = 12.73 - 9.36*x
A2 Frozen: r² = 0.98; y = 13.13 - 11.22*x
A3 Frozen: r² = 0.99; y = 12.53 - 8.52*x
Resistivity [kΩm]
Temperature [°C]
A1 Unfrozen
A2 Unfrozen
A3 Unfrozen
A1 Supercooled
A2 Supercooled
A3 Supercooled
A1 Frozen
A2 Frozen
A3 Frozen
a

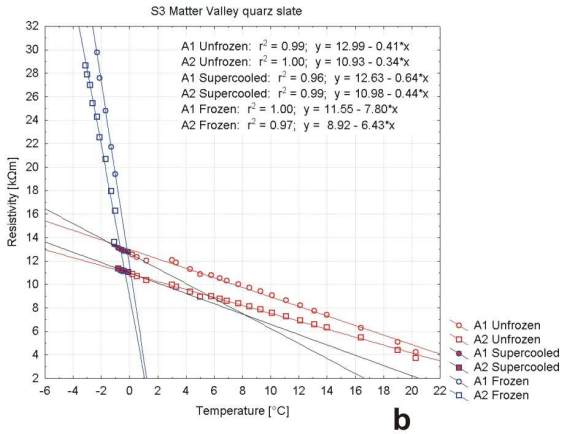
S3 Matter Valley quarz slate
A1 Unfrozen: r² = 0.99; y = 12.99 - 0.41*x
A2 Unfrozen: r² = 1.00; y = 10.93 - 0.34*x
A1 Supercooled: r² = 0.96; y = 12.63 - 0.64*x
A2 Supercooled: r² = 0.99; y = 10.98 - 0.44*x
A1 Frozen: r² = 1.00; y = 11.55 - 7.80*x
A2 Frozen: r² = 0.97; y = 8.92 - 6.43*x
Resistivity [kΩm]
Temperature [°C]
A1 Unfrozen
A2 Unfrozen
A1 Supercooled
A2 Supercooled
A1 Frozen
A2 Frozen
b

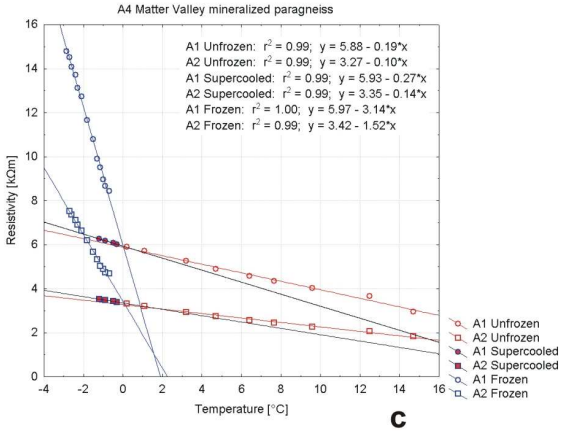
A4 Matter Valley mineralized paragneiss
A1 Unfrozen: r² = 0.99; y = 5.88 - 0.19*x
A2 Unfrozen: r² = 0.99; y = 3.27 - 0.10*x
A1 Supercooled: r² = 0.99; y = 5.93 - 0.27*x
A2 Supercooled: r² = 0.99; y = 3.35 - 0.14*x
A1 Frozen: r² = 1.00; y = 5.97 - 3.14*x
A2 Frozen: r² = 0.99; y = 3.42 - 1.52*x
Resistivity [kΩm]
Temperature [°C]
A1 Unfrozen
A2 Unfrozen
A1 Supercooled
A2 Supercooled
A1 Frozen
A2 Frozen
c

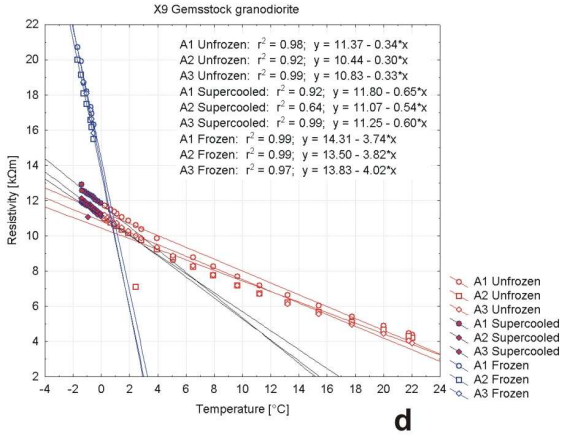
X9 Gemsstock granodiorite
A1 Unfrozen: r² = 0.98; y = 11.37 - 0.34*x
A2 Unfrozen: r² = 0.92; y = 10.44 - 0.30*x
A3 Unfrozen: r² = 0.99; y = 10.83 - 0.33*x
A1 Supercooled: r² = 0.92; y = 11.80 - 0.65*x
A2 Supercooled: r² = 0.64; y = 11.07 - 0.54*x
A3 Supercooled: r² = 0.99; y = 11.25 - 0.60*x
A1 Frozen: r² = 0.99; y = 14.31 - 3.74*x
A2 Frozen: r² = 0.99; y = 13.50 - 3.82*x
A3 Frozen: r² = 0.97; y = 13.83 - 4.02*x
Resistivity [kΩm]
Temperature [°C]
A1 Unfrozen
A2 Unfrozen
A3 Unfrozen
A1 Supercooled
A2 Supercooled
A3 Supercooled
A1 Frozen
A2 Frozen
A3 Frozen
d

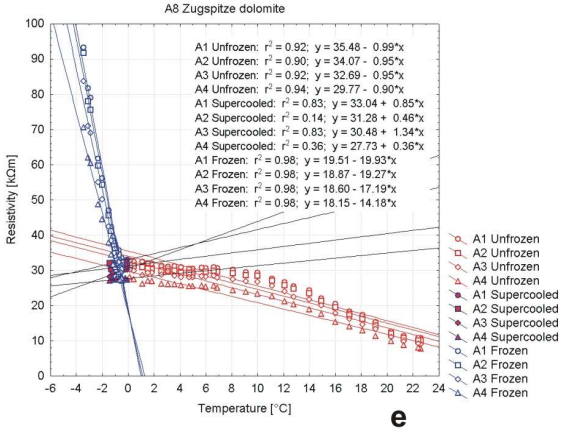
A8 Zugspitze dolomite
A1 Unfrozen: r² = 0.92; y = 35.48 - 0.99*x
A2 Unfrozen: r² = 0.90; y = 34.07 - 0.95*x
A3 Unfrozen: r² = 0.92; y = 32.69 - 0.95*x
A4 Unfrozen: r² = 0.94; y = 29.77 - 0.90*x
A1 Supercooled: r² = 0.83; y = 33.04 + 0.85*x
A2 Supercooled: r² = 0.14; y = 31.28 + 0.46*x
A3 Supercooled: r² = 0.83; y = 30.48 + 1.34*x
A4 Supercooled: r² = 0.36; y = 27.73 + 0.36*x
A1 Frozen: r² = 0.98; y = 19.51 - 19.93*x
A2 Frozen: r² = 0.98; y = 18.87 - 19.27*x
A3 Frozen: r² = 0.98; y = 18.60 - 17.19*x
A4 Frozen: r² = 0.98; y = 18.15 - 14.18*x
Resistivity [kΩm]
Temperature [°C]
A1 Unfrozen
A2 Unfrozen
A3 Unfrozen
A4 Unfrozen
A1 Supercooled
A2 Supercooled
A3 Supercooled
A4 Supercooled
A1 Frozen
A2 Frozen
A3 Frozen
A4 Frozen
e

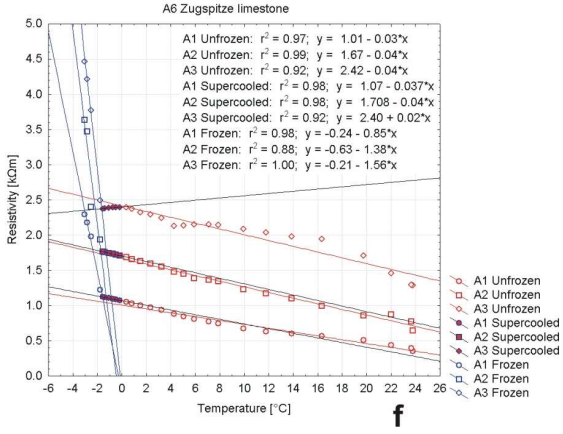
A6 Zugspitze limestone
A1 Unfrozen: r² = 0.97; y = 1.01 - 0.03*x
A2 Unfrozen: r² = 0.99; y = 1.67 - 0.04*x
A3 Unfrozen: r² = 0.92; y = 2.42 - 0.04*x
A1 Supercooled: r² = 0.98; y = 1.07 - 0.037*x
A2 Supercooled: r² = 0.98; y = 1.708 - 0.04*x
A3 Supercooled: r² = 0.92; y = 2.40 + 0.02*x
A1 Frozen: r² = 0.98; y = -0.24 - 0.85*x
A2 Frozen: r² = 0.88; y = -0.63 - 1.38*x
A3 Frozen: r² = 1.00; y = -0.21 - 1.56*x
Resistivity [kΩm]
Temperature [°C]
A1 Unfrozen
A2 Unfrozen
A3 Unfrozen
A1 Supercooled
A2 Supercooled
A3 Supercooled
A1 Frozen
A2 Frozen
A3 Frozen
f

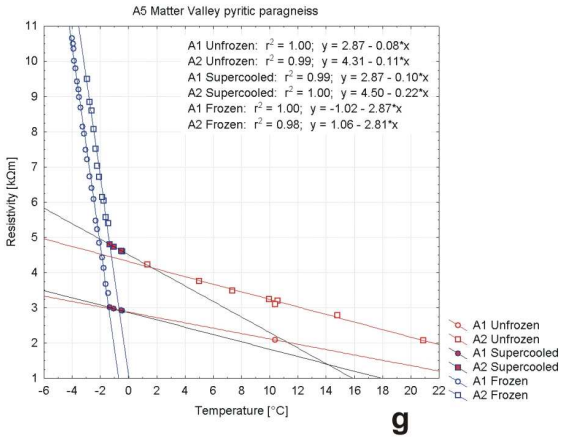
A5 Matter Valley pyritic paragneiss
A1 Unfrozen: r² = 1.00; y = 2.87 - 0.08*x
A2 Unfrozen: r² = 0.99; y = 4.31 - 0.11*x
A1 Supercooled: r² = 0.99; y = 2.87 - 0.10*x
A2 Supercooled: r² = 1.00; y = 4.50 - 0.22*x
A1 Frozen: r² = 1.00; y = -1.02 - 2.87*x
A2 Frozen: r² = 0.98; y = 1.06 - 2.81*x
Resistivity [kΩm]
Temperature [°C]
A1 Unfrozen
A2 Unfrozen
A1 Supercooled
A2 Supercooled
A1 Frozen
A2 Frozen
g

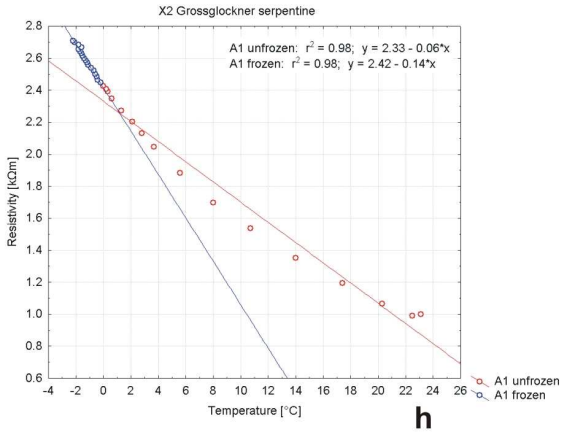
X2 Grossglockner serpentine
A1 unfrozen: r² = 0.98; y = 2.33 - 0.06*x
A1 frozen: r² = 0.98; y = 2.42 - 0.14*x
Resistivity [kΩm]
Temperature [°C]
A1 unfrozen
A1 frozen
h

Fig. 17: T-ρ paths of eight permafrost rock samples with linear approximation of up to four arrays.

Sample a – e show significant supercooling effects; h, in accordance with the physical theory, the serpentine sample with highly attractive antigorite pore walls has no definite freezing point.

Freezing in rocks occurs with a sudden increase in the T-ρ gradient (Fig. 17). Frozen and unfrozen resistivity trajectories can be fitted accurately by linear relations with an $R^2 > 0.88$. T-ρ gradient above 0 °C is -0.33 ±0.22 [kΩm/°C] with extremes ranging from -0.04 to -0.95. T-ρ gradient of frozen rocks is -6.82 ±4.67 [kΩm/°C] with extremes ranging from -1.26 to -17.64. Frozen T-ρ gradients are 12-34 times steeper than unfrozen gradients of the same sample. Except for carbonate rocks (Fig. 17, e, f), supercooled T-ρ gradients are slightly (factor 1.41-1.85) steeper than unfrozen T-ρ gradients. Unfrozen and frozen T-ρ gradients of low-permeability (<10 µD) rocks increase by a factor of 0.2 ($r^2 = 0.45$) and 2.8 ($r^2 = 0.32$) with every percent porosity but are independent of permeability (Fig. 18).

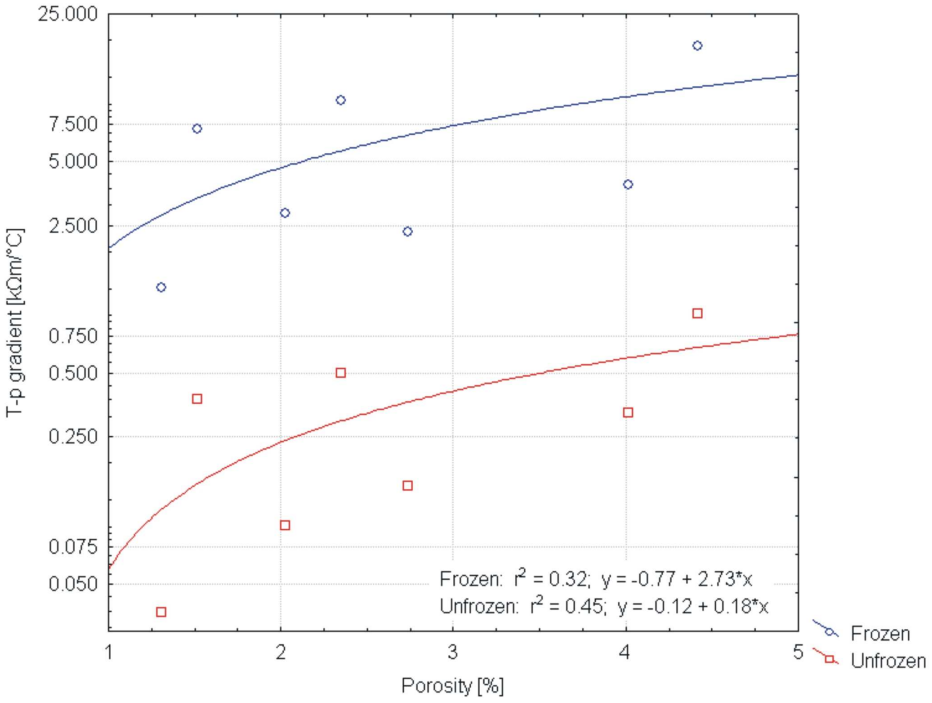

Fig. 18: The effect of porosity on frozen and unfrozen T-ρ gradients.

Table 2: Petrophysical and temperature-resistivity characteristics of permafrost rocks

Location (Country /*Ref.*)	**Lithology**	**Poro-sity [%]**	**Perme-ability [µD]**	**0 °C Resistivity (ρ) [kΩm]**	**-2 °C Resis-tivity [kΩm]**	**T-ρ gradient unfrozen [%/°C]**	**T-ρ gradient super-cooled [%/°C]**	**T-ρ gradient frozen [%/°C]**	**T_E [°C]**	**T_S [°C]**	**Mineral content [weight %]**
Matter Valley (CH)	Schisty quarz slate	2.35 ±0.15	0.816 ±0.07	13.3 ±0.8	32.2 ±2.2	3.7 ±0.2	5.7 ±2.1	30.1 ±3.1	-0.10	-0.90	Q 35.9; M 40.0; F 15.9; Gl 4.4; C 3.8
Matter Valley (CH)	Quarz slate	1.52 ±0.09	0.087 ±0.032	12.0 ±1.0	24.5 ±2.7	3.1 ±0.0	4.5 ±0.8	29.1 ±2.8	-0.10	-1.10	Q 46.6; M 27.5; F 15.5; C 10.4
Matter Valley (CH)	Mineralized paragneiss	2.74 ±0.27	4.73 ±0.85	4.6 ±1.3	9.4 ±2.9	3.1 ±0.1	4.5 ±1.4	24.9 ±8.7	-0.70	-1.20	F 58.7; M 26.0; Q 9.5; C 5.8
Matter Valley (CH)	Pyritic paragneiss	2.03 ±0.14	0.056 ±0.047	3.6 ±0.7	5.7 ±1.0	2.7 ±0.1	4.5 ±1.7	49.8 ±0.5	-1.35	-1.35	F 32.0; Z 21.7; M 15.1; C 10.0; Q 8.2; Ac 5.9; P 3.7; Ga 3.4
Zugspitze (D/A)	Limestone	1.31 ±0.22	4.48 ±0.11	1.7 ±0.5	2.6 ±1.0	2.3 ±0.5	0.8 ±1.3	49.2 ±10.7	-1.55	-1.55	Ca 98.8; Q 1.2
Zugspitze (D/A)	Dolomite	4.42 ±0.41	6.24 ±1.12	33.0 ±1.8	54.1 ±4.3	2.9 ±0.1	-2.3 ±1.0	32.6 ±3.6	-0.55	-1.40	D 74.6; Ca 25.4
Grossglock-ner (A)	Serpentine	1.27 ±0.11	28.7 ±3.9	2.3	2.7	2.6		5.2(?)	0.00(?)	0.00(?)	An. 95.2; W 4.8
Gemsstock (CH)	Grano-diorite	4.02 ±0.36	0.43 ±0.22	10.9 ±0.3	21.6 ±0.3	3.0 ±0.1	5.5 ±0.3	17.9 ±0.5	-0.55	-1.40	Q 37.4; F 21.5; Ch 29.8; M 11.3
Mean value				**10.2 ±7.1**	**19.1 ±14.0**	**2.9 ±0.3**	**3.3 ±2.3**	**29.8 ±10.6**	**-0.7 ±0.4**	**-1.2 ±0.2**	
Barre (US, *M*)	Granite	0.69		11.1	114.2	4.3		43.4			
Indiana (US, *M*)	Limestone	14.1		0.6	37.4	0.5		51.7			
Berea (Antarctica, *M*)	Sandstone	19.8		0.5	35.7	1.1		56.6			
Purtuniq (Quebec, *S*)	Peridotite	0.2		15.9	590.2	3.6		39.7			
Purtuniq (Quebec, *S*)	Pyroxenite	0.2		15.9	327.8	3.6		20.3			
Mean value (*M, S*)				**8.8 ±6.6**	**221.1 ±190.4**	**2.6 ±1.5**		**42.3 ±9.9**			
Berea (Antarctica, *P*)	NaCl-saturated-Sandst.	19.8		0.0088	0.0175	2.2		40.6			

References: M, Mellor 1973; S, Seguin 1978, P, Pearson 1983. T_E , Equilibrium freezing point; T_S , Spontaneous freezing point. Minerals: Q: Quartz; M: Mica; F: Feldspar; Gl: Glaucophane; C: Chlorite, Z: Zoisite; Ac: Actinolite; P: Pyrite; Ga: Garnet, Ca: Calcite; D: Dolomite; An: Antigorite; W: Wollastonite.

T_e ranges from -0.1 to -1.55 °C around a mean value of -0.7 (±0.4) °C (Table 2). When cooling, half of the samples only freeze subsequent to supercooling at a T_s of -1.2 (±0.2) °C . Freezing then occurs with an abrupt rise in temperature and resistivity within tens of seconds to a few minutes (Fig. 19). Self-induced warming by latent

energy dissipation of the sample by 0.1 – 1.0 °C coincides with a sudden increase in resistivity by 1.2 to 6.0 kΩm. When melting resistivity values decline linearly in a hysteresis until T_e.

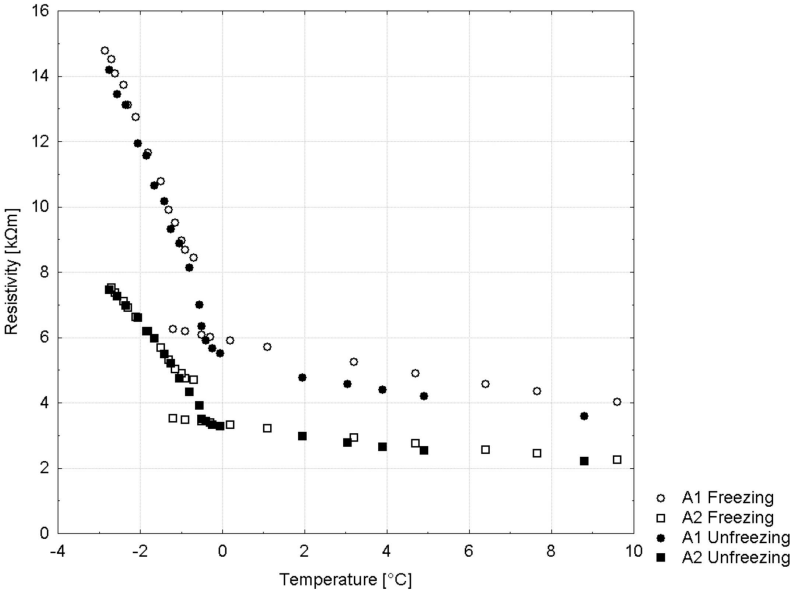

Fig. 19: Supercooling, spontaneous freezing and melting hysteresis of a mineralized paragneiss sample.

6.1.5 Discussion

6.1.5.1 Linear T-ρ approximation

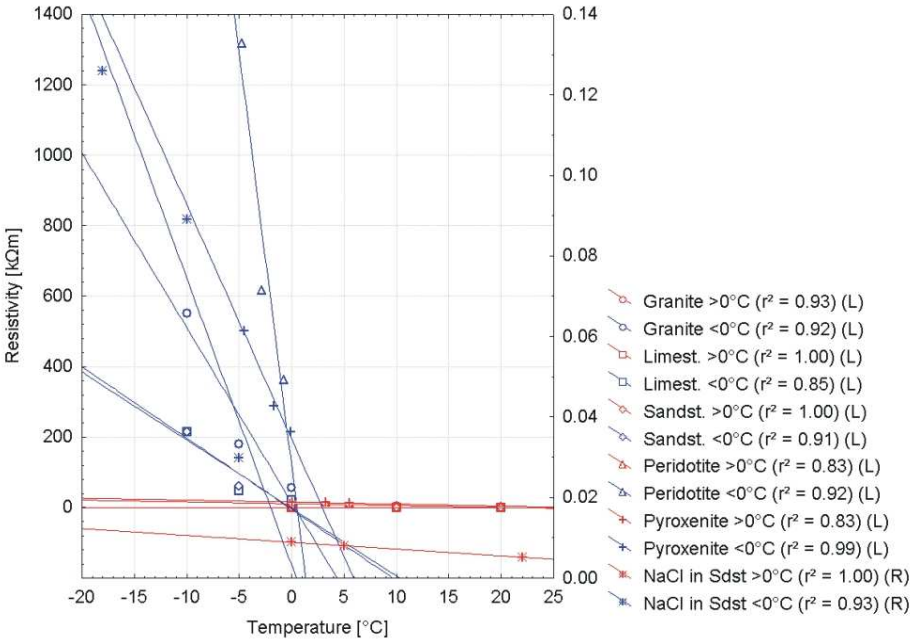

Fig. 20: Linear T-ρ approximation of reanalyzed data by Pearson et al. (1983), Seguin (1978) and Mellor (1973).

Seguin (1978) pointed out that resistivity is a powerful proxy for rock temperature. Two types of T-ρ relationships were proposed in the literature: linear and exponential (Hayley et al., 2007). Keller and Frischknecht (1966) postulated a quasi-linear T-ρ behavior above the freezing point. Our study confirms a linear approximation of all unfrozen samples with an R^2 of 0.92-1.00 and a reanalysis of prior studies (Mellor, 1973; Seguin, 1978) yielded a linear approximation with an R^2 of 0.85 to 0.99 (Fig. 20). Reanalyzed data with NaCl-saturated Berea sandstone by Pearson et al. (1983) indicates a linear approximation with an R^2 of 1.00.

In contrary, the exponential model introduced by McGinnis et al. (1973) is inappropriate to characterize T-ρ behavior of frozen low-permeability rocks. Their measurements were made at increments of 10-20 °C and did not intend to target the critical freezing range accurately. Rock samples presented here show an explicitly linear behavior of frozen T-ρ paths with an R^2 practically between 0.97-1.00, even better than for unfrozen T-ρ paths. Reanalysis of results provided by Mellor (1973) and Seguin (1978) showed that linear approximation matches T-ρ paths of frozen rocks with an R^2 of 0.85 to 0.99. Experiments conducted by Pearson (1983) result in a linear approximation with an R^2 of 0.93 and show that this behavior is independent of pore fluid. Exponential T-ρ behavior characterizes freezing in brines and different unconsolidated materials (Hauck, 2001; McGinnis et al., 1973) but is not applicable to low-permeability rocks where freezing occurs in confined space.

Absolute T-ρ gradients of unfrozen rocks in this study of 0.33 ±0.23 [kΩm/°C] closely resemble reanalyzed values of prior studies with unaltered pore chemistry of 0.33 ±0.25 [kΩm/°C] (Mellor, 1973; Seguin, 1978). Absolute T-ρ gradients of frozen rocks approach 6.8 ±4.7 [kΩm/°C] and are at the lower limb of those measured by the mentioned studies of up to 234 [kΩm/°C]. All studies show pronounced absolute increases in T-ρ gradients of 1-3 magnitudes at the freezing point.

Keller and Frischknecht (1966) introduced "α" as a relative measure of T-ρ gradients that is normalized to absolute resistivity values and is expected to approach 2.5 %/°C for most electrolytes. Our values of 2.9 ±0.3 %/°C, reanalyzed values by Mellor (1973) and Seguin (1978) 2.6 ±1.5 %/°C and even reanalyzed data from brine-saturated Berea sandstone 2.2 %/°C by Pearson (1983) resemble the postulated value closely. We introduced a "β" for supercooled/superheated rocks that applies for the temperature range between 0 °C and the spontaneous freezing point up to -1.55 °C when cooling and "γ" for frozen rocks. Supercooled/superheated T-ρ paths are only slightly steeper than unfrozen paths for siliceous rocks (4.5 ±1.5 %/°C) but horizontal and even reversed for carbonate rocks (-0.7 ±1.2 %/°C). Respectively, "γ" as a measure of relative T-ρ increase of frozen rocks (29.8 ±10.6 %/°C) is one magnitude steeper than "α" and "β". Reanalyzed γ values of prior studies with unaltered pore chemistry (42.3 ±9.9 %/°C) (Mellor, 1973; Seguin, 1978) and brines (40.6 %/°C) (Pearson et al., 1983) show similar results.

6.1.5.2 Supercooling

Physical studies in artificial pores show that freezing point depression in confined media is dependent on pore size and material (Alba-Simionesco et al., 2006). The freezing point depression in rocks with confined pore space was not resolved in prior rock resistivity studies (McGinnis et al., 1973; Seguin, 1978). Our values indicate that the equilibrium freezing point in permafrost rocks is depressed to -0.7 ±0.4 °C. Supercooling up to -1.2

±0.2 °C occurred in four samples. Instantaneous freezing of supercooled samples occurred in tens of seconds to a few minutes with sudden warming of -0.8 ±0.1 °C. The jump in resistivity at the freezing point was already found by Mellor (1973) but has been poorly adapted since that. The resistivity gap coincidental to spontaneous freezing was observed to be 2.9 ±1.4 kΩm.

Three lithological exceptions were included. The greatest irregularity derives from a serpentine that consists to 95 % percent of Antigorite, a layered mica-shaped serpentine mineral. Strongly attractive pore walls increase the freezing point in contrast to most silica minerals (Alba-Simionesco et al., 2006) and may impede a defined freezing transition. Carbonates indicate altered or reversed T-ρ response to cooling below 0 °C which could be due to enhanced pore water solution effects at low temperature and under elevated pressure. A pyritic slate was included to test the effect of electronic conduction in matrix grains. In spite of a pyrite content of 3.7 %, T-ρ gradients remained unaltered.

6.1.6 Conclusion

Exponential T-ρ behavior postulated by McGinnis (1973) may be applicable to loose materials and high-permeability rocks, but is inappropriate for water-saturated low-permeability rocks in high mountains. Physics of freezing are determined by confined pore space. Stable equilibrium freezing temperature is lowered to -0.7 (±0.4) °C. Supercooling until the spontaneous freezing temperature of -1.2 (±0.2) °C occurs for half of the samples. Spontaneous freezing subsequent to supercooling coincides with a self-induced temperature increase of 0.8 (±0.1) °C due to the dissipation of freezing energy and a sudden increase in resistivity of 2.9 (±1.4) kΩm. Latent heat emission and electrical properties show that significant nucleation of ice in pores only occurs after the spontaneous freezing temperature is reached. Melting occurs on a hysteresis without supercooling.

T-ρ behavior is approximated accurately by separate linear functions for unfrozen, supercooled and frozen relations. T-ρ paths below 2 °C and above 0 °C can be defined straightforward by four values: 0 °C unfrozen resistivity (10.2 ±7.1 kΩm) and the unfrozen resistivity gradient of 2.9 ±0.3 %/°C as well as –2 °C frozen resistivity (19.1 ±14.0 kΩm) and the frozen resistivity gradient of 29.8 ±10.6 %/°C. Supercooled T-ρ gradients of 3.3 ±2.3 %/°C resemble unfrozen gradients especially for siliceous rocks. Results emphasize the potency of resistivity as a temperature proxy in instable permafrost rocks.

6.2 Field application to monitor annual active layer processes

Source: Krautblatter and Hauck (2007). Electrical resistivity tomography monitoring of permafrost in solid rock walls. Journal of Geophysical Research, Earth-Surface. Vol. 112(F2), doi: 10.1029/2006JF000546.

This article describes the first attempt to conduct ERT (electrical resistivity tomography) in solid permafrost-affected rock faces. Electrode design, instrument settings, and processing routines capable of measuring under relevant conditions were developed. Four transects, with NW, NE, E and S aspects, were installed in solid rock faces between Matter Valley and Turtmann Valley, Switzerland at 3070-3150 m a.s.l.. DC-resistivity in the transects was measured repeatedly during the summer and compared by applying a time-lapse inversion routine. Resistivity values were calibrated using observed rock surface conditions of thawed, damp rocks (1-8 kΩm), deeply frozen rocks (18-80 kΩm) and the transition from thawed to frozen rocks (8-18 kΩm).

Mean surface layer resistivities of transects respond to air temperatures below 0° C with a rapid increase by a factor of 1.4 to 2.9 from values of 12 – 15 kΩm to values of 22 – 31 kΩm. Rock layers at depths of 2-6 m display a general trend of resistivity decrease in summer, corresponding to a persistent thawing process. Their response to anomalously cool August temperatures occurs with a time lag of two to four weeks. Only the E, NE and NW transects display persistent, high resistivity permafrost bodies (> 50 kΩm) mostly at depths of 6-10 m. The maximum thaw depth of a continuous thawing front above permafrost is 6 m. However, the ERT results emphasize the role of heat transfer by deep-reaching cleft water systems. Thus, permafrost occurs in lenses rather than layers. ERT provides rapid detection of ice and water distribution in permafrost-affected bedrock.

6.2.1 Introduction

Numerous rockfall events involving permafrost-affected rock walls have been observed over the course of the last century. Noetzli at al. (2003) reported 19 cliff falls (10^4 – 10^6 m³) and bergsturz (> 10^6 m³) events since the beginning of the 20th century in the European Alps. Recent observations indicate that the frequency of rockfalls originating from permafrost rock walls has increased. Gruber et al. (2004a) described and modeled the effects of the hot 2003 summer on rock wall permafrost in the Alps, with implications mainly for mid- and high-magnitude rockfalls. Sass (Sass, 2005b) measured elevated levels of small-scale rockfall in rock walls with degrading permafrost in the German Alps. While small-magnitude rockfalls on average cause more casualties than high-magnitude rockfalls (Hungr et al., 1999), single high-magnitude rockfalls can cause catastrophic damages, such as the Huascarán ice and rock avalanche in 1970, which was detached from a permafrost rock area and buried two villages with 20,000 inhabitants (Erismann and Abele, 2001). Although the effects of global warming on rock wall permafrost are not yet fully understood, predictions point towards rapid degradation of permafrost in rock walls in the next few decades (Salzmann et al., 2007) contributing to elevated levels of permafrost-related hazards.

At present, information about the spatial distribution of permafrost in rock walls is derived from two sources. Several boreholes drilled in permafrost rocks provide information on thermal profiles up to a hundred meters

depth (Gruber et al., 2004b; Harris et al., 2003b). This information is supplemented with data sets from temperature loggers that record surface rock temperatures, usually in small holes of several centimeters depth. These data sets are then used to create energy-balance models that calculate the spatial distribution of rock temperatures even in geometrically complex rock walls (Gruber et al., 2004a; Gruber et al., 2004b; Noetzli et al., 2006; Peter, 2003). Two problems associated with this approach are that temperature loggers and boreholes provide only point measurements with unknown spatial representativeness, and that validation of the models at depth is difficult to achieve.

A systematic comparison of different geophysical methods for monitoring permafrost in high-mountain environments has been published by Hauck (2001). From the large variety of geophysical methods, electrical resistivity tomography (ERT, also named DC-resistivity tomography), was considered well suited for a number of permafrost-related problems. The major advantage in applying resistivity measurements to assess mountain permafrost lies in the fact that freezing and thawing of most materials is associated with a resistivity change of several orders of magnitude, which, in turn, is easily detectable with geoelectrical instruments. The installation of permanent electrodes and modeling of subsequent resistivity data sets within the same inversion routine (so-called time-lapse inversion) allows direct monitoring of the spatial and temporal permafrost variability in loose materials and rock masses beneath loose debris covers (Hauck, 2002; Hauck and Vonder Mühll, 2003). The first attempt to derive spatial information from solid rock faces by ERT was conducted by Sass (2003). In subsequent studies, Sass provided further evidence that ERT measurements are capable of measuring the degree of rock moisture (Sass, 2005a) and temporal and spatial variations of freeze and thaw limits (Sass, 2004) in solid rock faces. These ERT measurements were confined to the upper weathering crust (centimeter- to decimeter-scale) of rock faces with electrode spacing of only several centimeters.

This study extended ERT to solid permafrost rock walls and monitored depths up to 10 meters by enlarging electrode spacing to the meter-scale. The scope of the electrical resistivity profiles includes subsurface information from depths in which permafrost in high-altitude rock walls is presumed by modeling and determined through borehole measurements (Gruber et al., 2004b). Possible applications include spatialization of point information obtained from surface temperature and borehole measurements to two-dimensional information and validation of rock wall temperature models. When calibrated sufficiently for different environmental conditions, the technique could provide a fast method to derive the spatial distribution of frozen and thawed rock sections for rockfall hazard evaluation, and possibly for prediction.

Four questions are addressed in this study: (i) Is ERT capable of measuring and monitoring permafrost in solid rock faces? (ii) What technical equipment, instrument settings, and processing routines create reliable results? (iii) What seasonal and short-term changes of rock freezing can be monitored with ERT? (iv) What conclusions can be drawn for the spatial distribution of permafrost in rock walls?

6.2.2 Theory

6.2.2.1 Factors influencing short-term resistivity changes in rocks

Rocks in the study area can be envisaged as semiconductors, in which electric current propagates by electrolytic conduction. Rock conductivity reflects the amount of pore space, its spatial distribution, the water saturation of

pores and the resistivity of pore water, including the ion content. Archie (1942) developed an empirical formula for the resistivity of damp rocks (ρ_e) from the porosity (Φ), pore space occupied by liquid water (S), and resistivity of pore water (ρ_w),

$$\rho_e = a\Phi^{-m} S^{-n} \rho_w$$

Equ. 6.7

where n, m, and a are constants. Assuming that porosity remains constant over brief intervals, changes in rock mass resistivity must result from changes in pore water resistivity or saturation of pore space with water. The decrease of rock temperatures above the freezing point results in a decrease of the mobility of ions, and this corresponds to a linear reduction of resistivity values. Thus, resistivity (ρ) can be calculated as a linear decrease with temperature difference (T-T_0) from the resistivity value (ρ_0) at a reference temperature (T_0):

$$\rho = \frac{\rho_0}{1+\alpha(T-T_0)} \quad .$$

Equ. 6.8

The constant α approaches values of 0.025 K^{-1} for most electrolytes (Keller and Frischknecht, 1966). For temperatures below the freezing point, resistivity depends mainly on unfrozen water content until most of the pore water is frozen. For the range of temperatures encountered in Alpine environments, resistivity can be calculated as an exponential response to the temperature below the freezing point (T_f) according to McGinnis et al. (1973):

$$\rho = \rho_0 e^{b(T_f - T)} \quad .$$

Equ. 6.9

The factor b determines the rate of resistivity increase and can be derived empirically (Hauck, 2001; Hauck, 2002). Resistivity changes along a monitoring transect can be attributed to changes in pore water content and temperature, while changes in porosity and water chemistry can be neglected over daily to monthly measurement intervals in low-porosity rocks.

6.2.2.2 Error sources

Distortions of measurements could derive from the electrokinetic potential created by water percolating in rock clefts. Streaming potential is usually restricted to values below 100 mV (Telford et al., 1990: 293), and is at least one to two orders of magnitude lower than the voltages applied during DC-resistivity measurements. Moreover, standard geoelectric instruments reverse currency direction with a frequency of 1-2 Hz, eliminating the effect of steady potentials.

Additional distortions could derive from large resistivity contrasts at the boundary of suspected permafrost bodies, which are usually orientated parallel to the surface. This may result in slight over- or underestimation of the depth of the transition layer. The same is true for measurements taken when the rock surface was frozen and

therefore included high resistivity sections. Finally, it is inevitable that certain topographic distortions are included when measurements are taken on a structured rock face. Resistivity values tend to be slightly overestimated in prominent rock spurs and underestimated in rock niches (Holcombe and Jiracek, 1984). However, the deviation of the transects normal to the strike of the four transects presented here, in relation to transect length, was smaller than in previous studies (Sass, 2003; Sass, 2004; Sass, 2005a).

It is important to consider that all distortions mentioned above, except electrokinetic potentials, do not influence the comparability of subsequent resistivity measurements, as they remain constant through time. In addition, it is not clear to what degree changes in water chemistry influence measurements. Due to the low permeability of intact gneissic rocks (10^{-10}-10^{-13} m/s) (Prinz, 1997), pore water resistivity is probably relatively stable. Solute rejection and the formation of brines in a "pore"-scale (Hall et al., 2002; Murton et al., 2000) should be addressed in detail if this method is extended to more porous rock media. However, the permeability of fissured gneiss along discontinuities can be significantly higher (up to 10^{-3}-10^{-4} m/s) (Terrana et al., 2005) and solute rejection along discontinuities could cause changes in cleft water conductivity in the micro-scale.

6.2.3 Study area and methods

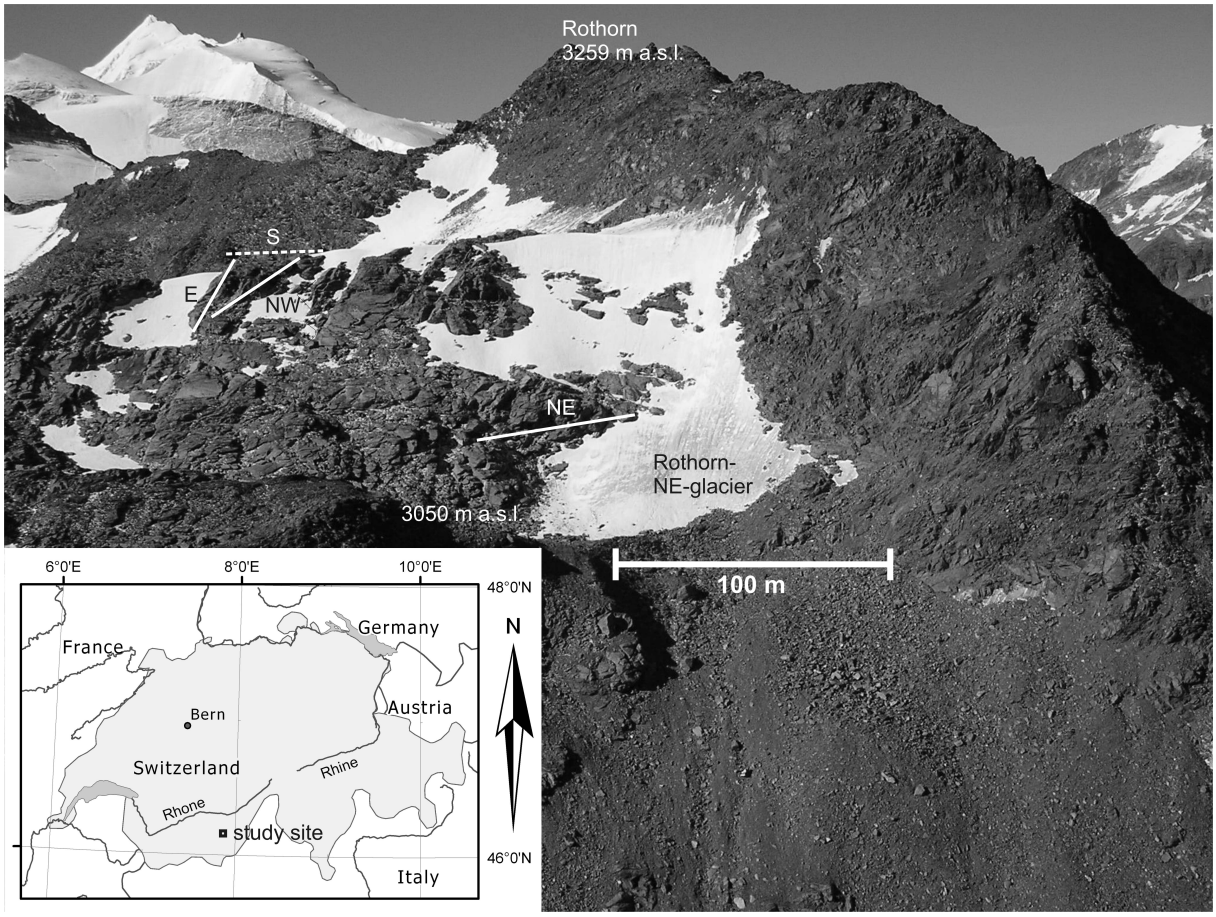

Fig. 21: The position of the DC-resistivity monitoring transects in the study area "Steintälli".

Transects were named according to their dominant aspect.

6.2.3.1 Study area

The study area “Steintälli” is located at the crest line between Matter and Turtmann Valleys in Valais, Switzerland at an altitudinal range of 3070 to 3150 m a.s.l. adjacent to the Rothorn summit (Fig. 21). Lithology in the study area is dominated by slaty paragneisses with homogeneous structure. The warming tendency after the Little Ice Age resulted in the retreat of the Rothorn NE Glacier, which lost more than 300 meters of its maximum length. Presently, the Rothorn NE Glacier is dissected by newly exposed rock bars in several small ice relics, which are subject to further melting.

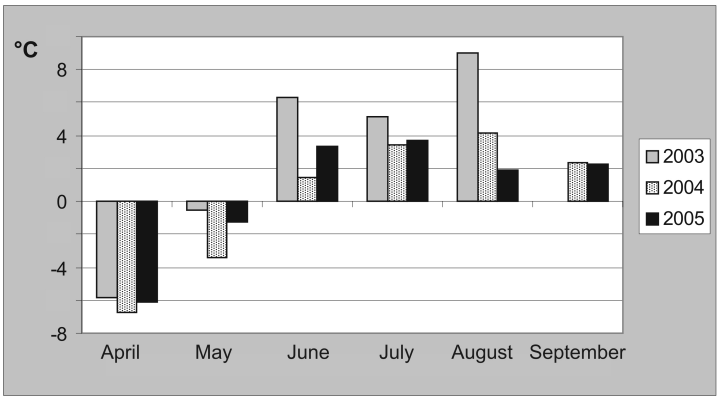

Fig. 22: Mean monthly temperatures measured at the study site during the thaw periods 2003 to 2005.

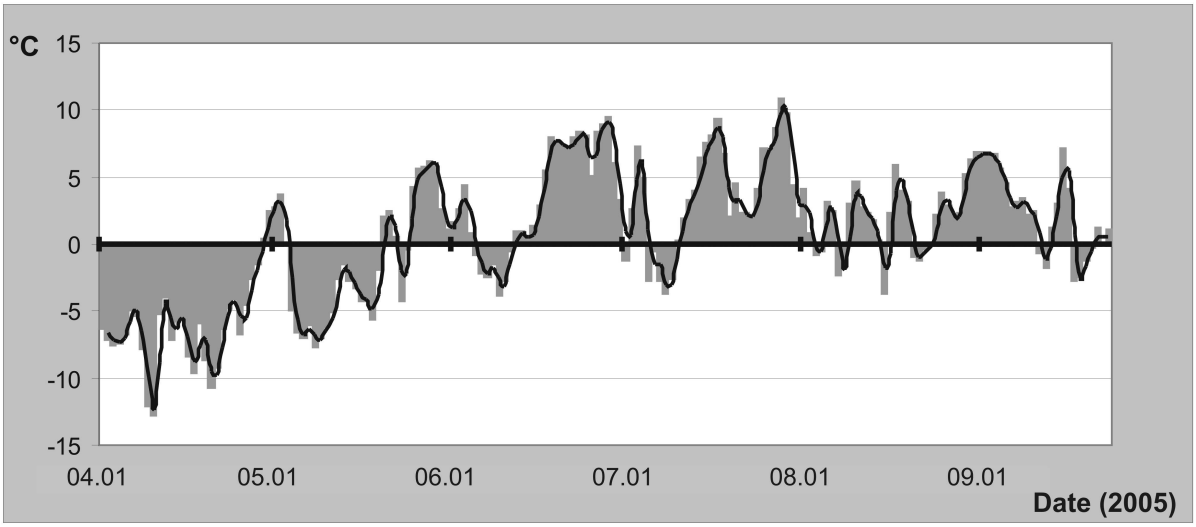

Fig. 23: Daily air temperatures and moving average of air temperature in 2005.

The annual average air temperature of the Steintälli approached values of – 3.5 °C according to measurements taken in the Matter Valley between 1962-90. The permafrost study conducted by Gruber and Hoelzle (2001) in the Matter Valley ranked the whole Steintälli as a “likely permafrost area.” Climatological data have been recorded since July 2002 at a meteorological station located at a horizontal distance of 900 m and at an altitudinal

difference of 330 m from the study site (average 3100 m a.s.l.). Temperature data were corrected by -1.98 °C (0.6 °C per 100 m) for the altitudinal difference. The average annual temperature of 2004 at the study site was –3.7 °C, which is in accordance with the long-term average value. Although no complete dataset was recorded for 2003, existing data from April until August indicate an air temperature several degrees higher than in 2004 and 2005 (Fig. 22). August 2005, when geoelectric monitoring was initiated, was anomalously cool after two summer months with average temperatures (Fig. 23). As all rock bars in the study area are surrounded by ice, local air temperatures can be significantly lower than those measured at the meteorological station. The glacier relics also perform hydrological heat transfer with the rock bars, which is especially evident in the monitoring transect NE, due to the topographic position under an ice relic. The other transects only have lateral contact with glacier remnants (Fig. 21).

6.2.3.2 Data acquisition

Four rock wall sections in the study area were chosen according to following criteria: (i) Rock walls should represent different aspects (NW, NE, S, E); (ii) Lithology and discontinuity patterns should be homogeneous within the rock face exposure and at the depth covered by ERT measurements; (iii) In accordance with criteria established for the positioning of rock wall temperature loggers by the University of Zurich (Peter, 2003), the central part of the measurement transects should represent a free rock face steeper than 60°, in which electrodes were positioned a few meters above the ground to avoid snow covering them in winter; (iv) Planar rock walls were preferred in order to reduce the topography included in the ERT inversion process. As a tradeoff between depth information of ERT and the availability of suitable planar rock faces, 60 m long monitoring transects with electrode spacing of 1.5 m were installed in August 2005. To achieve optimal electrical contact with the rock mass, we used 10 mm thick and 10 cm long stainless steel screws as electrodes that were placed firmly in holes drilled in the rock face. The screws remained in the rock wall and were used for all subsequent ERT measurements.

In the S and NE resistivity transects, we measured the topography of the electrode line three-dimensionally using a tachymeter with accuracy of 5 cm. The same method was applied for 20-30 electrodes visible from accessible viewpoints in the E and NW transects. Missing electrode positions were interpolated using information derived from ruler measurements. As deviations normal to the strike cause significant distortions in the two-dimensional analysis (Holcombe and Jiracek, 1984; Telford et al., 1990; Maurer pers. com.), deviations in the z-direction of a linear function were calculated from the tachymeter datasets and implemented in the topographic modeling of the inversion software RES2Dinv (Loke and Barker, 1995; Loke and Barker, 1996).

We applied an ABEM SAS 300C Terrameter multi-electrode resistivity instrument, designed for 41 electrodes. All measurements were conducted with the same current strength settings. In the rare case that resistance variability greater than 1 % for a single datum point was observed, additional values were measured automatically. All measurements were conducted using a Wenner array with 190 different electrode combinations, as this array yields the highest signal-to-noise ratios for mountain permafrost environments (Hauck and Vonder Mühll, 2003). The contact resistance of each electrode was tested before the measurement. As the electrode contact with the ground is difficult in frozen and ice-coated rock faces, even with the electrode design described above, we excluded up to three electrodes if the contact resistance was too high or not constant with time. If more than three electrodes indicated contact problems, the measurement was not included in the time-lapse inversion.

6.2.3.3 Data processing

Subsequent resistivity measurements in the four transects were inverted using the time-lapse inversion routine of the software RES2Dinv (Loke and Barker, 1996). Use of time-lapse inversion guarantees that all subsequent measurements over a certain transect are processed with the same inversion model used for the first measurement in this transect (Hauck and Vonder Mühll, 2003). Settings of RES2DInv were adapted to the special conditions present in rock faces. We inverted the data with half electrode spacing of 0.75 m and used a finer mesh size, to cope with high-resistivity contrasts. Robust inversion was applied to avoid smoothing of the resistivity gradients expected in the data sets (Sass, 2004). Finally, we chose a model with an increase of 10 % in layer thickness per layer, as this option provided more stable inversion results.

When applying time-lapse inversions in partially frozen rock walls, it is difficult to obtain resistivity models with a root-mean-square (RMS) error between modeled and observed data of less than 10 %. This is partly due to the fact that one to three of the 41 fixed electrodes had insufficient electrical contact and that only the datum points obtained in the first time-lapse measurement can be used for subsequent measurements. A conventional, non time-lapse inversion of the later measurements gives smaller RMS errors (e.g., 6 % for time series 2, 3, and 4 of the NW transect), but produces similar resistivity tomograms. Thus, the resistivity tomograms show low susceptibility to the datum points that were removed from the dataset due to the time-lapse inversion process. Measurements taken on dewed rock surfaces generally resulted in lower RMS errors (e.g., transect NE August 13, RMS = 6.1 %), while measurements on freshly ice-coated rock faces lead to inversion models with insufficient data fit (e.g., the NE transect, August 15, RMS > 18 %).

6.2.4 Results

Fig. 24: Test measurement of frozen rock surface resistivity values at the NE transect (August 15, 2005).

6.2.4.1 Raw resistivity data

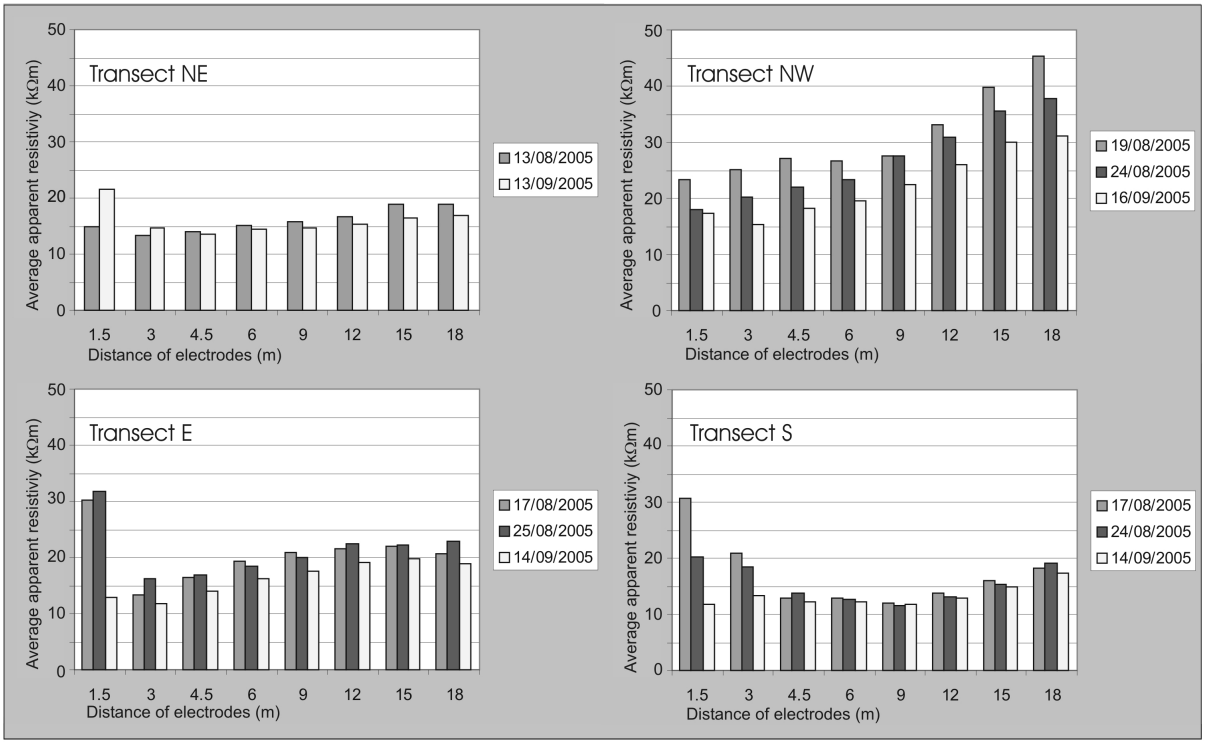

Fig. 25: Apparent resistivity data of Transects NE, NW, E and S

To assess the quality of the data sets, preliminary analysis of the measured apparent resistivities was performed for each measurement. Apparent resistivity is calculated from the measured ratio between potential difference and injected current (resistance), multiplied with an appropriate geometric factor depending on the electrode spacing. If data quality is sufficient, the apparent resistivity data can be inverted on a two-dimensional grid to yield two-dimensional specific resistivity models. As can be seen in Fig. 25, resistivity measurements with small electrode spacing (1.5 m) indicate high variability in apparent resistivity values. Resistivity changes, measured with larger electrode spacings, occur much slower. This means that the uppermost rock layer (decimeter-scale), which is measured with an electrode spacing of 1.5 m, reacts fast and sensitively to frozen or unfrozen conditions at the rock surface. Subsurface layers (1-10 m depth), which are measured with larger electrode spacing (3-18 m), reacted in a slower and less pronounced manner.

The apparent resistivity of 40 datum points with electrode spacing of 1.5 m was compared at each measurement position with corresponding environmental conditions. The occurrence of superficially frozen rock surfaces in the north-facing transects (NE and NW) was observed to reflect mostly air temperatures and the presence of snow and ice. The rock surface of the E and S transects melts quickly in response to direct solar radiation and, therefore, often two or three days earlier than north-facing transects. The best illustration of this behavior is provided by subsequent measurements on the NW transect on September 15th and 16th. On September 15th, following four partly snowy days with average air temperature of 0.5 °C, the NW transect was still frozen and partially ice covered, and yielded a mean apparent resistivity of 24.9 kΩm for all surface values (electrode spacing of 1.5 m). Being that September 15th was the warmest day in September (7.1 °C), the average 1.5 m spacing resistivity

declined to 13.6 kΩm in late afternoon of the following day (September 16th, 4.30-6.30 p.m.), when the rock face was observed to be mostly ice-free and damp. Transect NE showed mean surface layer resistivity of 15.0 kΩm on August 13th, subsequent to four days with air temperatures ranging from 2.2-4.6 °C, in contrast to mean values of 21.6 kΩm on September 13th, following a drop of temperature ranging from -1.6 °C to -0.6 °C over a two-day period. Transects E and S, respectively, thawed in response to intense direct solar radiation on September 14th and showed average 1.5 m electrode spacing resistivities of 12.9 kΩm and 11.8 kΩm. On August 17th, following a two-day snow-rich drop in temperature with average temperature of -0.7 °C, the same transects had average surface layer resistivities of 30.2 kΩm and 30.7 kΩm. In contrast to the general high temporal variability, rock surface sections that remained permanently damp as a result of cleft water outflow (transects NE, S, NW), yielded low (2-8 kΩm) and extraordinarily stable apparent resistivity values, which persisted even during phases of intense freezing. The plunge in temperature from August 20th to August 23rd coincided with a significant redistribution of snow by high wind speeds and, therefore, yielded a less uniform reaction between different transects. In conclusion, absolute apparent resistivity values of single datum points of the deeply frozen surface rock were observed to range between 18 and 100 kΩm, while damp rocks typically have values of 2-8 kΩm, with transitional values ranging from 8-18 kΩm. Average 1.5 m electrode spacing resistivity values, consisting of 40 datum points that reflect transitional freezing in surface bedrock, typically increased from 11-15 kΩm (unfrozen rock) to 22-31 kΩm (frozen rock).

Two criteria reveal the subsurface information gathered in the raw data measured with electrode spacing larger than 1.5 m (Fig. 25). (i) Transect NW stands out due to high (average) absolute apparent resistivity values, which are in the range of frozen rock (> 18 kΩm) at all depths. Average values in the E and NE transects range between 15 kΩm and 23 kΩm, which corresponds with the transition of thawed to frozen rock. Transect S shows relatively low apparent resistivity values of 12 kΩm to 18 kΩm. (ii) The change of apparent resistivity values with time is remarkably homogeneous in all transects and at all subsurface depths. All values, measured with electrode spacings larger than three meters, declined from mid-August to mid-September. The decrease in resistivity with time is more pronounced in the high-resistivity NW transect, with factors up to 1.5. In the lower-resistivity NE, S and E transects, the resistivity decline involves a factor of only 1.05. Only Transect NE was recorded before the snowy plunge in temperature at August 14-15 and, thus shows a less pronounced decline (Figs. 4, 5). The fact that subsurface apparent resistivity values at the end of August are in a few cases slightly lower than those of mid-August and mid-September can be better explained in combination with the spatial information given in next section.

6.2.4.2 ERT tomographies

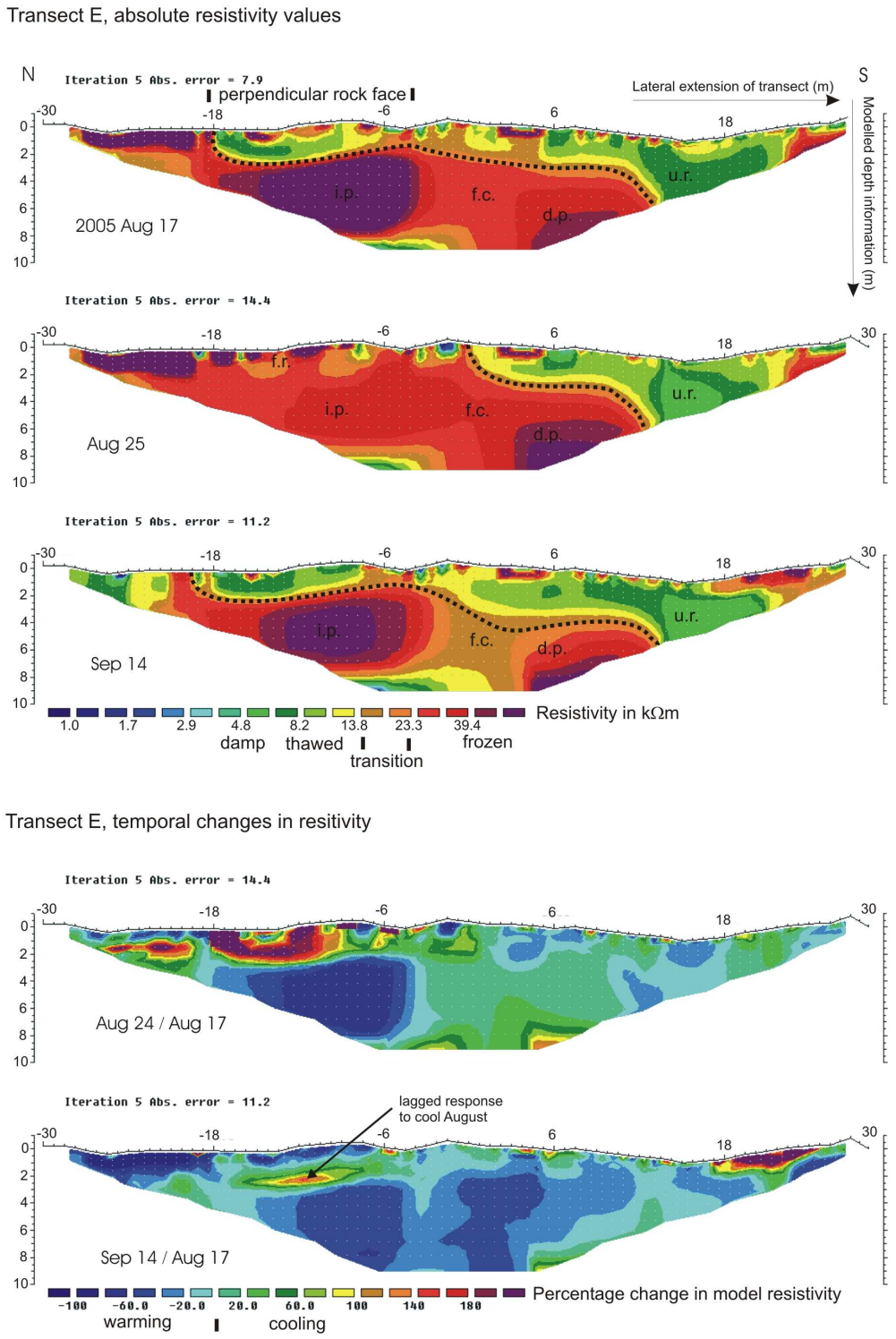

Fig. 26: Time-lapse ERT inversion models of Transect E with approximate freezing/thawing front (dashed line).

Note the response of the frost-susceptible surface layer (f.r.) to the cool second half of August. The freezing corridor (f.c.) extends between intermediate layer and bottom layer permafrost bodies (i.p., b.p.); deep-reaching unfrozen rock (u.r.) is apparent next to permanently water-filled clefts.

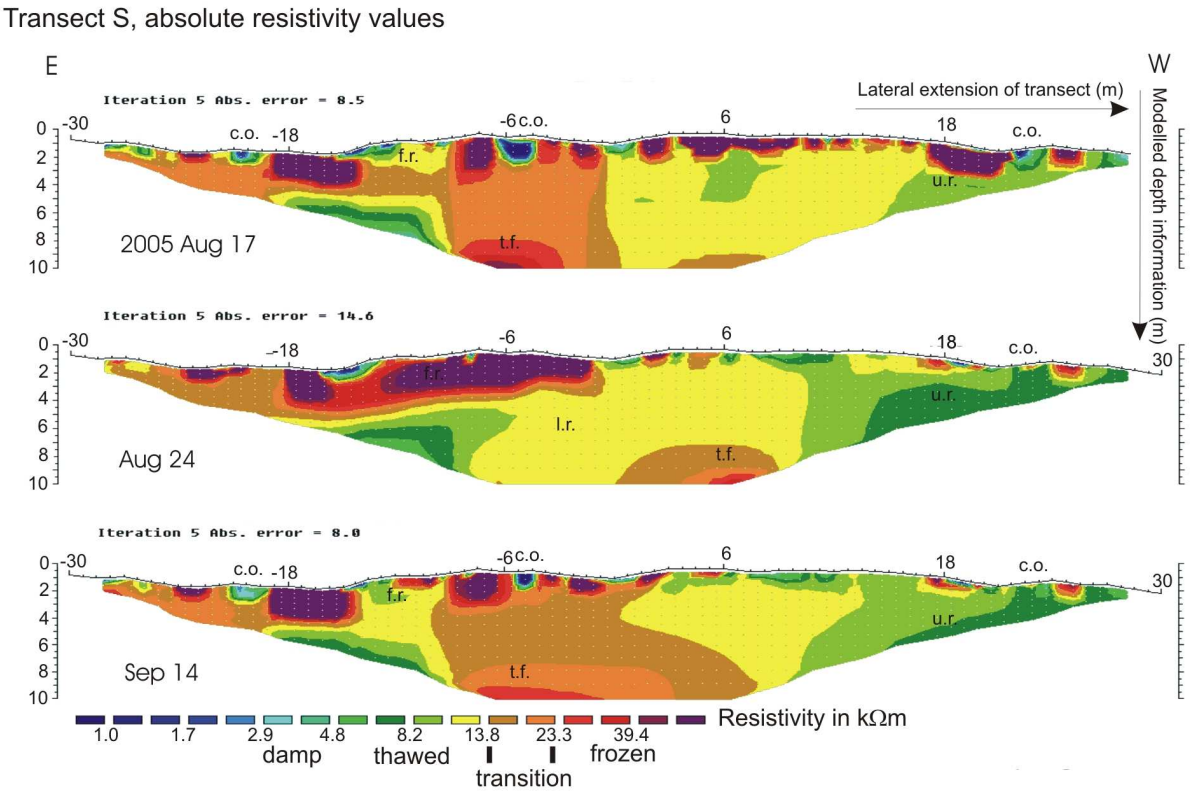

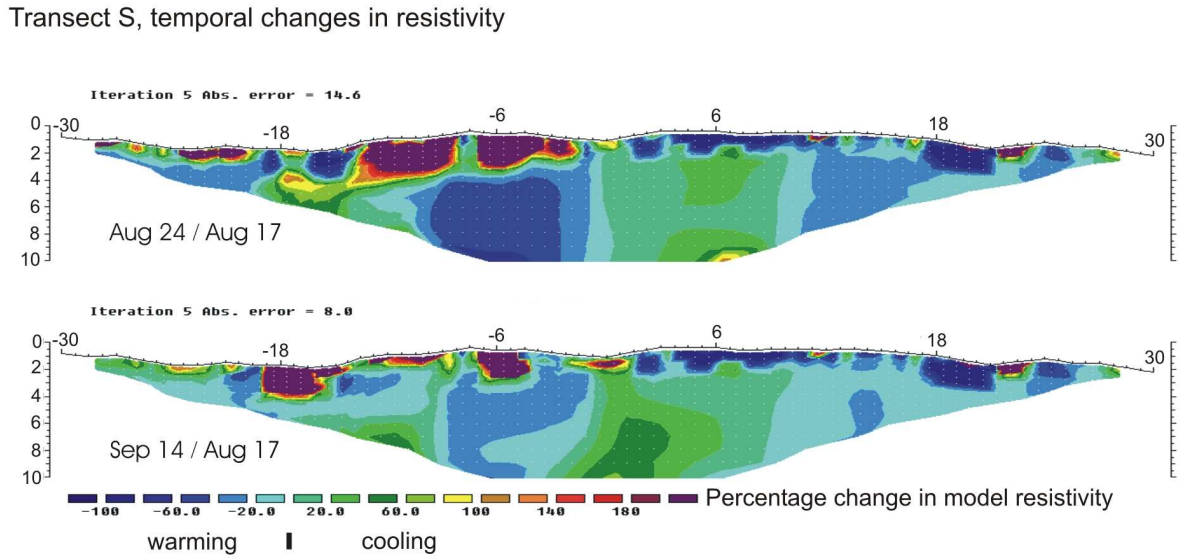

Fig. 27: Time-lapse ERT inversion models of Transect S illustrating damp unfrozen rock (u.r.) next to water-filled clefts that feed water outflows.

Note the lagged response (l.r.) of the intermediate layer to warm June/July temperatures and deep-seated transient frost-lenses (t.f.).

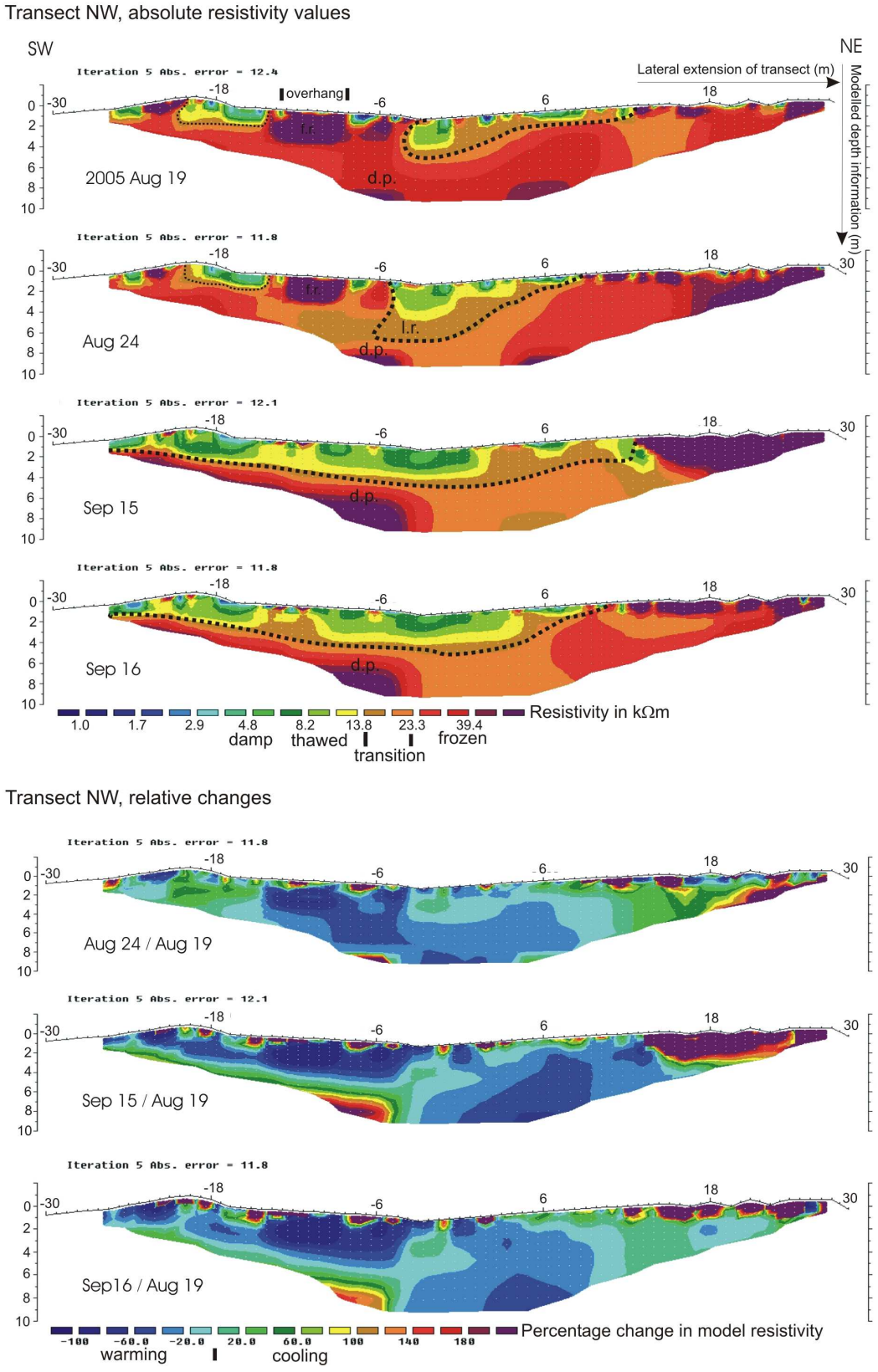

Fig. 28: Time-lapse ERT inversion models of Transect NW with approximate freezing/thawing front (dashed line) influenced by frost-susceptible surface rock (f.r.), the lagged response (l.r.) of the intermediate layer to warm June/July temperatures and a deep-seated permafrost body.

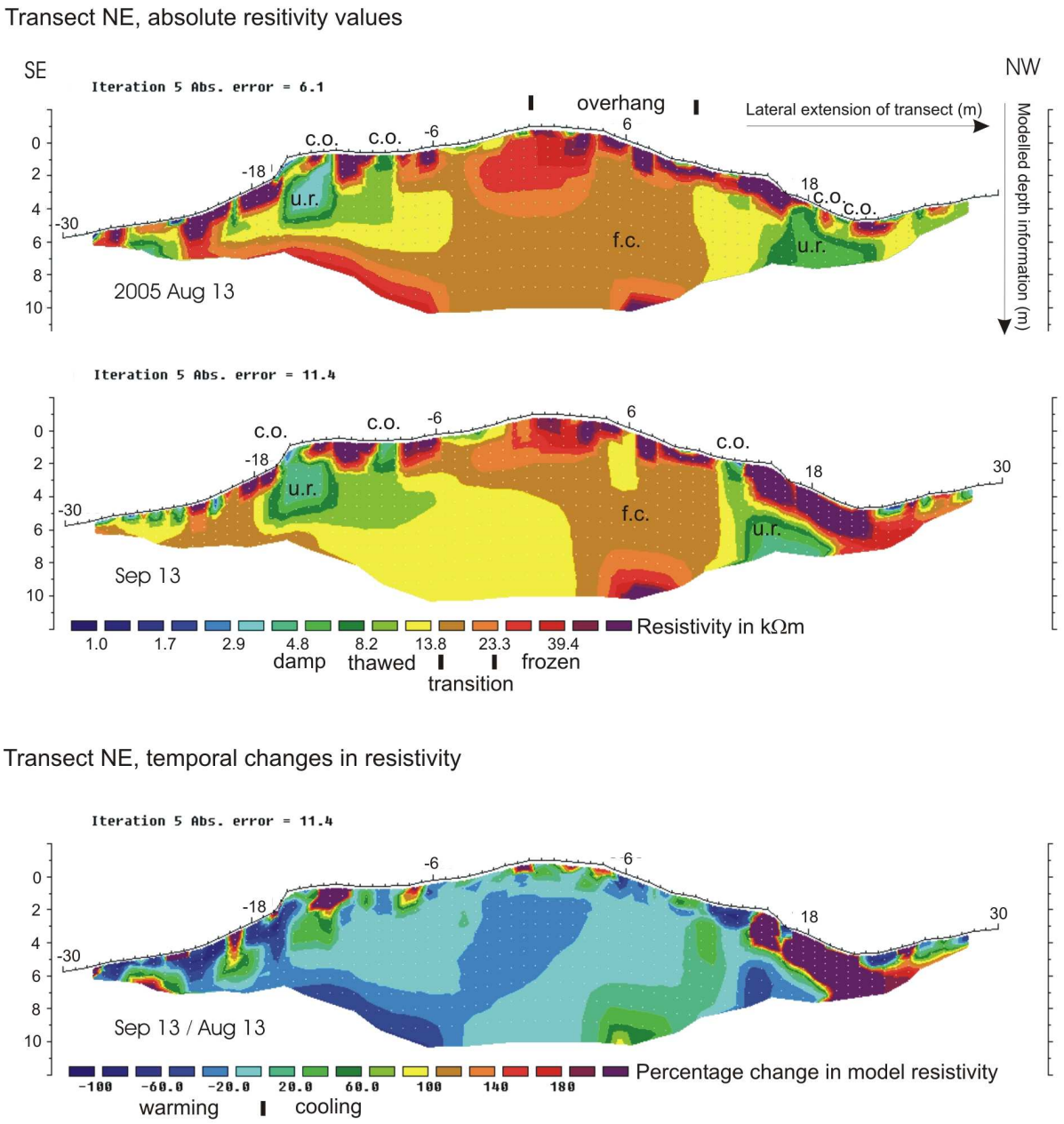

Fig. 29: Time-lapse ERT inversion models of Transect NE showing unfrozen bedrock (u.r.) in the intermediate and bottom layer next to water-filled clefts that feed permanent cleft water outflows (c.o.).

A freezing corridor (f.c.) is developed between frozen bodies in the surface (overhang position) and bottom section.

Table 3: Classification and characterization of typical features in the ERT transects

Position	**Resistivity (kΩm)**	**Spatial Persistence**	**Resistivity Change**	**Examples**	**Surface observation and Subsurface interpretation of Figures 6-9 (abbreviation in Figures)**
Surface layer (0-2 m)	6-120	low	Up to 2000 %	all transects	Frost susceptible rock surface (f.r.)
Surface layer (0-2 m)	2-8	high	< ±60 %	NE, NW, E	Permanent cleft water outflow from water-saturated clefts (c.o.)
Intermediate layer (2-6 m)	10-30	Steady retreat	Negative, -20 % - –100 %	Wide-spread in all transects	Seasonal retreat of frozen rock sections
Intermediate layer (2-6 m)	20-80	high	Temporary reduction 0 - -80 %	E	Intermediate layer permafrost body (i.p.)
Intermediate layer (2-6 m)	2-8	high	< ±60 %	NE, E	Unfrozen rock next to water-filled cleft (u.r.)
Intermediate layer (2-6 m)	10-23	low (weeks)	Temporary reduction 0 - –60 %	S, NW	Lagged response (thawing) of intermediate layer to warm June/July temperatures (l.r.)
Intermediate layer (2-6 m)	15-25	Transient phenomenon	< ±60 %	E, S, NE	Freezing corridor between different frozen sections (f.c.)
Bottom layer (6-10 m)	20-80	high	Positive, 0-140 %	NW, NE, E	Deep-seated permafrost bodies (d.p.)
Bottom layer (6-10 m)	3-14	high	< ±60 %	E	Unfrozen rock next to water-filled cleft (u.r.)
Bottom layer (6-10 m)	18-30	Transient phenomenon	< ±100 %	S	Temporary local frost-lens (t.f.)

Results from the ERT inversions include a range of specific resistivity values between 1 and 120 kΩm. Spatial patterns of resistivity distribution can be classified according to (i) position; (ii) resistivity range; (iii) spatial persistence; (iv) temporal variability of resistivity; and (v) neighborhood characteristics (see Table 3). As described in Section 6.2.4.1, the largest part of the surface rock layer down to 2 m depth is characterized by frequent and quick resistivity changes up to a factor of 20 in response to rock surface temperatures. Results presented in this article also relate to specific resistivity measurements of rocks at depths of 2-6 meters (“intermediate layer”) and 6-10 meters (“bottom layer”).

Three types of resistivity zones can be observed in the bottom layer. (i) Highly resistive “lenses” with an extent of several meters, high spatial persistence, and a remarkable increase in resistivity up to 140 % during the summer period (“d.p.” = deep-seated permafrost, in Fig. 26, Fig. 28 and Fig. 29). (ii) A low resistivity body in the bottom layer is only visible in the tomographies of Transect E (Fig. 26). However, due to its position under a high resistivity zone it is difficult to judge to what degree its values are influenced by the inversion routine. (iii) Spatially non-persistent bodies in Transect S, which have resistivity values ranging from 18-30 kΩm (“t.f.” = temporary frost lenses, in Fig. 27).

A typical feature in the intermediate layer is (i) the decline in resistivity values ranging from –20 to –80 % in comparison to the first mid-August measurement. This is the most wide-spread phenomenon and can be observed in all tomographies. In all transects that include a measurement at the end of August, the minimum resistivity values in the intermediate layer are apparent at this time (“l.r.” = lagged response, in Fig. 26, Fig. 27 and Fig. 28), while resistivities increase from the end of August until mid-September. (ii) In some cases the high-resistivity zones of the surface and the bottom layer are connected by corridors with resistivity values between 15 kΩm and 25 kΩm (“f.c.” = freezing corridors, in Fig. 26 and Fig. 29). (iii) Persistent cleft water outflows (“c.o.”, in Fig. 27 and Fig. 29) observed at the rock face often correspond to low-resistivity zones extending to depths of 6 m (“u.r.” = unfrozen rock, Fig. 26, Fig. 27 and Fig. 29) and thus into the intermediate layer. Similar to the surface cleft water zones, these patches experience relatively small temporal resistivity changes.

6.2.5 Discussion

The electrode design, measurement settings, and inversion parameters applied in our ERT transects resemble those recommended by Sass (2003) for ERT measurement in rocks. Sass applied steel nails or screws, 5 mm in diameter, driven 10 mm into boreholes. We used stainless screws, 10 mm in diameter, driven 100 mm into boreholes to achieve optimum contact in frozen rock. The GeoTom-2D system applied by Sass and our ABEM SAS300 system have different strategies to cope with high resistivities. While the GeoTom system, as modified by Sass, can measure amperages as low as 0.005 mA in response to voltages up to 0.24 V, the ABEM system is capable of applying high voltages up to 160 V to create a stable current of 0.2 mA. Thus, the maximum resistance that can be measured by the ABEM device is 800 kΩ (GeoTom modified by Sass 48 kΩ). This restricts the range of measurable resistivities to 1200 kΩm for an electrode spacing of 1.5 m or 2,400 kΩm for an electrode spacing of 3 meters and so on. All measured resistivities, including those of frozen rock, were significantly smaller than the 1200 kΩm resistivity limitation of the measurement device for the minimum electrode spacing of 1.5 m. One advantage of the ABEM device is that the noise of possible distortions, such as electrokinetic potentials, is reduced when applying voltages two or three orders of magnitude higher than these potentials. The settings of the inversion routines such as fine mesh, robust inversion, 4 nodes, and topography modeling resemble those recommended by Sass (2003). The advantages of applying time-lapse inversion for data derived from fixed monitoring transect were investigated extensively by Hauck (Hauck, 2002).

Several outcomes support the hypothesis that the monitored rock transects reflect frozen and thawed rock conditions. The transition of thawed to frozen rock conditions observed at the rock surface coincides with a sudden increase of surface resistivity values by a factor of 1.4 to 2.9 in all transects. Mean values of thawed surface rock indicated values of 12 – 15 kΩm, while frozen rock surface conditions typically yield values of 22 – 31 kΩm.

Due to the fact that the mean apparent resistivity value includes forty data points with electrode spacing of 1.5 m for every measurement at every transect, this assumption compares the average signal of a few hundred data points and is highly significant. The effect of cooling on the resistivity of non-frozen rock typically causes resistivity gradients of 0.4 per 10 °C temperature change and cannot, therefore, be responsible for this phenomenon (Hauck, 2001; Hauck, 2002; Keller and Frischknecht, 1966; Telford et al., 1990). The laboratory measurements conducted by Hauck (2001) showed that an exponential increase of resistivity with declining temperature in dry and saturated materials occurs only at or below the freezing point (McGinnis et al., 1973). Comparison with field data taken at the Schilthorn, Switzerland yielded evidence that this relation is also true for natural conditions. Moreover, similar gradients for the transition of thawed rock to frozen rock were observed by Sass (2004). Thus, there is little doubt that the range of resistivity values from 15 kΩm to 22 kΩm marks the transition between thawed and frozen rock. Completely dry rocks are virtually absent in this system due to the steady presence of snow, ice, and cleft water on the rock surface. According to these results, an approximate 0 °C-isoline is drawn at 18 kΩm in Transects E and NE (Fig. 26 and Fig. 28) where continuous freezing/thawing fronts are developed. The uncertainty is given in all figures as the "transition zone" reaching from 14-23 kΩm (brown and orange). It is derived from the 15.0-21.6 kΩm-range plus approximately 10 % for additional distortions.

The measurements provide relatively well-calibrated values for different surface rock conditions. Due to reduced physical weathering activity with distance from the rock surface (Lautridou, 1988; Matsuoka, 1990; Matsuoka, 2001; Sass, 1998; Viles, 2001), slightly smaller rock porosities with increasing depth could result in reduced maximum resistivity values in frozen rocks. However, previous studies suggest that this effect does not influence resistivity values significantly (Sass, 2003; Sass, 2004). It is, therefore, a straightforward approach to assume that the resistivity values of surface and subsurface layers of rocks react similarly to freezing.

The distinction between temporarily frozen rock and permafrost occurrences is a difficult task and must rely on characteristics such as; (i) the spatial persistence of frozen rock sections; (ii) high resistivities that indicate a deeply frozen body capable of resisting a phase of seasonal heat transfer; and (iii) a low ambient resistivity decline next to the central permafrost body. High-resistivity bodies that fulfill these criteria can be found at depths of 6 to 10 m in the NE transect below electrode position 6 and in the NW transect below electrode position –6. Transect E stands out because it shows a high-resistivity lens in the bottom layer below –6 m, and an even more pronounced high-resistivity lens reaching into the intermediate layer from –4 m to –8 m. All those bodies in the bottom layer are branded by persistent resistivities exceeding values of 40 kΩm in the center of the lens, combined with a trend of increasing resistivities during the summer that can exceed 200 %. The resistivity of the intermediate layer high-resistivity body in Transect E (Fig. 26) declines to values of 30-40 kΩm at the end of August but soon recovers to values exceeding 50 kΩm. Considering, that ERT based on Wenner arrays tend to underestimate subsurface maximum resistivities (Hauck and Vonder Mühll, 2003) it is virtually certain that these bodies consist of a permanently deep frozen bedrock capable of surviving even warm summers without disappearing. These permafrost bodies show the same inverse temperature trend with surface temperature documented by the 7.3 m deep thermistor in the Stockhorn borehole (Gruber et al., 2004b). In contrast to the other three profiles, Transect S does not display a stable high-resistivity body. Moreover, high-resistivity zones in the bottom layer do not exceed resistivities of 30 kΩm. Thus, the high-resistivity bodies in the bottom layer of transect S could be better interpreted as a unique transient or seasonal event that could result from a reversed temperature

trend in the bottom layer, or from other transient cooling effects. However, interpretation of unstable phenomena based on such a short time series should be treated with caution.

Comparison of subsurface information from ERT with modeling approaches based on measurements from rock-surface temperature loggers can yield further insights. According to a modeling approach by Gruber et al. (2004a), the expected mean annual rock-surface temperature for the NE and NW transects is ca. 0°C and, respectively, 2 °C and 4 °C for the E and S transects. In fact, Transects NE and NW provide evidence for permafrost bodies while Transect S only shows transient frost lenses. The permafrost body in Transect E could be explained by local rock wall topography (perpendicular rock face) (Fig. 26) and microclimatic features (ambient chilling by glacier relict). According to this model, thaw depth for the NE and NW transects would range between 5 and 7 meters. In fact, the continuously developed thawing lines in the E and NW transects indicate thaw depths of 4-5 m and 6-7 m, respectively.

There is some evidence that the thawing line already retreats in September and that late-August tomographies display the annual maximum of thaw depth in 2005. The apparent resistivity data show a uniform decreasing trend of subsurface resistivity values from mid-August to mid-September. The reduction of resistivity generally indicates warming and melting. This reduction is also demonstrated in the tomographies that illustrate resistivity changes. The intermediate layer (2-6 m) of all transects is dominated by a decreasing trend of resistivities with a range up to –80 %. Nevertheless, the reduction of resistivity shows high spatial variability. Transect NW (Fig. 28) provides the best data set for deriving average thaw depth. When observing the transition between brown and orange colors at 18 kΩm, a value that approximately marks the transition to deeply frozen rock, it appears that the average freezing line in the central part retreated from 2-2.5 m in mid-August to 6 m at the end of August and moved back to approximately 4 m by mid-September. A similar continuous appearance of the thawing line can be detected in Transect E. Here, the frost line penetrated 3-4 m into the rock face in mid-August, disappeared by the end of August, and readvanced to 3-4 m in mid-September. In contrast to this, Transects NE and S display an inhomogeneous appearance of frozen and unfrozen rock sections without persistent layers.

All transects recorded at least three times provide information on thermal conduction from the rock surface to the intermediate layer (2-6 m). In Transects E, NW, and S maximum thaw depths were reached on August 24-25th while transects recorded on September 14-15th already indicate readvance of the frost line. The difference between the intensively frozen rock surface and the deeply thawed intermediate layer at the end of August is clearly visible in these transects. The effects include thawing of temporarily frozen sections to more than 6 m depth (“l.r.” = lagged response, in Fig. 26 and Fig. 28) and warming of intermediate layer permafrost bodies (“i.p.”, in Fig. 26, Aug 25). Keeping in mind the cool period extending from 2nd to 23rd of August (average air temperature 1.1 °C), followed by an extended warmer period (average air temperature 4.1 °C) from August 24th to September 10th, the temperature signal in the intermediate layer is delayed by approximately two to four weeks. The propagation of the “August” freezing front is best illustrated in the tomographies showing temporal resistivity changes of Transect E (Aug 24/Aug 17, Sep 14/Aug 17, in Fig. 26). The formation of freezing corridors (“f.c.”, in Fig. 26 and Fig. 27) between two frozen rock sections in Transects S and E coincides with readvance of the freezing front in September, and can be interpreted as bilateral chilling that initiates a rapid cooling process. Propagation of heat occurs several times faster than expected from theoretical heat conduction modeling (see e.g., Yershov, 2004). This is, however, in accordance with empirical results for heat propagation at the Stockhorn borehole (Gruber et al., 2004b), obtained for comparable conditions at depths of 0.3 m, 1.3 m, 1.8 m,

2.3 m, 3.3 m, 7.3 m and 13.3 m. The cool September and warm October anomalies of 2002 are visible in the thermal profile at 2.3 m depth with a time lag of 1-2 weeks, in accordance with our observations. However, in the Stockhorn data set this signal disappears at about 3.3 m depth, while our tomographies illustrate monthly signal propagation up to 6-7 m depth (Fig. 27 and Fig. 28). The Stockhorn borehole is located at 3400 m a.s.l., 300 m higher than our study site. It experiences lower average temperatures and is insulated by a decimeter- to meter-thick debris cover and more latent and sensible heat transfer is, therefore, necessary for freeze-thaw transitions than at our study site. The time lag is expected to be smaller in our measurements and monthly events can propagate to greater depths. These results match with the time-lag observed for rockfalls in the hot summer 2003 (Gruber et al., 2004a). The discrepancy between theoretical calculations and empirical values (borehole temperatures, ERT, rockfalls) of heat propagation underlines the need for further research, especially on latent and convective heat transfer in these systems.

According to ER tomographies, heat transfer by cleft water is an important determinant of the overall distribution of frozen and thawed rock. This is especially apparent for the low resistivity zone below the permanent cleft water outflows ("c.o.") in Transect NE (Fig. 29). Movement of cleft water in Transect NE is probably a result of the glacier relic above the rock bar (see Fig. 21) that feeds water into the cleft system. Smaller outflows of water were observed in Transects E and S and also match persistent low-resistivity zones in the tomographies. In Transects NE, S and E, heat transfer by these cleft water systems plays a key role for the development of frozen rock sections at the surface and in the subsurface. Wegmann (1998) noted the importance of percolating cleft water in the thermal regime of rock permafrost, the thickness of the active rock layer, and the mechanical properties and deformation of rock based on laboratory measurements and observations in two boreholes adjacent to the Jungfrau Peak at 3700 m a.s.l.. However, present understanding of the latent and sensible heat transfer between percolating water in clefts and permafrost rocks remains poor. This topic could profit enormously from further ERT monitoring transects, especially when combined with other geophysical techniques and "traditional" permafrost temperature measurements and models.

6.2.6 Conclusion

ERT is applicable in permafrost rock walls if several technical requirements are considered. These requirements include a special electrode design and certain instrument settings, such as the usage of high voltages and low electrical currents. Time-lapse measurements with fixed electrodes can delimit frozen and thawed rock sections and their temporal evolution. Resistivity values measured under observed conditions at the rock surface indicate values below 15 kΩm for thawed rocks and greater than 22 kΩm for frozen rock, with the intermediate range corresponding to the transition between thawed and frozen rocks. Permafrost bodies were found in Transects NE and NW, in accordance to rock permafrost models but also in Transect E, possibly favored by microclimatic and microtopographic conditions. Continuous thawing fronts above permafrost (Transects E, NW) reached a maximum depth of 4-7 m in late August. Rock layers at 2-6 m depth respond to the temporary interruption of summer heat conduction caused by cool August temperatures, with a delay of approximately two to four weeks. The speed of heat transfer is in the range of values reported from borehole measurements at comparable permafrost sites nearby, but much higher than expected from theoretical heat conduction models. Micro-scale features, such as overhangs and clefts with percolating water, have a high impact and result in a distribution of permafrost in

lenses rather than layers. ERT can detect the spatial distribution of frozen and thawed rocks rapidly, but requires careful assessment and calibration according to local environmental conditions. Future improvements of this method should address the error sources described in section 6.2.2.2. Additional laboratory and complementary geophysical measurements and improved inversion modeling techniques will increase the reliability of ERT measurements in permafrost-affected bedrock.

6.3 Field application to monitor multiannual permafrost response

Source: Krautblatter (2009, in press). Patterns of multiannual aggradation of permafrost in rock walls with and without hydraulic interconnectivity (Steintälli, Valley of Zermatt, Swiss Alps). Lecture Notes in Earth Sciences. Vol 105. (Section "System settings" is excluded as it was moved to section 5.1 Thermal properties)

This article shows monthly, annual and multiannual response of two rock permafrost systems with and without hydraulic interconnectivity. It is hypothesized, that interconnective systems with cleft water percolation from glacierets close to 0 °C are high-entropy systems that balance rock masses at 0 °C and prevent cooling but are not effective in excessive melting, as thermal conduction away from water pathways into compact rock is a function of sensitive temperature gradients. This was tested using static (permafrost distribution in 2005) and dynamic (permafrost aggradation 2005-2007) performance of two adjacent north-exposed transects with similar geometries, geology and discontinuity patterns. Transect NW is only affected by heat transfer from the rock surface. Transect NE conducts hydraulic heat transfer with glacierets by meltwater seepage. Electrical resistivity tomography (ERT) time-sections and mean apparent resistivity – median depth of investigation (AR/DOI) gradients of steep sections (> 60°) were analysed from 2005 to 2007. (i) In 2005, a body in a transitory (0 °C) resistivity range (< 20 kΩm) was developed in Transect NE. Transect NW indicated a deeply frozen body (> 40 kΩm) of several meters diameter. (ii) Negative AR/DOI surface gradients indicate a pronounced short-term response of surface resistivities in Transect NW to surface chilling (Aug. 13, 2007: -3.3 kΩm/m) and cool pulse propagation whereas Transect NE is well buffered (Aug. 13, 2007: -0.1 kΩm/m). (iii) Cool mid-summer conditions in 2005 and 2006 initiated permafrost aggradation in both transects. In Transect NW, ERT displays resistivity increases by more than 70 %, a spatially aggrading permafrost body and the formation of a new perennially frozen rock body. Resistivity in Transect NE increases 10-30 % in the transitory body. (iv) In Transect NW, the AR/DOI gradient increased from 5 kΩm/m in August 2005 to 11 kΩm/m in August 2007, indicating significant permafrost aggradation and cooling. In Transect NE, AR/DOI increased from 0.6 kΩm/m in August 2005 to 1.0 kΩm/m in August 2007 but resistivities still do not exceed the initial freezing range significantly at any depth of investigation. Data reliability of both transects is assessed in terms of uncertainty and relative sensitivity plots.

6.3.1 Introduction

Recently, much attention is spent to bedrock permafrost systems as rockwall instabilities and permafrost-related rockfalls appear to be an increasing threat to human lives and anthropogenic structures in high-mountain areas (Gruber and Haeberli, 2007; Harris et al., 2001). The Dzhimarai-khokh rock/ice avalanche in 2002 (Russian Caucasus) detached approximately 4 million m³ from a permafrost-affected starting zone and caused more than 140 casualties (Haeberli, 2005; Haeberli et al., 2003; Kääb et al., 2003). Even smaller permafrost rockfalls, such as the 2003 Matterhorn rockfall are considered as major hazards in densely populated high mountain areas (Gruber et al., 2004a). Inventories show that the frequency of these rockfalls has considerably increased in the

warm 1990s and was boosted by the hot summer of 2003 (Schoeneich et al., 2004). Moreover, slow rock creep in permafrost rocks causes significant damage especially to tourist infrastructure in high mountain areas.

Besides temperature logger data, borehole information and rock temperature modeling approaches, geophysical applications provide a new perspective for the spatial and temporal analysis of rock permafrost (Krautblatter and Hauck, 2007). Permafrost geophysics provide a new insight into the spatial and temporal internal behavior of rock permafrost systems in response to external climatic forces on a monthly, annual and multiannual scale. A review of external factors influencing the rock permafrost system has been given by Gruber and Haeberli (2007) and these factors will not be discussed here. This article rather concentrates on internal system behaviour and tries to answer three questions:

(i) What factors govern response in hydraulically connective and non-connective rock permafrost systems in terms of thermodynamics? (ii) Do resistivity signals reveal spatial and temporal patterns of rock permafrost aggradation over time? (iii) How reliable is such data in terms of data uncertainty and sensitivity? (iv) Do time-lapse geophysics reveal systemic differences of permafrost aggradation in hydraulically connective and non-connective rock masses?

6.3.2 Field site

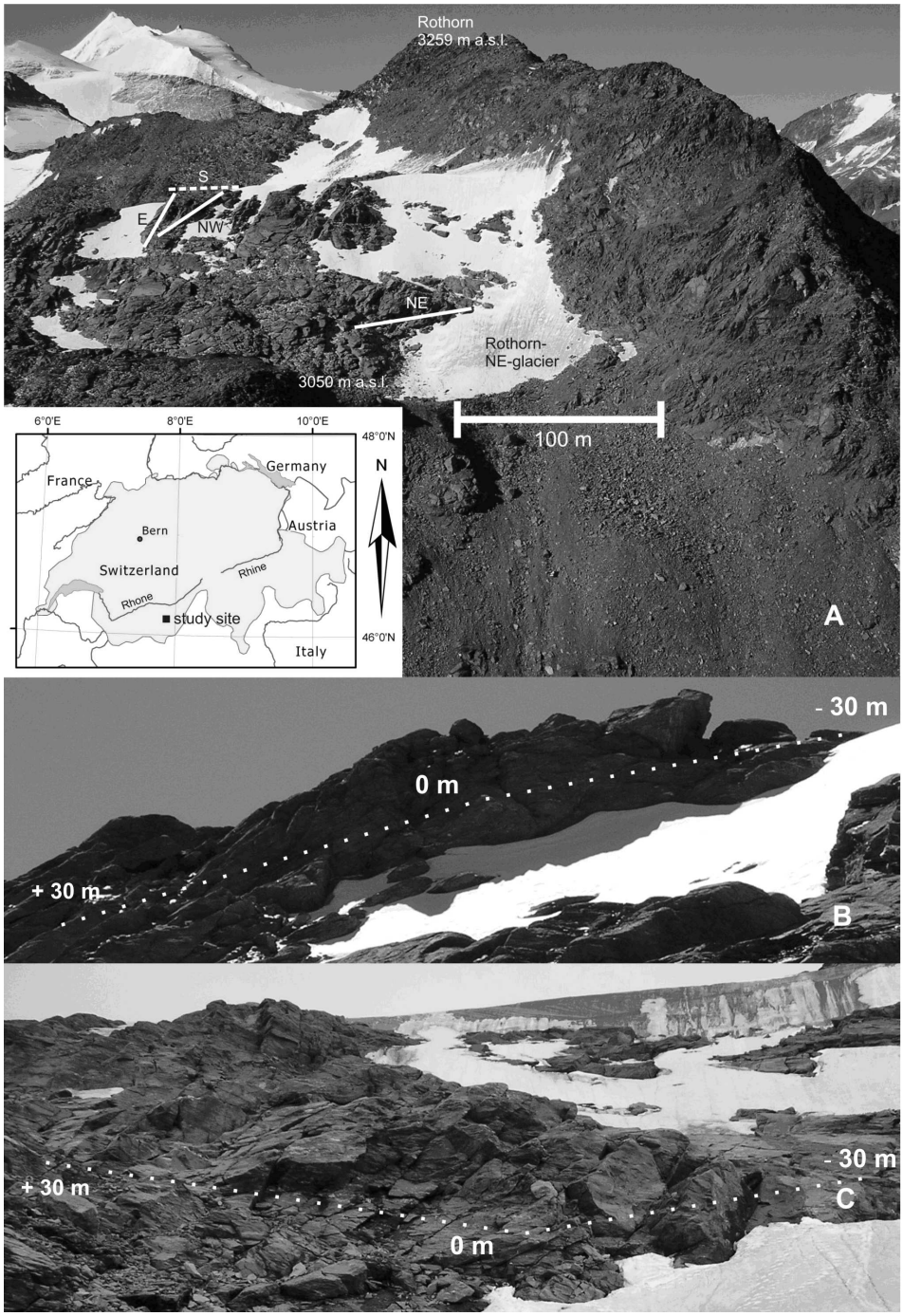

Fig. 30: Position of transects in the Steintaelli.

A) Overview of the study site "Steintälli". The Turtmann Valley is situated right (West) of the Rothorn, the Matter Valley is visible on the left hand side (East). Positions of ERT-transects are indicated. B) Transect NW is affected by marginal onfreezing of a lateral glacieret but no hydraulic exchange in the level of the transect. The approximate position of the 60 m long electrode line is indicated by white points. The discussed part (-30 m to -6 m) is the steep rock face above the glacieret. C) Transect NE is situated below a glacieret that feeds meltwater into bedrock cleft systems. The approximate position of the 60 m long electrode line is indicated by white points. The discussed part (-30 m to +3 m) is the steep right part of the transect.

The geophysical measurements described in this article were conducted in the “Steintälli”, a N-S exposed crestline (Matter-/Turtmann Valleys, Switzerland) at about 3070-3150 m a.s.l. that consists of slaty paragneiss (Fig. 30A). The annual average air temperature of the Steintälli approached values of – 3.5 °C according to measurements taken in the adjacent Matter Valley 1962-90. A local permafrost study conducted by Gruber and Hoelzle (2001) in the Matter Valley ranked the whole Steintälli in the highest possible permafrost category as “likely permafrost area”. As all rock bars are surrounded by ice, the local air temperatures can often be significantly lower than the temperature calculated from the meteorological station. Transect NE receives meltwater from a glacieret above that performs intensive advective heat transfer in cleft systems, while Transect NW has only lateral contact to glacieret ice, with marginal onfreezing (Fig. 30B and C).

6.3.3 Geophysical evidence

ERT is a key method in permafrost research as freezing and thawing of most materials are associated with a resistivity change that spans one or more orders of magnitude, which is, in turn, easily detectable. The first approach to derive spatial information from steep rock faces by ERT was applied by Sass (2003). In subsequent studies, he provided further evidence that ERT measurements are capable of measuring the degree of rock moisture (Sass, 2005a) and temporal and spatial variations of freeze and thaw limits (Sass, 2004) in rock faces. These ERT measurements were confined to the monitoring of the upper weathering crust (centimeter- to decimeter-scale) of non-permafrost rock faces. Krautblatter and Hauck (2007) extended this method to a decameter-scale and applied it to the investigation of active-layer processes in permafrost-affected rock walls. Due to the large electrode spacing and the resulting spatial resolution, the ER tomographies presented here are prone to investigate monthly to multiannual responses but are less applicable to short time series (see Sass, 2004).

6.3.3.1 Applied methods and error sources

A systematic discussion of error sources associated with ERT measurements in rocks is given by Krautblatter and Hauck (2007). These include electrokinetic potentials created by percolating water, high resistivity gradients along the suspected permafrost bodies that can result in an over- or underestimation of the depth of the transition layer, high resistivities of frozen rock surface that may disturb electrode contact as well as topographic distortions when measuring on a structured rock face. Errors associated with different ERT-arrays were assessed quantitatively alongside with the impact of topography and other geometric error sources by Krautblatter and Verleysdonk (2008a).

A number of hardware and software adaptations were made to cope with these error sources. Arrays with centimeter-long steel screws, lubricated with battery grease, were drilled into solid rock as electrodes to gain stable electric contact. These were left in place for identical monitoring conditions and were measured repeatedly with high voltages (mostly 10^2-10^3 V) to improve the signal to noise ratio. We applied a SAS 300C 41-electrode system that was sometimes supplemented with a booster to yield higher voltages. Resistivities were repeatedly measured with reversed currents to exclude the influence of self potentials. A detailed survey of hardware and

software adaptations is provided by Krautblatter and Hauck (2007). The RES2DINV software was chosen as it is capable of topographic correction and time-lapse inversion of subsequent measurements. To cope with high resistivity gradients, inversion models with mesh size smaller than the electrode distance and robust inversion routines provide better results. Resistivity values that correspond to the transition between frozen and thawed rock were measured repeatedly at the rock surface along different arrays and yielded evidence that the transition occurs between 13 and 20 kΩm for the slaty paragneiss present at the Steintälli (Krautblatter and Hauck, 2007) and is in the same range as the one established for carbonate rocks at the Zugspitze, German Alps, by Sass (2004).

The relation between measured resistivity and rock temperature changes at the freezing point. For temperatures below the freezing point, resistivity (p) depends mainly on unfrozen water content until most of the pore water is frozen. In Alpine environments, resistivity can be calculated based on a reference value p_o as an exponential response to the temperature below the freezing point (T_f) according to McGinnis et al. (1973):

$$\rho = \rho_0 e^{b(T_f - T)}$$

Equ. 6.10

The factor *b* determines the rate of resistivity increase and can be derived empirically (Hauck, 2001; Hauck, 2002). Short-term changes in resistivity can be attributed to changes in pore water content and temperature, while changes in porosity and water chemistry can be neglected over daily to monthly measurement intervals in low-porosity rocks. Due to the exponential response of resistivity to temperatures below 0 °C, freeze-thaw transitions correspond to an increase in resistivity by one order of magnitude and are thus, a very sensitive method for detecting the state of rock permafrost close to 0 °C.

6.3.3.2 Data quality

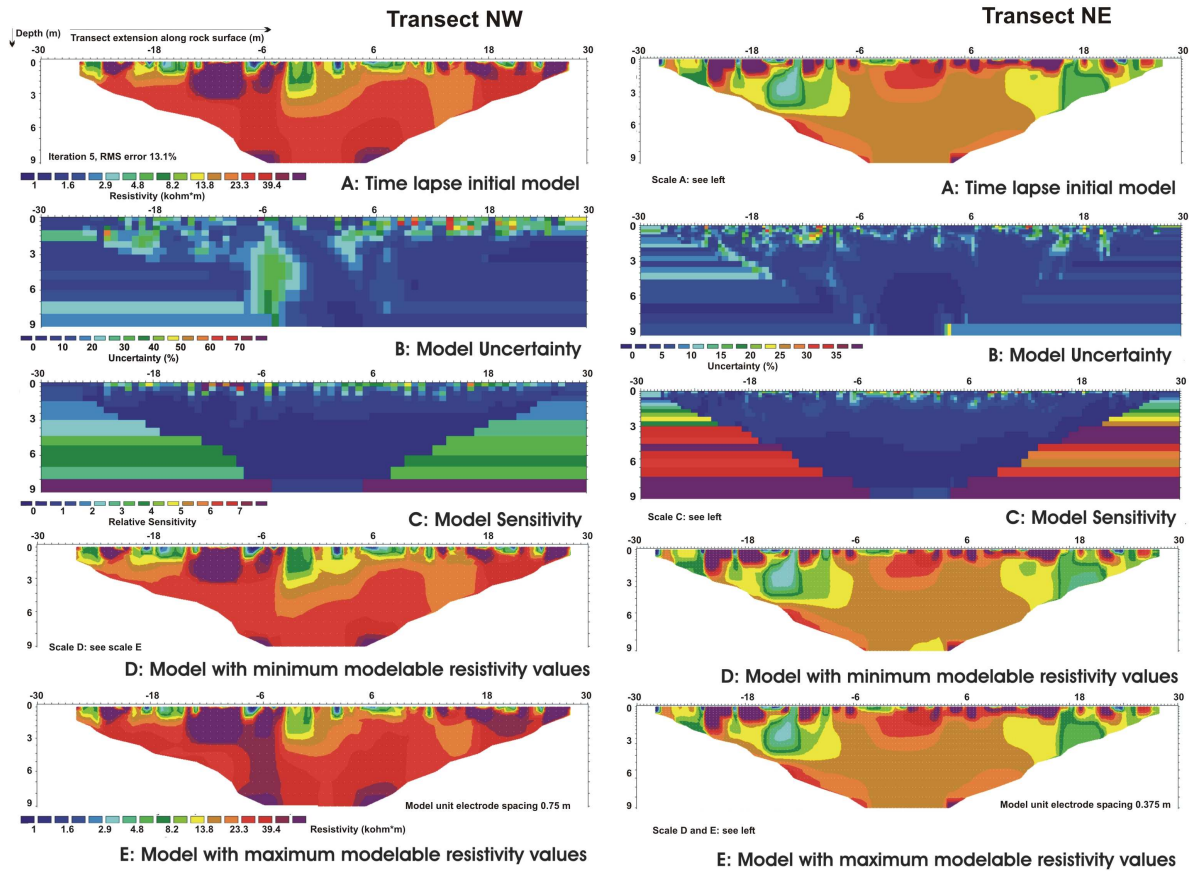

Fig. 31: Model uncertainty and relative sensitivity of the time lapse initial models of Transect NW and NE.

Even if the RMS error provides some information on outliers, i.e. measurements that were take at a transitorily deeply frozen rock surface with decreased electrode contact, it is not a straightforward approach to judge data quality in terms of RMS errors. This is due to two factors. Firstly, rock permafrost systems have high resistivity gradients and even small distortions between apparent and modelled resistivity sections result in high RMS errors that are not comparable to systems with lower gradients (Blaschek et al., 2008). Secondly, RMS errors are possibly a systematic proxy for fractured rock masses as these show significant anisotropic behaviour in the subscale, that is not resolved by ERT measurements with meter-scale spacings (Linde, 2005).

To restrict overfitting of results, no more than five iterations were applied. Typical RMS errors usually range between 5 % and 15 % for 1.5 m electrode spacing at the Steintälli when measured under convenient conditions with only slightly frozen rock surfaces. Hardware errors of subsequent measurement with identical electrodes are mostly below 1 %. Measurements during intensely frozen and ice-coated rock surface conditions inherit worse hardware measurement errors (>1 %) and result in RMS errors ranging from 20 %-30 % with visible distortions in the inversion results. These were excluded from time-lapse interpretations.

Model uncertainties were calculated in RES2DInv according to the model covariance matrix method described in Alumbaugh and Newman (2000) (Fig. 31). Minimum and maximum models display average models plus or

minus model uncertainty. Relative sensitivity is displayed in Fig. 31 and is divided by average sensitivity. Mention that high sensitivity of side blocks is an artificial effect due to their large size.

Uncertainties range between 0-5 % in sections of *Transect NE* that are primarily interpreted in the article (-6 to +6; 3-8 m depth). Minimum and maximum modelable resistivities show only small alterations in the interpreted section. Interpreted monthly resistivity changes of 20-30 % (-6 to +6; 3-8 m depth) in Fig. 34B and D exceed model uncertainty by at least 4 times in the largest part of the section. Interpreted annual changes of 10-30 % (-6 to +6; 3-8 m depth) in Fig. 34C and E exceed model uncertainty by several times. The distribution of relative sensitivity indicates that the depth of investigation is higher in Transect NE and thus, to depth resistivity information is more reliable than in Transect NW (Fig. 31C).

Frozen surface rock (–15 m to –3 m) in *Transect NW* causes model distortions centred at –6m/2.5-8 m depth with model resistivity uncertainties ranging from 15-35 %. Interpreted monthly changes of mean thaw line propagation (23 kΩm line) in Fig. 36A and B could vary up to 1-1.5 m according to minimum and maximum models (Fig. 31D and E). Interpreted annual changes (>70 %) in the left part (-20 m to -4.5 m/3-9 m depth) in Fig. 36C and D are located in a part of the pseudosection with 0-20 % model resistivity uncertainty. Interpreted annual changes in the right part (4.5 m to 20 m / 2-9 m depth) in Figures Fig. 36C and D have model resistivity uncertainties ranging from 5-15 % with interpreted changes being in the range of 50 to 70 %.

6.3.3.3 Seasonal and multi-annual response in a rock wall without hydraulic interconnectivity

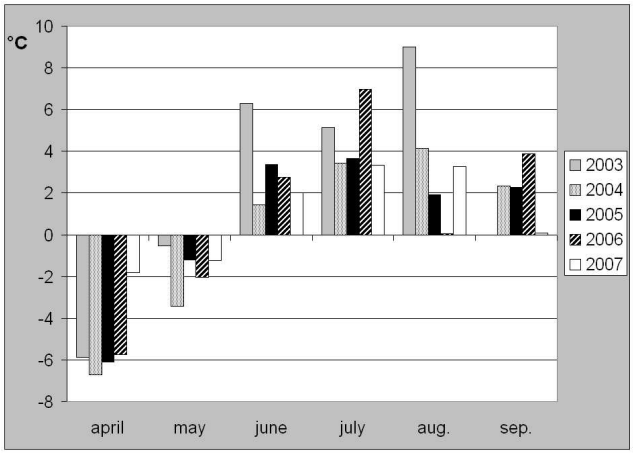

Fig. 32: Average monthly temperatures from 2003 to 2007 measured at a meteorological station located at a horizontal distance of 900 m and at an altitudinal difference of 330 m from the study site (2770 m a.s.l.).

Temperature data were corrected by -1.98 °C (0.6 °C per 100 m) for the altitudinal difference to the Steintälli 3100 m a.s.l.. The average annual temperature of 2004 at the study site was – 3.7 °C, which is in accordance with the long-term average value. Data from Sep. 2003 are incomplete and, therefore, not displayed.

6.3.3.3.1 Raw data

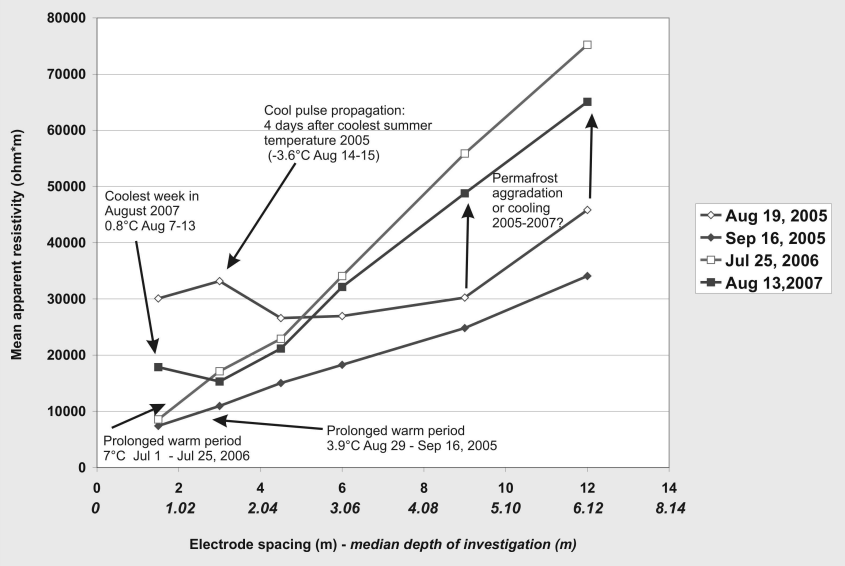

Fig. 33: Apparent resistivities of the permafrost-affected left side (electrode array midpoints –30 m to –6 m) of Transect NW with increasing electrode spacing.

The median depth of investigation (MDOI) is written in italics. It shows approximately at what depth one-half of the total resistivity signal originates from above and one-half from below (Barker, 1989).

Fig. 33 shows mean apparent resistivities for different electrode spacings corresponding to different depths (Barker, 1989; Edwards, 1977) for Transect NW. Measurements taken after prolonged warm periods show constant resistivity gradients with increasing depth of investigation. This is in line with slow linear heat propagation in summer from the warm rock surface to a permafrost rock interior. Cool pulses cause significant distortion of this general behaviour at the rock surface. The plunge in temperature of the August 14-15, 2005 appears to propagate as a high resistivity pulse. After four days, at August 19, is no longer apparent at a MDOI of 0.8 m, is most pronounced at a MDOI of 1.5 m and has not reached a MDOI of 2.3 m. This corresponds to a mean speed of cool pulse propagation ranging from 30-50 cm/day to a MDOI of 1.5 m. Mean apparent resistivity data of August 2005 and August 2007 indicate an increase by 20 kΩm for a median depth of investigation of 4 to 6 m. This could be due to significant cooling or/and due to aggradation of frozen rock.

Table 4: Resistivity increase with increasing penetration depth in the rock face.

Date	**Gradient of a linear regression of median depth of investigation and mean apparent resistivity (AR/DOI).**	**Apparent resistivity (at maximum recorded MDOI)**
Transect NW-not hydraulically connective (steep > 60° section, electrode array midpoints –30 m to –6 m)		
Aug. 19, 2005	4.9 kΩm/m (R^2=0.83)	46 kΩm (6.1 m)
Sep. 16, 2005	4.9 kΩm/m (R^2=0.99)	34 kΩm (6.1 m)
Jul. 25, 2006	12.7 kΩm/m (R^2=0.99)	75 kΩm (6.1 m)
Aug 13, 2007	11.1 kΩm/m (R^2=0.99)	65 kΩm (6.1 m)
Transect NE- hydraulically connective (steep > 60° section, electrode array midpoints –30 m to + 3 m)		
Aug. 13, 2005	0.6 kΩm/m (R^2=0.90)	19 kΩm (9.2 m)
Sep. 13, 2005	0.4 kΩm/m (R^2=0.70)	17 kΩm (9.2 m)
Aug 13, 2007	1.0 kΩm/m (R^2=0.81)	21 kΩm (9.2 m)

Data sets are identical with those displayed in Fig. 33 and Fig. 35. High AR/DOI gradients and high resistivities at maximum recorded depths correspond to deeply frozen permafrost conditions. Increases in AR/DOI gradients point towards permafrost aggradation. Surface distortions (1.5 and 3 m electrode spacing) due to cold surface condition in August 2005 and 2007 in Transect NW were excluded from the linear regression. As the analysed steep (>60°) section of Transect NW only extends from –30 m to –6 m, the maximum recorded MDOI is restricted to 6.1 m.

6.3.3.3.2 ERT results

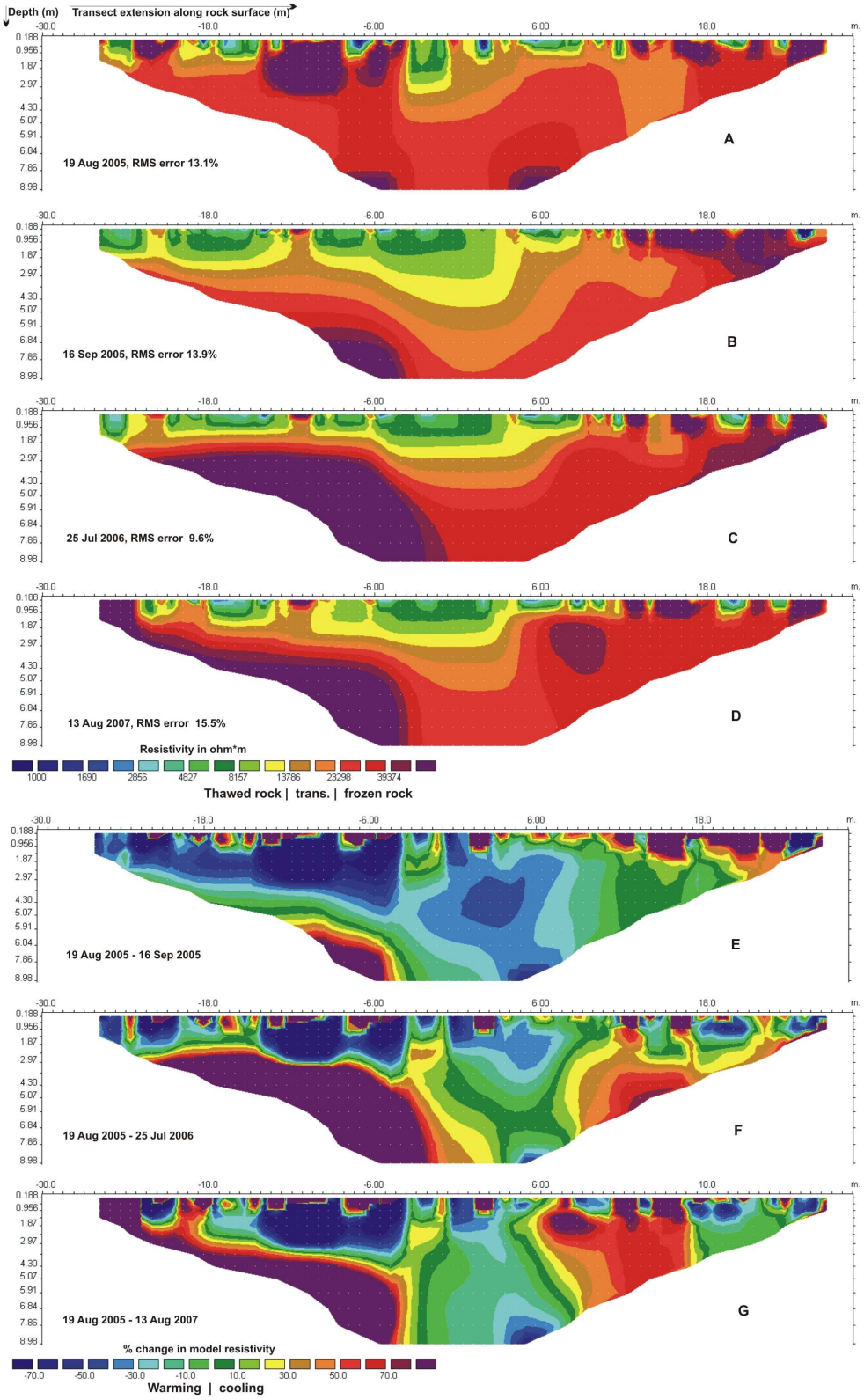

Fig. 34: Four ERT time-sections of Transect NW, which are apparently determined by the rock surface temperature regime.

4A-4D show absolute resistivity values while 4E-4G show relative changes in resistivity. Raw data is displayed in Fig. 33.

Fig. 34 presents four time sections of a permafrost-affected rock face exposed to NW (see Fig. 30B). The most pronounced appearance of high resistivity bodies close to the rock surface is apparent in Fig. 34A following unusually cool Mid-August conditions in 2005. The warm September 2005 (3.9 °C) coincides with the most pronounced advance of the 23 kΩm line from 5 m depth to almost 9 m in the centre of the transect (0 m), where the most reliable depth information is attained (Fig. 34B). The high resistivity body on the left side (-20 m to -4.5 m) in 3-9 m depth, increases significantly in size and resistivity in the following two years (Fig. 34C and D). On the right side (4.5 m to 20 m) in 2-9 m depth a new high resistivity body evolves in 2006 and 2007 (Fig. 34C and D).

6.3.3.3.3 ERT interpretation

Fig. 34 shows two time-scales of response times. On a monthly scale (Fig. 34A and B) the impact of a warm month following a cool summer period can be observed. On annual and multiannual scale permafrost aggradation in response to cool summer conditions 2005 and 2006 can be observed. For a better description, Transect NW will be divided in a (i) left section (-30 m to -6 m), a (ii) middle section (-6 m to 6 m) and a (iii) right section (6 m to 30 m).

The surface layer of the *right section* is of stepped appearance and more exposed to radiation. Simultaneous ERT and P-wave velocity measurements (Krautblatter et al., 2007) yielded evidence that high ERT values in this part in the upper 1-2 m match with low P-wave velocities in the range of 3000 m/s, that correspond to a dry, air-filled rock mass, while in the middle and left part, high ERT-values coincide with high P-wave velocities in the range of 4000 m/s and above and are, thus attributed to frozen, ice-filled rock mass. This affects the interpretability of the monthly response. On the annual and multiannual timescale a permafrost body builds up between 6 m – 18 m with deeply frozen resistivity values that exceed 40 kΩm in 2007. Fig. 34F and G indicate a 20-60 % increase in model resistivity until 2006 and a 30-80 % increase when comparing 2007 and 2005. This data shows significant aggradation and cooling of rock permafrost from 2005 to 2007.

The *middle section* (-6 m to 6 m) highlights a monthly response of the melting line in warm late summer conditions (Fig. 34A and B). Resistivity losses of 20-50 % illustrate enhanced heat transmission from the rock surface to the rock interior at all depths. The 14 kΩm line, which approaches thawed conditions slightly above the freezing point, advances as much as 2-3 m and the 23 kΩm line, which corresponds to frozen conditions slightly below the freezing point, advances as much as 4 meters in one month. The transition zone between 14 kΩm and 23 kΩm appears to increase in thickness from roughly 1.5-2.5 m to 2-5 m. In the annual and interannual scale permafrost aggradation is visible in the proximity to the left section but is less pronounced than in the two other sections.

The *left section* also indicates strong surface heat transmission in late summer 2005 and resistivity values decrease more than 50 % in the upper 3 m. This results in a 0-3 m advance of the 14 kΩm line and a 0-4 m advance of the 23 kΩm line gapped by a transition zone mostly smaller than 2 m. The impact of the warm summer is less pronounced than in the middle section and is possibly compensated by the deeply frozen permafrost lens (>50 kΩm) below. On an annual and multiannual scale, permafrost aggrades spatially only 1-2 m but resistivity values

strongly increase by more than 70 %. Below a relatively constant 3 m thick active layer the permafrost lens appears to cool down.

Two features visible in Fig. 34 represent additional factors that interfere with rock permafrost response and cause additional complexity. A totally shaded overhang position between -10.5 m and -12 m, causes near surface rock permafrost that is also evidenced by permanently ice-filled crevasses in the field. Intense snow accumulation in 2006 caused an increase in thickness of the glacieret close to the left part of the transect up to two meters and intense heat transmission from ice frozen to the rock up to the electrode level is visible from 24 m to 27 m.

6.3.3.4 Seasonal and multi-annual response in a rock wall with hydraulic interconnectivity

6.3.3.4.1 Raw data

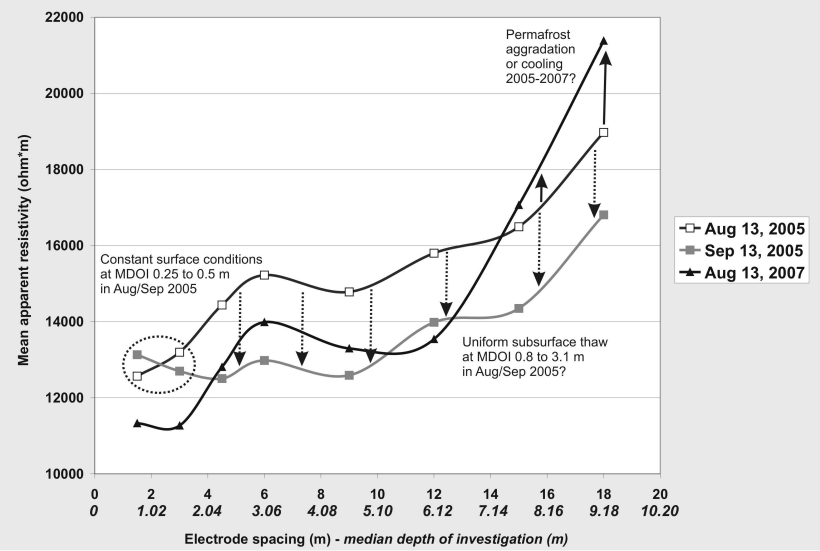

Fig. 35: Mean apparent resistivities of the left side of Transect NE (electrode array midpoints –30 m to + 3 m) with increasing electrode spacing.

The median depth of investigation, where half of the at which one-half of the total resistivity signal originates from above and one-half is given in italics (Barker 1989).

Melting in Transect NE in summer 2005 causes a decrease in apparent resisitivities at depth while mean surface resistivities (electrode spacings 1.5 m and 3 m) remain stable with a change of -0.0 (±0.5) kΩm (Fig. 35). Mean subsurface apparent resistivities, covering median depths of investigation greater than 2.5 m, decrease uniformly for all electrode spacings (4.5 m, 6 m, 9 m, 12 m and 18 m) by 2.1 (±0.1) kΩm. In accordance to Transect NW mean apparent resisitivity values with a MDOI greater than 7 m possibly indicate aggradation of frozen rock and/or cooling.

Table 4 shows that the AR/DOI gradient of Transect NE is an order of magnitude lower than the AR/DOI of Transect NW. This indicates that resistivity values do not significantly exceed the transitory range of freezing (13-20 kΩm) around 0 °C at any depth.

6.3.3.4.2 ERT results

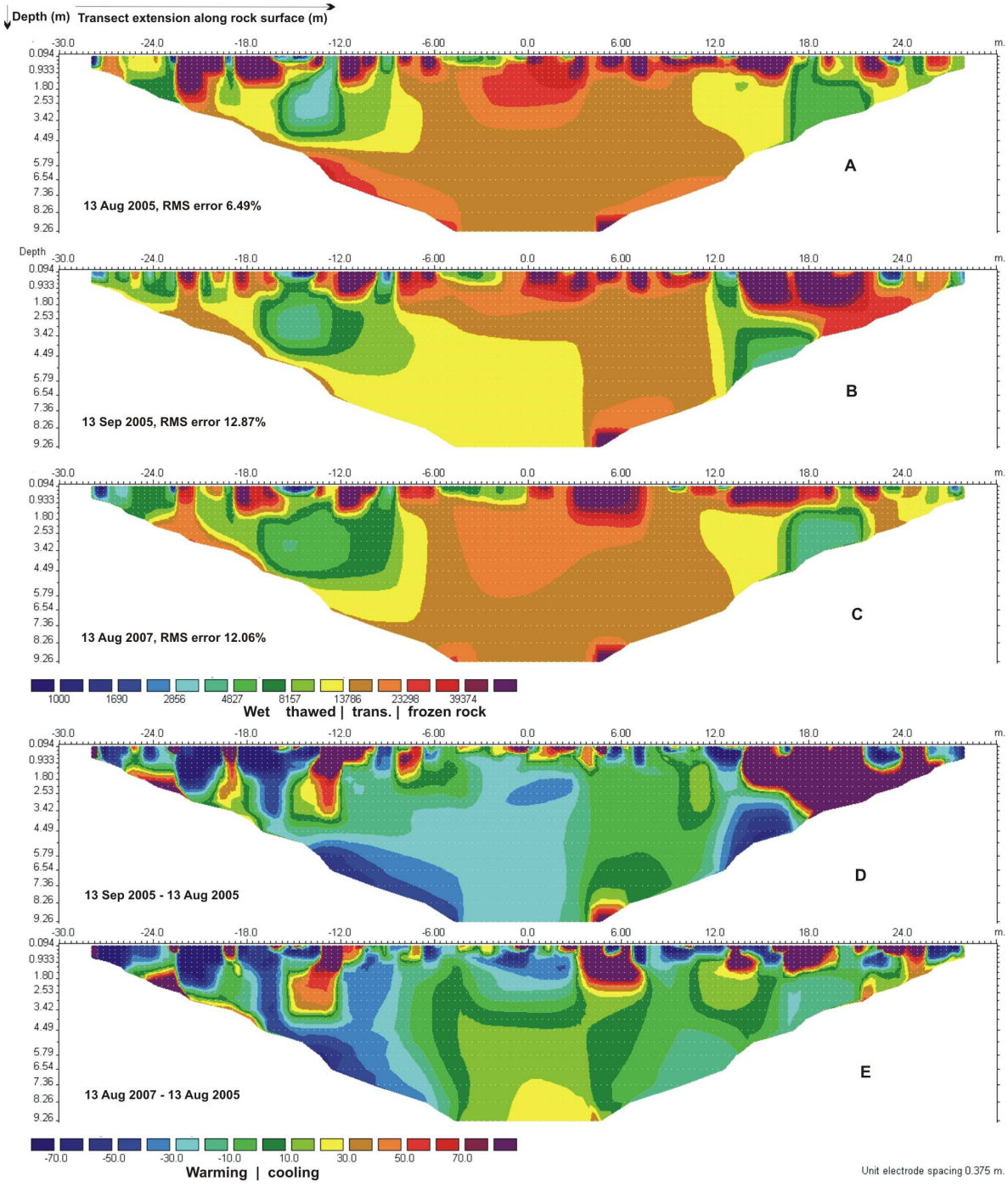

Fig. 36: Four ERT time-sections of Transect NE determined by both, the rock surface temperature regime and heat transfer by meltwater in water-filled cleft systems.

6A-6C show absolute resistivity values while 6D-6E show relative changes in resistivity.

Fig. 36 displays a central high-resistivity body (–7 m to 11 m) that is in the range of the transition from frozen to thawed rock and is restricted by two pronounced wet rock low-resistivity bodies at –22m to –8m and 12m to 22m. The central high-resistivity body shows a decrease in resistivity in the range of 10-40 % that is more pronounced at greater depths in September 2005. Two years later resistivity values in the central transitory body increase by 0-40 %.

6.3.3.4.3 ERT interpretation

Fig. 36 shows meta-stable rock permafrost (-6 to 12 m) close to the freezing point. Its spatial extension is delimited by two cleft water systems that create significant cleft water outflow at the rock surface with water temperatures close to 0 °C.

On a monthly scale (Fig. 36B and D), the 14 kΩm line at position –9m to 3m at 3.5m to 9 m depth retreats several meters in September 2005 which is also apparent as a 2.1 (±0.1) kΩm shift for 4.5m, 6m, 9m, 12m and 18 m electrode spacing in the raw data (Fig. 35). There are some indications that this melting is due to cleft water propagation as heat transmission in the ERT and the raw data does not originate from the rock surface but starts in 2.5m to 3 m depth and the core zone of the cleft water body at –12 m to –7 m with wet rock resistivity values indicated by the 8.2 kΩm and 10.6 kΩm (transition green – yellow) line extends simultaneously.

On a multiannual scale (Fig. 36C and E) the transitory permafrost body shows an increase in resistivity by 10-30 % in the core area, that points towards a shift from a metastable permafrost body towards a more deeply frozen body with twice the extension of September 2005, but still close to 0° C. This cooling clearly derives from the rock surface. However, ERT and AR/DOI indicate (i) that cleft water systems are still effective restricting the size of permafrost bodies (no significant aggradation) and (ii) even if weather conditions yielded significant cooling in the adjacent Transect NW, the transitory Transect NE did cool significantly below 0 °C at any observed depth (no significant cooling).

6.3.4 Conclusion

In homogeneous rock wall sections, mean apparent resistivity – median depth of investigation (AR/DOI) diagrams appear to reveal information on the state of permafrost. Measurements after prolonged warm periods in Transect NW, not disturbed by cleft water, show constant resistivity gradients with increasing DOI corresponding to linear heat propagation from the warm rock surface to a permafrost rock interior. Cool pulse signals from transitorily chilling of the rock surface propagate through these linear functions as local maxima with speed 3-5 decimetres per day to a depth of 1.5 m. AR/DOI gradients are steep in the range of 5-13 kΩm/m. Apparent resistivity values reach values of 30-80 kΩm at depth indicating deeply frozen conditions. In Transect NE, disturbed by cleft water percolation, the AR/DOI curve deviates from a linear function with local maxima and minima that remain constant over time. Cool pulses are already buffered at the surface, AR/DOI gradients are low reaching

values from 0.4 to 1 kΩm/m and apparent resistivities at depth do not significantly exceed 20 kΩm. This indicates that resistivity gradients with depth have persistent minima, possibly due to cleft water, and that no deeply frozen rock body can develop in this system.

In Transect NW, as a response to a monthly warm late summer period in 2005, the melting line was observed to propagate up to 4 meters per month and significant melting evidenced by wide-spread resistivity changes above 30 % were observed up to 9 m depth. As an annual response to cool summer conditions an existing permafrost body (-18 to –6 m) extends its deeply frozen core (>40 kΩm) from more than 7 m to 3-4 m from the rock surface which results in an resistivity increase greater than 70 % in most of its extension. Transect NE is heavily affected by the heat transfer of two cleft water systems which only allow for the development of a meta-stable permafrost body, whose resistivity values indicate temperatures close to 0 °C. There are some indications that the impact of cleft water-induced melting is visible on a monthly scale in September 2005.

From 2005 to 2007, both rock transects provide indications of permafrost aggradation and/or cooling. Anomalously cool August temperatures in 2005 (1.9 °C) and 2006 (0.1 °C) with fresh snow and ice-coating of rock faces reduced active layer propagation during the short summer period significantly. *Transect NW* indicates both, the consolidation of existing permafrost bodies and the development of new perennial frozen rock bodies. Above the existing permafrost body in the steep section (-30m to -6m), ERT indicates a reduction of the active layer thickness and an increase in resistivity by more than 70 %. For this body mean apparent resistivity data of August 2005 and August 2007 indicate an increase by 20 kΩm for a MDOI of 4.6 m and 6.1 m which is interpreted as permafrost aggradation and/or cooling. A new high-resistivity body builds up at 6-18 m mostly with resistivity changes of 30-70 % from 2005 to 2007. In *Transect NE*, ERT indicates a moderate cooling in the high-resistivity body with a resistivity increase of 10-30 % from 2005 to 2007 paralleled by apparent resistivity raw data. In spite of similar surface climate conditions from 2005 and 2007, Transect NW shows both, permafrost aggradation and cooling while the hydraulically-interconnective Transect NE shows nor pronounced aggradation nor pronounced cooling.

Aggradation in permafrost rocks with and without active cleft water systems evokes significantly different patterns. While heat propagation in cleft-water affected systems occurs locally and is necessarily delimited by hydrological conductivity, systems without cleft-water influence indicate a fast and deep-reaching transmission of heat from all parts of the rock surface. While permafrost aggradation in the latter is merely an integral signal from cool pulses coming from the rock surfaces, sealing of subordinate cleft systems with ice may constitute a major influence on lateral permafrost aggradation in cleft water-disturbed systems. 3D thermal effects could play a vital role in this context.

6.4 Towards quantification of temperature changes in ERT field-measurements

Source: Krautblatter, M., Verleysdonk, V., Flores-Orozco, A. and Kemna, A. (accepted): Quantitative temperature-calibrated imaging of seasonal changes in permafrost rock walls by high-resolution ERT and implications for rock slope stability (Zugspitze, German/Austrian Alps). Journal of Geophysical Research, Earth-Surface. (submitted version)

Changes of rock and ice temperature inside permafrost rock walls crucially affect their stability. Permafrost rocks at the Zugspitze were involved in a 0.3-0.4 km³ rockfall at 3.7 ka B.P. whose deposits are now inhabited by several thousand people. A 107-year climate record at the summit (2962 m a.s.l.) shows a sharp temperature rise in 1991-2007. This article applies electrical resistivity tomography (ERT) to gain insight into spatial thaw and refreezing behavior of permafrost rocks and presents the first approach to calibrate ERT with frozen rock temperature. High-resolution ERT was conducted in the north face adjacent to the Zugspitze rockfall scarp in February and monthly from May to October 2007. A smoothness-constrained inversion is employed with an incorporated error model, calibrated on the basis of normal-reciprocal measurement discrepancy. Laboratory analysis of Zugspitze limestone indicates a bilinear temperature-resistivity relationship divided by a 0.5 (±0.1) °C and 30 (±3) kΩm equilibrium freezing point and a 20-fold increase of the frozen temperature-resistivity gradient (19.3 (±2.1) kΩm/°C). Temperature dominates resistivity changes in frozen rock below -0.5 °C, while in our specific case geological heterogeneity appears to be less important. ERT shows recession and readvance of frozen conditions in rock correspondingly to temperature data. Maximum resistivity changes in depths up to 27 m coincide with maximum measured water flow in fractures in May. Here we show, that laboratory-calibrated ERT does not only identify frozen and unfrozen rock but provides quantitative information on frozen rock temperature relevant for stability considerations.

6.4.1 Introduction

An increasing number of hazardous rockfalls/rockslides of all magnitudes is reported from permafrost-affected rock walls. Ice-rock avalanches of bergsturz-size (>1 mio. m³) were documented e.g. at Mt. Steller, Alaska ($5(\pm1)*10^7$ m³) in 2005, at Dzhimarai-Khokh, Russian Caucasus ($4*10^6$ m³) in 2002, and at the Brenva ($2*10^6$ m³) and the Punta Thurwieser ($2*10^6$ m³) in the Italian Alps in 1997 and 2004 (Bottino et al., 2002; Crosta et al., 2007; Haeberli et al., 2004; Huggel et al., 2008). Accordingly, enhanced activity of cliff falls (10^4-10^6 m³), block falls (10^2-10^4 m³), boulder falls (10^1-10^2 m³), and debris falls (<10 m³) was observed from permafrost-affected rock faces (Fischer et al., 2007; Rabatel et al., 2008; Ravanel et al., 2008; Sass, 1998; Sass, 2005b). The time-gap between climate warming and rockfall response is expected to increase with rockfall magnitude from years to millennia for hundreds of meters thick rockslides (Wegmann, 1998). In that sense the detachment of a $3.5(\pm0.5)*10^8$ m³ rockslide in 3700 B.P. from the permafrost-affected Zugspitze North Face (today 2962 m a.s.l.) was interpreted as a delayed response to the Holocene Climatic Optimum (Gude and Barsch, 2005; Jerz and Poschinger, 1995).

Rock instability in permafrost-affected bedrock is governed by shear stress, hydrostatic pressures, and friction along one or several planes of weakness in the rock mass. Friction along planes of weaknesses (without fine-grained cleft fillings) is susceptible to subzero temperature changes due to alterations in intact rock mass strength and ice-mechanical properties along planes of weaknesses. Assuming a translational sliding mechanism, a two-step conceptual model can show the influence of temperature on (i) rockslide preparation and (ii) acceleration. (i) Rock slope failure is commonly prepared by brittle fracture propagation of a sliding horizon due to step-path failures, cracking of cohesive rock bridges, and ductile internal shearing (Eberhardt et al., 2004). During the initiation of rockslides, tensile and shear rock mass strength of "asperities" delimit the speed of brittle fracture propagation (Fleming and Johnson, 1989; Kemeny, 2003). Both decrease exponentially up to more than 50 % in water/ice-saturated rocks between –5 °C and 0 °C (Mellor, 1973) and help to initiate the abrasion of a sliding plane. (ii) As soon as a sliding plane is prepared, ice-mechanical properties of frozen joints become more important and govern the acceleration of the rockslide. Laboratory results suggest that ice-mechanical properties relevant for small rockslides (equivalent to the normal stress of less than 20 m rock overburden) may include breaking the connection of ice and rock surface while those for larger rockslides (>20 m rock overburden) are governed by ductile shear deformation of ice itself (Guenzel, 2008). Transferability in natural rock slopes is restricted by two factors: Normal stresses are unequally distributed across the sliding surface and prolonged ductile deformation of ice evokes the transition of primary to secondary and tertiary creep and fracture of polycrystalline ice. However, both deformation mechanisms, breaking of the rock-ice contact and all stages of ductile ice deformation, respond strongly to temperature increases from –5 °C to 0 °C (Barnes et al., 1971; Budd and Jacka, 1989; Davies et al., 2001; Davies et al., 2000; Paterson, 2001; Sanderson, 1988). An exponential stress-strain behavior with temperature is at least well-established for secondary and tertiary creep of ice, which may play a vital role in the self-enforced acceleration of rock slides (Budd and Jacka, 1989; Weertman, 1973). Yet it must be recognized that rock mechanical modeling techniques have evolved beyond the capability to confidently constrain the input (Eberhardt et al., 2004). We argue that rock permafrost geophysics has the potential to provide spatially resolved input for stability models (Krautblatter, 2008).

Surface-based geophysical methods represent a cost-effective approach to permafrost characterization (Harris et al., 2001). Hauck (2001) and Kneisel et al. (2008) provide a systematic comparison of different geophysical methods for monitoring permafrost in high-mountain environments. Electrical resistivity tomography (ERT) is considered well suited as freezing and thawing of most materials is associated with a resistivity change of orders of magnitude, which is easily detectable. The installation of permanent electrodes allows direct assessment of spatial and temporal permafrost variability in loose materials and rock masses beneath loose debris covers (Hauck, 2002; Hilbich et al., 2008; Kneisel, 2006). In that sense, the attempt by Hauck et al. (2008) to quantify water, ice, air, and rock debris contents in loose materials numerically by combined ERT and refraction seismic modeling heralds a shift from qualitative to quantitative interpretation in permafrost geophysics.

The first approach to derive spatial information from solid rock faces by ERT was applied by Sass (2003). ERT was proved capable of measuring the degree of rock moisture (Sass, 2005a) and temporal and spatial variations of freeze and thaw limits (Sass, 2004) in solid rock faces. Measurements were confined to the monitoring of the upper weathering crust (centimeter- to decimeter-scale) of rock faces with electrode spacing of only several centimeters. Results were confirmed by synchronized surface logging of temperature and resistivity in the wireless sensor logging network "PermaSense" (Hasler et al., 2008). Krautblatter and Hauck (2007) extended this

method to a decameter-scale and applied it to the investigation of active-layer processes in permafrost-affected solid rock walls. Rock-walls have a number of advantages for quantitative interpretation of geophysical results: Rock mass is the only constituting material and in the case of a homogeneous rock mass the corresponding pore space can be accurately defined. In the longer term, pore-water conductivity is controlled by rock chemistry and resistivity gradients due to temperature changes are mostly below one order of magnitude.

Quantitative interpretation of ERT results represents a non-trivial task as there are numerous factors which have an influence on the inverted resistivity distribution and the absolute values thereof, such as electrode arrangement, measurement scheme, and regularization approach (technique to overcome the ill-posedness of the pure ERT inverse problem, normally by imposing a smoothness constraint on the resistivity distribution) (Binley and Kemna, 2005). Of particular importance, is an appropriate description of the data errors in the inversion. Underestimation of data errors results directly in the fitting of data noise and thus the creation of artifacts in the ERT image, while overestimation does not fully exploit the information given in the data at the cost of contrast in the final image. In time-lapse applications, an inconsistent data error handling at different time steps can lead to additional artifacts in inferred difference images (i.e., images of temporal changes). Here we use the data error model proposed by Slater et al. (2000) and determine its parameters by analyzing the differences between normal and reciprocal measurements (i.e., measurements with swapped current and voltage dipoles) in individual resistance ranges (bins) following the approach of Koestel et al. (2008). This “calibration” of the error model for each individual data set is essential to avoid the creation of artifacts and guarantees consistency among data sets collected at different times, allowing a quantitative interpretation of the obtained resistivity distributions.

Thus, this articles aims to show that a shift from a qualitative interpretation of ERT results in terms of permafrost distribution in bedrock to a quantitative interpretation in terms of temperature- and stability-relevant factors is possible if (i) laboratory measurements are conducted to reveal specific temperature-resistivity characteristics of studied bedrocks, (ii) ERT data error characteristics are properly accounted for in the inversion process to yield error-referenced resistivity distributions without significantly over- or underfitting the data, and (iii) “uncontrolled external noise” on the resistance measurements, for instance associated with geological variations, can be excluded.

6.4.2 Study site

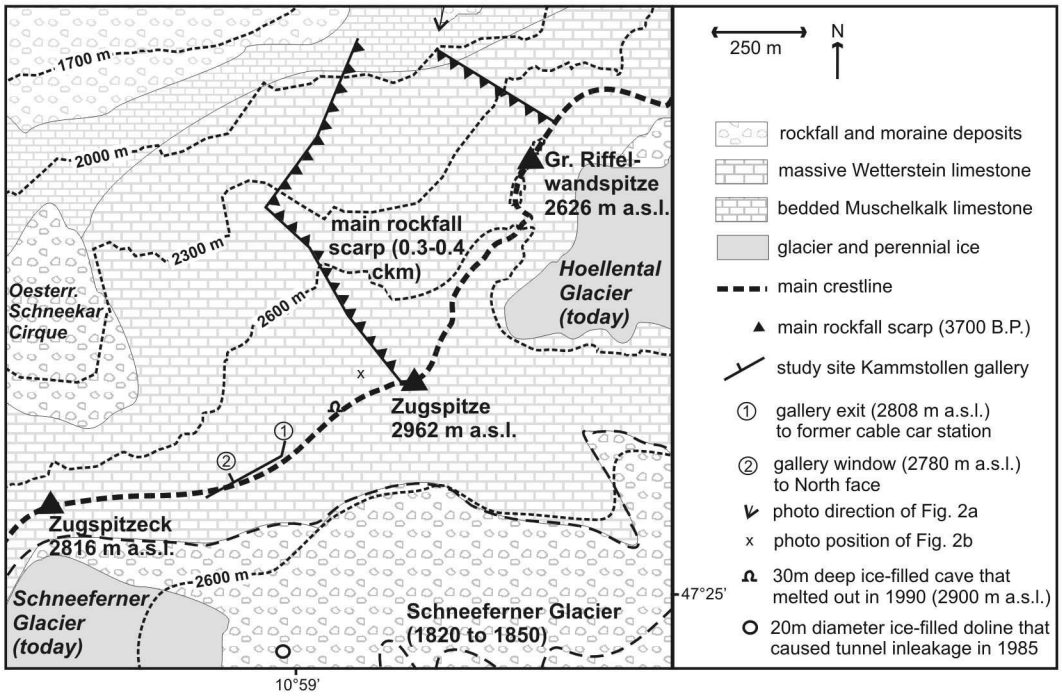

Fig. 37: Map of the study site showing the ERT transect, geology, and features that were attributed to permafrost degradation after the Holocene climatic optimum (rockfall scarp) and at present.

6.4.2.1 Geographical and geological setting

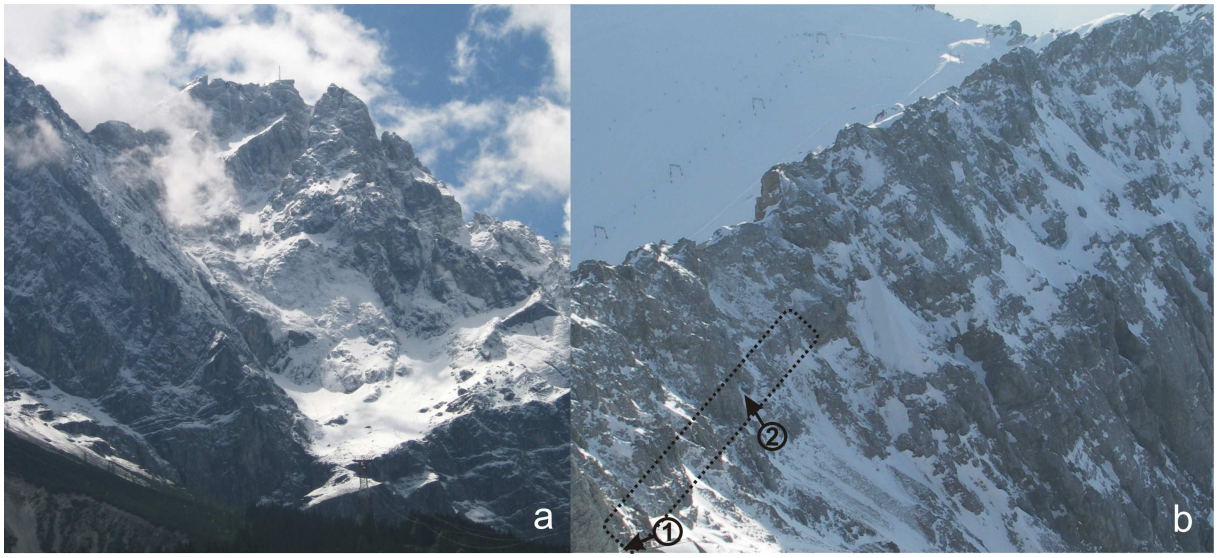

Fig. 38: Picture of the rockfall scarp and rock wall section covered by the ERT transect.

a. The 0.3-0.4 km³ wedge-shaped rockfall scarp below the Zugspitze (2962 m a.s.l.). The wedge starts in the top left part (Gr. Riffelwandspitze) as a steeply inclined sliding plane, covers the whole width of the picture and bottoms out at approximately 1900 m a.s.l. in the snow-covered "Bayerisches Schneekar"-Cirque. The transition

from massive Wetterstein Limestone to layered Muschelkalk sequences is visible at the bottom left part. b. Position of the rock wall section monitored by ERT. According to Fig. 37, No. 1 and No. 2 indicate entrances to the gallery. The rock wall encircled by the dotted line indicates the length of the transect monitored by ERT. The steep snow-free rock face left of window No. 2 is the only part where rock permafrost persists undisturbed until today according to temperature and ERT measurements.

The Zugspitze summit (2962 m a.s.l.) is Germany's highest mountain located in the Northern Calcareous Alps at the German-Austrian border. Up to 10,000 people visit the Zugspitze per day by two cable cars and the cog wheel train. The exposed topographic appearance of the Zugspitze results from an 800 meters thick massive Triassic limestone layer (Wettersteinkalk) stratified in tens of meter thick beds (Miller, 1961). Carstic dissolution since the Miocene created subsurface cave drainage that is sometimes blocked by permafrost above 2500 m a.s.l.. Brecciated zones extend tens of meters below presently exposed crestlines. These are up to 1 m thick and consist of limestone breccia and red loam, which is, in the presence of permafrost, often frozen and intercalated with centimeter to decimeter thick ice layers (Körner and Ulrich, 1965). Brecciated zones, which dip steeply (60°-90°) in direction NW-ENE, heavily influence the susceptibility of the north face to rock instability (Ulrich and King, 1993). Intersecting discontinuities in these directions are held responsible for the $3.5(\pm 0.5)*10^8$ m^3 rockslide in 3700 B.P. (Körner and Ulrich, 1965) while the gently SE dipping layering is less important for rock instability.

6.4.2.2 Indications of historical and Holocene climate change and permafrost

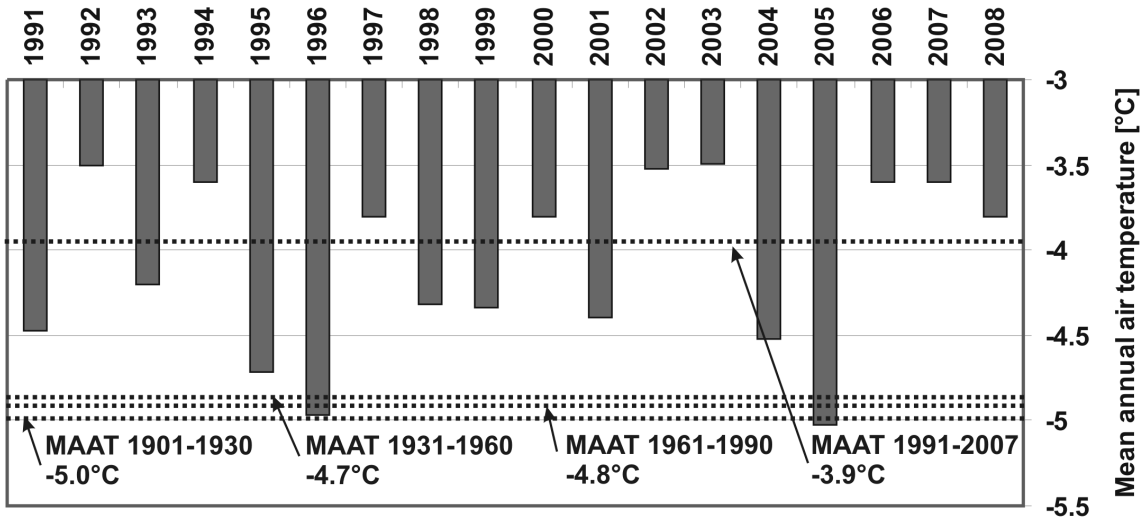

Fig. 39: MAAT of the Zugspitze meteorological station (2962 m a.s.l.) from 1991 to 2007 in comparison to 30-year reference periods since 1901.

Data indicate an abrupt rise in temperature in the last 17 years.

Meteorological data recorded at the summit since 1900 show a significant rise in temperatures starting in the late 1980s. The mean annul air temperature (MAAT) in 1991-2007 was –3.9 °C; this is 0.8-1.1 °C warmer than the prior reference periods (Fig. 39). A 90 % glacier shrinkage of the formerly 3 km² large Schneeferner Glacier since 1820 (Fig. 37) is among the fastest rates in the European Alps (Hera, 1997). Hirtlreiter (1992) provided evidence of glacier changes in the Mid/Late Holocene that exceeded those of the $19^{th}/20^{th}$ century significantly. These indicate an elevated sensitivity of the Zugspitze area at the northern fringe of the Alps to climatic fluctuations. Several technical descriptions highlight the presence of permafrost and the impact of increasing temperatures. During the drilling of the rock tunnel for the cog wheel car from 1928-1930, frozen rock was found frequently close to the North Face from 1640 to 2650 m a.s.l. (AEG, 1931). During the construction of the cable car station at the summit in the early 1960s rock permafrost was found in all construction pits at the Zugspitze summit, especially as ice intercalations in the clayey joint fillings (Körner and Ulrich, 1965). In 1985, during the extension of the rock tunnel on the south side of the crestline, a 19 m long –0.5 °C warm massive ice body was penetrated at 2570 m a.s.l. and subsequently led to a water inleakage of 800 m/s (Ulrich and King, 1993). In 1990, a 30 m deep undisturbed ice-filled cave (cadastre no. 1234/124) melted out at the crestline at approximately 2900 m a.s.l. indicating changing thermal conditions for permafrost. Temperature modeling by Noetzli (2008) based on mean annual ground surface temperature from 2000-2006 indicated permafrost from 2500 m to the summit but only close to the steep north face and in the range of 0 °C to –2 °C. First data from the borehole directly under the summit indicate that permafrost in the not seasonally disturbed part is more in the range of –2 °C to –4 °C (v. Poschinger, pers. comm.), possibly a transient effect due to colder conditions in the past.

6.4.2.3 Rockfall evidence

Jerz and Poschinger (1995), Jerz (1999), and Gude and Barsch (2005) point out that permafrost degradation is likely to be the trigger for the 0.3-0.4 km³ rockfall that occurred in 3700 B.P. after the Holocene climatic optimum. Presently, several thousand people have settled on the deposits of the Eibsee rockfall. Gude and Barsch (2005) postulate that rising permafrost lines due to global warming will herald a new increase in rockfall activity in the Zugspitze area. Glawe (1991) found indications of several preparing rockfalls in the range of 10^4 m³ at the crestline west of the Zugspitze. Mustafa (2002) listed nine 10^3 to 10^4 large rockfalls from north-exposed rock walls from 1700-2900 m a.s.l. that occurred from 1995-2001 close to the Zugspitze. At least three more in the range of 10^5 m³ have occurred since that, two of those in the hot summer 2003. During a comparative quantitative rockfall measurement in the Northern Alps, Sass (2005b) found strongly enhanced rockfall activity at the Zugspitze compared to other study sites sporting similar geotechnical parameters and attributed increased rock instability to present and recently degraded permafrost.

6.4.3 Methods

6.4.3.1 Laboratory calibration of temperature-resistivity relationship

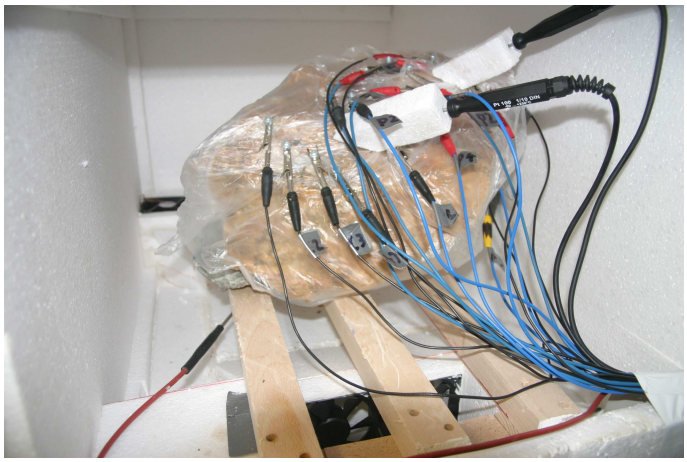

Fig. 40: Wetterstein limestone sample instrumented with electrodes and high-precision thermometers in the freezing chamber.

Resistivity behavior as a function of temperature of Wetterstein limestone in the laboratory was measured using 40 cm * 20 cm * 20 cm cuboid samples taken directly from the study site. The Wetterstein limestone is a hundreds of meters thick, homogeneous, fine-grained and pure limestone from a back-reef sedimentation and shows no vertical or lateral change in lithological properties (Miller, 1961) in the transect. Wetterstein limestone was cooled and frozen in a self-constructed freezing chamber in which the temperature of the stone sample can be controlled with an accuracy of 0.1-0.2 °C in a range of 20 to –4 °C (Fig. 40). Two calibrated 0.03 °C high-accuracy thermometers were used to measure rock temperature during freezing. Rock temperature inside the sample was recorded approximately at the median depth of electric current flow according to Barker (1989) for the employed Wenner-type four-electrode configuration. This array was chosen for the resistance measurements as a laboratory analogue to the geometry of the field measurements. Stainless steel electrodes of 5 mm diameter and 16 mm length were firmly placed in holes drilled to a depth of a 2-3 millimeters with a constant separation of 8 cm. Galvanic contact was improved by adding conductive grease along the rock-electrode contact. Resistance was measured in accordance with field measurements with an ABEM SAS 300B device at 0.2 mA and up to 160 V. To imitate natural conditions, we applied initial and refreezing freezing cycles. Resistivity was then calculated under the assumption of a half-space measurement geometry. This assumption is justified given the dimensions of the rock samples compared to the electrode array length.

6.4.3.2 ERT data acquisition

Fig. 41: Geophysical instrumentation in the Kammstollen gallery 25 m from the North Face at 2800 m a.s.l.. Permafrost is evidenced by perennial ice on the floor; the picture shows electrodes and a temperature logger on the right side.

As outlined by Krautblatter and Hauck (2007), 10 mm diameter stainless steel electrodes were drilled 10 cm into the rock and firmly connected by electrode grease (Fig. 41). Contact resistances range mostly between 10^0 to 10^2 Ω. The electrodes were placed in three profiles: the main profile along a 276 m section of the main gallery, with an electrode spacing of 4.6 m (Fig. 42). Two secondary profiles with an electrode spacing of 1.533 m were located in the permafrost-affected part, with electrodes placed along the main gallery and perpendicular to this direction in the side gallery to improve the spatial resolution and coverage. In February 2007, the 127 electrodes were deployed to collect 750 resistance measurements with a Wenner array, which offers a favorable signal-to-noise ratio. Subsequently, measurements were performed with a high-resolution array combining Wenner, Schlumberger, and Gradient configurations, resulting in an average of 1550 measurements. Due to a lightning stroke, which caused a damage of the instrument, the data set for June is reduced to 1050 measurements, practically performed just along the main gallery.

6.4.3.3 ERT inversion

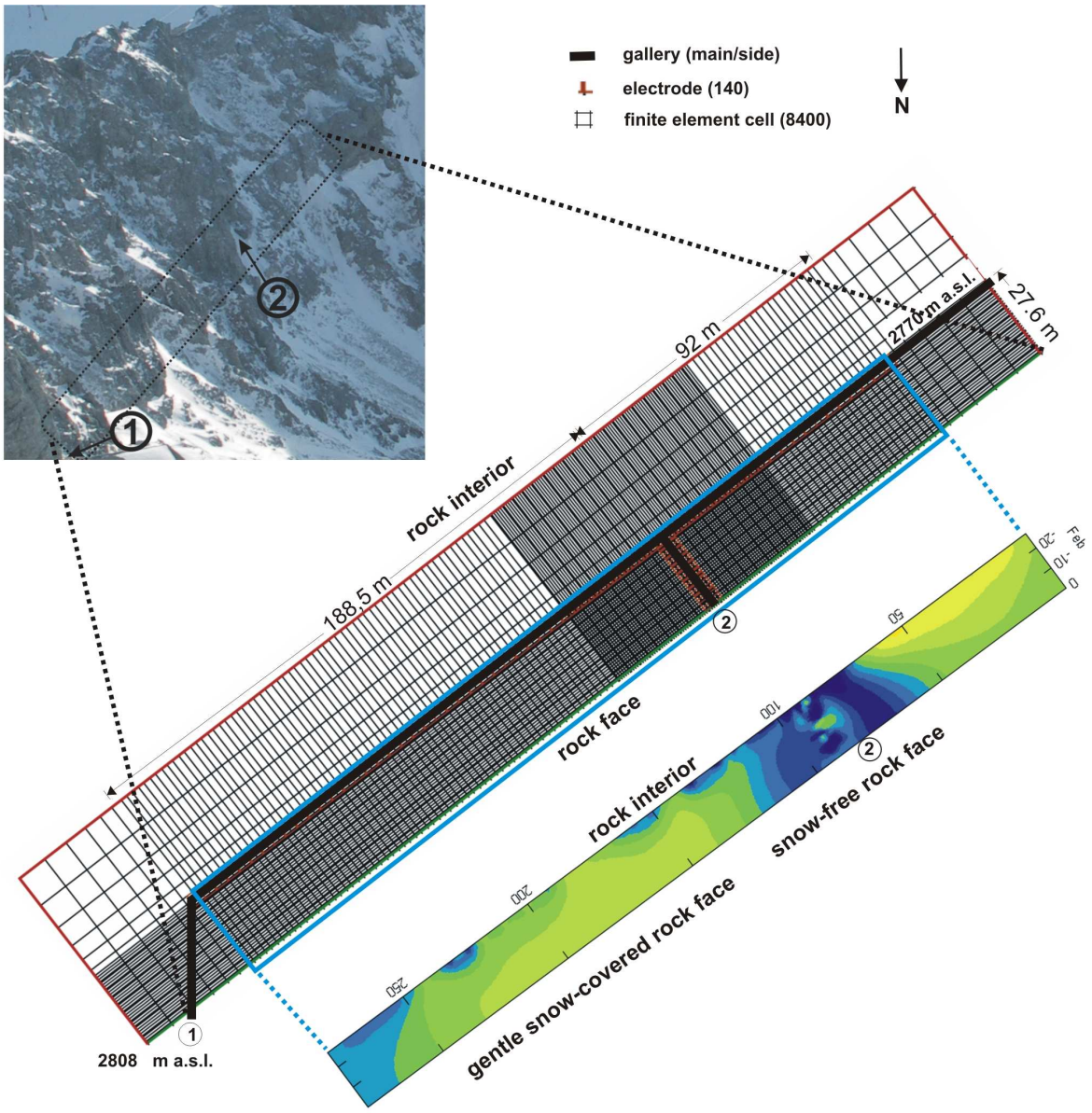

Fig. 42: ERT grid with 127 electrodes along the gallery.

Different cell sizes adjust to data sampling density (electrode separation) and expected highest resolution is in the permafrost area close to the side gallery. Note that for the ERT forward problem, a no-flow boundary condition is imposed at the rock face boundary (green line) and a mixed boundary condition at the remaining grid boundaries inside the rock (red line).

Images of electrical resistivity presented in this work were obtained using the 2D smoothness-constrained inversion algorithm by Kemna (2000). Here, inversion is accomplished by solving an optimization problem in which the model roughness is minimized subject to fitting the data to a pre-defined degree (LaBrecque et al., 1996). Model roughness is quantified as the norm of the gradient of the log electrical conductivity distribution,

$\ln\sigma(y,z)$, integrated over the considered two-dimensional domain, which is evaluated on the basis of the given parameterization **m** of $\ln\sigma$ by a roughness matrix **R**, i.e.,

$$\left\|\mathbf{Rm}\right\|^2 \approx \iint \left\|\nabla_{2\mathrm{D}}(\ln\sigma)\right\|^2 \mathrm{d}x\,\mathrm{d}y$$

Equ. 6.11

The regularization of the inverse problem by a smoothness constraint, i.e., the assumption of smooth model characteristics, represents a reasonable approach particularly for the present application, because in permafrost rocks thermal diffusion along temperature gradients acts to smooth out temperature-induced gradients.

The smoothness-constrained inverse problem is solved by minimizing the objective function

$$\Psi(\mathbf{m}) = \Psi_{\mathrm{d}}(\mathbf{m}) + \lambda \left\|\mathbf{Rm}\right\|^2$$

Equ. 6.12

by means of the Gauss-Newton method (Kemna, 2000). Ψ_{d} is the data misfit function and λ the so-called regularization parameter which controls the influence of data misfit versus model roughness in the objective function. The data misfit is given as the misfit between the measured log resistance data, **d**, and the corresponding predicted data, **f**(**m**), for a given model **m**, weighted according to the individual data uncertainties by a weighting matrix **W**, i.e.,

$$\Psi_{\mathrm{d}} = \left\|\mathbf{W}\left(\mathbf{d} - \mathbf{f}(\mathbf{m})\right)\right\|^2$$

Equ. 6.13

A diagonal weighting matrix is used, which corresponds to the assumption of uncorrelated Gaussian data errors, the standard deviations of which are given by the inverse of the entries of **W**, i.e., $w_{ii} = \varepsilon_i^{-1}$, where w_{ii} is the ith diagonal element of **W**, ε_i is the standard deviation of the ith datum $d_i = \ln R_i$, and R_i is the ith resistance measurement. Provided that the correct standard deviations are used, an acceptable data fit is achieved when the data misfit RMS (root-mean-square) value,

$$RMS = \left(\Psi_{\mathrm{d}}/N\right)^{1/2}$$

Equ. 6.14

is equal to one, where N is the number of given data points. It is emphasized that such an approach, where the data are fitted to a well-defined degree based on an adequate data error description – in contrast to the widely used approach of just minimizing the data misfit – is essential for a quantitative interpretation of ERT results.

The 2D ERT forward problem, defining the operator **f** in Equation (3), is given by the 1D Fourier transform of the Poisson equation for a 3D point source in the image plane at (x_s, y_s) with current strength I:

$$\frac{\partial}{\partial x}\left(\sigma\frac{\partial\phi}{\partial x}\right)+\frac{\partial}{\partial y}\left(\sigma\frac{\partial\phi}{\partial y}\right)-k^2\,\sigma\phi=-I\,\delta(x-x_s)\,\delta(y-y_s)$$

Equ. 6.15

In Equation (5), k is the wave number corresponding to the assumed strike direction (z), ϕ is the electric potential in the Fourier domain, and δ is the Dirac delta function. For given boundary conditions, Equation (5) is solved by means of the finite-element (FE) method, where the discretization is chosen such that each model cell of the parameterization is represented by a set of lumped finite elements. Once the transformed electric potential distribution is computed for each current injection position, inverse Fourier transform and appropriate superposition yields the transfer resistance R_i of any desired electrode configuration (Kemna, 2000). The boundary conditions are generally expressed as

$$\sigma\frac{\partial\phi}{\partial n}+\beta\phi=0$$

Equ. 6.16

,where n denotes the outward normal and the parameter β defines the type of boundary condition. We here impose a no-flow boundary condition ($\beta = 0$) at the rock face boundary and so-called mixed boundary conditions ($\beta \neq 0$) at the grid boundaries within the rock (Fig. 42), where β is determined based on the assumption that ϕ behaves asymptotically as in the homogeneous half-space case (Dey and Morrison, 1979). The employed finite-element grid with the imposed boundary conditions resembles the actual field situation with electrodes being placed along the galleries inside the rock.

6.4.3.4 ERT data error characterization

Errors present in the ERT data can be both systematic and random. Systematic errors are characterized by some sort of correlation within the data set, or over time for a series of data sets. It is for instance associated with a malfunction of the measurement equipment, bad galvanic contact of electrodes, or misplaced or misconnected electrodes. Data contaminated by systematic errors should be rejected, or corrected, before the inversion. Random errors cannot be predicted or controlled and arise primarily from fluctuations in the contact between the electrodes with the air/ground, in the current injected, and due to changes in the current pathways (Binley et al., 1995; Slater et al., 2000). Random errors are uncorrelated and normally assumed to have a normal distribution (Gaussian noise).

An efficient procedure to characterize random error in geoelectrical measurements is based on the analysis of differences between measurements taken with normal and reciprocal configurations (Koestel et al., 2008; LaBrecque et al., 1996; Slater and Binley, 2006; Slater et al., 2000). For a given “normal” four-pole measurement configuration, the reciprocal configuration is the one with swapped current and voltage dipoles. In theory, both measurements should be identical. However, in practice they differ to some degree, and the deviation can be considered as a measure of the present random error. We here adopt the model of Slater et al. [2000] to describe the data error, where the resistance error, ΔR_i, is assumed to be a linear function of the resistance R_i:

$$\Delta R_i = a + b R_i$$

Equ. 6.17

where a represents an absolute resistance error, dominating the error model for small resistances, and parameter b a relative resistance error, dominating the error model for large resistances. Given the use of log-transformed data in the inversion, ΔR_i is related to the data error ε_i according to

$$\varepsilon_i \approx \frac{\Delta R_i}{R_i} = \frac{a}{R_i} + b$$

Equ. 6.18

The final inversion result depends strongly on the chosen parameters a and b. Overestimating the error present in the data will lead to a smooth, low-resolution image due to under-fitting of the data in the inversion. If the error is underestimated, the data will be over-fitted and artifacts in the final image are likely to be generated. We here follow the procedure of Koestel et al. (2008) to determine appropriate values for the parameters a and b. Here, the range of resistances covered by the data set is subdivided into a number of "bins", and this way sub-data sets are obtained. For each bin (or sub-data set), the distribution of normal-reciprocal differences, i.e., R_n–R_r with R_n and R_r denoting resistance measured with normal and reciprocal configuration, respectively, is statistically evaluated for its standard deviation. The linear model of Equ. 6.17 is then fitted to the obtained standard deviations for the different bins as a function of the mean resistance of the respective bin (Fig. 45), yielding estimates for the parameters a and b. The diagonal entries of the data weighting matrix **W** in the inversion are then calculated from Equ. 6.18.

6.4.3.5 Rock-wall temperature validation

Rock wall temperature loggers were placed in the side gallery at a distance of 2.5 m, 5 m, 10 m, 15 m and 20 m from the north face. The exits of the side gallery are firmly closed at both sides by a wood construction. To reduce the influence of the side gallery loggers were placed at 40 cm rock depth. We applied UTL II Loggers that were calibrated in ice water beforehand and data recording was set to hourly intervals.

6.4.4 Results

6.4.4.1 Laboratory temperature-resistivity behavior of unfrozen, super-cooled, and frozen rocks

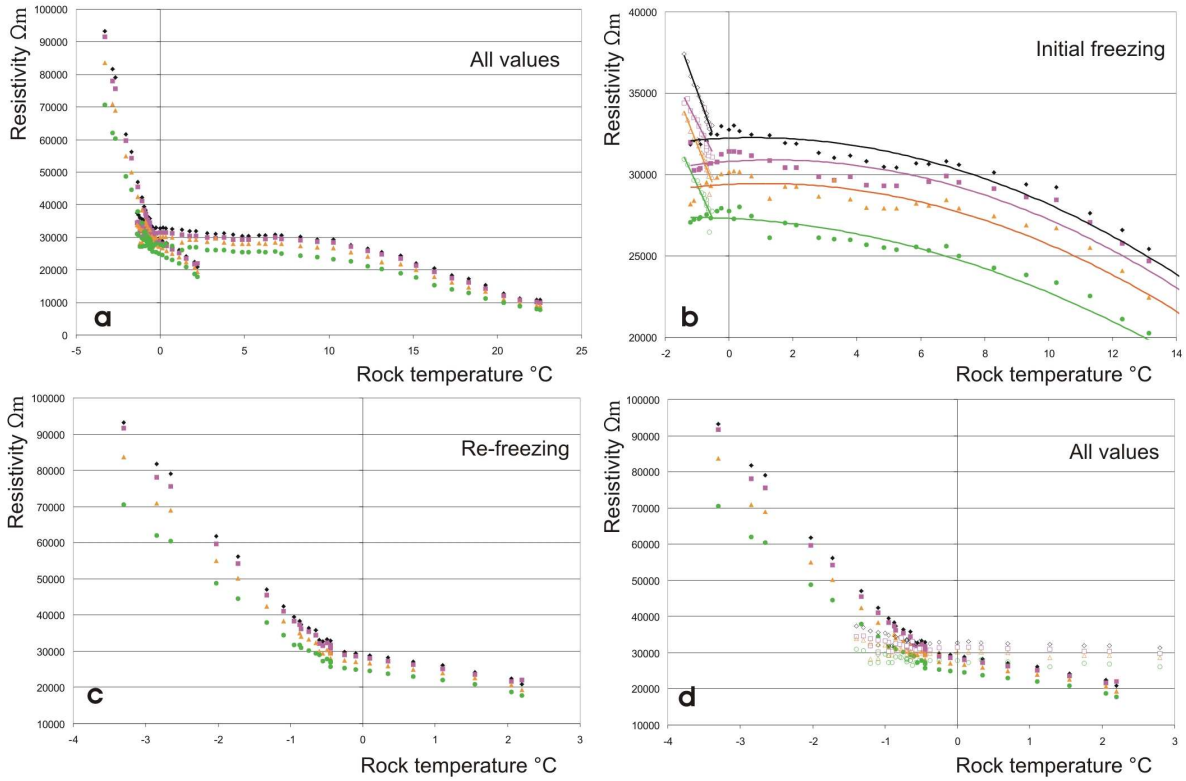

Fig. 43: Laboratory calibration of Wetterstein limestone from the Kammstollen study site.

Four arrays (black, pink, orange, green) were installed on water-saturated limestone and exposed to initial freezing, re-thawing, and refreezing. In 7d, initial freezing is indicated by unfilled dots while filled dots represent refreezing values.

Fig. 43 shows that both freezing and refreezing of Wetterstein limestone occurs at –0.5 (±0.1) °C and 30 (±3) kΩm. Initial cooling-resistivity behavior follows a linear trend from 22 °C to 12 °C and stagnates from 12 °C to 0 °C. Fig. 43b highlights supercooled conditions below the freezing point (–0.5 °C to –1.1 °C), which indicate even a resistivity decrease with declining temperature. This is evidenced by a sudden increase of rock temperature to –0.5 °C by latent heat emission and subsequently a stagnation of temperature at the freezing corridor –0.5 (+0.1) °C for approximately one hour in a –6 °C cool freezing chamber, and finally a new linear temperature-resistivity behavior with a much steeper gradient. When refreezing the limestone (Fig. 43c), no supercooling below the freezing point occurs as pores are no longer fully saturated with water and the resistivity-temperature gradient of frozen rock is steeper than for initial freezing (see Fig. 43d).

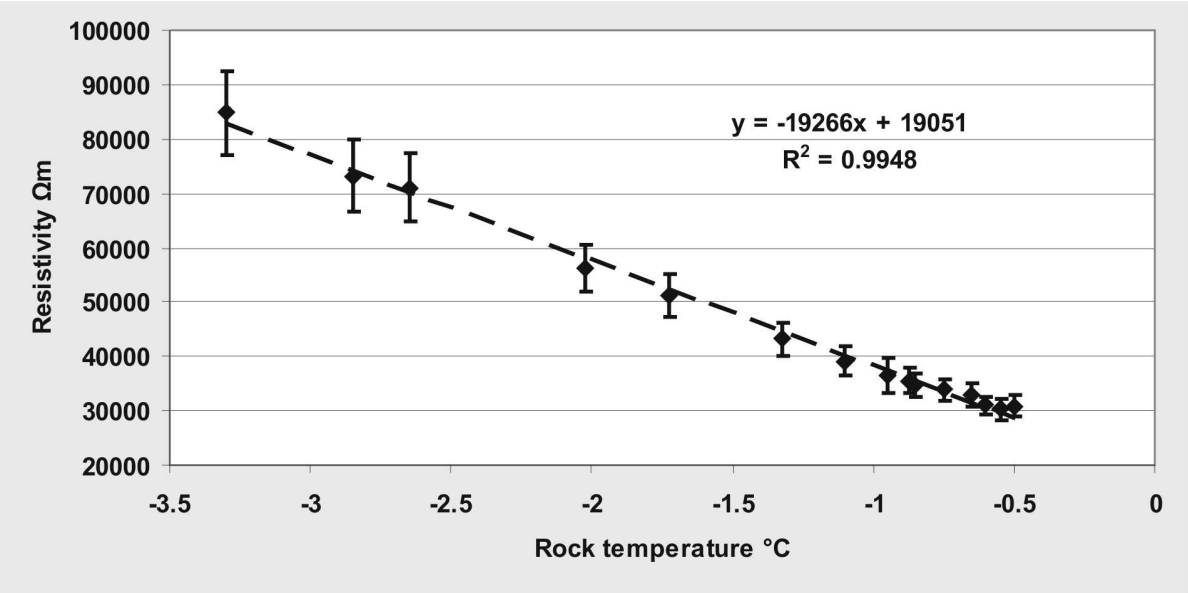

Fig. 44: Mean resistivity behavior of refrozen Wetterstein limestone with mean deviations.

Refrozen Wetterstein limestone exhibits a very steep resistivity-temperature behavior with small deviations (19.3 (±2.1) kΩm/°C). As temperature-dependent alterations are much higher than internal deviations, referencing resistivity to temperature below –0.5 °C appears to be a promising task. Unfrozen resistivity-temperature paths above –0.5 °C are less suited for temperature-referencing due to lower gradients and higher internal variability.

6.4.4.2 Error model parameters

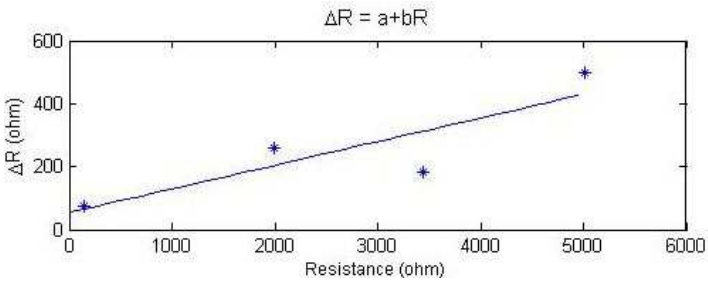

Fig. 45: Error model based on a bin analysis of the differences between normal and reciprocal measurements.

Fig. 45 presents a plot of calculated standard deviations of the normal-reciprocal differences in four bins as a function of the mean resistance in each bin for an exemplary data set, together with the fitted linear model to obtain estimates for the error model parameters *a* and *b*. The bin analysis yields $a = 48\ \Omega$ (absolute resistance error for small resistances) and $b = 8.0\ \%$ (relative resistance error for large resistances). For a different number of bins in the analysis, similar values are obtained. The values above were used for the inversion of all data sets to ensure consistency among the ERT images at different times and avoid the creation of artifacts in difference images.

6.4.4.3 ERT images

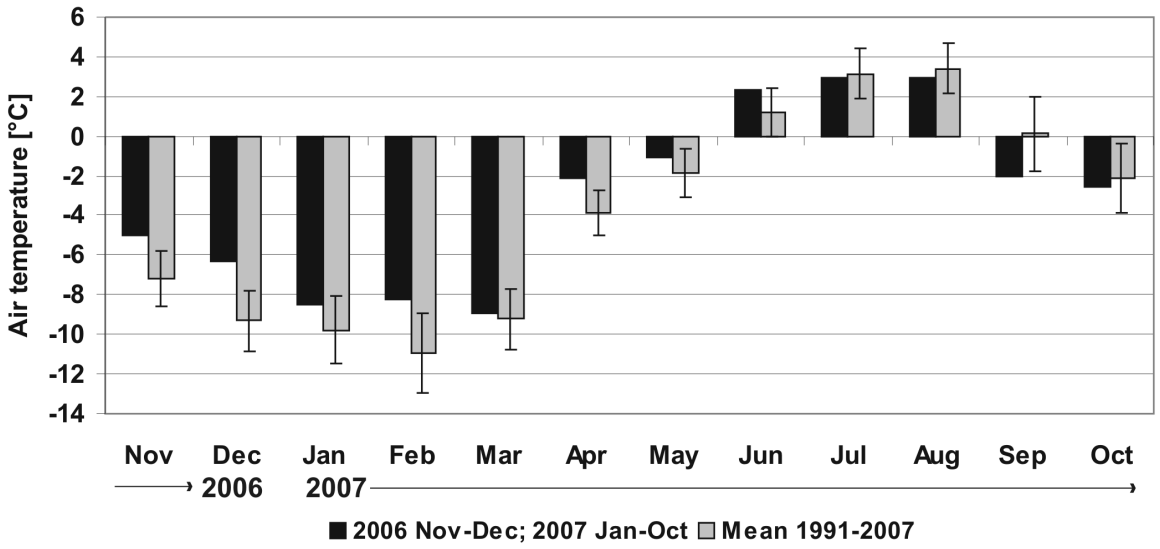

Fig. 46: Mean monthly air temperature in 2006 and 2007 referenced to 1991-2007 mean values and mean deviation.

The ERT record in 2007 starts after a 2.3 °C warmer than average November to February winter period in comparison to the mean of 1991-2007 (Fig. 46). The observed period (February to October 2007) is 0.4 °C warmer than average (1991-2007). From 1991 to 2007, February to October temperatures deviated on average by 1.5 °C from the mean; therefore the temperatures of 2007 are, with the exception of April, well in the representative range for the last 17 years.

6.4.4.4 *Absolute values*

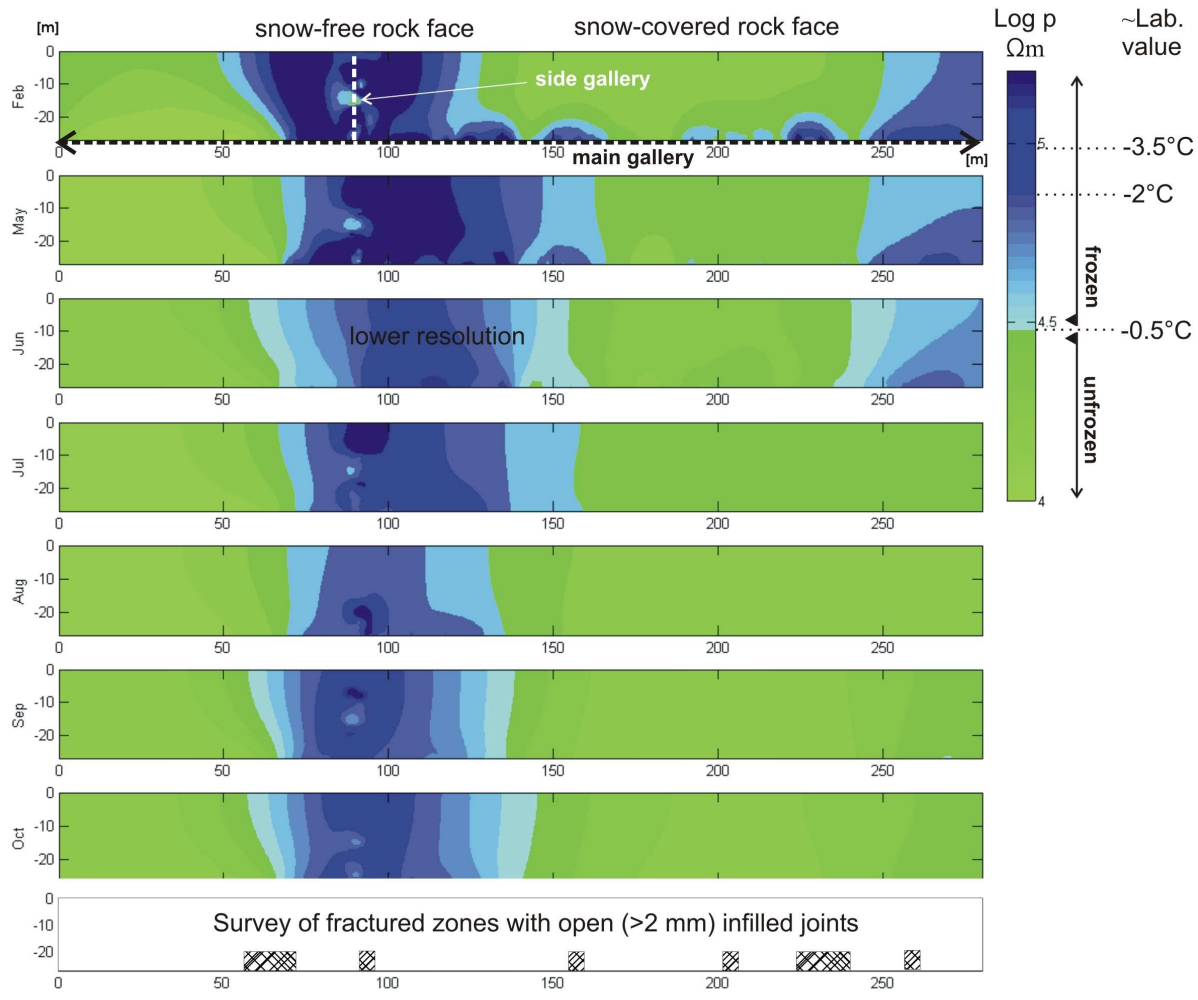

Fig. 47: ERT inversion results based on 127 electrodes and on average 1550 resistance measurements per ERT frame.

Due to a lightning puncture of instruments in the side gallery, the image of June has a lower resolution from 55-135 m. We found that geotechnical parameters, such as the degree of fracturing shown below the ERT plot, virtually have no influence on ERT results in this transect.

The ERT images in Fig. 47 show no obvious correspondence to variations in discontinuity patterns in the observed rock sections. Thus, geological variability seems to have little influence on the resistivity distribution in the rock. The gallery section with perennial ice and temperature logger data indicating permafrost appears as a central high-resistivity body from 50 m to 150 m with pronounced seasonal resistivity variation. Resistivities greater than $10^{4.5}$ Ωm (≈ lab value –0.5 °C) that correspond to frozen rock laboratory values are concentrated close to the steep snow-free section, while the snow-covered snow face indicates resistivities smaller than $10^{4.5}$ Ωm in all time frames. A transitorily frozen rock body is found from 240 m to 276 m, also connected to a snow-free rock face (Fig. 38b).

The central high-resistivity body is characterized by a core section $\geq 10^{4.7}$ Ωm (≈ lab value –2 °C) and laterally aggradading or degrading of marginal sections $\geq 10^{4.5}$ Ωm (≈ lab value –0.5 °C). February and May, with rock temperature logger data from –2 °C to –4.5 °C, yield highest resistivities of all sections ($\geq 10^{4.95}$ Ωm ≈ lab value –3.5 °C). Following May, the high-resistivity section close to the rock face diffuses to the rock interior. Resistivities of $10^{4.7}$ Ωm fade starting from the rock face and nearly disappear in August. Horizontal diffusion to 27 m depth away from the rock face is observable until August, while lateral diffusion peaks in May/June and is then substituted by a lateral contraction of the marginal $10^{4.5}$ Ωm section in July/August. A new core-section input is created in September and diffuses to depth and laterally in October. The following shape of the high-resistivity body can be extracted: In February, the high-resistivity section broadens from 50 m to 70 m towards the rock face. This trend reverses stepwise from May to August, with a pronounced narrowing towards the rock face of the $10^{4.5}$ Ωm and $10^{4.7}$ Ωm zone developed in August, and reappears in September coincidently with mean monthly air temperatures below 0 °C (Fig. 46). Remarkably, the section left of the side gallery (70-90 m) indicates an abrupt decrease in resistivity in May, opposing the general trend of high resistivities expanding from 90-160 m.

6.4.4.5 Absolute changes

The most pronounced change in resistivity occurs between February and May (Fig. 48). Resistivities values decrease rapidly in the 50-90 m section (note that the tomography covers three months), while the section from 100-150 m still shows a moderate increase of resistivity. Between May and July the decrease of resistivity values is centered in the central high resistivity section (80 – 140 m) and is more intense close to the rock surface. From July to August, a rapid decrease of resistivity values occurs at all depths in the central permafrost body. The cool September (Fig. 46) converts this trend and initiates resistivity increase e.g. close to the central high-resistivity body (60 - 95 m). Only small resistivity changes are observed in October.

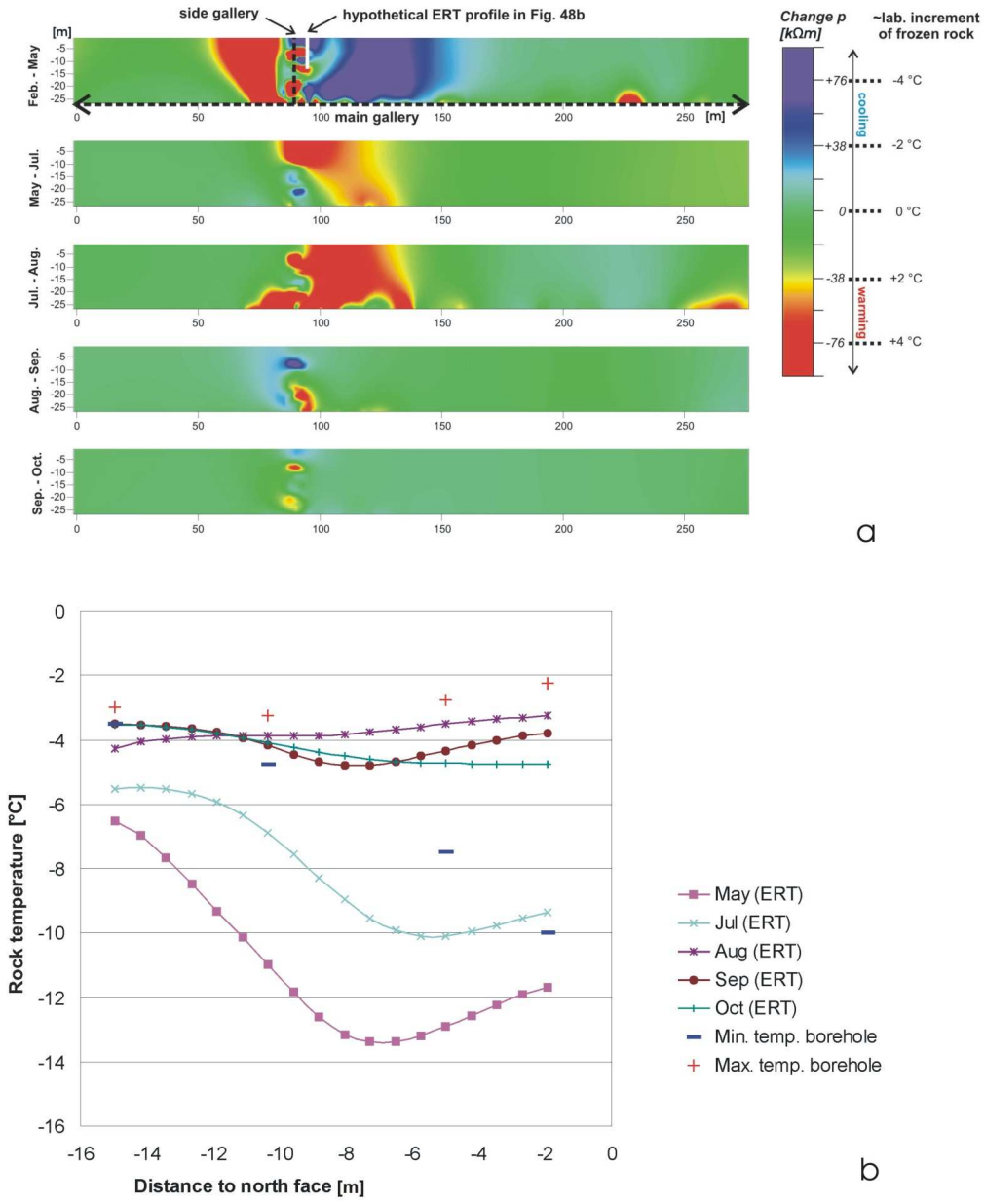

Fig. 48: a, Absolute changes of ERT plots from February to October 2007. b, Comparison of the temperature range obtained by borehole data at the north face below the Zugspitze summit (2920 m a.s.l.) and the values obtained by temperature-calibrated ERT at the Kammstollen North face (2800 m a.s.l., position see Fig. 12).

*Changes are related to the temperature-resistivity equation for frozen rock presented in Fig 43 (ρ [kΩm]=19.1-19.3 (±2.1]*t[°C]). The hypothetical ERT profile is the closest analogue to the borehole situation in this ERT section with the same aspect in a horizontal distance of 300 m and with an altitudinal difference of 100 m.*

6.4.4.6 Rock-wall temperature validation

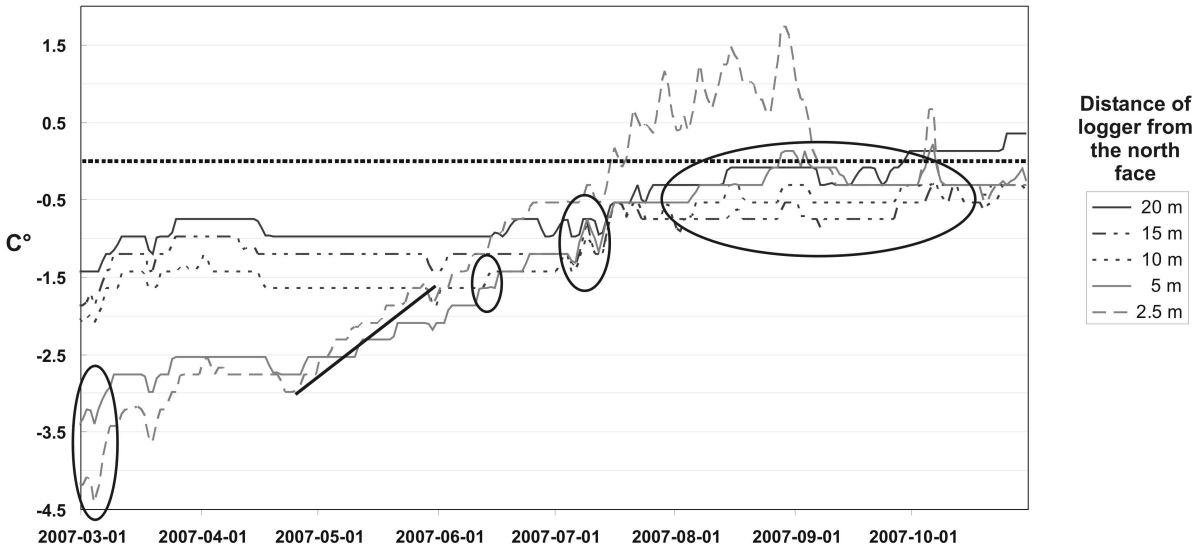

Fig. 49: Mean daily temperatures, 22 April to 30 October 2007, derived from hourly temperature measurements with sensor placed in the side gallery at 40 cm rock depth. Loggers are labeled according to their distance from the north face.

Loggers at a distance of 2.5 m and 5 m from the Zugspitze North Face show an abrupt linear temperature rise starting at the end of April. Temperature rise in 10 m depth is not visible until mid-June. July marks the near parallel temperature rise of loggers in 10 m, 15 m and 20 m depth, showing a different temperature regime compared to the 2.5 m and 5 m sensors. The signal at 10 m, 15 m and 20 m depth stabilizes around -0.1 °C to -0.8 °C in August to October, while directly coupled loggers at 2.5 m and 5 m show higher variation of data due to radiation changes.

6.4.5 Discussion

Mc Ginnis et al. (1973) suggested an exponential formula for temperature-resistivity behavior for subzero temperatures. Data derived from 10 °C to 20 °C increment laboratory measurements using Berea sandstones and limestones and did not precisely target on temperatures around the freezing point. Our laboratory testings at 0.1-0.2 °C increments indicate that freezing of low-porosity rocks is better approached by a two-fold linear relationship divided by a freezing point significantly below 0 °C. A number of new effects can be discussed concerning temperature-resistivity paths. (i) Resistivity decline from 22 – 12 °C follows the linear relation postulated by Keller and Frischknecht (1966). (ii) Resistivity increase stagnates from 12 °C to 0 °C, probably due to increasing conductivity of pore water resulting from better carbonate solution at lower temperatures (Le Guen et al., 2007), as we found this behavior in own studies only in carbonate samples. (iii) The shift depression of the freezing point below 0 °C in rocks with confined pore space was not resolved in prior rock resistivity studies (McGinnis et al., 1973; Mellor, 1973). Petrophysical and other studies show that the depression of the freez-

ing/thawing point in confined porous media is strongly dependent on pore space and pore material (Jähnert et al., 2008; Murton et al., 2000; Sliwinska-Bartkowiak et al., 2008) (iv) Resistivity decrease for supercooled conditions (-0.5 °C – -1.2 °C) points towards excessive pore pressure build up in pores fully saturated with water. According to Arenson (2003) pressures needed to reduce the freezing point of water to -1.2 °C are in the range of 11 MPa, while pore water geometry and chemistry may alter this value by a certain degree. Nevertheless, we suppose that at -1.2 °C, excessive pore water pressure alters rock permeability (Zisser et al., 2007) and leads to pore water extrusion and subsequently to instantaneous freezing. (v) The jump in resistivity at the freezing point and the bilinear temperature-resistivity relation for saturated natural rocks was already found by Mellor (1973) but has been poorly adapted since that. For water-saturated Wetterstein limestone initial freezing and refreezing of experiments confirmed a uniform freezing point at 30 kΩm at -0.5 (±0.1) °C while a hysteresis down to -1.2 °C was found for initial freezing. Unfrozen limestones increase by less than 10^4 Ωm/°C while refrozen specimen below -0.5 °C increase on average by 19.1 (±0.6) * 10^4 Ωm/°C. As all rocks at the study site have probably experienced repeated freezing we assume that the refreezing curve is more relevant for the calibration of ERT values than initial freezing. The refreezing curve of Wetterstein limestone is a good target for temperature-referencing of ERT results as the temperature gradient (19.1 * 10^4 Ωm/°C) is 30 times larger than the mean deviation due to internal lithological variability (±0.6 * 10^4 Ωm/°C).

Few publications have targeted the problem of how laboratory-scale electrical experiments can be transferred to a decameter field scale (Day-Lewis et al., 2005; Singha and Gorelick, 2006). Zisser et al. (2007) show that pore volume, degree of interconnection of the pores through pore throats, and the distribution and orientation of open cracks and fractures are the petrophysical values that determine electrical properties of limestone. Thus, resistivity values to jointed rock masses in the field can vary from intact laboratory sample values. Jouniaux et al. (2006) show that stress-induced crack formation in intact saturated limestone can increase conductivity up to 4 % with lower values for partly saturated conditions. However, a survey of joint width, spacing orientation and infillings showed little correspondence to ERT behavior along the monitored main gallery (see Fig. 45). This is likely due to homogeneous lithological conditions in the Wetterstein limestone (Miller, 1961) and transfer to heterogeneous rock sequences will require more geological input into the resistivity model. Friedel et al. (2006) emphasized the role of high resolution ERT for slope stability applications in layered media. Resolution is not only a spatial problem, it also affects the degree to which ERT is quantitatively reliable (Singha and Gorelick, 2006). We applied two spacings of 4.6 m along the main gallery and 1.533 m along the central permafrost body in the main and the side gallery. Due to a lightning strike of instruments the June Transect was measured without 66 1.533 m spacing electrodes most of which are in the side gallery. ERT of June, does not provide inconsistent results but only alters the spatial resolution and is generally consistent with prior and following sections. Our results indicate that high-resolution resistivity raw data (here > 1500 datum points) significantly increases spatial definition of ERT (Fig. 47 May, July-October) but has a limited effect on the general outcome.

A bin analysis of misfits against average of normal and reciprocal measurements (Binley et al., 1995) yielded an absolute error of 48.3 Ω and a relative error of 7.95 %. These are reasonable values considering that the high resistances measured, with values up to 5000 Ω. As the interpretation focuses on values greater than $10^{4.5}$ Ωm, the relative error of 7.95 % is the relevant error parameter for interpretability. Laboratory experiments in Koestel et al. (2008) derived relative errors of up to 1.1 %. The error parameters obtained here were similar using different amount of bins for the analysis, which reflects the stability of the parameters obtained. Even when the linear

model is not fitting the points exactly there is a reasonable correspondence. The range of measured resistances is very wide, therefore it is important to obtain a model which can describe the entire data set in a proper manner. Thus, error model settings are capable of avoiding under- or overestimations over the entire range of values. Smoothness-constrained inversion of the data with the error model setting shows consistent results for all different data sets and resolutions.

A shift from qualitative to quantitative interpretation of geophysical results, as heralded by Hauck et al. (2008), appears to be possible for frozen permafrost-affected bedrock. All incorporated values lie within a realistic range in comparison to borehole temperature data. The images gained appear to be free of artifacts and their high resolution permits the detection of seasonal resistivity changes in frozen rock. In this specific case, the homogeneous lithology and the steep temperature-resistivity gradient of frozen rock (19 kΩm/°C) facilitate the temperature-calibrated interpretation of ERT. In correspondence to the rock temperature data and the air temperature record, the absolute ERT plots shows that the main thawing occurs from May to August with a massive retreat of high-resistivity sections above $10^{4.7}$ Ωm (≈ lab value at –2 °C) to distances of 20 m from the rock face. The onset of thawing processes in May, subsequent to the warm April, is pronounced by resistivity decreases corresponding to 5 °C (95 kΩm) and more up to 27 m depth (Fig. 47). Whether ice decay in fractures could also contribute to this resistivity decrease is discussed in the next paragraph. The speed of temperature change cannot be explained by heat conduction alone (Noetzli et al., 2007) and is concentrated close to a fracture zone with open (>2 mm) joints (60 – 80 m). Coincidently, joint water seepage into the gallery below the permafrost body was observed and measured on May 20. Water of 2.5-3.8 °C seeped at 0.03 l/min at 10 a.m. with a maximum of 0.28 l/min at 6 p.m. and a subsequent decline to 0.20 l/min (10 p.m.) from a 34 cm long joint with an aperture of 2-3.5 cm. We hypothesize that the deep-reaching decline in resistivity is due to meltwater percolation in joints transporting large amounts of latent and sensible heat. Daily variations of joint water seepage below a tens of meters thick rock mass indicate rapid percolation through a highly permeable joint system as previously observed by Wegmann (1998). 3D-effects due to rock wall topography (Gruber and Haeberli, 2007) could also act to accelerate response times. A deep-reaching thawing response is apparent in the August-July change plot also in the part of the rock face that was covered by snow until mid-July. In the cold September and October (Fig. 46) resistivity increases around the permafrost body and resistivity values greater than $10^{4.7}$ Ωm (≈ lab value at –2 °C) reappear between the permafrost body and the north face. Positive rock temperature values at 20 m in October may respond to air circulation in the main gallery. The existence of the shielded side gallery locally influence the thermal regime, but its impact is too small to affect much of the 60*20 m large and decameter thick permafrost lens. Local authorities (Bayerische Zugspitzbahn AG) report that the main gallery was perennially floored with ice along the whole observed transect in the 1970s and that the length of frozen section of the main gallery decreased enormously in summer 2003.

Some parts still yield high resistivity values up to $10^{5.2}$ Ωm. Possibly, we are not fully capable of resolving anisotropic effects caused by ice-filled joints in the surficial fractured parts at 10 m or less to the rock face. Tensorial non-conductivity of ice-filled joints of unknown orientation may cause series disconnection or parallel disconnection and thus influence directional resistivity in a yet not exactly determined way (Herwanger et al., 2004; Matias, 2008). This is underlined by apparent resistivities up to $10^{5.1}$ Ωm along gallery sections with cm-thick ice-filled joints in a distance of less than 10 m to the rock wall. Comparison of temperature logger point data with ERT volume data stays a difficult task, especially as those obtained from the side gallery are slightly dis-

torted by air circulation inside the otherwise isolated side gallery. Temperature distribution in a highly dissected crestline is clearly a 3D-problem (Noetzli et al., 2007) complicated by partial snow cover (Gruber and Haeberli, 2007). Enhanced measurements if surface temperatures, cleftwater influence and 3D-modeling will be necessary to fully understand spatial thermal patterns as indicated by ERT time section. ERT and 3D thermal modeling provide the first opportunity of a mutual control of more-dimensional spatial permafrost monitoring. Temperature-referenced ERT could provide calibration data, initial conditions and validation data for temperature models and could vice versa be assessed by its consistency with thermal results.

While GPR and seismic surveys are well implemented in the characterization of rock mass properties relevant for instability considerations (Heincke et al., 2006a; Heincke et al., 2006b), ERT has only been applied in a few cases and only in the in the field of fracture characterization (Choi et al., 2006; Deparis et al., 2008). Given that ERT described here targets temperature of frozen rock, the link between temperature and rock mechanics (Mellor, 1973) and ice mechanics (Budd and Jacka, 1989) opens up a new application for geophysical stability analysis. Understanding the influence of temperatures on ERT could also help to filter other stability relevant signals in rock geophysics such as hydrostatic pressure (Fischer et al., 2007; Krautblatter, 2008).

6.4.6 Conclusion

High-resolution ERT with 127 electrodes and on average 1550 datum points was conducted along a 276 m long gallery in the permafrost-affected north face of the Zugspitze in 2800 m a.s.l. in Februray, May, June, July, August, September and October 2007. Data inversion was performed using an 8400 finite element grid with adjusted boundary conditions. To receive quantitatively reliable ERT values, we fitted a smoothness-constrained Occam's inversion to an empirically measured normal-reciprocal error model. Water-saturated Wetterstein limestone was measured in the laboratory to freeze at -0.5 (±0.1) °C with resistivity values close to 30 (±3) kΩm. The resistivity of unfrozen limestones increases by less than 10^4 Ωm/°C. The temperature-resisitivity relationship below -0.5 °C can be described by $p\ [in\ k\Omega m] = 19.1 - 19.3\ (\pm 2.1) * t\ [C°]$ with an R^2 of 0.99. The temperature-resistivity relation of frozen rock was then applied to the quantitative ER tomographies along the permafrost gallery. Absolute resistivity values and monthly resistivity changes are generally consistent with seasonal air temperature changes and rock temperatures observed in the adjacent borehole. Differences in snow coverage dominate the general distribution of permafrost. Pronounced thaw occurs from May to August. Rapid melting occurs along fracture zones coincident to joint water seepage into the gallery in May. Refreezing from the rock wall starts in September and is apparent in both, increasing resistivity values and the expansion of the high-resistivity body. Temperature-resistivity calibration in the laboratory and error-controlled inversion of high-resolution field data present the first step towards quantitative temperature-referenced geophysics in permafrost rocks.

6.5 Towards 3D-characterisation of permafrost rocks

Unpublished data.

6.5.1 Introduction

Seasonal changes at the Zugspitze have shown that three-dimensional effects inside rock walls crucially affect thawing and refreezing patterns. To fully decipher the spatial impact of external inputs on rock permafrost, properties have to be measured in a full three-dimensional space. This section aims to give a perspective on how three-dimensional can be conducted and discusses results recorded in a 3D array from 2006 to 2008 in the Steintälli, Switzerland (see Section 6.2.3.1).

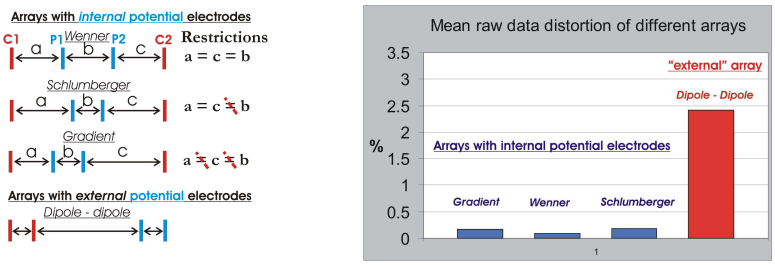

Fig. 50: Implemented arrays (left) and raw data distortion of different arrays measured subsequently with conventional protocol files along the same transects with identical conditions.

"P" refers to potential electrodes whereas "C" refers to current electrodes. Mean raw data distortions refer to distortions observed when measuring identical electrode combinations several times consecutively.

3D tomographies pose an additional challenge for data collection and processing. Measurements can be conducted as 2.5D data, where parallel transects are collated into a merged 3D file or by "real" 3D measurements where current flow is measured in all directions. Real 3D arrays usually apply pole-pole and dipole-dipole arrays, but test measurements at the Zugspitze yielded evidence that these arrays have a worse signal to noise ratio in comparison to Wenner, Schlumberger and Gradient arrays, where potential electrodes lie between the current electrodes (Krautblatter and Verleysdonk, 2008a) (Fig. 50). Therefore, a 2.5D combination of parallel Wenner-arrays appeared to be more suitable for a first 3D characterization of rock permafrost. It is commonly assumed, that the distance between parallel arrays should not be greater than 3 times the minimum electrode spacing inside the arrays. However, this rule of thumb was established for conventional surveying in soft sediment materials and may not be applicable to highly anisotropic and heterogeneous rock masses. This section aims to show that 3D measurements in rock walls require a much more elaborated approach, as (i) rock walls have enormous 3D topography and electrodes can only be placed and rectified with the aid of high-resolution tachymeter measurements, (ii) topographic gradients require the construction of specially adopted finite-element grids, and (iii) the assumption that close-lying 2D transects can be collated into 3D tomographies may not be justified for highly anisotropic and heterogeneous rock masses.

6.5.2 Methods

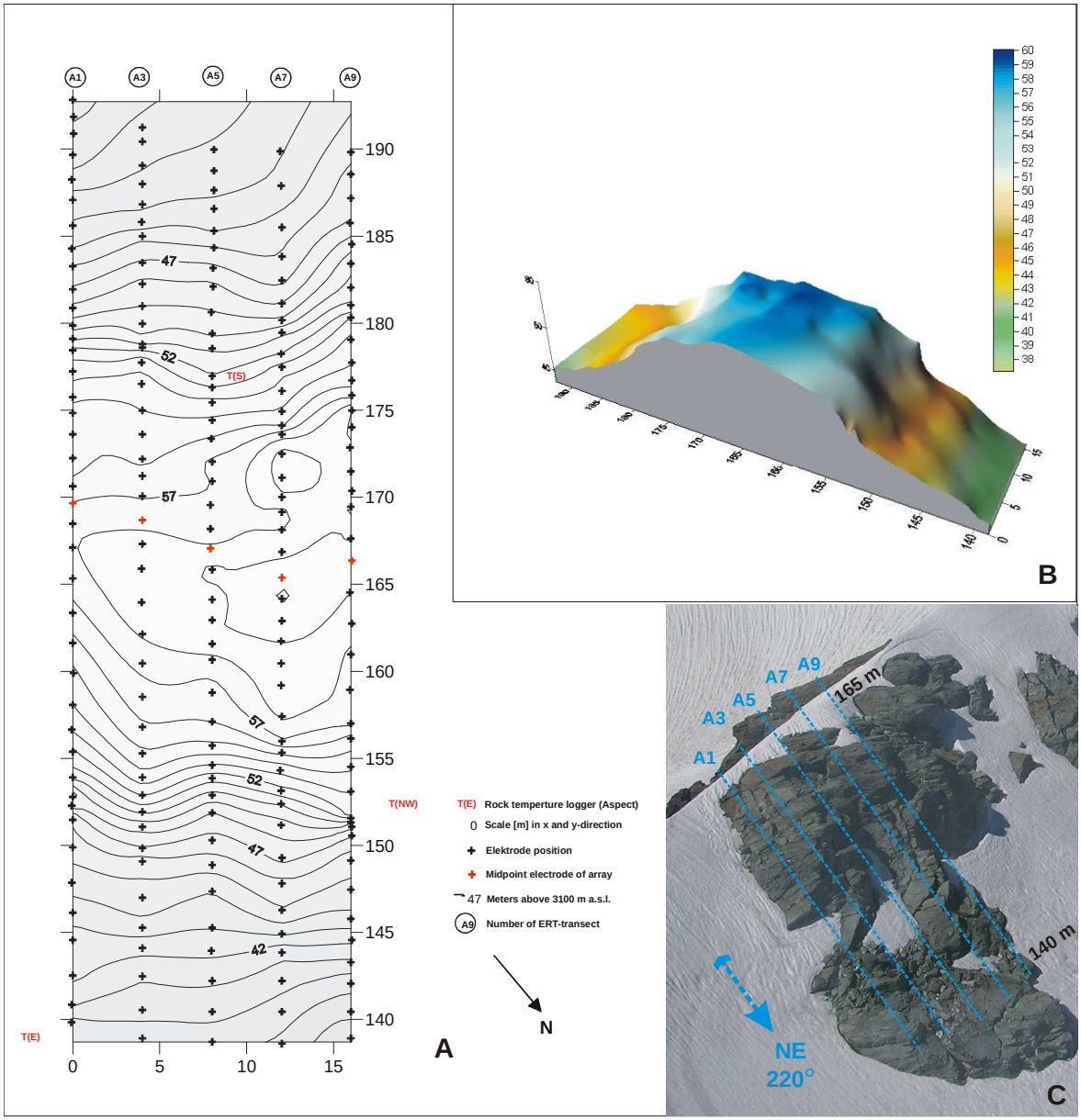

Fig. 51: Electrode positions of a 3D-ERT measurement across a rock crestline with NE and SW-exposed rock faces.

A, Exact position of electrodes derived from tachymeter measurements. B, Decimetre-resolution DEM calculated from tachymeter measurements. C, Picture of the NE-face of the Steintaelli with the position of the transects. In 2006 ice persisted over the summer in protected positions in the NE-facing rock slope (e.g. 4-10m, 145-150 m).

In July and August 2006, a 3D array consisting of 205 steel screw electrodes was drilled according to the method described in section 6.2.3.2 (Fig. 51). Arrays have a minimum electrode spacing of 2 m along the rock surface and spacing between the arrays is 4 m. Exact positions of all electrodes was measured with a Leica TCA 1800 L tachymetre with an accuracy of a few centimetres. This data was used to create a high-resolution DEM of the study site.

Table 5: Error model parameters for different transects of the 3D ERT measurements in the Steintaelli

	Transect 1	Transect 3	Transect 5	Transect 7	Transect 9
a	23.19	47.50	32.33	35.01	66.82
b	8.42	8.33	9.13	9.29	9.34

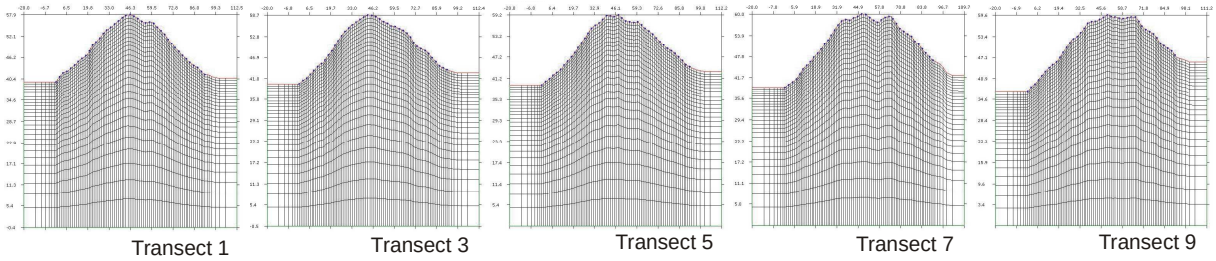

Fig. 52: Finite-element ERT mesh adjusted to smoothed topographies of all five transects (for dimensions see Fig. 55; processed by A. Flores-Orozco).

3D Wenner measurements were conducted in 2006, 2007 and 2008. In 2008 an additional reciprocal measurement with 190 datum points was conducted in all five transects to calculate individual error model parameters. The standard deviations of the normal-reciprocal differences as a function of the mean resistance were calculated in four bins. A linear model was fitted to obtain estimates for the error model parameters *a* and *b* (Table 5) (see also section 6.4.3.4). For a different number of bins in the analysis, similar values are obtained. *b* is the relevant error parameter for high-resistance measurements and approaches similar values from 8-9 % in all transects. The values were used for the inversion of all data sets to ensure consistency among the ERT images at different times and avoid the creation of artefacts in difference images. Finite-element ERT-grids adjusted to the individual topography of the five transects were constructed by Adrian Flores-Orozco (Fig. 52). All datasets were inverted in CRTomo (Kemna, 2000) using the obtained individual error model parameters (Section 6.4).

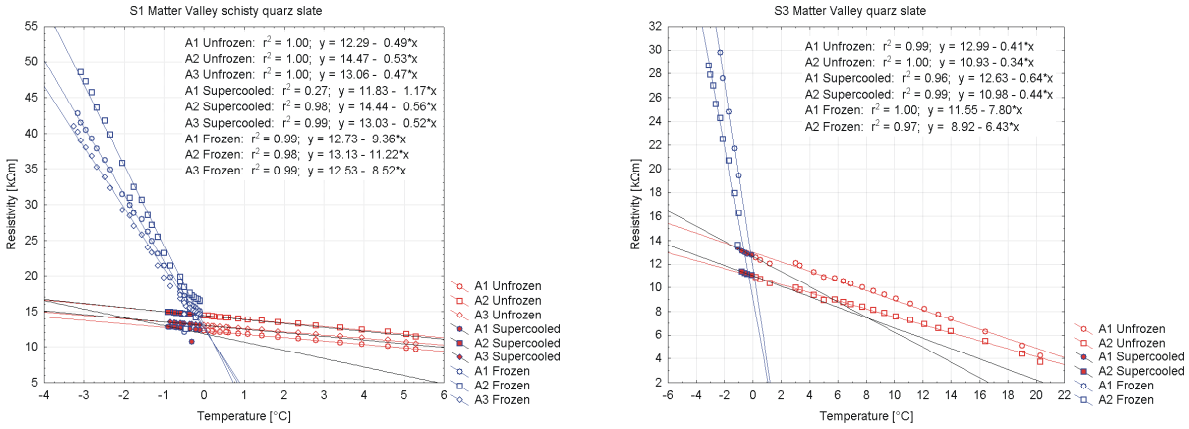

Fig. 53: Laboratory results of two rock specimen sampled inside the 3D ERT array.

Laboratory treatment of the samples is described in Section 6.1. The rock mass inside the array is homogeneous and only ranges from quartz slate with a more gneissic appearance (S3) to quartz slate with a more schisty appearance (S1). Rock specimen from the study site Steintaelli indicate 0 °C values ranging from 10.9 to 14.5 kΩm and freeze at 14-16 kΩm (Fig. 53). In tomographies, resistivities above $10^{4.2}$ Ωm (15.8 kΩm) indicate frozen rock, while those between $10^{4.2}$ Ωm and $10^{4.05}$ Ωm (11.2 kΩm) indicate the freezing transition of rock close to 0 °C. The T-ρ gradient of frozen rock approaches values of 8.7 ±1.3 kΩm/°C. Thus, values above 10^5 Ωm would indicate temperatures below –10 °C which are improbable in summer measurements. According to laboratory measurements, these values rather indicate ice intercalations (e.g. segregation ice) and values above 10^6 Ωm stand for the presence of massive ice in crevices.

Fig. 54: Air temperature and temperature in 10 cm rock depth in different aspects measured in the Steintaelli (NW, S and E: 3150 m a.s.l., NE : 3060 m a.sl.).

Geo-Precision loggers recorded rock temperature in 10 cm rock depth at three positions close to the 3D ERT array (Fig. 51) and one close-by in Transects NE (Fig. 21) at 3060 m a.s.l.. They were positioned according to the recommendations given in Peter (2003) in respect to steepness (>60°), height above snow accumulations and other factors. Loggers were removed in autumn 2007 according to the end of the GRK437-financed schedule and reinstalled as part of the SPCC (Sensitivity of permafrost to climate change)-funded bundle project in 2008.

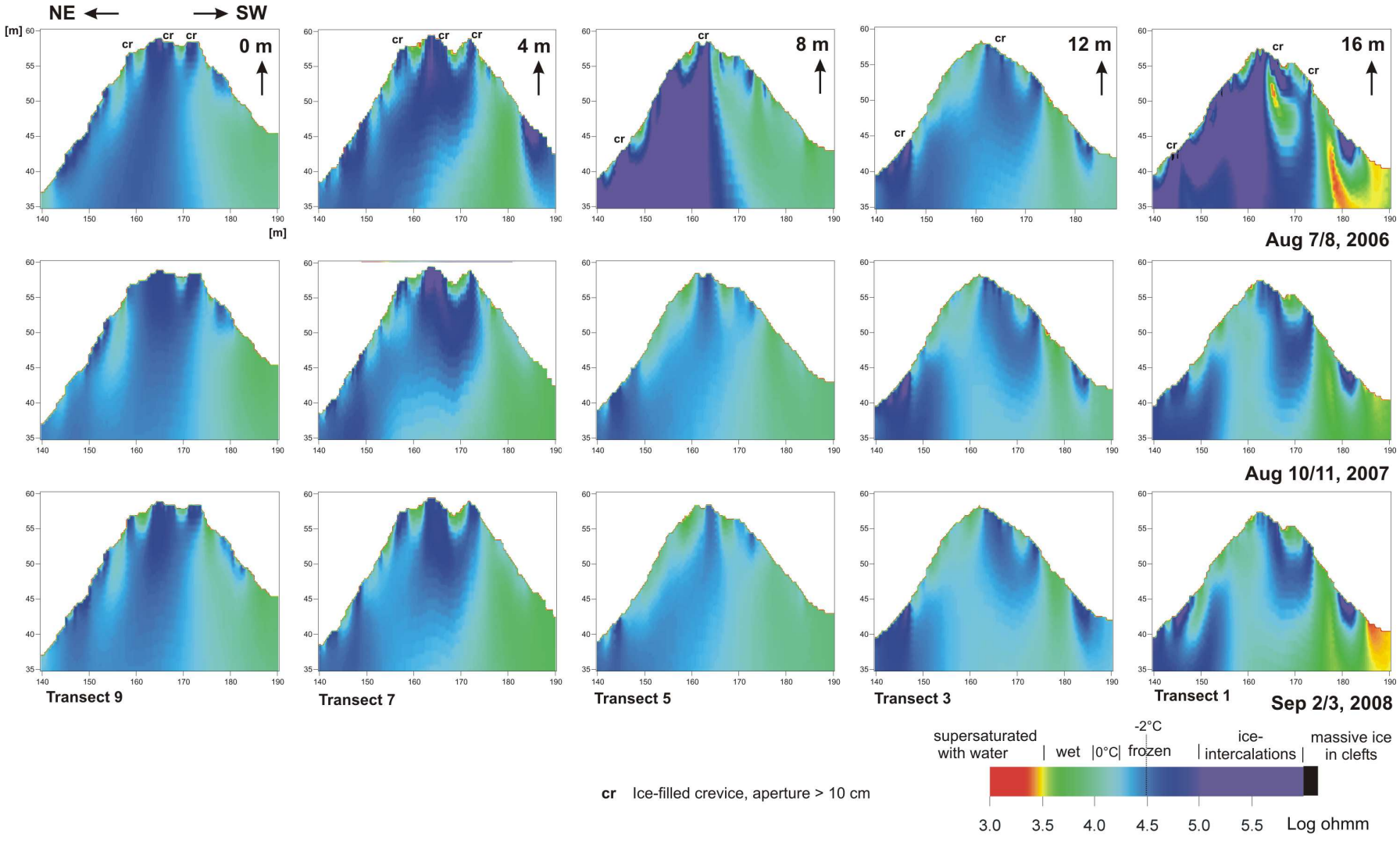
NE
SW
[m]
0 m
4 m
8 m
12 m
16 m
cr
[m]
Aug 7/8, 2006
Aug 10/11, 2007
Sep 2/3, 2008
Transect 9
Transect 7
Transect 5
Transect 3
Transect 1
cr Ice-filled crevice, aperture > 10 cm
supersaturated with water
wet
0°C
-2°C
frozen
ice-intercalations
massive ice in clefts
3.0
3.5
4.0
4.5
5.0
5.5
Log ohmm

Fig. 55: Five parallel, vertical ERT-sections cutting through the NE-SW facing Steintaelli crestline recorded in 2006, 2007 and 2008 (for crevices see Fig. 56).

The offset between the vertical transects is 4 m.

According to rock temperature logger data, winter 2005/2006 is 4 – 5 °C colder than winter 2006/2007. In 2006 massive ice in rock crevasses was detected in Transect 1 with resistivities close to 10^6 Ωm. The surface ice disappeared in the following years. Resistivities above 10^5 Ωm (ice-intercalated rock) appear to extend several meters deep below ice-filled cleft systems in Transects 1 and 5 in 2006, but also disappear the following years. Frozen rock ($10^{4.2}$ – $10^{4.5}$ Ωm) dominates the northern half of all transects and extends under the crestline, especially close to ice-filled clefts up to the surface. Except Transects 1 and 5 in 2006, values exceed the $10^{4.5}$ Ωm line (equivalent to –2°C) only near the surface or close to ice-filled clefts. Small isolated frozen rock bodies with a few meters diameter are indicated on the SW-exposed side. Those at steep and overhanging positions in Transects 1 and 3 (180 m, see Fig. 51) persist from 2005 to 2007, while those in less inclined parts (Transect 7, 180-190, see Fig. 51) melt out. Resistivities in the range of freezing/melting rock of $10^{4.05}$ – $10^{4.2}$ Ωm occur widespread around frozen bodies. Unfrozen rock ($10^{3.5}$ – 10^4 Ωm) dominates the southern half of the transects. An up to 5 m thick continuous active layer is developed on the NE-exposed rock face but thaw is much deeper in small elongated structures. Water-supersaturated conditions occur superficially above ice-filled clefts but are more obvious in the lower southern limb of Transect 1.

6.5.4 Discussion

Results were reassessed in terms of data quality. Normal-reciprocal error measurements in September 2008 showed that the accuracy of *b*, which determines the reliability of high resistance raw data, ranges between 8-9 %, so quantitative interpretation should not rely on changes smaller than this value. Raw data of all transects was checked in respect to contact resistances. This is especially interesting for the 2006 measurements in Transect 1 and 5 with high resistivities. Both measurements indicate good coupling of all 41 electrodes, error of consecutive measurements is 0.7 % and 1.9 % and resistances measured did not exceed 14 kΩ and 6 kΩ, which is well in the reliable range of the ABEM SAS 300C device according to our laboratory measurements. This shows that absolute differences recorded in the subsequent measurements refer to changes in rock mass resistivity and not to changes in electrode coupling.

The application of an empirical error–controlled inversion with CRTomo in a topography-adjusted finite-element grid shows very consistent results for all transects and time steps. Apart from Transect 1 and 5, which indicate the presence of massive ice in 2006, all transects show smooth and gradual changes at depth apart from cleft systems which is probably a good quality control in a system that is determined by slow heat transmission. However, significant changes in active layer depth are apparent in subsequent transects and are concentrated along clefts systems that indicate massive ice intercalations in 2006, which is also consistent with heat transmission theory.

Major improvements of the ERT interpretation could derive from both, a better laboratory calibration of the electrical effect of free (segregation) ice in clefts as well as massive crevices in rock samples and a better implementation of anisotropy in the inversion. Laboratory experiments could follow the idea of Jouniaux et al. (2006) who observed changes in electrical properties during stress-induced crack formation in unfrozen rocks. In addition, more thought has to be spent on the question of how laboratory results can be upscaled to a decameter field scale (Singha and Gorelick, 2006). Tensorial non-conductivity of ice-filled joints of unknown orientation may cause series disconnection or parallel disconnection and thus influence directional resistivity in a yet not exactly determined way (Herwanger et al., 2004; Matias, 2008).

The measurement provides several outcomes for permafrost research: (i) The Steintaelli was deliberately chosen as an environment that is at the fringe of present permafrost distribution. According to Gruber et al. (2004a), a mean annual ground surface temperature (MAGST) between 0 °C and –2 °C is assumed for a 70° steep and NE-exposed rock slope at 3150 m a.s.l., on the basis of climatic data from the last 21 years. In view of the 20th century warming, a 1 °C warming of MAGST or a 150 m uplift of the 0 °C line is expected to better approach the present situation (Gruber et al., 2004a; Haeberli and Beniston, 1998). Thus the Steintaelli is expected to develop towards a transient temperature state, where only some years have a MAGST below 0 °C. Our data suggests that all NE-exposed transects still have decametre large permafrost bodies inside, but the $10^{4.5}$ Ωm (31.6 kΩm) line which represents a definite transition to the 2 °C range is not reached in any of the transects apart from ice-filled clefts or at the surface. According to Gruber (2004a) the SW exposed side at 3150 m a.s.l. should be free of permafrost with a MAGST ranging from 2 to 4 °C. This is in accordance with ERT measurements that show mostly unfrozen rock on the SW exposed rock slopes.

(ii) The importance of ice-filled rock crevices as highly-efficient semiconductors is strongly underestimated. The positions where massive ice in rock crevices is exposed at the surface can be detected in the 2006 time section in all transects and are especially obvious in Transect 1 and 5 (Fig. 56 F). These two transects show that ERT is not only sensitive to rock temperature. Ice intercalations result in highly anisotropic conductivities which are well detectable in the ER tomographies. All other ER tomographies show that ice-filled rock crevices efficiently chill their surroundings. This may be caused by a number of factors. Ice is a good thermal conductor (k = 2.2 W/(m*K)) and it only conducts cold thermal impulses. Those above 0 °C are buffered by its latent heat capacity. Conduction of cold thermal impulses in ice persists much longer during the year, as it is not necessary to freeze an active layer, which can take months, before cold thermal impulses can be transferred to greater depths. In some cases ice in crevasses is effectively coupled to the atmosphere due to direct exposure or contact to firn ice or wind-compacted snow. However, it is unclear to what extend the dominant thermal impact of the main crevice derives from the contact to the cornice (Fig. 56D) and its sheltering or simply to the dimensions from the crevice itself.

Fig. 56: Ice-filled rock crevices and topographic factors that influence the distribution of frozen rock in the 3D-ERT array.

A, Heavily thawed ice-filled rock crevice cutting across Transect 7 (in the front) and Transect 9 (behind) at 156 m on September 3, 2008. Black arrays point at electrodes. B, Ice-filled rock crevice frozen up to the surface at Transect 1 (171 m) in August 10, 2006. C, Main ice-filled crevice cutting across Transects 1 to 9 at 161 to 164 m. Mention that the crevice is split in two parts at the lower part of the picture (Transect 1 and 3), then merges into one strongly pronounced crevice where Mr. Moser stands (Transect 5) and extends to a broader highly-dissected zone (Transects 7 and 9) (September 2005). Same position in August 5, 2006 with a ca. 5 m wide and 3 m high cornice that persists usually at least half of the summer. E, Ice-filled crevasse in Transect 1 at 145 m (September 2008). F, Heavily dissected NE-exposed rock face in Transect 5 (155 m) that is susceptible to ice intercalations and intense chilling in 2006, as well as enhanced thawing in 2006 and 2007. G, Steep, north-exposed, shielded and partly overhanging section in Transect 9 (152-154 m) that is persistently frozen even near the surface.

Fig. 57: Disintegrated rock material on the SW-exposed slope of Transect 1 and 3 (180 m) that overlies a small permafrost lens with few meters diameter.

(iii) Small-scale topography such as vertical sections or overhangs in combination with totally dissected coarse blocky material (Gruber and Haeberli, 2007) appear to be capable of creating small permafrost lenses even on the SW-exposed rock slopes (Fig. 57). This is observable on Transect 1 and 3 at 180 m.

(iv) According to Gruber et al. (2004a) thawing depth on the NE-face is expected to range between 6-7 m and the warm summer of 2003 would have caused an increase of the thaw depth of 0.4-0.5 m. ERT sections show that it is difficult to define a mean thaw depth. The NE-slope of Transect 5 is the only that displays a 25 m long continuous section with a thaw depth of 3-4 m.

(v) Maximum thaw in the NE-slopes of Transects 1, 3, 7 and 9 occurs along elongated vertical recesses. These appear on ER tomographies as 5-10 m deep (Transect 9) and 2-3 m wide anomalies of unfrozen rock with resistivities ranging from $10^{3.5}$-$10^{4.2}$ Ωm. The dip of the elongated thawing anomalies can be vertical or steeply inclined (220°/70°). Their elongated shape, their orientation parallel to ice-filled fracture systems and their thermal separation from the rock surface indicate, that they are rather formed by seepage of cleft water than by thermal heat conduction from the rock surface.

(vi) All Transects show higher resistivity values and a larger extension of the frozen body in 2006. Mean annual air temperature of July 2006 was 7 °C, 3 °C warmer than prior years (Fig. 32). Thus, this signal must still result from winter 2005/2006 which was 4-5 °C colder than the following winter according to rock temperature logger data (Fig. 54). Especially Transects 1 and 5 indicate a widespread occurrence of ice-intercalated rock (>10^5 Ωm). In this case, the extension of high-resistivities at greater depths (>10 m) is not well detectable with our ERT-measurements. However, good evidence is provided that such ice-intercalations existed in the upper 5 m. This corresponds to the observation of ice-filled crevices that were frozen up to the surface at the beginning of August 2006 (Fig. 56B). ER tomographies in 2007 show a widespread contraction and warming of the frozen rock body. Permafrost occurrences appear to have degraded only marginally between 2007 and 2008.

The question to whether 2.5D collation of close-by parallel slices to a 3D tomography is a useful technique for permafrost rocks depends strongly on the research question (Fig. 72). 2.5D ERT plots can effectively show that permafrost is strongly dependent on aspect in all tomographies. However, the presented plots show that even with a close 4 m (1:2) spacing of individual sections, 2D information in a highly-dissected rock mass is two heterogeneous for a meaningful interpolation between transects.

6.5.5 Conclusion

In 2006, a 3D-ERT array was installed across a NE-SW exposed crestline at 3150 m a.s.l. in the Steintaelli, Valley of Zermatt, Switzerland. The 3D array consists of 5 parallel 41-electrode arrays with midpoints on the crestline. To cope with the heterogeneity of dissected rock, an internal electrode spacing of 2 m was applied and the offset between the five arrays was 4 m. Electrode positions were aligned with a laser tachymeter and the x, y and z information was used to create a decimetre-resolution DEM. Topographic information was accommodated in five parallel smoothed finite-element grids. The 3D-array was measured repeatedly in 2006, 2007 and 2008. Error levels inherent in different transects were defined by normal-reciprocal error measurements and yielded a relative error of 8-9 % for high resistances. To yield quantitatively reliable ER tomographies, resistivity data was processed in an error-controlled, smoothness-constrained inversion routine in topography-adjusted grids. Temperature-resistivity behaviour of two rock samples was measured in the laboratory. Three loggers recorded rock temperatures in 10 cm depth.

ER tomographies show consistent results for all transects. Decametre large frozen rock bodies (>$10^{4.2}$ Ωm) dominate NE-exposed slopes. Permafrost at depth ranges between $10^{4.2}$ and $10^{4.5}$ Ωm, which refers to frozen rock between –0.1 °C and –2 °C, and is surrounded by a large zone in the range of $10^{4.0}$-$10^{4.2}$ Ωm indicating freezing or melting round –0.1 °C. The presence of ice-filled crevices on the crestline and the NE-face appears to have a crucial influence on spatial and temporal permafrost development. Next to 3-4 m deep melting from the surface, elongated recesses of unfrozen rock indicate melting by cleft water up to 10 m depth. Isolated permafrost bodies of a few meters size can persist under steep fragmented rock even on the SW-exposed rock slope. ER tomographies in August 2006, after the cool winter 2005/2006, indicate the presence of massive ice-intercalations in two transects, while those of 2007 and 2008 indicate gradual widespread permafrost degradation. These results show the first approach to measure 3D ERT in alpine permafrost rocks.

7 Implications for rock instability

Fig. 58: Rockfall accumulation on the Rothorn-NE glacieret in the Steintaelli subsequent to the warm July 2006 (Photo August 5, 2006).

Rock wall instability in permafrost rocks is usually observed by means of rockfall occurrence. While most rock instability in steep rock faces culminates in rockfall, the rockfall itself provides only poor information on the mechanical situation that has prepared its detachment. Statistical analysis of temporal and spatial occurrence is a key approach to the understanding of rockfalls, but the understanding of processes that dispose, detach and trigger rockfalls is equally important. While geophysical sounding in rock walls with highly active rockfall regime is impossible, the 3D-ERT array in the Steintaelli provides insight into active rock deformation and sliding processes that could play a key role in the preparation of meter to decametre-thick rockslides.

7.1 Slow rock deformation in permafrost

7.1.1 Introduction

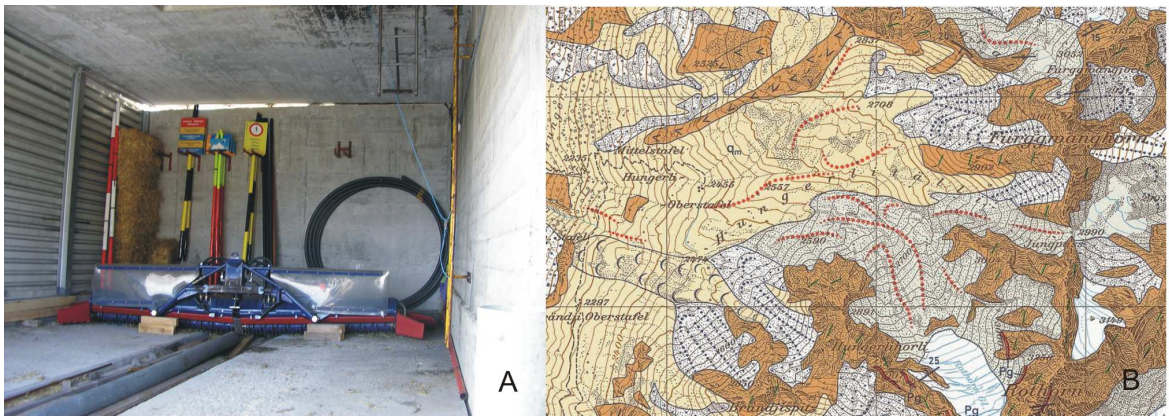

Fig. 59: A, Deformation of the Gemsstock (Andermatt, CH) summit cable car station by recent rock creep in thawing permafrost rocks. B, Widespread rock creep („sackung“) mapped in the geological map close to the Steintaelli in the same geological unit (Bearth, 1980).

The map is orientated north, grid indicates 1 km spacing. “V”- and scarp signatures indicate the extend of rock creep north of the Hungerlitaelli, brown indicates two – mica gneisses and schists. The Steintaelli is situated around the “3149 m” point at the lower right corner.

While rock falls from permafrost-affected bedrock have recently received increased attention, slow rock deformation is still a poorly addressed phenomenon. However, the latter causes significant damage to structures built and founded on permafrost rocks and may cause more reconstruction efforts than rockfalls (Fig. 59). Moreover, slow rock deformation processes often prepare rockfalls especially if they occur in positions with exposed topography (Hewitt et al., 2008). The term slow rock deformation includes a variety of rock mechanical concepts and geomorphologic implications. The term slow refers to Varnes (1978) and indicates movement rates below 1.5 m/a. Exact classification of the type of movement is difficult. Slow rock deformations could be described as (i) rock creep as this is basically defined by its slow velocity, (ii) some will be covered by the term “slow rock slide” as the movement occurs predominantly on relatively thin zones of intense shear strain (Varnes, 1978) and some could also be termed “lateral spreads” or “sackung” as the movement propagates as a distributed lateral extension in a fractured mass (Hansen, 1984).

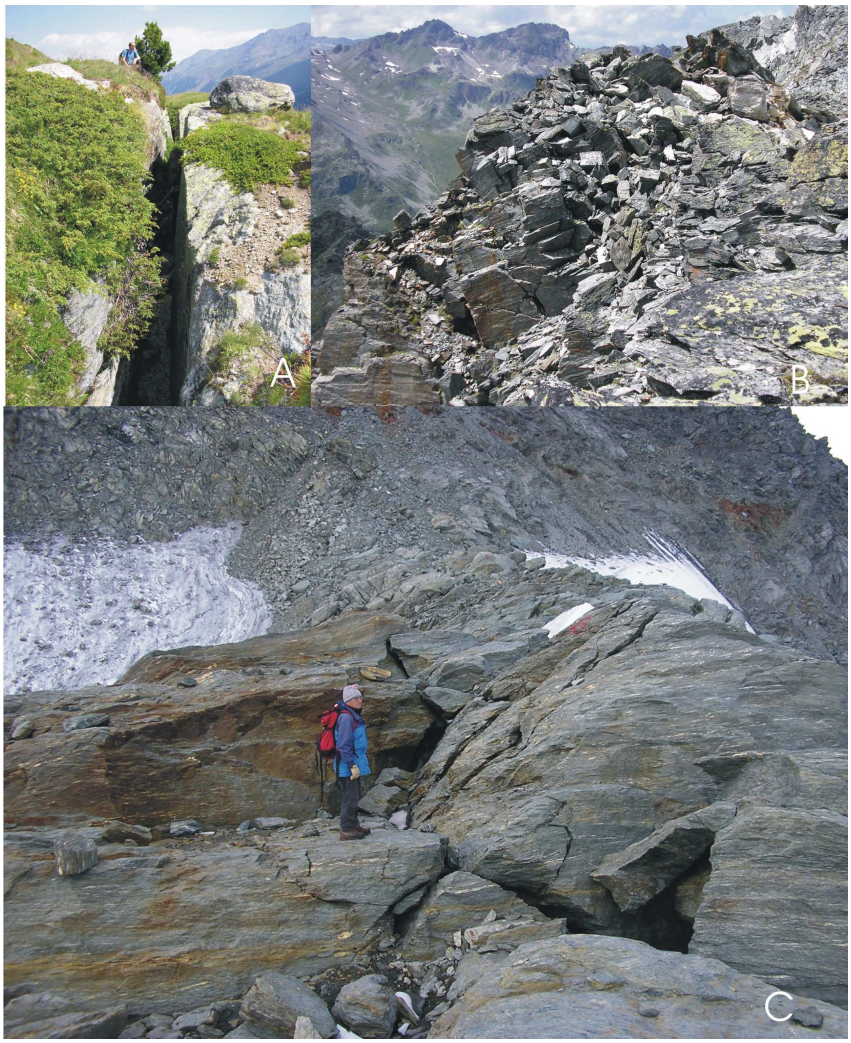

Fig. 60: Indications of rock creep at different altitudes with the same underlying lithology (two – mica paragneisses and schists).

A, Inactive rock crevasse at 2230 m a.s.l. at the "Alb Blueomatt". B, Probably recently active "sackung" behaviour at the Hungerlitaelli/Braenditaelli crest line at 2940 m a.s.l.. C, Highly active "sackung" behaviour in the Steintälli at 3150 m a.s.l..

Indications of "sackung" behaviour such as rock crevices and in situ disintegrated rock block assemblages occur frequently in the Turtmann-Valley (Valais, Switzerland) and were mapped by Bearth (1980) and by Otto and Dikau (2004). However, there is no full inventory of active and relic sackung behaviour. It appears that these phenomena are concentrated on three different levels. (i) Relic sackung phenomena without any indications of recent activity occur at the through shoulder at 2200 m to 2300 m a.s.l. (Fig. 60A). (ii) In the geological map, sackung phenomena were frequently mapped between 2400 and 2900 m a.s.l. and some have indications of more or less recent activity such as disrupted or compressed vegetation (Fig. 60B). (iii) Presently active sackung phenomena in combination with frequent release of small boulders falls occur mainly above 2900 m a.s.l. according to our observations from 2005 to 2008 (Fig. 60C). To test the present activity of "sackung" behaviour in the Steintaelli, several extensometer transects were installed.

7.1.2 Methods

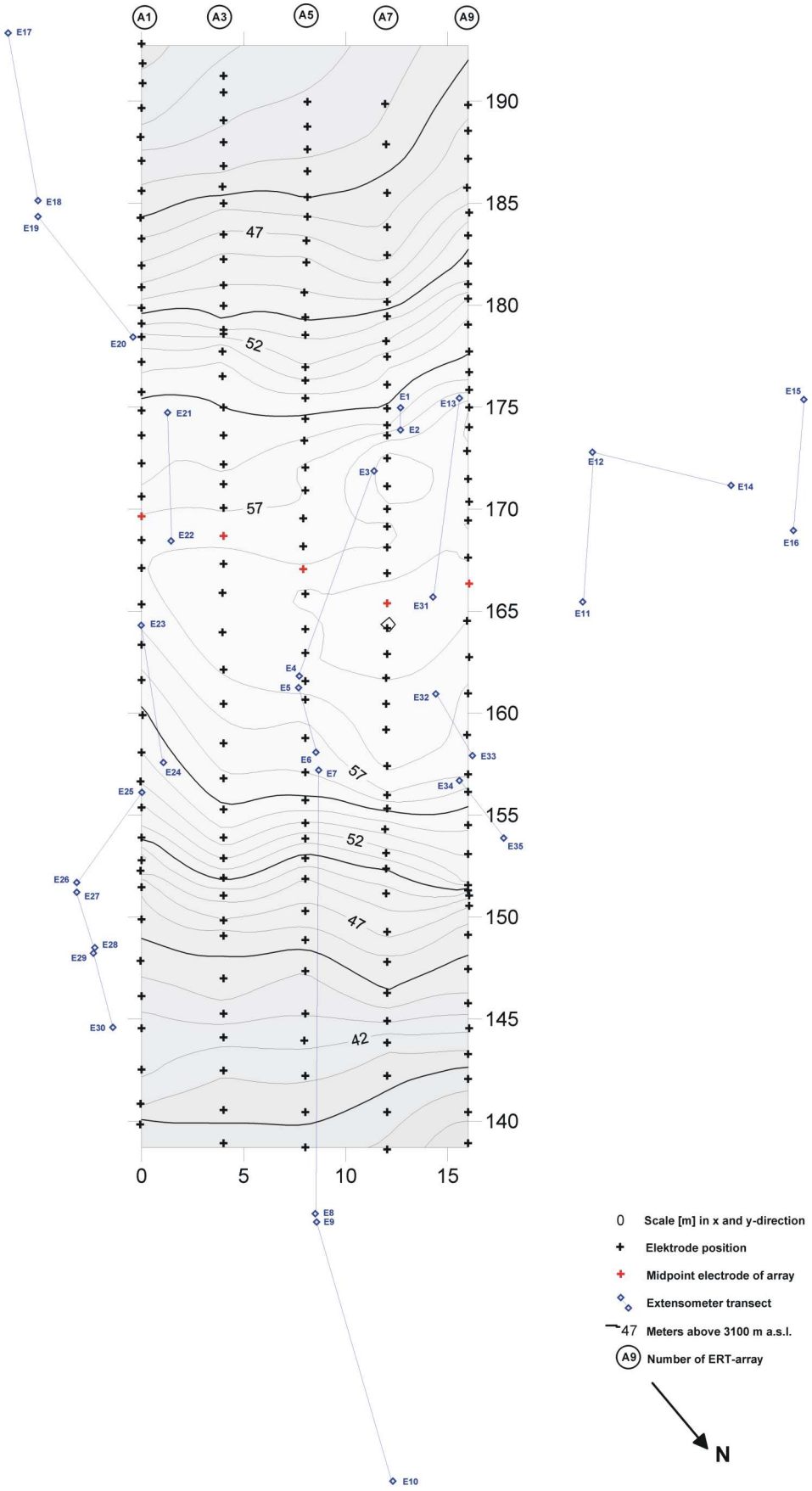

Fig. 61: Position of extensometer transects relative to the 3D ERT grid.

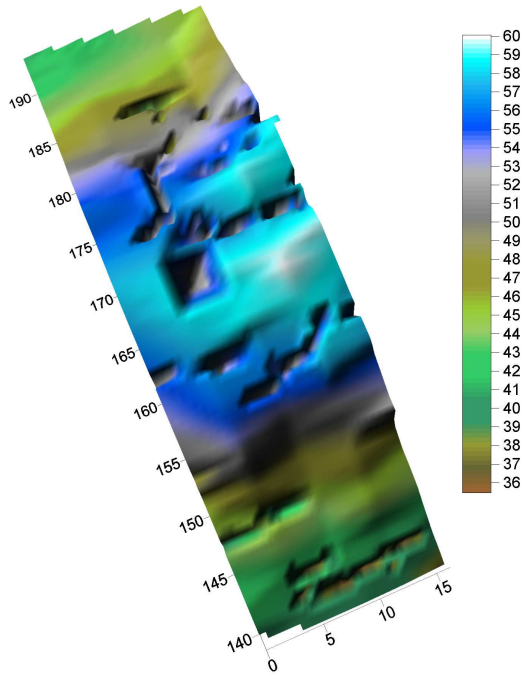

Fig. 62: Major crevices (>1 m depth) in the 3D-ERT grid.

Mapping of crevices by D. Oertel. The scale indicates altitude in m above 3100 m a.s.l..

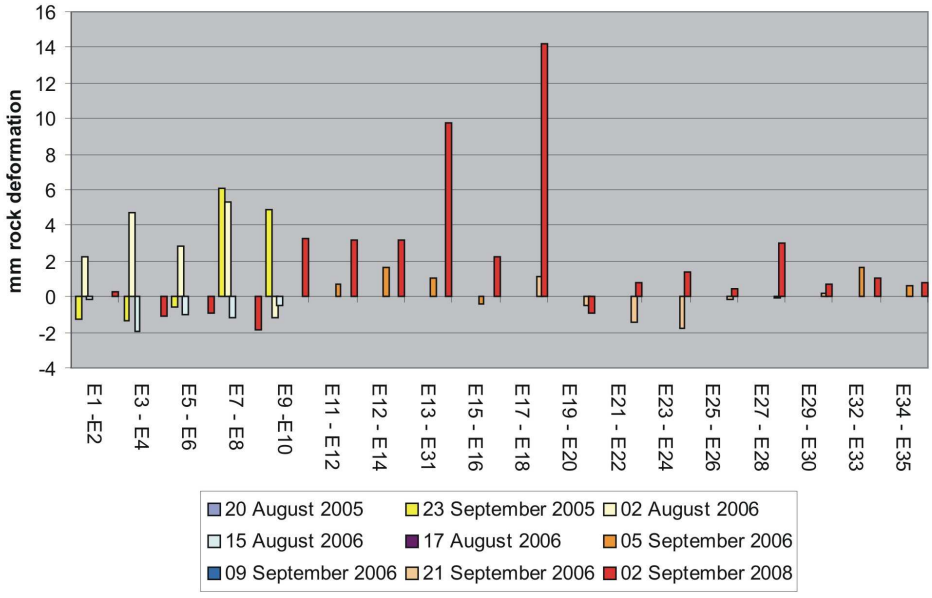

Fig. 63: Measured rock deformation in nine reference measurements along 18 transects from 2005 to 2008.

Columns are arranged according to their (horizontal) order in the caption. Mention that extension in most transects exceeds the accuracy of the steel extensometer of 0.05 mm by far. Figure displays only the reference measurements that were conducted with exactly identical tension and were calibrated to ambient temperature.

Five extensometer transects were installed in August 2005 and another 13 in August/September 2006 (with support from S. Wolf). Transects were measured with a manual steel tape extensometer with a nominal accuracy of 0.05 mm. Temperature was measured alongside and measurements were corrected for temperature-related extension. Topography of the observed rock bar and the extensometer transects was measured with a Leica TCA 1800 tachymetre. Positions of extensometer tracks are given in Fig. 61. Photos were taken to control field data. Additional measurements were taken by diploma candidate D. Oertel with a slightly higher, but defined tension in August 11 and 19, 2007 as well as September 11, 2009 that could result in an inaccuracy of maximum 0.2 mm according to test measurements. The latter measurements were excluded in Fig. 63.

7.1.3 Results

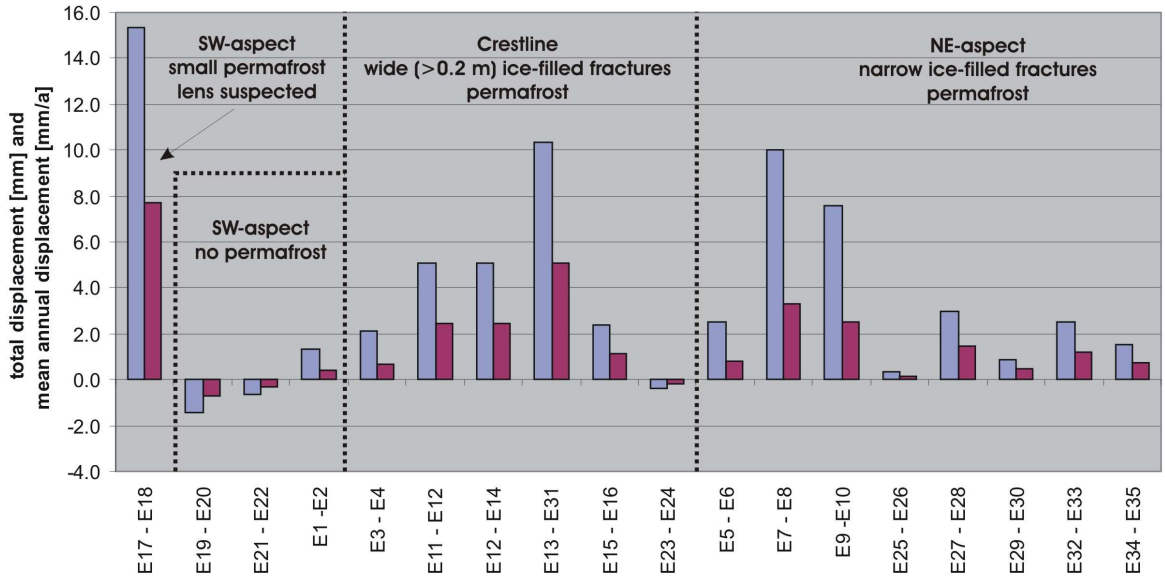

Fig. 64: Absolute total displacements (blue) and annual displacements (red) of all extensometer transects in respect to their position (Fig. 61) and permafrost occurrence (Fig. 55).

Mean annual displacements of extensometer transects in permafrost-affected bedrock approach values of 2.0 ±1.3 mm/a at the crestline and 1.3 ±0.8mm/a at the steep NE-facing slope (Fig. 64). Transects on SW-exposed rock slopes without permafrost indicate movements of 0.5 ±0.1 mm/a. Transect E17 – E 18 extends 7.7 mm/a.

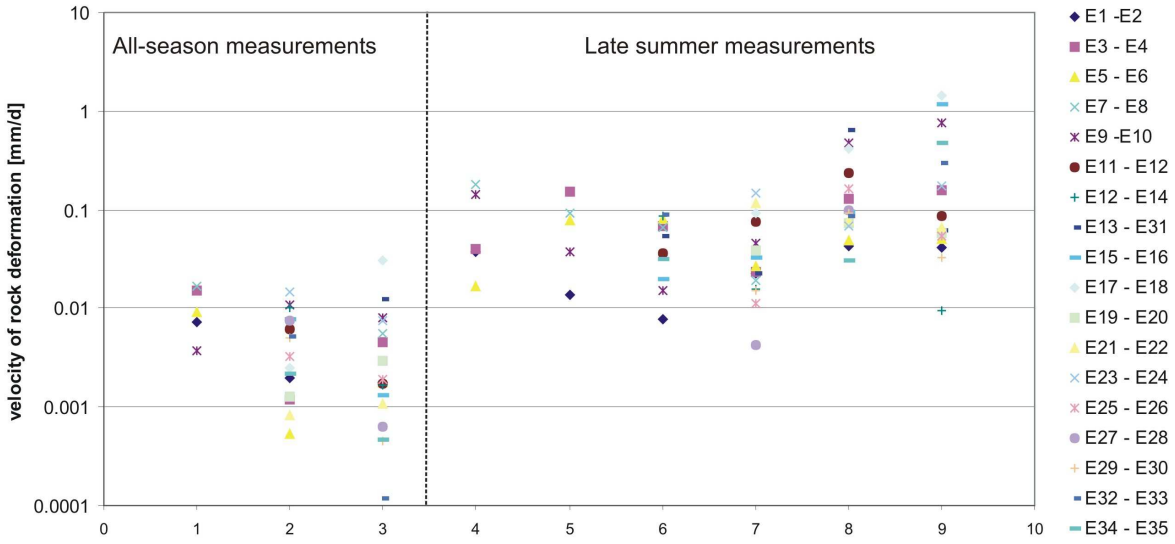

Fig. 65: Absolute velocities of rock deformation in all-year measurements (1-3) and late summer measurements (4-9).

***1**, Sep 24 to Aug 02, 2006; **2**, Sep 22, 2006 to Aug 11, 2007; **3**, Aug 20, 2007 to Sep 02, 2008; **4**, Aug 20 to Sep 23, 2005; **5**, Aug 02 to Aug 15, 2006; **6**, Aug 16 to Sep 05, 2006; **7**, Sep 06 to Sep 21, 2006; **8**, Aug 12 to Aug 19, 2008; **9**, Sep 3 to Sep 11, 2008.*

The absolute speed of rock deformation in late summer (0.121 ±0.077 mm/d) is approximately 20 times higher than in all-season measurements (0.007 ±0.002 mm/d). As can be seen in Fig. 65, velocities in all measurement campaigns in late summer (0.045-0.307 mm/d) exceed all-season measurements (0.005-0.01 mm/d) by at least five times.

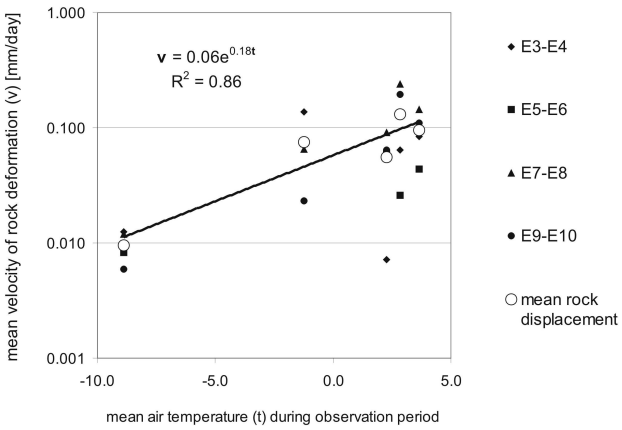

Fig. 66: The relation of mean rock displacement and mean air temperature of transects with direct permafrost evidence from ERT measurements from 2005 to 2006 (Fig. 55, Transect 5).

Fig. 66 shows the velocity of four transects whose permafrost foundation is directly allocated by ER tomographies. E3 to E8 are covered by Array 5 in Fig. 55, permafrost occurrence from E9-E10 is known from the 2D-Transect E (Section 6.2). Data display a ten-fold increase in late summer displacement velocity recorded in 2005 and 2006. No significant differences are observable for different summer temperatures, but it appears that there must be a distinct threshold for the onset of movements close to the melting point.

7.1.4 Discussion

Extensometer data plotted in Fig. 63 shows rock displacements in the range of millimetres for most transects. Applying steel extensometers with a nominal accuracy of 0.05 mm is an appropriate method for the detection of the velocity field of rock deformation.

Rock displacements reach higher values in the permafrost-affected crest line and the north face with annual rates of displacement that exceed displacements in the SW-exposed slope (0.5 mm/a) by 3 to 4 times (Fig. 64). Only one extensometer records displacements in a probably perennially frozen body at the SW-facing slope. Transect E17-E18 runs across a dissected overhanging structure similar to those that cause small permafrost lenses at 180-185 m in Transect 1 and 3 (Fig. 55). Perennially frozen bodies on the SW-facing slope (Fig. 55) are highly susceptible to warming and thus probably very close to 0 °C, but more displacement data and ERT measurements directly along Transect E17-E18 are necessary to provide further evidence. It is interesting to consider, that the spatial arrangement of deep rock crevices shown in Fig. 62 matches with the information on rock deformation. Most crevices occur on the crest line and on the NE slope where the speed of deformation is highest. The only occurrence of crevices on the south slope is at position 185 m where permafrost and transitorily frozen rock is indicated in several transects and at the same slope position where maximum creep is recorded in Transect E17-E18. Thus, the geomorphologic situation on the slope appears to reflect present deformation processes.

Late summer rock deformation occurs 20 times faster than all-season rock deformation. This provides good evidence that ice and thaw related processes play a vital role in rock instability (Fig. 65). Movements along Transects E3 to E10, for which permafrost evidence is provided by ERT directly along the transects, can readily be explained with an r^2 of 0.86 using an exponential function based on mean air temperature (Fig. 66).

Several lines of evidence exist for the factors that determine rock instability in the Steintaelli. (i) Deep-reaching crevices observed at the surface (Fig. 62) and in ER tomographies (Fig. 55) point towards a movement that occurs in dissected, meters to decametres large rock blocks. (ii) The speed of displacement is too high for rock-internal creep or thermal expansion. Therefore, a sliding process is most likely the major source of rock deformation. (iii) Spatial distribution of the velocity field shows that permafrost is necessary for high displacement rates while seasonal frost is much less effective (Fig. 64).

While it is common knowledge that many installations founded on permafrost rocks shows signs of creep deformation, few quantitative data on rock creep in permafrost has been published yet. The idea of active and relic rock deformation phenomena in relation to periglacial conditions was described in a few case studies. Norton and Redden (1960) and Mears (1997) describe indications of flexural rock creep in the upper 1.5 to 3 m and

more in gneiss, schists and sedimentary rocks in South Dakota and Wyoming that is presently inactive. Wegmann (1998) reported low seasonal strain rates from the Jungfrau and Eiger (Switzerland) that followed seasonal temperature fluctuations even in rock below 0 °C but did not cause significant rock instability. Certainly, rock deformation data exists from many cable car installations in the Alps but data is confidential information and not publicly available. It appears, that there is presently no other published dataset on the kinematic behaviour of active rock block sliding in Alpine rock permafrost slopes and very few articles have covered this topic.

7.1.5 Conclusion

Altogether 18 extensometer transects were installed in 2005 and 2006 on a NE/SW facing crestline in the Steintaelli (Matter Valley, Switzerland). The transects were measured repeatedly with a 0.05 mm accuracy steel extensometer from 2005 to 2008 and displacements up to 14 mm were recorded in single measurements. Data on permafrost distribution derive from a 3D-ERT array (Section 6.5). Transects across perennially frozen crevices at the crestline (2.0 ±1.3 mm/a) and on the permafrost affected NE-slopes (1.3 ±0.8 mm/a) dilate three to four times faster than transects in non-permafrost positions on the SW-slope (0.5 ±0.1 mm/a). The speed of deformation in late summer measurements is 20 times higher than in all-season measurements. Zones of maximum deformation are reflected by the occurrence of deep ice-filled crevices. Rock deformation above permafrost can be explained with an R^2 of 0.86 as an exponential response to mean air temperature during the observed period. According to the short response time, the observed velocities up to mm per month, a survey of ice-filled crevices and 3D-ERT information on the extend of crevices, we assume a sliding mechanism that is strongly controlled by rapidly fluctuating ice temperatures with effects on cohesion and frictional properties of ice in rock fractures.

7.2 Rockfalls

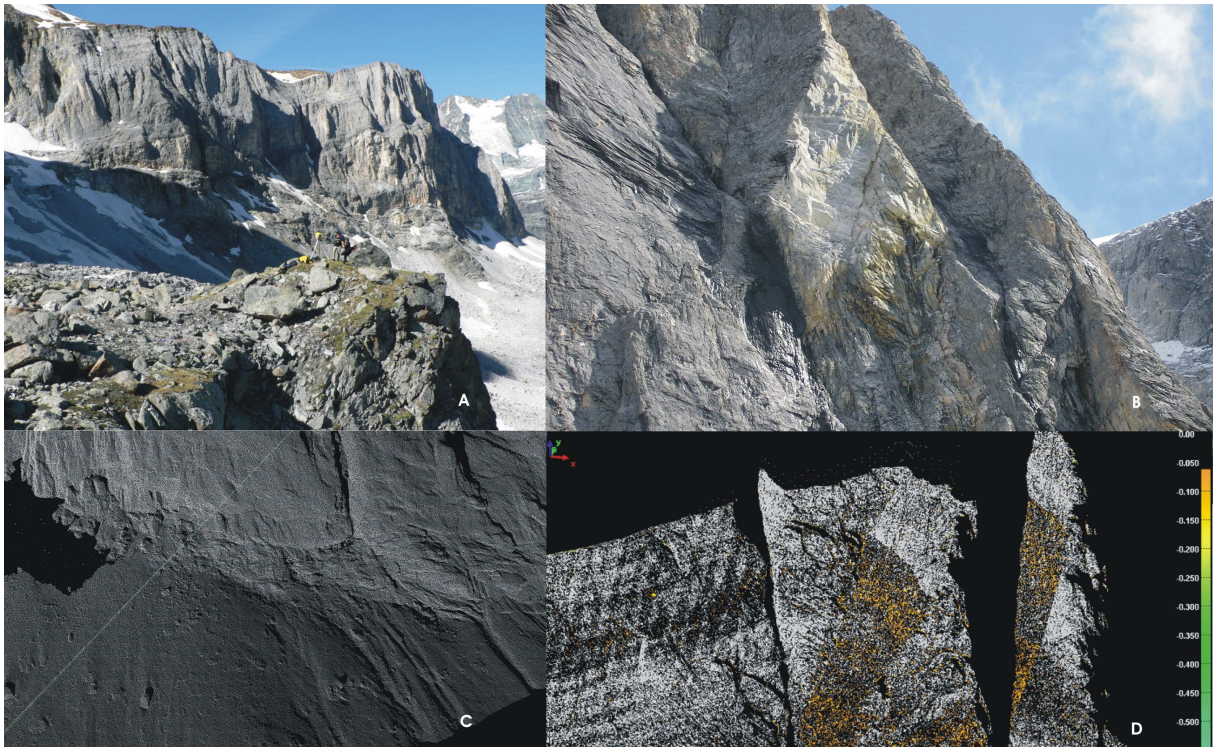

Fig. 67: Laserscanning of the Barrhorn/Barrwang North Faces (Turtmanntal, Valais, Switzerland).

A, Laserscanning of the Barrwang Rock Face with an Optech Lasercsanner in July 2006; B, 60 m high rockfall scarp of a rockfall that probably occurred in 2003. C, Example of 6 cm resolution xyz-data of the rockwall apex and the scree slope below, showing that both, detachment and deposition can be monitored accurately. D, differential plot of the scarp shown in B (from a different angle of sight) shows rockwall retreat between July and September 2006 (2 cm resolution scan). Debris fall activity with up to 10 cm rockwall retreat is shown in orange; larger rock falls (yellow/green) were not observed.

Originally, laserscanning was thought to contribute significantly to the understanding of magnitude and frequency of rockfalls in this thesis but unstable weather and poor visibility in late summer 2006 and 2007 made recurrent laserscanning impossible. Laserscanning was conducted in July 2006 in different aspects at gneiss rock faces in the Steintaelli (3050-3200 m a.s.l.) and in the adjacent Pipji hanging valley at the north-facing Barrhorn and Barrwang marble rock walls (2800-3400 m a.s.l.). While repeated scanning of the whole Barrhorn and Barrwang North face with 3-6 cm resolution was possible in September 2006, no recurrent laserscanning could be conducted in the Steintaelli due to bad weather conditions in autumn 2006. Preliminary analysis of laserscanning data with support from P. Deline and S. Jaillet at EDYTEM (Bourget du Lac, France) showed that no rockfalls larger than 10 cm, which is close to the resolution limit, had occurred at the Barrhorn and the Barrwang marble rock faces between July and September 2006. Therefore, no analysis of rockfall laserscanning data will be included here.

7.3 Geophysical detection of rock mass instability

Source: Krautblatter (2008). Rock Permafrost Geophysics and its Explanatory Power for Permafrost-Induced Rockfalls and Rock Creep: a Perspective. Paper presented at the 9th Int. Conf. on Permafrost, Fairbanks, Alaska, US: 999-1004.

7.3.1 Introduction

Degrading permafrost in rock walls is hazardous, partly due to the amount of potential energy that is released in case of instabilities (Harris et al., 2001). In 2002, the Dzhimarai-khokh rock/ice avalanche (Russian Caucasus) detached approximately 4 million m³ from a 1 km wide starting zone and caused more than 140 casualties (Haeberli, 2005; Kääb et al., 2003). Even smaller permafrost rockfalls, such as the 2003 Matterhorn rockfall, are considered as major hazards in densely populated high mountain areas (Gruber et al., 2004a). Inventories show that the frequency of these rockfalls has considerably increased in the warm 1990s and was boosted by the hot summer of 2003 (Schoeneich et al., 2004). Moreover, slow rock creep in permafrost rocks causes significant damage especially to tourist infrastructure in high mountain areas.

Besides temperature logger data, borehole information and rock temperature modeling approaches, the geophysical applications described here provide a new tool for the spatial and temporal analysis of rock permafrost. In some cases, information on the thermal state of permafrost reveals sizeable information for stability consideration (Davies et al., 2001), but changing hydrological properties of ice such as water content may also play a vital part in decreasing resistive forces of ice-contained rock masses (Gruber and Haeberli, 2007). This paper combines a review of existing geophysical techniques that are applicable in permafrost rocks and a perspective how these can contribute to the understanding of mass movements in permafrost-affected bedrock in future. It will address three questions:

(i) What geophysical methods can be applied in permafrost rocks? (ii) What properties do they detect? (iii) What is their explanatory power for permafrost-induced mass movements?

7.3.2 Investigation sites

Methods described in this article were tested at three investigation sites: the “Steintälli” a N-S exposed crestline (Matter-/Turtmann Valleys, Switzerland) at about 3070-3150 m a.s.l. with slaty paragneiss (see Fig. 1); the North Face of the Zugspitze limestone summit (Wetterstein Mountains, Germany/Austria) at about 2800 m a.s.l. and the gneissic Gemsstock crestline (Switzerland) at 2900 m a.s.l. in collaboration with Marcia Phillips. Fig. 1 shows a typical arrangement of a 2D-ERT in steep permafrost-affected bedrock. More detailed site characteristics can be sourced from Krautblatter and Hauck (2007) and Gude and Barsch (2005). Problems associated with the comparison of different field sites and extrapolation of results are discussed in Krautblatter & Dikau (Krautblatter and Dikau, 2007).

Fig. 68: Electrical resistivity measurement along Transect South at the Matter-/Turtmann Valleys crestline, 3150 m a.s.l., Switzerland.

41 large steel screws serve as electrodes along each transect.

7.3.3 Geophysical methods for rock permafrost and detectable properties

Surface-based geophysical methods represent a cost-effective approach to permafrost mapping and characterisation (Harris et al., 2001). Hauck (2001) provided a systematic comparison of different geophysical methods for monitoring permafrost in high-mountain environments. However, the application of geophysical methods to permafrost rock walls just began in 2005 (Krautblatter and Hauck, 2007). This section will give a quick overview of methods that have successfully been applied to permafrost rocks in the last three years. Data used for Figures 2, 6 and 8 was previously published in Krautblatter & Hauck (2007) and are described there in detail.

7.3.3.1 Electrical resistivity tomography (ERT)

ERT is a key method in permafrost research as freezing and thawing of most materials are associated with a resistivity change that spans one order of magnitude, which is, in turn, easily detectable. The first approach to derive spatial information from rock faces by ERT was applied by Sass (2003). In subsequent studies, he provided further evidence that ERT measurements are capable of measuring the degree of rock moisture (Sass, 2005a) and temporal and spatial variations of freeze and thaw limits (Sass, 2004) in rock faces. These ERT measurements were confined to the monitoring of the upper weathering crust (centimeter- to decimeter-scale) of non-permafrost rock faces. Krautblatter and Hauck (2007) extended this method to a decameter-scale and applied it to the investigation of active-layer processes in permafrost-affected rock walls.

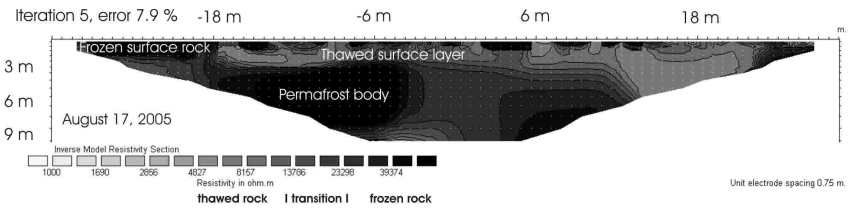

Fig. 69: ERT in an east-facing rock wall recorded at August 17, 2005 at the Matter-/Turtmann Valleys crestline, 3130 m a.s.l. Switzerland)

Arrays with centimeter-long steel screws as electrodes were drilled into solid rock (see Fig. 68) and were measured repeatedly with high voltages (mostly 10^2 -10^3 V) to improve the signal to noise ratio. A detailed survey of hardware and software adaptations and a systematic discussion of error sources is provided by Krautblatter and Hauck (2007). Errors associated with different ERT-arrays were assessed alongside with the impact of topography and other geometric error sources (Krautblatter and Verleysdonk, 2008a). The Res2DInv software was chosen as it is capable of topographic correction and "real" time-lapse inversion of subsequent measurements. To cope with high resistivity gradients, inversions models with mesh size smaller than the electrode distance and robust inversion routines provide better results. Resistivity values that correspond to the transition between frozen and thawed rock were measured repeatedly at the rock surface along different arrays and yielded evidence that the transition occurs between 13 and 20 kΩm for the gneissic rocks at the Steintälli (Krautblatter and Hauck, 2007) and are in the same range as those established for carbonate rocks at the Zugspitze by Sass (2004) and own measurements (Krautblatter and Verleysdonk, 2008b). Fig. 69 shows an ERT that was measured close to Fig. 1 at an east-facing part of the rock crestline between Matter- and Turtmann Valleys. It shows a 3 m thick thawed surface layer of rock above a constantly frozen permafrost layer; a plunge in temperature following the 14th of August is evident due to frozen rock close to the surface in all parts of the transect. Resistivity-temperature patterns of rock samples of all field sites are currently tested in a freezing chamber in the laboratory.

The relation between measured resistivity and rock temperature is straightforward. For temperatures below the freezing point, resistivity (p) depends mainly on unfrozen water content until most of the pore water is frozen. In Alpine environments resistivity can be calculated based on a reference value p_o as an exponential response to the temperature below the freezing point (T_f) according to McGinnis et al. (1973):

$$\rho = \rho_0 e^{b(T_f - T)}$$

Equ. 7.1

The factor *b* in Equation (1) determines the rate of resistivity increase and can be derived empirically (Hauck, 2001; Hauck, 2002). Short-term changes in resistivity can be attributed to changes in pore water content and temperature, while changes in porosity and water chemistry can be neglected over daily to monthly measurement intervals in low-porosity rocks. Due to the exponential response of resistivity to temperatures below 0 °C, freeze-thaw transitions correspond to an increase in resistivity by one order of magnitude and are thus, a very sensitive method for detecting the state of rock permafrost close to 0 °C. On the other hand, deeply frozen bedrock (below –5 °C) along the measured transects causes problems for the electrode contact.

7.3.3.2 Refraction Seismic Tomography (RST)

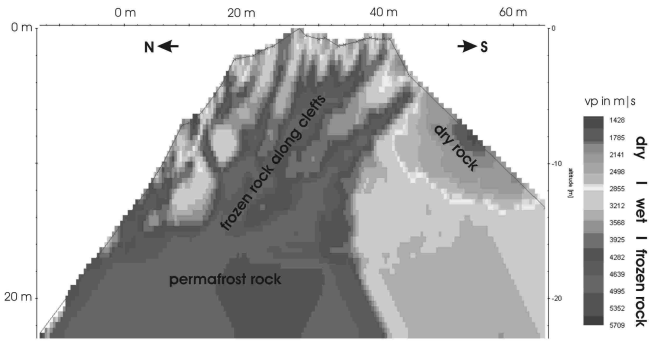

Fig. 70: RST- North-south transect 9 (September 20, 2006), measured at the Matter-/Turtmann Valleys crestline, 3150 m a.s.l..

The application of refraction seismics in permafrost studies is based on the interpretation of refracted headwaves that indicate the transition of a slower unfrozen top layer to a frozen layer with faster P-wave propagation below. Recent approaches apply tomographic inversion schemes (Otto and Sass, 2006) often based on high-resolution data sets (Maurer and Hauck, 2007; Musil et al., 2002). Seismics are also applied to determine 2D and 3D rock mass properties and potential instabilities (Heincke et al., 2006b). Preliminary results from Krautblatter et al. (2007) indicate that refraction seismics are applicable for permafrost detection in solid rock walls, even if they provide less depth information than ERT measurements. On the other hand, it appears that they resolve small-scale features such as ice-filled clefts in more detail. For instance, Fig. 70 shows a cross-cut through the E-W trending Steintälli crestline at Transect 9. Thoroughly frozen rock aligns along ice-filled discontinuities indicating the good thermal conduction (k = 2.2 W/(m*K)) without latent buffers in the readily frozen ice in clefts.

In practice, P-Waves were stimulated with a 5 kg sledgehammer. Per transect, 24 drilled geophone positions in bedrock and 40 marked and fixed shot positions were arranged in line with the ERT transects so that RST and ERT were measured simultaneously (Krautblatter and Hauck, 2007). A direct comparison of ERT and RST showed that frozen high-resistivity rocks in the ERT typically have P-wave velocities significantly above 4000 m/s (see section below) while wet and dry rock masses indicate a significantly slower propagation. As P-wave velocities of frozen and thawed rock differ only by a few hundred m/s in velocity it is important to define the geometry of shot and recording position exactly, which was done using a high-resolution tachymeter. High P-wave velocities in rock necessitate high temporal resolution of geophone signals. Surface waves are not decelerated by a soft surface layer such as soil and thus often disturb signals recorded by geophones close to the shot position. We applied REFLEXW, Version 4.5 by Sandmeier Scientific Software, with model settings, such as initial P-wave velocity assumption, adjusted to bedrock conditions.

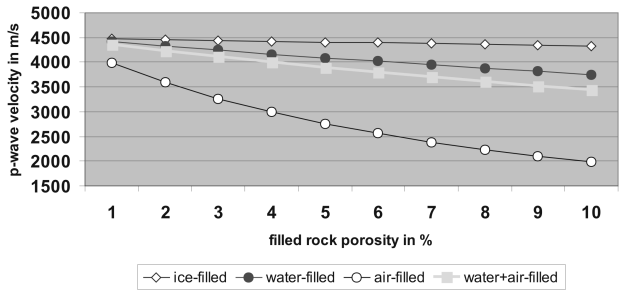

Fig. 71: Estimation of P-wave velocities of rock with different porosity and pore content.

Air-, water- and ice-filled pores in rock lead to significantly different attenuation of P-wave-velocities. This is especially true for air-filled porosity. Fig. 71 shows theoretical P-wave velocity for different pore-fillings and rock porosities derived from mixing laws. However, it appeared in simultaneous ERT and RST measurements that carefully conducted RST can resolve the difference between water and ice-filled rock even in low-porosity (2-3 %) bedrock, and that velocity differences are larger than expected from mixing laws for certain rock porosities. This could be due to the fact that melting in low-permeability rocks leads to a small gas content in pores to compensate the ice-water volume reduction or that the seismic velocities provide a more integral signal that includes ice in discontinuities in the rock mass.

7.3.3.3 The third dimension: 3D ERT and RST

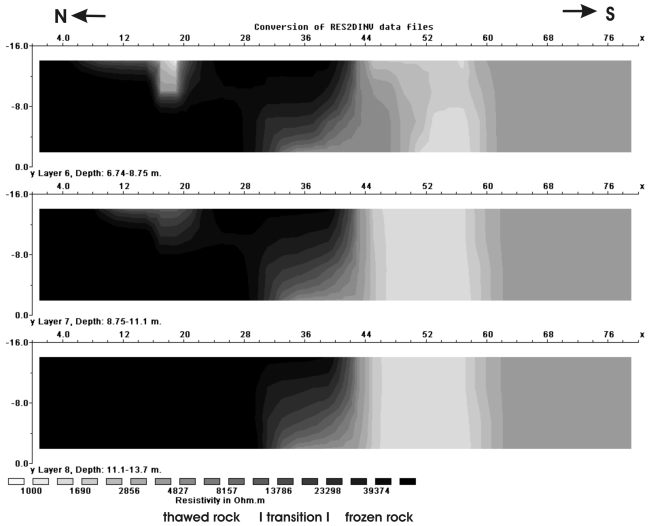

Fig. 72: 3D-ERT cross sections at three different depths cutting the Turtmann-/Matter Valley crestline N-S. Measured with ca. 1000 datum points from ca. 200 electrodes at September 5-9, 2006.

ERT and RST can be conducted in 3D. Fig. 72 shows three horizontal sections cut at depths of 7-9 m, 9-11 m and 11-14 m with N-S orientation that indicate a sharp divide between frozen rock to the north and thawed rock to the south at meter 44. Problems that arise when conducting three-dimensional geophysics in permafrost rocks, are time-consuming measurements (ca. one week of uninterrupted measurements), the necessity of highly-

precise topographic information and the required high resolution due to the enormous resistivity/seismic velocity gradients present in permafrost rock systems. Moreover, traditional 3D arrays (e.g. Pole-Pole or Dipol-Dipol ERT) result in bad signal to noise ratios (Krautblatter and Verleysdonk, 2008a) and electrode/geophone spacing and arrays must be adjusted to local conditions. Therefore, the first 3D ERT and 3D RST array in permafrost rocks, that was conducted in 2006, relied on a very close (2 m) arrangement of geophones (120), electrodes (205) and shot positions (200) (Fig. 72) (Krautblatter and Hauck, 2007) and is based on Wenner-arrays that yield much better signal to noise ratios than Pole or Dipole-type arrays.

7.3.3.4 The fourth dimension: Time-lapse ERT

The installation of permanent electrodes and modeling of subsequent resistivity data sets within the same inversion routine (so-called time-lapse inversion) allows for a direct assessment of spatial and temporal permafrost variability (Hauck, 2002; Hauck and Vonder Mühll, 2003). Fig. 73 shows the freezing of the previously thawed surface rock up to 3m depth following a plunge in temperature after the 14th of August 2005. While time-lapse routines for ERT are already in place, time-lapse routines for RST are still more difficult to perform.

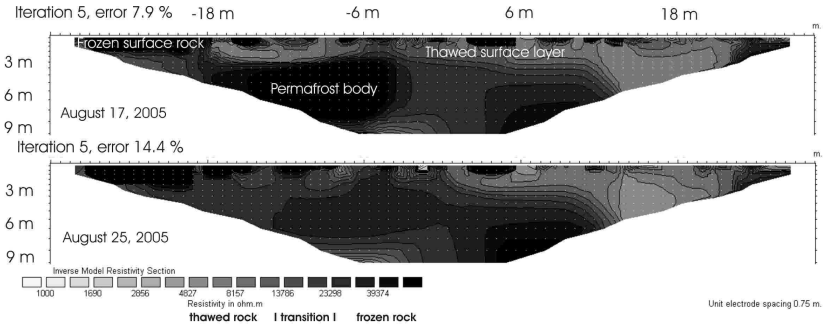

Fig. 73: Freezing of surface rock from August 17 (top) to August 25, 2005 (bottom) due to a severe drop in air temperature recorded at the Steintälli E-transect (3130 m a.s.l., Matter-/Turtmann Valleys, Switzerland)

Time-lapse inversion of subsequent measurements provides insights into short-term and long-term freeze-thaw thermal regimes (Krautblatter and Hauck, 2007), response times (Krautblatter and Verleysdonk, 2008b), changes in hydrological rock conductivity and permafrost aggradation and degradation. Moreover, changes in subsequent time sections can definitely be attributed to changes in rock moisture or the state of freezing, while changes in geological properties can be ruled out for short-timescales.

Table 6: Geophysically detectable properties of permafrost rocks

ERT	Space-referenced integral tomography of frozen and thawed rock and hydrological conductivity at all measured depths Temperature estimation (0 °C to -5 °C) in combination with laboratory measurements (McGinnis)
RST	Space-referenced integral tomography of air-, water and ice filled rock porosity. Exact positions of the uppermost freezing/thawing front and dominant air-, water and ice-filled rock discontinuities
3D-measurements	3D spatial information on the freezing/melting front, hydraulic conductivity and the persistence/ importance of discontinuity zones
Time-lapse inversions	Development of heat fluxes, the permafrost system (aggradation/degradation), and the hydraulic system over time

7.3.4 Explanatory power for permafrost-induced mass movements

We define permafrost-induced mass movements as those, whose kinematical behavior is at least partly influenced by ice mechanics and permafrost hydrology. The most common types are rockfalls and rock block creep. These are usually explained (i) by a reduction of the resisting force e.g. shear-strength in ice-filled clefts (Davies et al., 2001; Davies et al., 2000) or (ii) an increase in the driving force e.g. hydrological pressure (Fischer et al., 2007).

7.3.4.1 Ice-filled discontinuities

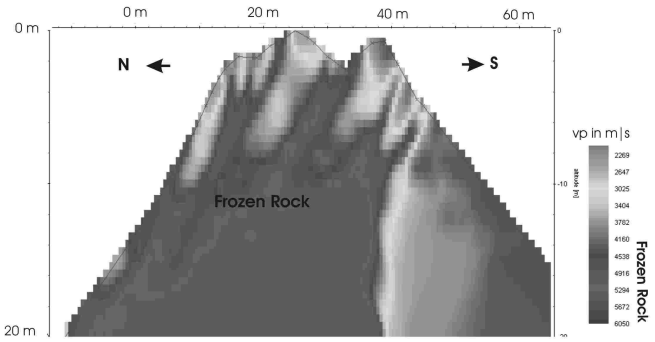

Fig. 74: RST- North-south transect 7 (August 31, 2006) of the Matter-/Turtmann Valleys crestline, 3150 m a.s.l.. Mention the disposition of the frozen discontinuity zones as possible detachment zones with daylighted bedding.

A cross-cut through the E-W trending Steintälli crestline is shown in Fig. 74. Geometrical position, orientation and persistence of ice-filled clefts in the upper 10 meters can be well detected in RST surveys. It is assumed that ice-filled discontinuities react according to stress-strain behavior of weight-loaded polycrystalline ice. The deformation of ice at constant stress is characterized by four phases: Elastic deformation (1) that is followed by

permanent deformation, firstly at a decreasing rate (2, primary creep), then at a constant rate (3, secondary creep) and finally at an increasing rate (4, tertiary creep) (Budd and Jacka, 1989). Mostly secondary creep and tertiary creep occur at speeds relevant for mass movements. The flow relation for secondary creep relates the shear strain rate ε_{xy} to the shear stress τ_{xy},

$$\varepsilon_{xy} = A\tau_{xy}^{n}$$

Equ. 7.2

where A depends mainly on ice temperature, anisotropic crystal orientation, impurity content and water content and n increases at shear stresses greater than 500 kPa (Barnes et al., 1971). Crystal orientation, impurity content and shear stresses remain more or less constant over short timescales. In contrary, ice temperature and water content in mass movement systems are subject to major annual and interannual changes. Thus, for temperatures above –10 °C, A can be approached by

$$A = A_0 \exp(-\frac{Q}{RT}) \approx A_0 \exp(-\frac{16700}{T})$$

Equ. 7.3

where A_0 is independent of temperature, R is the universal gas constant and Q is the activation energy (Weertman, 1973) and A_{0t} for tertiary creep

$$A_{0t} = (3.2 + 5.8W) * 10^{-15} (kPa)^{-3} s^{-1}$$

Equ. 7.4

can be related to the percentage water content W. It must be stressed that the water content strongly decreases with temperature. Paterson (2001) states –2 °C as the lowest temperature at which the effect of water in the ice is relevant for the stress-strain behavior.

Equ. 7.3 and Equ. 7.4 show, that both, ice temperature and water content play a dominant role for the mechanical behavior of ice-filled clefts at temperatures close to 0 °C. Assuming moderate water content of 0.6 %, the creep rate at 0 °C is three times the rate at –2 °C (Paterson, 2001), which has serious effects on displacement rates and factors of safety considerations of mass movements.

As has been shown above, ERT and refraction seismic are highly susceptible to water/ice content inside the rock system just below the freezing point. Thus, the susceptibility range of seismic velocity and resistivity (ca. -0 to –5 °C) corresponds to the most important changes in ice-mechanical properties. This means, the values temperature and water content, which are relevant for stability considerations in well-jointed permafrost rocks, are targeted by ERT and refraction seismics and combined interpretation strategies.

7.3.4.2 Hydrological pressure

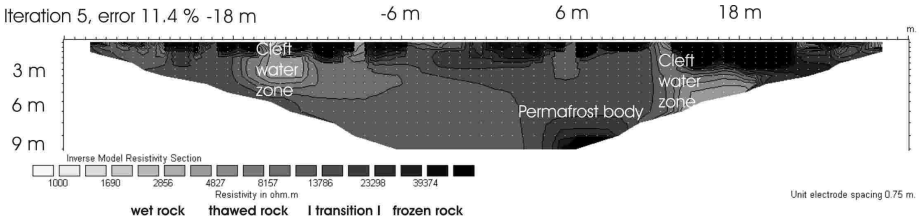

Fig. 75: ERT of Transect NE (September 13, 2005). Mention the persistently thawed deep- reaching cleft water zones.

Fig. 75 shows light-colored low-resistivity cleft water zones percolated by glacial melt water that were observed to persist over several years and to limit the spatial extension of permafrost bodies. While pressure effects only have a small effect on the stress-strain behavior of ice itself (resisting force) (Weertman, 1973), the reduction of applied normal stress and the increase in shear stress (driving force) may play a key role in preparing and triggering mass movements (Fischer et al., 2007; Terzaghi, 1962). According to Wegmann (1998), permafrost degradation and aggradation in rocks in response to altered hydraulic conductivity occurs at all depths and quickly responds to annual melting patterns. He could also show that rock deformation quickly responds to spatial changes in permafrost rock conductivity. Unfrozen cleft zones can easily be detected at the surface with RST and with ERT measurements possibly up to the maximum depth of the applied array (e.g. 80 m at the Zugspitze, 400 m Schlumberger-array). As shown in Fig. 8, resistivity in water-filled cleft zones and frozen rock typically differs by 1-2 orders of magnitude and is, thus, easily detectable even at greater depths (Krautblatter and Hauck, 2007). This opens up a whole range of new possibilities e.g. for the investigation of rock permafrost hydrology (Wegmann, 1998), glacier-permafrost interconnectivity (Moorman, 2005) and rock deformation processes that are closely linked to freeze-thaw processes by latent heat transfer in clefts (Murton et al., 2006; Wegmann, 1998).

7.3.5 Conclusion

Resistivity monitoring may provide indications on temperature changes and water saturation, while refraction seismics help to gain insight into discontinuity zones and exact geometric properties of instable bodies. Repeated time-sections reveal interannual, annual and multiannual time-patterns as well as response times, the fourth dimension of rock permafrost systems.

For permafrost-induced mass movements, with secondary and tertiary creep of ice close to 0 °C, three highly-variable forces play a key role in unbalancing resisting and driving forces. The resisting force of ice-creep in clefts, is mainly controlled by (i) temperature and (ii) water content in the ice. Due to the laws of electrolytic conductivity, resistivity values assessed by ERT react sensitively to both parameters and water content is a key control for P-wave velocity. The highly variable driving force (iii) hydrological pressure is well detectable in ERT time-sections as pore and cleft space supersaturation lead to a plunge in electrolytic resistivity. However, many other anisotropic factors distort ERT and seismic measurements and further field and laboratory experience is needed for the allocation of their influence and for the “suppression” of such noise.

8 Main findings and short discussion

As all chapters include a separate discussion, only a short recapitulatory review on the hypotheses postulated in Section 4 will be given here.

8.1 Theory

A better understanding of the instability of permafrost-affected bedrock subsequent to warming could derive from a combination of the relaxation time concept (Brunsden and Thornes, 1979) and its rock mechanical analogue, the subcritical and time-dependent brittle fracture propagation (Kemeny, 2003).

The theoretic outline showed that the *reaction time* of rockslides on *existing sliding planes* is likely to be dominated by ice-mechanical properties of the basal sliding plane. Creep rates and the stress level needed for "failure" of ice in clefts react instantaneously to warming and can be held responsible for rapid response within days to weeks. Evidence is provided by (i) the presence of ice on the sliding planes of rockfalls that detached with short reaction time in summer 2003 (e.g. Matterhorn July 17, 2003) (Gruber and Haeberli, 2007). (ii) Ice-dominated sliding processes in the Steintaelli show a peak deformation in late summer. Velocities of ice-supported sliding increase on average by a factor of 20 in comparison to all season measurements. This indicates a short reaction time in the range of weeks and the high susceptibility of ice stability to warming.

Applying the laws of *subcritical fracture propagation* (Kemeny, 2003), it appears that *relaxation time*, until a new equilibrium slope is approached, will take hundreds to thousands of years. In its time-dependent presentation, the approach by Kemeny (2003) shows sources of path-dependence of slope adaptation. The underlying processes, i.e. the reduction of total friction and critical fracture toughness due to reduced compressive strength of thawing saturated rock, react much slower to warming than the ice-mechanical properties described above. Much of the slow response is explained by a gradual reduce of the total friction which causes additional loading and slow subcritical destruction of rock bridges. Evidence comes from the 6000 year delay of large rockslides to deglaciation (Prager et al., 2008; Soldati et al., 2004). The same line of evidence is followed by the delayed response of large rockslides from permafrost-affected bedrock (Gude and Barsch, 2005; Jerz and Poschinger, 1995; Jerz, 1999; Tinner et al., 2005), but reasoning is more difficult.

Thermal and the geomorphologic understanding of "transience", while different, provide an approach to understand path-dependent behaviour where the thermal balance was upset by large rock slides or climate change.

Kohl (1999) could show that complex topographies affect transient thermal fields even at depths of several hundred meters below the surface. In accordance, Noetzli and Gruber (2008) point out that alpine rock summits such as the Matterhorn are large enough to have preserved transient thermal signals deriving from the Last Glacial Maximum. Climatic fluctuation such as the Little Ice Age as well as the Holocene or Medieval Climatic Optimum alternate faster than relaxation times of large rock slopes. While shallow rockslides may be predictable in terms of present day thermal regimes, large rockslides are not. It is worth considering, whether large rock sum-

mits have a decoupled core permafrost systems that is not explainable in terms of present day surfaces fluxes. The detachment of a 200 m thick rockslide at the Zugspitze 3700 B.P. and subsequent exposure of the scarp to the atmosphere may have caused a more significant thermal shift than millennia of warming on the prior rock surface. It is, thus, rather the rule than the exception that large rock permafrost summits inherit not reworked thermal and stability signals that may in the case of large instabilities be more important than present day thermal fluxes. Warming since the Little Ice Age and especially in the last two decades initiated a new transient regime that may incorporate unprecedented changes. In view of the geomorphologic transience theory, it is worth considering whether these might evoke unforeseen “nonlinear” changes in the thermal system such as a decameter deep reaching and rapidly advancing heat transfer by cleft water. A good example is the presently observed thawing of a tertiary karst system in the Zugspitze summit, which may open a hydraulic and heat transfer system that was probably blocked during most of the Quaternary.

8.2 Methodology

Resistivity is an accurate proxy of rock temperature.

Laboratory data has shown that temperature-resistivity paths of hard rocks are different from those established for brines and soft sediments (McGinnis et al., 1973). Stable alterations of the equilibrium freezing point, metastable supercooling effects, pore wall attraction and the effects of confinement create a different physical system setting for freezing behaviour. Separate linear functions for unfrozen, supercooled and frozen temperature-resistivity paths describe accurately the change in electrical properties. The supposition by Seguin (1978) that ERT may substitute temperature measurements where these are difficult to conduct, can be confirmed for frozen rocks, where temperature gradients of 1 °C are higher than the distortion due to internal variability of the rock sample.

ERT can monitor changes in active layer thickness as well as multiannual permafrost aggradation and degradation accurately in a two-dimensional and three-dimensional space.

Several arguments support the applicability of ERT in permafrost rocks: (i) Repeated measurements with the same electrodes deliver identical results with an accuracy level much better than 1 %. (ii) Normal-reciprocal error level measurements yield error levels of approximately 7-9 % for high resistances in all measurements. (iii) Observed conditions (surface freezing, warm periods, ice-filled crevasses, cleft water outflow, snow overburden and overhang positions) are matched by ER tomographies in their spatial and the temporal dimension. (iv) Resistivity values measured in the field for the freezing transition of Steintaelli gneiss (Krautblatter and Hauck, 2007) could later be confirmed by laboratory experiments. (v) 3D ERT transects subsequent to the cold winter of 2005/2006 indicate much higher resistivities than those of later years. Multiannual measurements deliver resembling freezing patterns with larger change confined to the surface and gradual changes in deeper layers.

Measurement of active layer depths is a straightforward application of ERT as the electric field expands in a relatively homogeneous half space above the frozen body. Allocation of unfrozen bodies below a frozen layer poses a greater challenge and requires careful analysis of raw data, uncertainty propagation and depth of investigation (Alumbaugh and Newman, 2000; Oldenburg and Li, 1999). However, the usual application of ERT in

permafrost rocks is to monitor the active layer depth or the increase or decrease of the resistivity of the frozen rock body below, which has shown to produce consistent results in two and three-dimensional applications.

Quantitative interpretation of temperature and ice-content is possible.

Applying temperature calibrated data from Zugspitze rock samples to field measurements yielded a temperature range from –3.5 °C to –0.5 °C for the central permafrost body which is consistent with core permafrost temperatures observed in the borehole nearby. Only in February and May lower temperatures are indicated close to the rock surface which is in accordance with borehole data. Differential plots of temperature data of subsequent months show temperature alterations (apart from one cleft wit observed water flow) that diminish away from the rock face. The permafrost body contracts away from the rock face in summer and readvances as soon as air temperatures below 0 °C occur in September. ERT generally corresponds with temperature logger data from the Zugspitze borehole but underestimates winter temperatures possibly due to the effects of ice-filled fractures.

8.3 System understanding

Ice- and water-filled discontinuities have a dominant influence on permafrost development in fractured rocks. Hydraulic interconnectivity of dissected rock may prevent effective cooling of decametre large rock walls. Ice in rock factures can dominate permafrost development in dissected rock.

It has been shown in Section 6.3, that percolation of cleftwater from two dominant fracture systems can prevent cooling of a 40 m long rock section. The data may provide an interesting insight for modelling as virtually no data exists on (i) the dimension of cleftwater systems in permafrost rocks, (ii) the extend to which fluid temperature transport away from the main cleft is effective and (iii) to the potency of such systems to react to changing hydraulic and thermal conditions.

All 3D-arrays (Fig 55) show that the presence of ice-filled fractures has an overwhelming importance for heat propagation in dissected rock. After the cool winter of 2005/2006, ice content was significantly higher close to the surface which could result from enhanced ice segregation. Next to the aspect of the slope, ice-filled fractures appear to have a dominant influence on the state of freezing along the crestline. Bedrock next to the fractures is perennially frozen up to the surface and indicates the highest observed resistivities in the range of –2 °C and below. While the cooling influence of the perfect semiconductor “frozen fracture” has been pinpointed before (Haeberli, et al. 2000: Lecture Notes in Peter, 2003), ERT provides detailed insights into importance, dimensions, temporal variability and resilience of frozen fractures.

Local topography can create limited permafrost bodies in all aspects

It appears that not only ice-filled fractures but also fractures that allow the circulation of air in winter (Hanson and Hoelzle, 2004) can create significant thermal anomalies in steep positions. Such effects occur in several of the 3D ERT transects on a SW exposed slope that is, otherwise, not perennially frozen. This effect appears to be sensitive to air temperatures in winter as it occurs more wide-spread subsequent to winter 2006 than after winter 2007.

ER tomographies operate at the scale of permafrost rock instability and help to gain insight into the principles of rock destabilisation.

All extensometer transects with elevated velocities were situated above or adjacent to permafrost positions indicated in the 3D ERT sections. Rock deformations above permafrost were on average three to four times faster and all extreme rates of several mm/month were found in permafrost affected bedrock. Moreover, ER tomographies display position and depths of discontinuities, approximate sliding depths and the degree of disintegration, which are essential inputs for rock stability modelling.

9 Outlook

There are many ways to proceed with this topic. As has been shown, geophysical soundings can directly provide meaningful input data for thermal, hydraulic, mechanic and slope geomorphology applications and it must be the aim of future work to establish reliable interfaces. While only ERT was included in this thesis, other techniques such as refraction seismics and IP were successfully applied in the meantime to permafrost rocks and provide complementary input e.g. for critical fracture toughness (seismics) and joint infillings (IP). The observed slow rock deformations challenge our rock- and ice-mechanical understanding and full instrumentation at the Steintaelli and at the Zugspitze in 2009 in combination with laboratory work on stability and rethinking will hopefully provide further insights into the processes and dimensions of ice-supported rock sliding. While this thesis operated on a laboratory scale and a decametre field scale, it might be possible to modify geophysical techniques for the use on a mountain scale. As has been shown in the conceptional part, the questions that arise on this scale in terms of path-dependence and transient thermal/stability configuration may be among the most important questions in future mountain permafrost research. “If we use the chance that the geomorphic experiment by global change probably presents to us, it seems that periglacial geomorphology has a great future ahead (Barsch, 1993).”

Acknowledgements:

I owe thanks to Michael Moser, Dave Petley and Heather Viles who engaged my interest for geomorphology and slope instability, to Richard Dikau who supported and inspired my work at all stages, to Oliver Sass for mentoring my work on rockfall and ERT, to Christian Hauck who made ERT in the Steintaelli possible and offered steady personal support, to Wilfried Haeberli for friendly support, to the Bonn crew (Thomas H., Jan, Jutta, Michael N., Ole, Herwig, Rainer B., Thomas P.) for mental and scientific support, to the hard-working “Permafrost rocks”-crew (Sarah and also Pauline, Daniel F., Daniel D., Basti W.) for rendering every assistance, to Matthias S. for the self-designed freezing laboratory and the climbing work, to the geophysics/petrophysics crew (Andreas Kemna, Adrian and Norbert) for the great collaboration, to the permafrost people from Zürich and Chambéry (Philip, Stephan, Christian H., Ludovic, Jeannette, Andi, Luzia) for all kinds of assistance, to Julian Murton for helpful reviews, to all who ascended 1200 m in the morning to help me with the exhausting work in the Steintaelli (Olaf K., Levke F., Michele R., Chris & Wossi, Stefan-Daniel H., Frank L., Jan B., Katharina B., Winfried S., Milla V., Dennis Ö.) and to the Berckum family (Oberems United) for all kinds of hospitality.

Abbreviations

Equ.:	Equation
Fig.:	Figure
ERT	Electrical resistivity tomography
IPCC	Intergovernmental Panel for Climate Change
DEM	Digital elevation model
MAGST	Mean annual ground surface temperature
MAAT	Mean annual surface temperature
MART	Mean annual rock temperature
ρ	Resistivivty
T	Temperature
a	annum (year)
SPCC	research bundle “Sensitivity of Permafrost to Climate Change”
m	metre
2D	two-dimensional
3D	three-dimensional
cal. B.P.	calibrated (years) before present
ka	1000 years

SI-units are used in accordance with their established abbreviations.

Index of Tables

Index of Figures

Bibliography

Abele, G., 1972. Kinematik und Morphologie spät- und postglazialer Bergstürze in den Alpen. Z. Geomorph. N.F., Suppl.-Bd. 14: 138-149.

AEG, 1931. Die bayerische Zugspitzbahn. AEG-Mitteilungen. AEG, Berlin.

Ahnert, F., 1970. Functional relationships between denudation, relief and uplift in large mid-latitude drainage basins. Am. J. Sci., 268: 243-263.

Ahnert, F., 1994. Equilibrium, Scale and Inheritance in Geomorphology. Geomorphology, 11(2): 125-140.

Alba-Simionesco, C., Coasne, B., Dosseh, G., Dudziak, G., Gubbins, K.E., Radhakrishan, R. and Sliwinska-Bartkowiak, M., 2006. Effects of confinement on freezing an melting. J. Phys.: Condens. Matter, 18: 15-68.

Alumbaugh, D.L. and Newman, G.A., 2000. Image appraisal for 2-D and 3-D electromagnetic inversion. Geophysics, 65(5): 1455-1467.

Archie, G.E., 1942. The electric resistivity log as an aid in determining some reservoir characteristics. Trans. AIME, 146: 54-62.

Arenson, L., 2003. Unstable Alpine Permafrost: A Potentially Important Natural Hazard - Variations of Geotechnical Behavior with Time and Temperature. Ph.D. Thesis, ETH Zurich, Zurich.

Arenson, L.U., Hoelzle, M. and Springman, S.M., 2002. Borehole deformation measurements and internal structure of some rock glaciers in Switzerland. Permafrost and Periglac. Process., 13(2): 117-135.

Arenson, L.U., Johansen, M.M. and Springman, S.M., 2004. Effects of volumetric ice content and strain rate on shear strength under triaxial conditions for frozen soil samples. Permafrost and Periglac. Process., 15(3): 261-271.

Arenson, L.U. and Springman, S.M., 2005a. Mathematical description for the behaviour of ice-rich frozen soils at temperatures close to zero centigrade. Canadian Geotechnical Journal, 42(2): 431-442.

Arenson, L.U. and Springman, S.M., 2005b. Triaxial constant stress and constant strain rate tests on ice-rich permafrost samples. Canadian Geotechnical Journal, 42(2): 412-430.

Atkinson, B.K., 1984. Subcritical Crack-Growth in Geological-Materials. Journal of Geophysical Research, 89(NB6): 4077-4114.

Augustinus, P.C., 1992. The Influence on Rock Mass Strength on Glacial Valley Cross-Profile Morphometry: A Case Study from the Southern Alps, New Zealand. Earth Surf. Process. Landforms, 17: 39-51.

Barker, R.D., 1989. Depth of investigation of collinear symmetrical four-electrode arrays. Geophysics, 54(8): 1031-1037.

Barnes, P., Tabor, D. and Walker, J.C.F., 1971. Friction and creep of polycrystalline ice. Proc. of the Royal Society of London, Series A, 324(1557): 127-155.

Barsch, D., 1993. Periglacial geomorphology in the 21st century. Geomorphology, 7: 141-163.

Barton, N. and Choubey, V., 1977. The shear strength of rock joints in theory and practise. Rock Mech., 10: 1-54.

Bearth, P., 1980. Geologische Karte St. Niklaus 1:25.000, Geologischer Atlas der Schweiz. Schweizer Geologische Kommission, Basel.

Beniston, M., 2004. Climatic Change and its Impacts: An overview focusing on Switzerland. Kluwer Academic Publishers, Dordrecht.

Berkowitz, B., 2002. Characterizing flow and transport in fractured geological media: A review. Advances in Water Resources, 25(8-12): 861-884.

Binley, A. and Kemna, A., 2005. Electrical methods. In: Y. Rubin and S.S. Hubbard (Editors), Hydrogeophysics. Springer: 129-156.

Binley, A., Ramiraz, A. and Daily, W., 1995. Regularised image reconstruction of noisy electrical resistance tomography data, 4th Workshop of the European Concerted Action on Process Tomography, Bergen, Norway.

Blaschek, R., Hördt, A. and Kemna, A., 2008. A new sensitivity-controlled focusing regularization scheme for the inversion of induced polarization data based on the minimum gradient support. Geophysics, 73(2): 45-54.

Bottino, G., Chiarle, M., Joly, A. and Mortara, G., 2002. Modelling rock avalanches and their relation to permafrost degradation in glacial environments. Permafrost and Periglac. Process., 13(4): 283-288.

Brunsden, D., 2004. Relaxation time. In: A. Goudie (Editor), Encyclopedia of Geomorphology. Routledge, London: 838-840.

Brunsden, D. and Thornes, J.B., 1979. Landscape sensitivity and change. Transactions of the British Institute of Geographers, 4(4): 463-484.

Budd, W.F. and Jacka, T.H., 1989. A review of ice rheology for ice-sheet modeling. Cold Regions Science and Technology, 16: 107-144.

Bussian, A.E., 1983. Electrical conductance in a porous medium. Geophysics, 48(9): 1258-1268.

Chan, T., Christiansson, R., Boulton, G.S., Ericsson, L.O., Hartikainen, J., Jensen, M.R., Mas Ivars, D., Stanchell, F.W., Vistrand, P. and Wallroth, T., 2005. DECOVALEX III BMT3/BENCHPAR WP4: The thermo-hydro-mechanical responses to a glacial cycle and their potential implications for deep geological disposal of nuclear fuel waste in a fractured crystalline rock mass. International Journal of Rock Mechanics and Mining Sciences, 42(5-6): 805-827.

Chang, S.-H., Lee, C.-I. and Jeon, S., 2002. Measurement of rock fracture toughness under modes I and II and mixed-mode conditions by using disc-type specimens. Engineering Geology, 66(1-2): 79-97.

Choi, J.S., Ryu, H.H., Lee, I.M. and Cho, G.C., 2006. Rock mass classification using electrical resistivity - An analytical study. In: S.S. Lee, J.H. Lee, S.J. Song and M.Y. Choi (Editors), Advanced Nondestructive Evaluation. Key engineering materials. Trans Tech Publications LTD, Zurich-Uetikon: 1411-1414.

Chorley, R.J. and Kennedy, B.A., 1971. Physical Geography - A Systems Approach. Prentice-Hall, London.

Crosta, G.B., Hungr, O., Sosio, R. and Frattini, P., 2007. Dynamic analysis of the Punta Thurwieser rock avalanche. Geophysical Research Abstracts, 9: 09602.

Cruden, D.M., 2003. The shapes of cold, high mountains in sedimentary rocks. Geomorphology, 55(1-4): 249-261.

Davies, M.C.R., Hamza, O. and Harris, C., 2001. The effect of rise in mean annual temperature on the stability of rock slopes containing ice-filled discontinuities. Permafrost and Perigl. Process., 12(1): 137-144.

Davies, M.C.R., Hamza, O. and Harris, C., 2003. Physical modelling of permafrost warming in rock slopes. In: M. Phillips, S. Springman and L. Arenson (Editors), 8th Int. Con. on Permafrost. Balkema, Zürich: 169-174.

Davies, M.C.R., Hamza, O., Lumsden, B.W. and Harris, C., 2000. Laboratory measurements of the shear strength of ice-filled rock joints. Annals of Glaciology, 31: 463-467.

Day-Lewis, F.D., Singha, K. and Binley, A.M., 2005. Applying petrophysical models to radar travel time and electrical resistivity tomograms: Resolution-dependent limitations. Journal of Geophysical Research - Solid Earth, 110(B8): B08206.

Deline, P., 2002. Etude géomorphologique des interactions écroulement rocheux/glaciales dans la haut montagne alpine (versant sud-est du massif Mont Blanc). Ph.D. Thesis, Universite de Savoie, Bourget du Lac.

Deline, P., Jaillet, S., Rabatel, A. and Ravanel, L., 2008. Ground-Based LiDAR data on permafrost-related rock fall activity in the Mont-Blanc massif. In: D.L. Kane and K.M. Hinkel (Editors), 9th Int. Conf. on Permafrost. Inst. of. North. Engineering, UAF, Fairbanks, Alsaka, US: 349-354.

Deparis, J., Fricout, B., Jongmans, D., Villemin, T., Effendiantz, L. and Mathy, A., 2008. Combined use of geophysical methods and remote techniques for characterizing the fracture network of a potentially unstable cliff site (the 'Roche du Midi', Vercors massif, France). Journal of Geophysics and Engineering, 5(2): 147-157.

Dey, A. and Morrison, H.F., 1979. Resistivity modelling for arbitrarily shaped two-dimensional structures. Geophysical Prospecting, 27: 106-136.

Dikau, R., 2006. Komplexe Systeme in der Geomorphologie. Mitt. Österr. Geogr. Ges., 148: 125-150.

Dorren, L.K.A., 2003. A review of rockfall mechanics and modelling approaches. Progress in Physical Geography, 26(1): 69-87.

Eberhardt, E., Spillmann, T., Maurer, H., Willenberg, H., Loew, S. and Stead, D., 2004. The Randa Rockslide Laboratory: Establishing brittle and ductile instability mechanisms using numerical modelling and microseismicity, 9th Int. Symposium of Landslides A.A. Balkema, Rio de Janeiro: 481-487.

Edwards, L.S., 1977. A modified pseudosection for resistivity and IP. Geophysics, 42(5): 1020-1036.

Erismann, T.H. and Abele, G., 2001. Dynamics of Rockslides and Rockfalls. Springer, Heidelberg.

Fischer, L. and Huggel, C., 2008. Methodical Design for Stability Assessments of Permafrost-Affected High-Mountain Rock Walls. In: D.L. Kane and K.M. Hinkel (Editors), 9th Int. Conf. on Permafrost. INE-UAF, Fairbanks, Alaska, US: 439-444.

Fischer, L., Huggel, C. and Lemy, F., 2007. Investigation and modeling of periglacial rock fall events in the European Alps. Geophysical Research Abstracts, 9: 08160.

Fischer, L., Kääb, A., Huggel, C. and Noetzli, J., 2006. Geology, glacier retreat and permafrost degradation as controlling factors of slope instability in a high-mountain rock wall: the Monte Rosa east face. Nat. Hazards Earth Syst. Sci., 6: 761-772.

Fleming, R.W. and Johnson, A.M., 1989. Structures associated with strike-slip faults that bound landslide elements. Eng. Geol., 27: 39-114.

Frauenfelder, R., 2005. Regional-scale modelling of the occurrence and dynamics of the distribution of paleopermafrost. Ph.D. Thesis, University of Zurich, Zurich.

French, H. and Thorn, C.E., 2006. The changing nature of periglacial geomorphology. Géomorphologie: relief, processus, environnement, 3: 1-13.

Friedel, S., Thielen, A. and Springman, S.M., 2006. Investigation of a slope endangered by rainfall-induced landslides using 3D resistivity tomography and geotechnical testing. Journal of Applied Geophysics, 60(2): 100-114.

Glawe, U., 1991. Bericht über die geotechnischen Untersuchungen im Bereiche des Waxensteinkammes. Unpublished report for the Geological Survey of Bavaria.

Gruber, S., 2005. Mountain Permafrost: Transient spatial modelling, model verification and the use of remote sensing. Ph.D. Thesis, Universität Zurich, Zurich.

Gruber, S. and Haeberli, W., 2007. Permafrost in steep bedrock slopes and its temperature-related destabilization following climate change. Journal of Geophysical Research - Earth Surface, 112(F2): F02S13.

Gruber, S. and Hoelzle, M., 2001. Statistical modelling of mountain permafrost distribution: Local calibration and incorporation of remotely sensed data. Permafrost and Periglac. Process., 12(1): 69-77.

Gruber, S., Hoelzle, M. and Haeberli, W., 2004a. Permafrost thaw and destabilization of Alpine rock walls in the hot summer of 2003. Geophys. Res. Lett., 31(13): L15054.

Gruber, S., Hoelzle, M. and Haeberli, W., 2004b. Rock-wall temperatures in the Alps: Modelling their topographic distribution and regional differences. Permafrost and Periglac. Process., 15(3): 299-307.

Gruber, S., Peter, M., Hoelzle, M., Woodhatch, I. and Haeberli, W., 2003. Surface temperatures in steep alpine rock faces – A strategy for regional-scale measurement and modelling. In: M. Phillips, S. Springman and L. Arenson (Editors), 8th International Conference on Permafrost, Proceedings. Swets & Zeitlinger, Lisse, Zürich: 325-330.

Gude, M. and Barsch, D., 2005. Assessment of the geomorphic hazards in connection with permafrost occurrence in the Zugspitze area (Bavarian Alps, Germany). Geomorphology, 66(1-4): 85-93.

Guenzel, F., 2008. Shear Strength of Ice-Filled Rock Joints. In: D.L. Kane and K.M. Hinkel (Editors), 9th Int. Conf. on Permafrost. INE-UAF, Fairbanks, Alaska, US: 581-586.

Hack, J., 1960. Interpretation of erosional topography in humid temperate regions. Am. J. Sci., 258-A: 80-97.

Haeberli, W., 1992. Construction, environmental problems and natural hazards in periglacial mountain belts. Permafrost and Periglac. Process., 3: 111-124.

Haeberli, W., 2005. Investigating glacier-permafrost relationships in high-mountain area: historical background, selected examples and research needs. In: C. Harris and J.B. Murton (Editors), Cryospheric Systems: Glaciers and Permafrost. Geological Society Special Publication, London: 29-37.

Haeberli, W. and Beniston, M., 1998. Climate change and its impact on glaciers and permafrost in the Alps. Ambio, 27: 258-265.

Haeberli, W., Huggel, C., Kääb, A., Polkvoj, A., Zotikov, I. and Osokin, N., 2003. Permafrost conditions in the starting zone of the Kolka-Kamadon rock/ice-slide of the 20th September 2002 in North Osetia (Russian Caucasus). . In: W. Haeberli and D. Brandova (Editors), ICOP 2003 Permafrost: Extended Abstracts, Zürich: 49-50.

Haeberli, W., Huggel, C., Kääb, A., Zgraggen-Oswald, S., Polkvoj, A., Galushkin, I., Zotikov, I. and Osokin, N., 2004. The Kolka-Karmadon rock/ice slide of 20 September 2002: an extraordinary event of historical dimensions in North Ossetia, Russian Caucasus. Journal of Glaciology, 50: 533-546.

Haeberli, W., Wegmann, M. and Vonder Mühll, D., 1997. Slope stability problems related to glacier shrinkage and permafrost degradation in the Alps. Eclogae Geologicae Helvetiae, 90: 407-414.

Hall, K., Thorn, C.E., Matsuoka, N. and Prick, A., 2002. Weathering in cold regions: some thoughts and perspectives. Progress in Phys. Geogr., 26(4): 577-603.

Hansen, M.J., 1984. Strategies for classification of landslides. In: D. Brunsden and D.B. Prior (Editors), Slope Instability. Wiley, Chichester.

Hanson, S. and Hoelzle, M., 2004. The thermal regime of the active layer at the Murtel rock glacier based on data from 2002. Permafrost and Periglac. Process., 15(3): 273-282.

Harris, C., Arenson, L.U., Christiansen, H.H., Etzelmüller, B., Frauenfelder, R., Gruber, S., Haeberli, W., Hauck, C., Hölzle, M., Humlum, O., Isaksen, K., Kääb, A., Kern-Lütschg, M.A., Lehning, M., Matsuoka, N., Murton, J.B., Nötzli, J., Phillips, M., Ross, N., Seppälä, M., Springman, S.M. and Vonder Mühll, D., 2009. Permafrost and climate in Europe: Monitoring and modelling thermal, geomorphological and geotechnical responses. Earth-Science Reviews, 92(3-4): 117-171.

Harris, C., Davies, M.C.R. and Etzelmüller, B., 2001. The assessment of potential geotechnical hazards associated with mountain permafrost in a warming global climate. Permafrost and Perigl. Process., 12(1): 145-156.

Harris, C., Davies, M.C.R. and Rea, B.R., 2003a. Gelifluction: viscous flow or plastic creep? Earth Surf. Process. Landforms, 28(12): 1289-1301.

Harris, C., Vonder Mühll, D., Isaksen, W., Haeberli, W., Sollid, J.L., King, L., Homlund, P., Dramis, F., Guglielmin, M. and Palacios, D., 2003b. Warming permafrost in European mountains. Global and Planetary Change, 39(3-4): 215-225.

Hasler, A., Talzi, I., Beutel, J., Tschudin, C. and Gruber, S., 2008. Wireless Sensor Networks in Permafrost Research: Concept, Requirements, Implementation, and Challenges. In: D.L. Kane and K.M. Hinkel (Editors), 9th Int. Conf. on Permafrost. INE-UAF, Fairbanks, Alaska, US: 669-674.

Hauck, C., 2001. Geophysical methods for detecting permafrost in high mountains. Ph.D. Thesis, ETH Zurich, Zurich.

Hauck, C., 2002. Frozen ground monitoring using DC resistivity tomography. Geophys. Res. Lett., 29(21): 2016.

Hauck, C., Bach, M. and Hilbich, C., 2008. A four-phase model to quantify subsurface ice content in permafrost regions based on geophysical data sets. In: D.L. Kane and K.M. Hinkel (Editors), 9th Int. Conf. on Permafrost. Institute of Northern Engineering, UAF, Fairbanks, US: 675-680.

Hauck, C. and Vonder Mühll, D., 2003. Inversion and interpretation of two-dimensional geoelectrical measurements for detecting permafrost in mountainous regions. Permafrost Periglac. Process., 14(4): 305-318.

Hayley, K., Bentley, L.R., Gharibi, M. and Nightingale, M., 2007. Low temperature dependence of electrical resistivity: Implications for near surface monitoring. Geophysical Research Letters, 34: L18402.

Heincke, B., Green, A.G., van der Kruk, J. and Willenberg, H., 2006a. Semblance-based topographic migration (SBTM): a method for identifying fracture zones in 3-D georadar data. Near Surface Geophysics, 4(2): 79-88.

Heincke, B., Maurer, H., Green, A.G., Willenberg, H., Spillmann, T. and Burlini, L., 2006b. Characterizing an unstable mountain slope using shallow 2-D and 3-D seismic tomography. Geophysics, 71(6): 241-256.

Hera, U., 1997. Gletscherschwankungen in den Nördlichen Kalkalpen seit dem 19. Jh. Münchner Geogr. Abh. Reihe B, 25: 1-205.

Herwanger, J.V., Pain, C.C., Binley, A., de Oliveira, C.R.E. and Worthington, M.H., 2004. Anisotropic resistivity tomography. Geophysical Journal International, 158(2): 409-425.

Hewitt, K., Clague, J.J. and Orwin, J.F., 2008. Legacies of catastrophic rock slope failures in mountain landscapes. Earth-Science Reviews, 87(1-2): 1-38.

Hilbich, C., Hauck, C., Hoelzle, M., Scherler, M., Schudel, L., Voelksch, I., Muehll, D.V. and Maeusbacher, R., 2008. Monitoring mountain permafrost evolution using electrical resistivity tomography: A 7-year study of seasonal, annual, and long-term variations at Schilthorn, Swiss Alps. Journal of Geophysical Research - Earth Surface, 113(F1): F01590.

Hirtlreiter, G., 1992. Spät- und postglaziale Gletscherschwankungen im Wettersteingebirge und seiner Umgebung. Münchner Geographische Abhandlungen, Beihe B, 15: 1-154.

Hoek, E., 2007. Practical Rock Engineering. Rocscience EBooks.

Hoek, E. and Bray, J., 1981. Rock Slope Engineering. Institution of Mining and Metallurgy, London.

Hoelze, M., 1994. Permafrost und Gletscher im Oberengadin. Grundlagen und Anwendungsbeispiele für automatisierte Schätzverfahren. VAW Mitteilungen, 132: 1-121.

Hoelzle, M., Mittaz, C., Etzelmüller, B. and Haeberli, W., 2001. Surface energy fluxes and distribution models of permafrost in European mountain areas: an overview of current developments. Permafrost and Periglac. Process., 12(1): 53-68.

Holcombe, H.T. and Jiracek, G.R., 1984. Three-dimensional terrain corrections in resistivity surveys. Geophysics, 49(4): 439-452.

Hormes, A., Muller, B.U. and Schluchter, C., 2001. The Alps with little ice: evidence for eight Holocene phases of reduced glacier extent in the Central Swiss Alps. Holocene, 11(3): 255-265.

Hovius, N., Lague, D. and Dadson, S., 2004. Processes, rates and patterns of mountain belt erosion. In: P.N. Owens and O. Slaymaker (Editors), Mountain Geomorphology. Arnold, London.

Huggel, C., in press. Recent extreme slope failures in glacial environments: effects of thermal perturbation. Quaternary Science Reviews.

Huggel, C., Gruber, S., Caplan-Auerbach, J., Wessels, R.L. and Molnia, B.F., 2008. The 2005 Mt. Steller, Alaska, Rock-Ice Avalanche: A Large Slope Failure in Cold Permafrost. In: D.L. Kane and K.M. Hinkel (Editors), 9th Int. Conf. on Permafrost. INE-UAF, Fairbanks, Alaska, US: 747-752.

Hungr, O., Evans, S.G. and Hazzard, J., 1999. Magnitude and frequency of rock falls and rock slides along the main transportation corridors of southwestern British Columbia. Canadian Geotechnical Journal, 36(2): 224-238.

Hurrel, J.W. and van Loon, H., 1997. Decadal variations in climate associated with the North Atlantic oscillation. Climatic Change, 36: 301-306.

Isaksen, K., Benestad, R.E., Harris, C. and Sollid, J.L., 2007. Recent extreme near-surface permafrost temperatures on Svalbard in relation to future climate scenarios. Geophysical Research Letters, 34(17): L17502.

Ivy-Ochs, S., Kerschner, H., Kubik, P.W. and Schluchter, C., 2006. Glacier response in the European Alps to Heinrich Event 1 cooling: the Gschnitz stadial. Journal of Quaternary Science, 21(2): 115-130.

Jaeger, J.C., Cook, N.G.W. and Zimmerman, R.W., 2007. Fundamentals of Rock Mechanics. Blackwell Publishing, Oxford.

Jähnert, S., Chavez, F.V., Schaumann, G.E., Schreiber, A., Schonhoff, M. and Findenegg, G.H., 2008. Melting and freezing of water in cylindrical silica nanopores. Physical Chemistry Chemical Physics, 10(39): 6039-6051.

Jerz, H. and Poschinger, A.v., 1995. Neuere Ergebnisse zum Bergsturz Eibsee-Grainau. Geologica Bavarica, 99: 383-398.

Jerz, U., 1999. Nacheiszeitliche Bergstürze in den Bayerischen Alpen. Relief, Boden, Paläoklima, 14: 31-40.

Jorgenson, M.T., Shur, Y.L. and Pullman, E.R., 2006. Abrupt increase in permafrost degradation in Arctic Alaska. Geophysical Research Letters, 33(2): L02503.

Jouniaux, L., Zamora, M. and Reuschle, T., 2006. Electrical conductivity evolution of non-saturated carbonate rocks during deformation up to failure. Geophysical Journal International, 167(2): 1017-1026.

Jungo, P. and Beniston, M., 2001. Changes in the anomalies of extreme temperatures in the 20th century at Swiss climatological stations located at different latitudes and altitudes. Theor. and Appl. Clim., 69: 1-12.

Kääb, A., Wessels, R., Haeberli, W., Huggel, C., Kargel, J.S. and Khalsa, S.J., 2003. Rapid aster imaging facilitates timely assessments of glacier hazards and disasters. EOS, 13(84): 117, 121.

Keller, F. and Gubler, H.U., 1993. Interaction between snow cover and mountain permafrost, Murtèl-Corvatsch, Swiss Alps, 6th Int. Conf. on Permafrost. South China University of Technology Press, Beijing, China: 332-337.

Keller, G.V. and Frischknecht, F.C., 1966. Electrical Methods in Geophysical Prospecting. Pergamon Press, Oxford.

Kemeny, J., 2003. The time-dependent reduction of sliding cohesion due to rock bridges along discontinuities: A fracture mechanics approach. Rock. Mech. Rock Eng., 36(1): 27-38.

Kemna, A., 2000. Tomographic inversion of complex resistivity—Theory and application. Ph.D. Thesis, University of Bochum, Bochum.

Kleinberg, R.L. and Griffin, D.D., 2005. NMR measurements of permafrost: unfrozen water assay, pore-scale distribution of ice, and hydraulic permeability of sediments. Cold Regions Science and Technology, 42(1): 63-77.

Kneisel, C., 2006. Assessment of subsurface lithology in mountain environments using 2D resistivity imaging. Geomorphology, 80(1-2): 32-44.

Kneisel, C., Hauck, C., Fortier, R. and Moorman, B., 2008. Advances in geophysical methods for permafrost investigations. Permafrost and Perigl. Process., 19(2): 157-178.

Koestel, J., Kemna, A., Javaux, M., Binley, A. and Vereecken, H., 2008. Quantitative imaging of solute transport in an unsaturated and undisturbed soil monolith with 3D ERT and TDR. Water Resour. Res., 44(12): W12411.

Kohl, T., 1999. Transient thermal effects below complex topographies. Tectonophysics, 306(3-4): 311-324.

Kohl, T. and Gruber, S., 2003. Evidence of paleotemperature signals in mountain permafrost areas, 8th Int. Conf. on Permafrost, Zurich: 83-84.

Kolditz, O., 2001. Non-linear flow in fractured rock. International Journal of Numerical Methods for Heat & Fluid Flow, 11(6): 547-575.

Körner, H. and Ulrich, R., 1965. Geologische und felsmechanische Untersuchungen für die Gipfelstation der Seilbahn Eibsee - Zugspitze. Geologica Bavarica, 55: 404-421.

Korup, O., 2008. Rock type leaves topographic signature in landslide-dominated mountain ranges. Geophysical Research Letters, 35(11): L11402.

Krautblatter, M., 2008. Rock Permafrost Geophysics and its Explanatory Power for Permafrost-Induced Rockfalls and Rock Creep: a Perspective. In: D.L. Kane and K.M. Hinkel (Editors), 9th Int. Conf. on Permafrost. INE-UAF, Fairbanks, Alaska, US: 999-1004.

Krautblatter, M. and Dikau, R., 2007. Towards a uniform concept for the comparison and extrapolation of rockwall retreat and rockfall supply. Geografiska Annaler, 89 A(1): 21-40.

Krautblatter, M. and Hauck, C., 2007. Electrical resitivity tomography monitoring of permafrost in solid rock walls. Journal of Geophysical Research - Earth Surface, 112(F2): F02S20.

Krautblatter, M., Hauck, C. and Wolf, S., 2007. Geophysical 2D and 3D-monitoring of permafrost in rock walls. Geophysical Research Abstracts, 9: A-09884.

Krautblatter, M. and Verleysdonk, S., 2008a. Rock wall permafrost monitoring with high-resolution 2D-ERT: lessons learnt from error estimates and a comparison of Wenner, Schlumberger, Gradient and Dipole-type arrays. Geophysical Research Abstracts, 10: A-10383.

Krautblatter, M. and Verleysdonk, S., 2008b. Thawing regime and response time of present-day and relict permafrost revealed by monthly geophysical monitoring (Zugspitze, German/Austrian Alps). Geophysical Research Abstracts, 10: A-10455.

Krus, M., 1995. Feuchtetransport und Speicherkoeffizienten poröser mineralischer Baustoffe - theoretische Grundlagen und neue Meßtechniken. Ph.D. Thesis, University of Stuttgart, Stuttgart.

Kukkonen, I.T. and Safanda, J., 2001. Numerical modelling of permafrost in bedrock in northern Fennoscandia during the Holocene. Global and Planetary Change, 29: 259-274.

LaBrecque, D.J., Miletto, M., Daily, W., Ramirez, A. and Owen, E., 1996. The effects of noise on Occam's inversion of resistivity tomography data. Geophysics, 61(2): 538-548.

Lachenbruch, A.H. and Marshall, B.V., 1986. Changing Climate - Geothermal Evidence from Permafrost in the Alaskan Arctic. Science, 234(4777): 689-696.

Lautridou, J.P., 1988. Recent advances in cryogenic weathering. In: J.M. Clark (Editor), Advances in Periglacial Geomorphology. Wiley, Chichester: 33-47.

Lawrence, D.M. and Slater, A.G., 2005. A projection of severe near-surface permafrost degradation during the 21st century. Geophysical Research Letters, 32(24): L24401.

Le Guen, Y., Renard, F., Hellmann, R., Brosse, E., Collombet, M., Tisserand, D. and Gratier, J.P., 2007. Enhanced deformation of limestone and sandstone in the presence of high P-co2 fluids. Journal of Geophysical Research - Solid Earth, 112(B5): B05421.

Linde, N., 2005. Characterization of Hydrogeological Media using electromagnetic geophysics. Ph.D. Thesis, University of Uppsala, Uppsala.

Lock, G.S.H., 2005. The growth and decay of ice. Studies in Polar Research. University Press, Cambridge.

Loke, M. and Barker, R., 1995. Least-square deconvolution of apparent resistivity pseudosections. Geophysics, 60(6): 1682-1690.

Loke, M.H. and Barker, R.D., 1996. Rapid least-squares inversion of apparent resistivity pseudosections by a quasi-Newton method. Geophysical Prospecting, 44(1): 131-152.

Matias, M.J.S., 2008. Electrical strike imaging and anisotropy diagnosis from surface resistivity measurements. Near Surface Geophysics, 6(1): 49-58.

Matsuoka, N., 1990. The rate of bedrock weathering by frost action: field measurements and a predictive model. Earth Surf. Process. Landforms, 15(1): 73-90.

Matsuoka, N., 2001. Microgelivation versus macrogelivation: Towards bridging the gap between laboratory and field frost weathering. Permafrost and Periglac. Process., 12(3): 299-313.

Matsuoka, N., 2008. Frost weathering: Recent advances and future directions. Permafrost and periglacial processes, 19(2): 195-210.

Maurer, H. and Hauck, C., 2007. Instruments and Methods: Geophysical imaging of alpine rock galciers. Journal of Glaciology, 53(180): 110-120.

McGinnis, L.D., Nakao, K. and Clark, C.C., 1973. Geophysical identification of frozen and unfrozen ground, Antarctica, 2nd Int. Conf. on Permafrost, Yakutsk, Russia: 136-146.

Mears, B., 1997. Pleistocene Gelifluction and Rock Deformation on Slopes in Southern Wyoming. Permafrost and Periglac. Process., 8: 251-255.

Mellor, M., 1973. Mechanical Properties of Rocks at Low Temperatures, 2nd Int. Conference on Permafrost, Yakutsk, Russia: 334-344.

Miller, H., 1961. Der Bau des westlichen Wettersteingebirges. Z. dt. geol. Ges., 113: 409-25.

Mittaz, C., Hoelzle, M. and Haeberli, W., 2000. First results and interpretation of energy-flux measurements over Alpine permafrost. Annals of Glaciology, 31: 275-280.

Montgomery, D.R., 2001. Slope distributions, threshold hillslopes, and steady-state topography. American Journal of Science, 301(4-5): 432-454.

Moon, B.P., 1984. Refinement of a technique for determining rock mass strength fro geomorphological purposes. Earth Surf. Process. Landforms, 9: 183-193.

Moore, I.D., Norton, T.W. and Williams, J.E., 1993. Modeling Environmental Heterogeneity in Forested Landscapes. Journal of Hydrology, 150(2-4): 717-747.

Moorman, B.J., 2005. Glacier-permafrost hydrological interconnectivity: Stagnation Glacier, Bylot Island, Canada. In: C. Harris and J.B. Murton (Editors), Cryospheric Systems: Glaciers and Permafrost. Geological Society Special Publication, London: 63-74.

Murton, J.B., Coutard, J.-P., Lautridou, J.P., Ozouf, J.-C., Robinson, D.A., Williams, R.B.G., Guillemet, G. and Simmons, P., 2000. Experimental design for a pilot study on bedrock weathering near the permafrost table. Earth Surf. Process. Landforms, 25: 1281-1294.

Murton, J.B., Peterson, R. and Ozouf, J.-C., 2006. Bedrock Fracture by Ice Segregation in Cold Regions. Science, 314: 1127-1129.

Musil, M., Maurer, H., Green, A.G., Horstmeyer, H., Nitsche, F., Vonder Mühll, D. and Springman, S., 2002. Shallow seismic surveying of an Alpine rock glacier. Geophysics, 67(6): 1701-1710.

Mustafa, O., 2002. Permafrostverbreitung an der Zugspitze - Modellierung und Geländebefunde. Diploma Thesis, University of Jena, Jena.

Noetzli, J., 2008. Modeling Transient Three-dimensional Temperature Fields in Mountain Permafrost. Ph.D. Thesis, University of Zurich, Zurich.

Noetzli, J., Gruber, S., Kohl, T., Salzmann, N. and Haeberli, W., 2006. Transient modeling of ground temperatures in an idealized high mountain topography. Geophys. Res. Abstracts, 8: A01957.

Noetzli, J., Gruber, S., Kohl, T., Salzmann, N. and Haeberli, W., 2007. Three-dimensional distribution and evolution of permafrost temperatures in idealized high-mountain topography. Journal of Geophysical Research - Earth Surface, 112(F2): F02S13.

Noetzli, J., Hoelzle, M. and Haeberli, W., 2003. Mountain permafrost and recent Alpine rock-fall events: a GIS-based approach to determine critical factors. In: M. Phillips, S. Springman and L. Arenson (Editors), 8th International Conference on Permafrost. Swets & Zeitlinger, Zurich.

Nogués-Bravo, D., Araújo, M.B., Errea, M.P. and Martínez-Rica, J.P., 2007. Exposure of global mountain systems to climate warming during the 21st Century. Global Environmental Change, 17: 420-428.

Norton, J.J. and Redden, J.A., 1960. Structure Associated with Rock Creep in the Black Hills, South-Dakota. Geological Society of America Bulletin, 71(7): 1109-1112.

NRC-Permafrost-Subcommitee, 1988. Glossary of Permafrost and related ground-ice terms. NRC Technical Memorandum, 142: 1-156.

Oldenburg, D.W. and Li, Y.G., 1999. Estimating depth of investigation in DC resistivity and IP surveys. Geophysics, 64(2): 403-416.

Otto, J.C. and Dikau, R., 2004. Geomorphologic system analysis of a high mountain valley in the Swiss Alps. Z. Geomorph. N.F., 48(3): 323-341.

Otto, J.C. and Sass, O., 2006. Comparing geophysical methods for talus slope investigations in the Turtmann valley (Swiss Alps). Geomorphology, 76(3-4): 257-272.

Paterson, W.S.B., 2001. The Physics of Glaciers. Butterworth & Heinemann, Oxford.

Patton, F.D., 1966. Multiple modes of shear failure in rock, 1st Congress Int. Society for Rock Mech. Lab. of Civil Engineering, Lisbon, Portugal: 509-513.

Pearson, C., Murphy, J., Halleck, P., Hermes, R. and Mathews, M., 1983. Sonic and resistivity measurements on Berea sandstone containing tetrahydrofuran hydrates: a possible analog to natural gas hydrate deposits, 4th Int. Conf. On Permafrost. UAF, Fairbanks, Alaska, US: 973-978.

Penck, W., 1924. Die morphologische Analyse. J. Engelshorn Verlag, Stuttgart.

Peter, M., 2003. Untersuchungen von Felstemperaturen im alpinen Permafrost. Diploma Thesis, University of Zurich, Zurich.

Petley, D.N. and Petley, D.J., 2005. On the initiation of large rockslides: perspectives from a new analysis of the Vajont movement record. In: S. Evans (Editor), Large Rock Slope Failures. Kluwer, Rotterdam (Nato Science Series).

Phillips, J.D., 2006. Evolutionary geomorphology: thresholds and nonlinearity in landform response to environmental change. Hydrology and Earth System Sciences, 10(5): 731-742.

Pogrebiskiy, M.I. and Chernyshev, S.N., 1977. Determination of the Permeability of the Frozen Fissured Rock Massif in the Vicinity of the Kolyma Hydroelectric Power Station. Cold Regions Research and Engineering Laboratory - Draft Translation, 634: 1-13.

Prager, C., Zangerl, C., Patzelt, G. and Brandner, R., 2008. Age distribution of fossil landslides in the Tyrol (Austria) and its surrounding areas. Natural Hazards and Earth System Sciences, 8(2): 377-407.

Prinz, H., 1997. Abriß der Ingenieurgeologie. Enke, Stuttgart.

Quinton, W.L. and Carey, S.K., 2008. Towards an energy-based runoff generation theory for tundra landscapes. Hydrological Processes, 22(23): 4649-4653.

Quinton, W.L., Shirazi, T., Carey, S.K. and Pomeroy, J.W., 2005. Soil water storage and active-layer development in a sub-alpine tundra hillslope, southern YukonTerritory, Canada. Permafrost and Periglac. Process., 16(4): 369-382.

Rabatel, A., Deline, P., Jaillet, S. and Ravanel, L., 2008. Rock falls in high-alpine rock walls quantified by terrestrial lidar measurements: A case study in the Mont Blanc area. Geophys. Res. Lett., 35(10): L10502.

Ravanel, L., Deline, P., Jaillet, S. and Rabatel, A., 2008. Quantifying rock falls/avalanches in steep high-alpine rock walls: three years of laserscanning in the MontBlanc massif. Geophysical Research Abstracts, 10: 10361.

Renshaw, C.E. and Schulson, E.M., 2001. Universal behaviour in compressive failure of brittle materials. Nature, 412(6850): 897-900.

Renwick, W.H., 1992. Equilibrium, Disequilibrium, and Nonequilibrium Landforms in the Landscape. Geomorphology, 5(3-5): 265-276.

Roberts, J.J., 2002. Electrical properties of microporous rock as a function of saturation and temperature. Journal of Applied Physics, 91(3): 1687-1694.

Salzmann, N., Noetzli, J., Gruber, S., Hoelzle, M. and Haeberli, W., 2007. Ground-surface temperature scenarios for complex high-mountain topography based on regional climate model results. Journal of Geophysical Research - Earth Surface, 112(F2): F02S12.

Sanderson, T., 1988. Ice mechanics and risks to offshore structures. Springer, Amsterdam.

Sass, O., 1998. Die Steuerung von Steinschlagmenge durch Mikroklima, Gesteinsfeuchte und Gesteinseigenschaften im westlichen Karwendelgebirge. Münchner Geogr. Abh., Reihe B, 29: 1-175.

Sass, O., 2003. Moisture distribution in rockwalls derived from 2D-resistivity measurements. Z. Geomorph. N.F., Suppl.-Bd., 132: 51-69.

Sass, O., 2004. Rock moisture fluctuations during freeze-thaw cycles: Preliminary results from electrical resistivity measurements. Polar Geography, 28(1): 13-31.

Sass, O., 2005a. Rock moisture measurements: Techniques, results, and implications for weathering. Earth Surf. Process. Landforms, 30(3): 359-374.

Sass, O., 2005b. Spatial patterns of rockfall intensity in the northern Alps. Z. Geomorph. N.F., Suppl.-Bd. 138: 51-65.

Sass, O., Krautblatter, M. and Morche, D., 2007. Rapid lake infill following major rockfall (bergsturz) events revealed by ground-penetrating radar (GPR) measurements, Reintal, German Alps. Holocene, 17(7): 965-976.

Schoeneich, P., Hantz, D., Vengon, M., Frayssines, M., Deline, P., Amelot, F. and Savary, J., 2004. A new Alpine rockfall inventory, Swiss Geoscience Meeting, Lausanne.

Seguin, M.K., 1978. Temperature-electrical resistivity relationship in continuous permafrost at Purtuniq, Ungava Peninsula. In: C.B. Crawford (Editor), 3rd Int. Conf. on Permafrost. NRC, Edmonton, Canada.

Selby, M.J., 1980. A rock mass strength classification for geomorphic purposes. Z. Geomorph. N. F., 24: 31-51.

Selby, M.J., 1989. Rock Slopes. In: M.G. Anderson and K.S. Richards (Editors), Slope stability. Wiley, Chichester.

Singha, K. and Gorelick, S.M., 2006. Effects of spatially variable resolution on field-scale estimates of tracer concentration from electrical inversions using Archie's law. Geophysics, 71(3): G83-G91.

Slater, L. and Binley, A., 2006. Synthetic and field-based electrical imaging of zerovalent iron barrier: Implications for monitoring long-term barrier performance. Geophysics, 71: 129-137.

Slater, L., Binley, A., Daily, W. and Johnson, R., 2000. Cross-hole electrical imaging of a controlled saline tracer injection. Journal of Applied Geophysics, 44: 85-102.

Sliwinska-Bartkowiak, M., Jazdzewska, M., Huang, L.L. and Gubbins, K.E., 2008. Melting behavior of water in cylindrical pores: carbon nanotubes and silica glasses. Physical Chemistry Chemical Physics, 10(32): 4909-4919.

Soldati, M., Corsini, A. and Pasuto, A., 2004. Landslides and climate change in the Italian Dolomites since the Late glacial. Catena, 55(2): 141-161.

Springman, S. and Arenson, L., 2008. Recent advances in permafrost geophysics. In: D.L. Kane and K.M. Hinkel (Editors), 9th Int. Conf. on Permafrost. INE-UAF, Fairbanks, Alaska, US: 1685-1694.

Springman, S.M., Jommi, C. and Teysseire, P., 2003. Instabilities on moraine slopes induced by loss of suction: a case history. Geotechnique, 53(1): 3-10.

Stocker-Mittaz, C., Hoelzle, M. and Haeberli, W., 2002. Permafrost distribution modeling based on energy-balance data: a first step. Permafrost and Periglac. Process., 13(4): 271-282.

Tang, G.Z. and Wang, X.H., 2006. Modeling the thaw boundary in broken rock zones in permafrost in the presence of surface water flows. Tunnelling and Underground Space Technology, 21(6): 684-689.

Telford, W.M., Geldart, L.P. and Sheriff, R.E., 1990. Applied Geophysics. University Press, Cambridge.

Terrana, S., Gambillara, R., Scesi, L. and Figaroli, M., 2005. Fissured aquifer in north-western area of Como lake basin: permeability calculation and relation with springs (central western Como lake, Italy). Geophys. Res. Abstracts, 7: A07069.

Terzaghi, K., 1962. Stability of steep slopes in hard unweathered rock. Geotechnique, 12: 251-270.

Tinner, W., Kaltenrieder, P., Soom, M., Zwahlen, P., Schmidhalter, M., Boschetti, A. and Schluchter, C., 2005. The postglacial rockfall in the Kander valley (Switzerland): ge and effects on palaeo-environments. Eclogae Geologicae Helvetiae, 98(1): 83-95.

Ulrich, R. and King, L., 1993. Influence of mountain permafrost on construction in the Zugspitze mountains, Bavarian Alps, Germany, 6th Int. Conf. on Permafrost, Bejing: 625-630.

Varnes, D.J., 1978. Slope Movement Types and Processes. In: R.L. Schuster and R.J. Krizek (Editors), Landslides Analysis and control. TRB, Special Report National Research Council, Washington, D.C.: 11-33.

Viles, H.A., 2001. Scale issues in weathering studies. Geomorphology, 41(1): 63-72.

Vogel, H.J., Cousin, I., Ippisch, O. and Bastian, P., 2006. The dominant role of structure for solute transport in soil: experimental evidence and modelling of structure and transport in a field experiment. Hydrology and Earth System Sciences, 10(4): 495-506.

Vosteen, H.D. and Schellschmidt, R., 2003. Influence of temperature on thermal conductivity, thermal capacity and thermal diffusivity for different types of rock. Phys. and Chem. of the Earth, 28(9-11): 499-509.

Wagner, W., Saul, A. and Pruß, A., 1994. International Equations for the Pressure along the Melting and along the Sublimation Curve of Ordinary Water Substance. J. Phys. Chem. Ref. Data, 23(3): 516-527.

Weertman, J., 1973. Creep of ice. In: E. Whalley, S.J. Jones and L.W. Gold (Editors), Physics and Chemistry of Ice. Royal Soc. of Canada, Ottawa: 320-337.

Wegmann, M., 1998. Frostdynamik in hochalpinen Felswänden am Beispiel der Region Jungfraujoch - Aletsch. Ph.D. Thesis, ETH Zurich, Zurich.

Wegmann, M., Gudmundsson, G.H. and Haeberli, W., 1998. Permafrost changes in rock walls and the retreat of Alpine glaciers: a thermal modelling approach. Permafrost and Periglac. Process., 9: 23-33.

Witherspoon, P.A., 2000. Inverstigations at Berkeley on Fracture Flow in Rock: From Parallel Plate Model to Chaotic Systems In: B. Faybishenko, P.A. Witherspoon and S.M. Benson (Editors), Dynamics of fluids in fractured rocks. American Geophysical Union, Washington D.C.: 1-58.

Wyllie, D.C. and Norrish, N.I., 1996. Rock strength properties and their measurement. In: A.K. Turner and R.L. Schuster (Editors), Landslides: Inverstigation and Mitigation. Transportation Research Board Special Report. NRC, Washington: 372-390.

Yershov, E.D., 2004. General Geocryology. University Press, Cambridge.

Zarnetske, J.P., Gooseff, M.N., Brosten, T.R., Bradford, J.H., McNamara, J.P. and Bowden, W.B., 2007. Transient storage as a function of geomorphology, discharge, and permafrost active layer conditions in Arctic tundra streams. Water Resources Research, 43(7): W07410.

Zisser, N. and Nover, G., in press. Anisotropy of permeability and complex resistivity of tight sandstones subjected to hydrostatic pressure. Journal of Applied Geophysics.

Zisser, N., Nover, G., Durrast, H. and Siegesmund, S., 2007. Relationship between electrical and hydraulic properties of sedimentary rocks. Zeitschrift dt. Gesellschaft für Geowissenschaften, 158(4): 883-894.